Influence of alloying and processing on the degradation behaviour of Mg-Zn based alloys

Dissertation

zur Erlangung des akademischen Grades
Doktor der Ingenieurwissenschaften
(Dr.-Ing.)
der Technischen Fakultät
der Christian-Albrechts-Universität zu Kiel

vorgelegt von

Yiming Jin

Kiel 2020

Erstgutachterin: Prof. Dr. Regine Willumeit-Römer

Zweitgutachter: Prof. Dr. Mikhail Zheludkevich

Termin der Disputation: 16.11.2020

Eidesstattliche Erklärung

Hiermit erkläre ich, dass die beigefügte Dissertation, abgesehen von der Beratung durch die Betreuer, nach Inhalt und Form meine eigene Arbeit ist.

Die Arbeit, ganz oder zum Teil, wurde nie schon einer anderen Stelle im Rahmen eines Prüfungsverfahrens vorgelegt und ist, abgesehen von den im Anhang angegebenen Veröffentlichungen, nicht anderweitig zur Veröffentlichung vorgelegt worden.

Außerdem ist die Arbeit unter Einhaltung der Regeln guter wissenschaftlicher Praxis der Deutschen Forschungsgemeinschaft entstanden.

Geesthacht, den 07/09/2020

Zusammenfassung

Bei der Entwicklung einer biologisch abbaubaren Mg-Legierung ist eine gute Korrosionsbeständigkeit, mechanischer Integrität, Biokompatibilität und Funktionalität erwünscht. Zn, ein essentielles Spurenelement im Körper, ist als Legierungselement in Mg weit verbreitet. Um das Korrosionsverhalten und die Biofunktionalität des Mg-Zn-Binärsystems weiter zu verbessern, werden in der Regel Zusätze von weiteren Legierungselementen und Verarbeitungen vorgenommen. Es ist von entscheidender Bedeutung zu verstehen, wie die Mikrostrukturen und das Korrosionsverhalten beim Legieren und Verarbeiten reagieren. In dieser Arbeit wurden Elemente ausgewählt, die in der Lage sind, die Knochenregeneration (Ca und Sr) und antibakterielle Wirkungen (Ag und Cu) zu fördern. Darüber hinaus wurde auch In (Indium) hinzugefügt, da es in Dentalmaterialien weit verbreitet ist. Der Gehalt an Zn wurde auf 0,5 Gew.-% und die von X auf 0,2 Gew.-% festgelegt, um die Bildung von intermetallischen Verbindungen zu reduzieren und die galvanische Korrosion zu verringern. Die Korrosionseigenschaften wurden hauptsächlich durch elektrochemische Methoden, H_2-Entwicklungstest und Ermittlung der Korrosionsmorphologie bewertet. Bei den Proben im Gusszustand unterschieden sich die Kornfeinungseffizienz und die Fähigkeit zur Bildung intermetallischer Phasen zwischen den Legierungselementen stark. Si-Verunreinigungen spielten ebenfalls eine wichtige Rolle bei der Bildung von Ausscheidungen in allen Mg-Zn(-X) Systemen. Im Allgemeinen besaß Mg-Zn-Ca aufgrund der geringeren Korngröße und begrenzter Mengen an intermetallischer Ausscheidungen eine gleichmäßigere Korrosion und dadurch die höchste Korrosionsbeständigkeit, während Mg-Zn-Cu aufgrund der hohen Körngröße und der höheren elektrochemischen Aktivität der intermetallischen Ausscheidungen starke Lochfraßkorrosiones und damit höchste Korrosionsrate aufwiesen. Mit Ausnahme von Mg-Zn-Cu waren die Korrosionseigenschaften von Mg-0,5Zn(-0,2X) mit denen höher legierter Systeme in der Literatur vergleichbar, was auf die Anwendbarkeit dieser Mikrolegierungssysteme für biomedizinische Anwendungen hinweist.

Da Mg-Zn-Ca das beste Korrosionsverhalten aufwies, wurden weitere Studien durchgeführt, um zu untersuchen, wie die Korrosion startet und sich entwickelt. Die Mg_2Ca-Phase erwies sich als anodisch und korrodierte bevorzugt nach dem Eintauchen innerhalb der ersten Stunde. $Ca_2Mg_6Zn_3$- und MgCaSi-Phasen wirken dagegen kontinuierlich über der 24 h als Kathoden. Nach dem Lösungsglühen führten die homogenere Mikrostruktur und die verringerten galvanischen Zellen zu einer höheren Korrosionsbeständigkeit von Mg-Zn-Ca. Im Gegensatz dazu begannen die intrinsischen Verunreinigungen (Fe und Si) das

Korrosionsverhalten von Mg-0,5Zn nach dem Lösungsglühen zu dominieren. Die Korrosionsbeständigkeit von Mg-0,5Zn mit der Dauer des Lösungsglühen, da die Fe-Konzentrationen in den Fe-Si-Partikeln ausbildeten. Um die Auswirkungen eines Umformschrittes auf die gebildeten Phasen und damit Eigenschaften der Legierungen zu ermitteln, wurden die Mg-0,5Zn-(0,2X)-Legierungen im stranggepressten Zustand charakterisiert. Die Legierungen hatten vergleichbare Korngrößen (~30 µm), sodass der Einfluss der Korngröße auf das Korrosionsverhalten vernachlässigt werden konnte. Im Gegensatz zu der in der Literatur weithin anerkannten Beobachtung, dass das Strangpressen die Korrosionsleistung verbessert, die Korrosionsraten von Mg-Zn, Mg-Zn-Ag und Mg-Zn-In im stranggepressten Zustand waren im Vergleich zu denen der Gegenstücke im Gusszustand deutlich höher. Dagegen wurde die Korrosionsraten von Mg-Zn-Ca nach dem Glühen und Strangpressen aufgrund der feineren Korngröße, der geschwächten Fasertextur und der begrenzten Menge an intermetallischen Phasen weiter reduziert. Darüber hinaus war die Korrosionsbeständigkeit von Mg-0,5Zn im stranggepressten Zustand genauso schlecht wie die des lösungsgeglühten Materials. Stattdessen konnte eine bessere Korrosionsbeständigkeit von Mg-0,5Zn im stranggepressten Zustand beobachtet werden, wenn vor dem Strangpressen keine Wärmebehandlung durchgeführt wurde. Daher wird vorgeschlagen, dass eine kürzere Behandlungsdauer oder eine reine Kaltverformung im Falle von mikrolegierten Mg-Systemen in Betracht gezogen werden sollte.

Abstract

Designing a biodegradable Mg alloy with good corrosion resistance, mechanical integrity, biocompatibility and functionality is desired. Zn, an essential trace element in the body, is widely used as an alloying element in Mg. To further improve the corrosion performance and biofunctionality of Mg-Zn binary system, additions of extra alloying elements and processings are usually performed. It is of vital importance to understand how the microstructures and the corrosion performances respond with alloying and processing. In this work, elements capable of promoting bone regenerations (Ca and Sr) and antibacterial effects (Ag and Cu) were selected. Moreover, In (Indium) was also added as it is widely used in dental materials. The addition amount of Zn was selected as 0.5 wt.% and that of X was 0.2 wt.% to reduce the formation of intermetallics and to downscale galvanic corrosion. The corrosion performances were evaluated mainly by electrochemical methods, H_2 evolution test and corrosion morphology observations. For the as-cast samples, the grain refinement efficiency and intermetallics forming ability differed greatly among the alloying elements. Si impurity also played a vital role in the precipitates formation in all Mg-Zn(-X) systems. Generally Mg-Zn-Ca possessed the highest corrosion resistance due to the refined grain size, limited intermetallics and uniform corrosion, whereas Mg-Zn-Cu showed the highest corrosion rate due to the coarse grains, intermetallics activity and severe pitting corrosion. Except Mg-Zn-Cu, the corrosion performances of Mg-0.5Zn(-0.2X) were comparable with those of the higher concentrated systems in literature, indicating the feasibility of these micro-alloying systems for biomedical applications.

As Mg-Zn-Ca had the best corrosion performance, further studies were carried out to investigate how the corrosion initiated and developed. Mg_2Ca phase was found to be anodic and was preferentially corroded within the first hour of immersion. Whereas, $Ca_2Mg_6Zn_3$ and MgCaSi phases continuously act as cathodes until 24 h immersion. After solution annealing, the more homogeneous microstructure and reduced galvanic couples resulted in a higher corrosion resistance in Mg-Zn-Ca. In contrast, the intrinsic impurities (Fe and Si) started to dominate the corrosion behaviour of Mg-0.5Zn after solution annealing. The corrosion resistance of Mg-0.5Zn deteriorated with the extension of solution treatment duration as the Fe concentrations in the Fe-Si particles were promoted. To investigate the impacts of further hot extrusion, the as-extruded Mg-0.5Zn-(0.2X) alloys were also characterised. The as-extruded alloys had comparable grain sizes (~30 μm) so that the effect of grain size on corrosion performance could be neglected. In contrast to the widely-recognised observation from literature that extrusion enhances the corrosion performance, the corrosion rates of as-

extruded Mg-Zn, Mg-Zn-Ag and Mg-Zn-In were significantly accelerated compared to those of the as-cast counterparts. Whereas the corrosion rate of Mg-Zn-Ca was further decelerated after annealing and extrusion, due to the finer grain size, weakened fibre texture and limited intermetallics. Moreover, the corrosion resistance of as-extruded Mg-0.5Zn was as poor as the solution annealed material. Instead, superior corrosion performance of as-extruded Mg-0.5Zn could be determined if no heat treatment was conducted prior to extrusion. It is suggested that shorter treatment duration or cold working should be considered in the case of micro-alloying Mg systems.

Table of Contents

1. Introduction

Mg and many Mg alloys are promising candidates for biomedical applications such as temporary implants, making the secondary surgeries redundant [1-6]. These lightweight biodegradable metals are endowed with low density, high specific strength and specific stiffness [7]. The density and Young's modulus of Mg are closer to those of natural bones compared to other permanent metallic implants such as steel and Ti, making Mg helpful in avoiding stress shielding [2, 3]. The mechanical strength of Mg is also higher than those of the bioresorbable polymers such as polylactic acid (PLA) and poly(lactic-co-glycolic acid) (PLGA) [8]. In addition, Mg is a trace element of the human body and excessive Mg ions can be excreted naturally through the kidneys [9].

However, one of the major hindrances for the wider market promotion still is the concern about the corrosion susceptibility of Mg alloys [10]. The corrosion behaviour of Mg alloys is affected by factors such as the compositions and microstructures of materials [1], corrosive media and atmosphere [11]. Although surface modifications such as coatings are also used to enhance the corrosion properties [12, 13], further developments are still needed for coatings with controlled corrosion and adequate adhesions [10].

The most widely studied Mg alloys are those of the Mg-Al-Zn system, which however, is not appropriate for biomedical applications due to the biosafety concern of Al (risk for Alzheimer's disease) [14]. Instead, to facilitate osteoblast maturation and bone regeneration, Ca [15] and Sr [16] are appropriate candidates for alloying elements. To promote antibacterial and anti-inflammatory effects after surgery, Ag [17] and Cu [18] can be good options. Although In (Indium) is not widely alloyed with Mg, it is commonly used in dental materials [19]. All these alloying elements provide specific functionalities in the body as long as the doses are within the safety range. In this work, the effects of alloying elements on the microstructures and corrosion performances of Mg-Zn reference material are evaluated. The corrosion performances are evaluated by electrochemistry methods, H_2 evolution and corrosion morphologies. The effects of microstructures (grain size, intermetallics) on the corrosion behaviour of these alloys are systematically studied. The microstructures are affected by compositions (alloying elements, impurities) and processings (heat treatment, extrusion). The ultimate aim of this study is to design a bare alloy with not only desired biocompatibility but also good corrosion resistance, mechanical integrity and functionalities.

2. State of the art

2.1 Mg and Mg alloys for biomedical applications

2.1.1. Current status of Mg and Mg alloys as implants

Currently, the two main aspects for Mg and Mg alloys in biomedical applications are vascular intervention such as cardiovascular stents [20] (**Fig. 2-1a**) and osteosynthesis such as screws and plates [21] (**Fig. 2-1b**). The stent should be able to maintain its optimal mechanical integrity without accelerating the corrosion rate during the initial stage to assist the arterial vessel remodelling process (**Fig. 2-1c**). It was reported by Hermawan et al. [22] that 6-12 months were needed to complete the remodelling process and 12-24 months were deemed as an appropriate period for the fully degradation of the stents. Similarly, when the Mg screws and plates are fixed into the bones, the materials should provide high mechanical integrity and high corrosion resistance during the bone fracture remodelling stage until the damaged bone tissues regain sufficient strengths (**Fig. 2-1d**) [23].

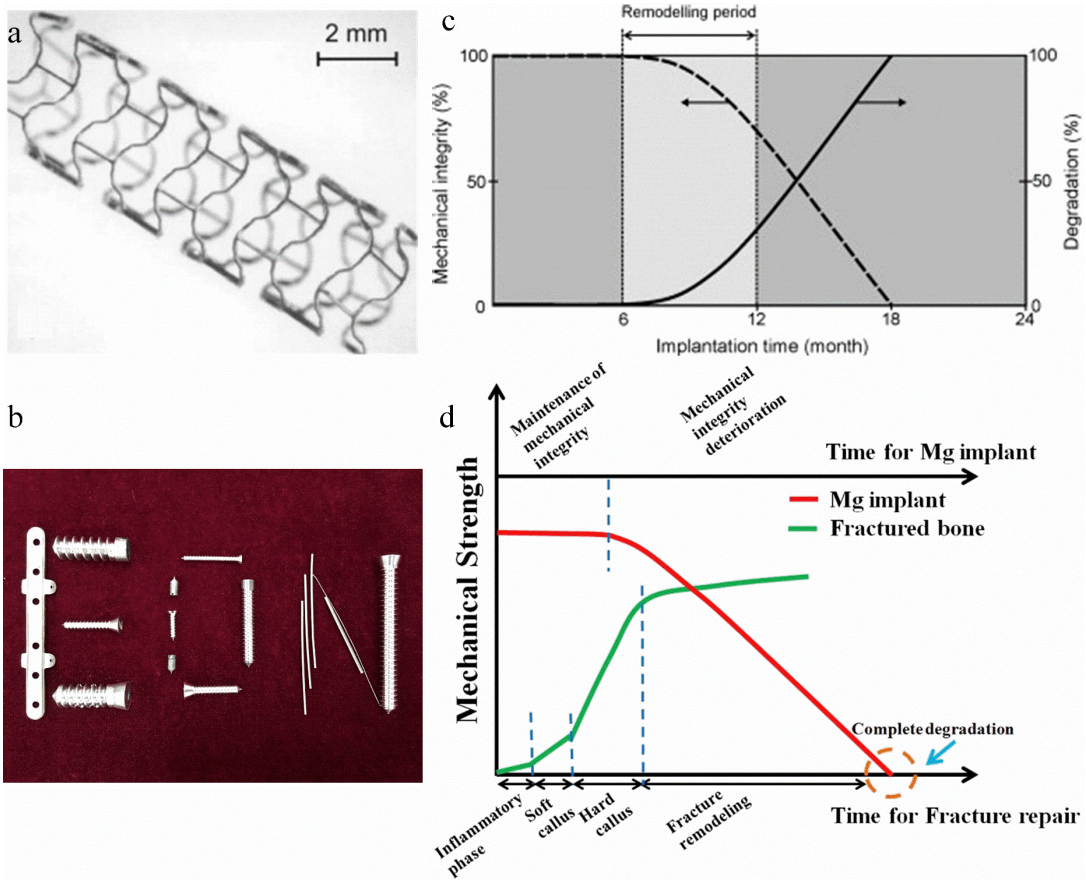

Fig. 2-1. (a) A WE43 coronary stent in its expanded state [24]; (b) Mg based implants for orthopaedic use [23]; (c) Illustration of an ideal compromise between mechanical integrity and degradation of a biodegradable stent [22]; (d) Optimal degradation behaviour of Mg-based implant in bone fracture healing [23] (reproduced with permission from Elsevier)

Among multiple clinical trials, three Mg-based systems have been granted for orthopaedic applications by the agencies in their respective countries [25]: the MAGNEZIX® WE43-based compression screw developed by Syntellix AG was the world's first Conformité Européenne (CE)-approved biodegradable osteosynthesis implant [26]; the Resomet™ Mg-Ca-Zn screws from U&I Corporation were approved by the Korean FDA for clinical use in 2015 [27]; and screws designed by Dongguan Eontec Co., Ltd with high purity (99.99%) Mg were approved by the Chinese FDA as medical device in 2019 [28]. As for biodegradable stents, Mg alloy based Magmaris RMS scaffold from BIOTRONIK AG received the CE mark in 2016; Mg alloy based Dreams 3G scaffold from BIOTRONIK AG and Mg/PLLA based UNITY stent from QualiMed are still in clinical or preclinical trials [29]. However, some problems still exist. For example, pure Mg is insufficient in mechanical properties and has limited slip systems. The rare earth elements in WE43 might accumulate in some organs thus their biosafeties still need further investigations [30]. The degradation rate of Mg-5Ca-1Zn alloy designed by U&I Corporation is 0.69 mm/year after implanted *in vivo* for 6 weeks [31], which still needs further improvement [32]. Thus, developments and designs of new Mg alloys/systems still await.

The mechanical properties, corrosion performance, the corresponding "functioning duration" and "fully-dissolution time" of the implant depend largely on the material itself. The yield strength of as-cast pure Mg is lower than that of bones (e.g. femur ~110 MPa) which needs to be improved to satisfy the biomedical application demands [33]. Alloying proves to be an effective way to strengthen Mg. So far, a series of commercial alloys, e.g. AZ31 [34], WE43, LAE442 [35] and a number of independently developed alloys, e.g. Mg-Nd-Zn-Zr [36], Mg-Zn-Y-Nd [37] have already been studied as potential candidates for biodegradable implant applications. In order to balance the mechanical properties and the corrosion performances of Mg alloys and to reduce potentially harmful effects of excessive alloying elements [30], micro alloying could be used as an optional method. For example, Hofstetter et al. [38] demonstrated that Mg-1Zn-0.3Ca could be a promising candidate for biodegradable implants with very slow and homogeneous degradation in a rat femur.

It is an encouraging fact that biodegradable Mg stent has already been successfully implanted in clinical trials [39]. As the inherently high corrosion susceptibility limits the further development of Mg and Mg alloys [10], it is important to know and understand the principles of corrosion.

2.1.2. Corrosion behaviour of Mg and Mg alloys

Uniformly corroding Mg alloy is desired due to the controllable corrosion rate while simultaneously maintaining proper mechanical integrity. Zhang et al. [40] found the material with long period stacking ordered (LPSO) structure exhibited slower corrosion rate and more uniform corrosion morphology. However, Mg alloys seldom corrode in a uniform manner due to their heterogeneities, i.e. intermetallics, impurities. The non-uniform corrosion process will incur local loss of the mechanical integrity of devices (e.g. breakage of single struts in stents) and lead to difficulties in predicting the corresponding lifetime [10]. Thus it is important to know the main types of non-uniform corrosion in Mg and Mg alloys.

Galvanic corrosion

Galvanic corrosion (**Fig. 2-2a**) occurs when two metals are in direct electrical contact and the active one serves as the anode and the noble one serves as the cathode. Unfortunately, Mg is considered as one of the most active metals in the galvanic series [41] and acts as an anode if it is in contact with other metals such as Al alloys, steels and Zn [42]. Coy et al. [43] also found corrosion occurred between the micro-constituent phases and the Mg matrix and addressed it as micro-galvanic corrosion (**Fig. 2-2b**), which was largely dependent on the relative Volta potential difference of each micro-constituent relative to the Mg matrix. These micro-constituents are mainly in the form of secondary phases and impurities. An example of the internal galvanic corrosion between the Fe impurity particles and α-Mg matrix is shown in **Fig. 2-2c, d.** The different electrochemical behaviour of these micro-constituents compared to the surrounding matrix gives rise to localised corrosion. A review of the Volta potentials of secondary phases measured via Scanning Kelvin Probe Force Microscopy (SKPFM) was conducted by Hurley et al. [44]. However, disagreements were seen among the acquired measurements possibly due to different preparations, testing conditions and calibrations of SKPFM. Generally the galvanic corrosion rate is increased with higher medium conductivity, larger potential difference between anode and cathode, lower polarisability of anode and cathode, larger area ratio of cathode to anode and smaller distance from anode to cathode [45].

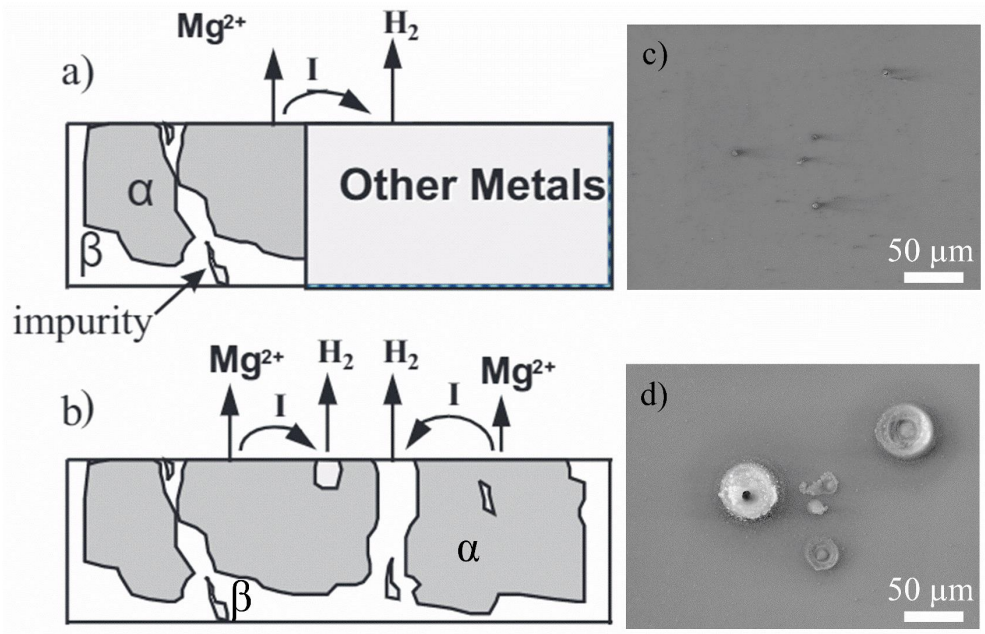

Fig. 2-2. (a) External and (b) internal galvanic corrosion [45]. α is the Mg matrix and β is the intermetallic particle or impurity (reproduced with permission from John Wiley & Sons); Quasi-in situ observation of internal galvanic corrosion (c) before and (d) after immersion [46] (reproduced with permission from Elsevier)

Localised corrosion

Pitting is one of the most common corrosion types in Mg alloy (**Fig. 2-3a, b**). The generation of pits is related to the chemical composition and microstructural features of the exposed surface and is promoted by noble metal contamination [47]. Lunder et al. [48] found pitting initiated around the AlMnFe containing intermetallics in AZ91 alloy. Zeng et al. [49] claimed that Mg_2Ca particles coexisting with Fe and Si resulted in pitting corrosion of Mg-Ca alloy. It is reported that pitting corrosion in Mg-Li alloy could be supressed with the addition of Zn and Y due to the refinement of grains and formation of Mg_3Zn_6Y phase [50]. The Mg_3Zn_6Y phase could act as effective barriers to suppress the growth of pits and the occurrence of filiform corrosion from the pits.

Filiform corrosion is commonly found on steel surfaces with coatings in humid atmosphere. Distinctly, filiform corrosion could also be found on bare Mg alloy surfaces exposed to air and NaCl solution due to an active corrosion cell moving across the alloy surface [47]. It seems that the inherently formed oxide film on the metal surface may also function as a coating to some extent. Song et al. [51] observed filiform corrosion on Mg-8Li alloy (**Fig. 2-3c, d**). As corrosion develops, OH^- reacts with Mg^{2+} and Li^+ to form $Mg(OH)_2$ and LiOH which makes the back end of filament tip alkalised and passivated as the filament tail. The hydrolysis

reaction acidifies the corrosion pits and drives the filament tip to propagate forward continually. Lunder et al. [52] reported the active corrosion filaments could propagate with a velocity of 6 μm/s.

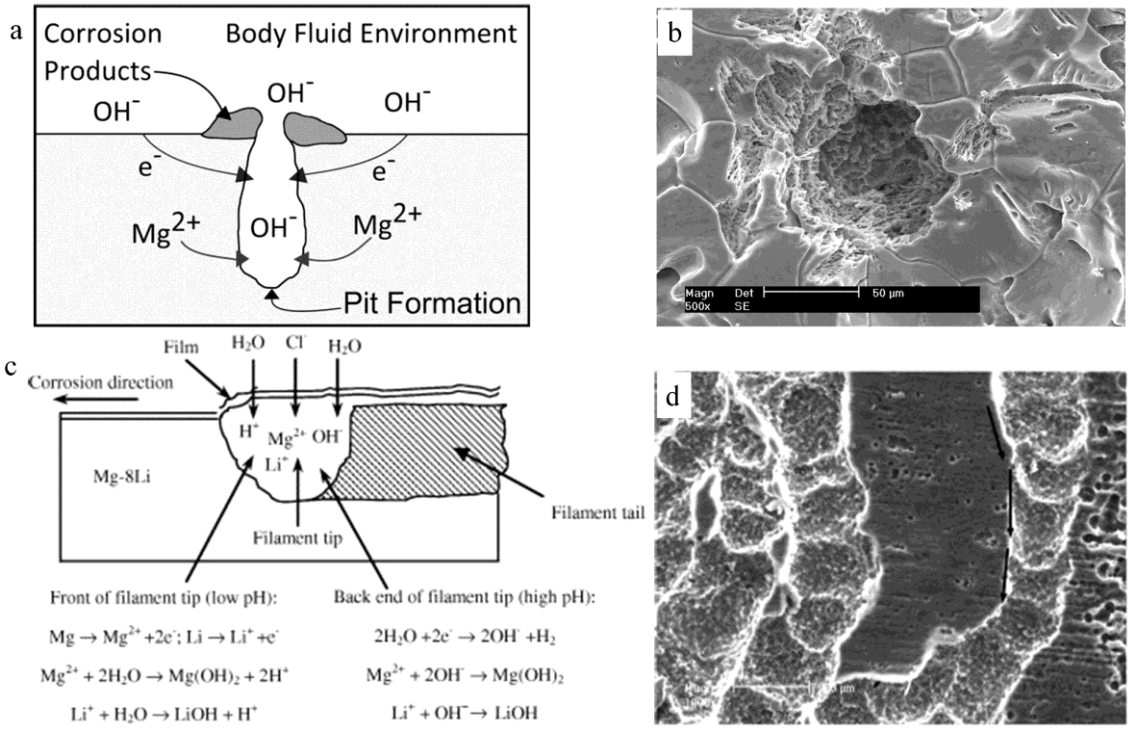

Fig. 2-3. (a) Sketch [53] (reproduced with permission from John Wiley & Sons) and (b) SEM image [54] of pitting corrosion in Mg alloy (reproduced with permission from Elsevier); (c) Sketch and (d) SEM image of filiform corrosion in Mg-8Li alloy [51] (reproduced with permission from Elsevier)

Intergranular corrosion

Song et al. [45] reported intergranular corrosion was only slightly susceptible in Mg and Mg alloys. The grain boundaries are mostly cathodic to the grain interiors thus corrosion is concentrated in the area near the grain boundaries until the grains are undercut. However, Zeng et al. [55] found intergranular corrosion in extruded ZK60 alloy in 3.5 wt.% NaCl solution (**Fig. 2-4**) which resulted from the microgalvanic corrosion between the MgZn precipitates at the grain boundaries and the adjoining grain interiors. These fine precipitates are local cathodes and will stimulate grain boundary attack.

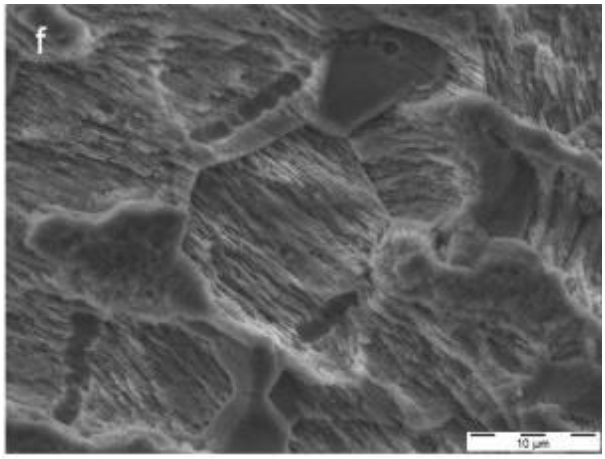

Fig. 2-4. Intergranular corrosion observed in ZK60 [55] (reproduced with permission from Elsevier)

Stress corrosion cracking

Stress corrosion cracking (SCC) is intergranular or transgranular, which occurs when stressed Mg subjects to wet conditions (**Fig. 2-5**). The SCC mechanisms basically include anodic dissolution and hydrogen embrittlement [47]. SCC in Mg is mainly transgranular whereas intergranular SCC could also occur in Mg-Al-Zn alloys when $Mg_{17}Al_{12}$ phases precipitate along the grain boundaries [45]. SCC is rare in as-cast Mg alloys however is more marked in wrought alloys following the twinning planes [45]. Alloying also affects SCC significantly. Mg-Al alloys have high SCC sensitivities which increase with the Al contents. Addition of Zn also promotes SCC whereas addition of Zr suppresses the susceptibility of SCC [47]. Mg alloys are resistant to SCC in alkaline media with pH above 10.2 or in fluoride-containing solution, whereas SCC might occur in neutral solution containing chlorides or even in distilled water [45].

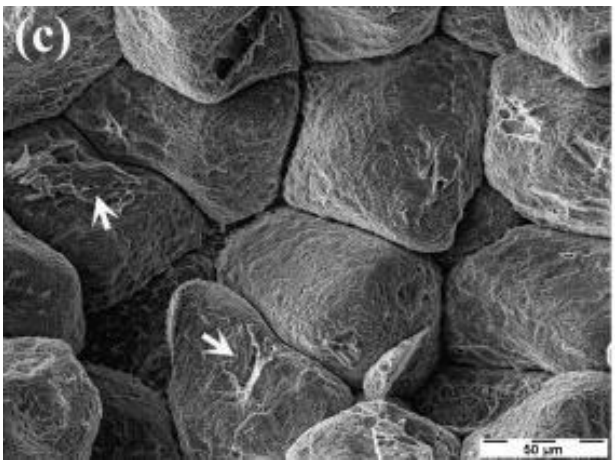

Fig. 2-5. Predominant intergranular and isolated transgranular (arrows) cracking in ZE41 [56] (reproduced with permission from Elsevier)

Corrosion fatigue

Corrosion fatigue is important to consider if the material undergoes cyclic mechanical loads. The fatigue life and fatigue crack propagation depend largely on the alloy microstructure, loading frequency, pH and compositions of the media, relative humidity and temperature [47].

2.2. Effects of impurities and alloying

2.2.1. Impurities

The amounts of impurities depend on the compositions of the raw materials as well as the production routes. The sites enriched with noble metals (e.g. Cu, Al, Ni, Zn, Fe, Mn) have higher exchange current density for hydrogen reduction and are favoured for the cathodic reaction [57]. The most characteristic impurities in Mg are Fe, Cu, Ni and Be, and the amount of which should be limited to less than 35-50, 100-300, 20-50 and 4 ppm, respectively [58]. The corrosion rate of Mg alloy increases by a factor of 10 to 100 if Fe, Cu, Ni exceed the corresponding tolerance limit [45, 59]. Although the detrimental effect of impurities to the corrosion resistance is Ni > Fe > Cu, Fe is the most commonly-found impurity in the system due to the possibly pickup from steel crucibles [60]. The tolerance limits of impurities differ for different alloys. Liu et al. [61] showed low corrosion rate of AZ91 in NaCl solution (below 5 mg/cm^2/day) if Fe/Mn ratio was below 0.032 (tolerance limit of Fe in Al-containing Mg alloys). Gandel et al. [62] found Mn might also be beneficial in promoting the corrosion resistance of Al-free Mg alloy. Mn will capture Fe and reduce the activeness of cathodic Fe particles. However, normally only ~200 ppm Mn is present in commercial Mg ingot and this is still too low to prevent the damage caused by Fe [61]. Blawert et al. [63] proposed high corrosion resistance could still be achieved if the impurities were incorporated in intermetallic phases. The Cu tolerance limit for AZ53 alloy increased up to 0.7-0.8 wt.% with corrosion rate comparable to that of AM50. The τ-phase (Mg-Al-Zn) was able to incorporate much more Cu (9-18 wt.%) compared with β-phase (Mg-Al), preventing the formation of additional Cu enriched phases.

Fe is the most common impurity in Mg and is very difficult to remove from processing [46]. Lamaka et al. [46] set up comprehensive database for Fe-complexing agents to inhibit the corrosion of Mg. These inhibitors could form stable soluble complexes with Fe^{2+}/Fe^{3+}, prevented Fe re-plating and thus inhibited corrosion. The salts of pyridine dicarboxylic and salicylic acids were found to be the most efficient and universal Mg corrosion inhibitors with inhibiting efficiency (reduced H_2 volumes) in the range of 80-90%. Based on the Mg-Fe phase

diagram, Liu et al. [61] proposed the Fe tolerance limit of as-cast pure Mg being 180 ppm. However, Qiao et al. [64] showed that the common high purity Mg ingot possessed a high corrosion rate even though the Fe concentration was within 26-48 ppm (depending on the specimen location in the ingot). The expected high purity ingot turned out to be only low purity possibly due to the presence of Fe containing particle during solidification. In addition, it is indicated from the phase diagram that the Fe tolerance limit of heat treated pure Mg was distinctly reduced to 5-10 ppm [61]. The precipitation of Fe-rich particles during heat treatment led to a significant increase in the corrosion rate [61, 65]. To address the impurity-induced corrosion resistance deficiency, many efforts have been made on the purification of Mg alloys preparation such as adding Zr in Mg melts [66] and low temperature melt treatment [67]. The ultrahigh-purity Mg (Fe < 2.5 ppm) proposed by Hofstetter et al. [68] degraded very slow (10 μm/year) in CO_2 buffered SBF. Likewise, the corrosion development of a commercial-purity Mg-5Zn-0.3Ca alloy (42 ppm Fe) was much severer than its ultrahigh-purity counterpart (0.5 ppm Fe) *in vitro* and *in vivo* [69]. Surface contamination after thermo-mechanical processing like rolling might be another source of impurities. Nwaogu et al. [70] found the corrosion resistance of AZ31 sheet was greatly enhanced after inorganic acid pickling (e.g. nitric acid, phosphoric acid). By tuning the concentration and pickling duration of the acid, at least 5 μm material is removed and the Fe concentration can be reduced from 250 ppm to less than 100 ppm. The undermined noble particles during acid cleaning and precipitation of insoluble film like $Mg_3(PO_4)_2$ might be the reasons for the increased corrosion resistance. Likewise, the Fe contaminations in as-rolled AZ31 sheet [71] and as-extruded Mg-xGd bars [72] could be significantly removed after cleaning by organic acid (e.g. acetic acid) with 2-9 μm material being etched. However, to date, the majority of the research centre on the influence of Fe/Fe-containing particle on the corrosion behaviour of pure Mg [68, 73, 74] and Mg-Al based alloys [75, 76].

2.2.2. Intermetallics

Due to the limited solubilities of many elements in Mg, different intermetallics precipitate in Mg alloys [77]. Although alloying could strengthen the mechanical properties of Mg alloys, it is also noteworthy that more galvanic corrosion would be promoted with the presence of more intermetallics. The electrochemical property (anodic or cathodic) and compositions of the intermetallics influence corrosion remarkably. For the most investigated Mg-Al alloys, the intermetallic particle $Mg_{17}Al_{12}$ usually acts as cathode and the surrounding α-matrix dissolves as anode (**Fig. 2-6a, b**) [78]. The $Mg_{17}Al_{12}$ phase is less active than Mg due to its more positive

Volta potential [44]. If the $Mg_{17}Al_{12}$ phases are nearly continuous and are distributed along the grain boundary, the Mg matrix could be protected from corrosion due to the presence of the corrosion products and β-phases on top (**Fig. 2-6c, d**) [79]. Südholz et al. [80] performed potentiodynamic polarisation tests on the intermetallic phases in Mg alloys with the additions of Al, Zn, rare earths, Y, Ca and Si, respectively. The derived corrosion potentials of these phases indicated that all of them were cathodic to Mg, with the exception of Mg_2Ca. In this sense, the Mg_2Ca phase would be corroded in preference to the Mg matrix. Unlike the Al-containing alloys, the continuous Mg_2Ca phase would promote pitting and undercutting of the Mg matrix (**Fig. 2-6e**) [15, 81]. Similarly, Cai et al. [82] stated that if Zn content was over 5 wt.% (i.e. Mg-7Zn), the hydrogen evolution rate would be accelerated due to the continuous network structure of MgZn intermetallic phase.

Another major factor that influences corrosion is the size and distribution of the intermetallics. To study the effect of intermetallics on corrosion individually, Bland et al. [83] designed Mg-Al model with pure Al (99.999 wt.%) wires embedded into the holes on the Mg surface (hole sizes approximately equal to that of the Al wires). By changing the diameters and the in-between spaces of the Al wires, Mg-Al models with different size, area fraction and distribution of the intermetallics (Al electrodes) were obtained. It is found that the corrosion rate increased with the increasing area fractions of Al electrodes due to the enhanced galvanic corrosion. For a fixed area fraction of Al electrodes, the corrosion rate became lower in the case of larger and more distanced electrodes, possibly attributed to the less overlapping of galvanic potential and less anode-cathode sites for corrosion activation.

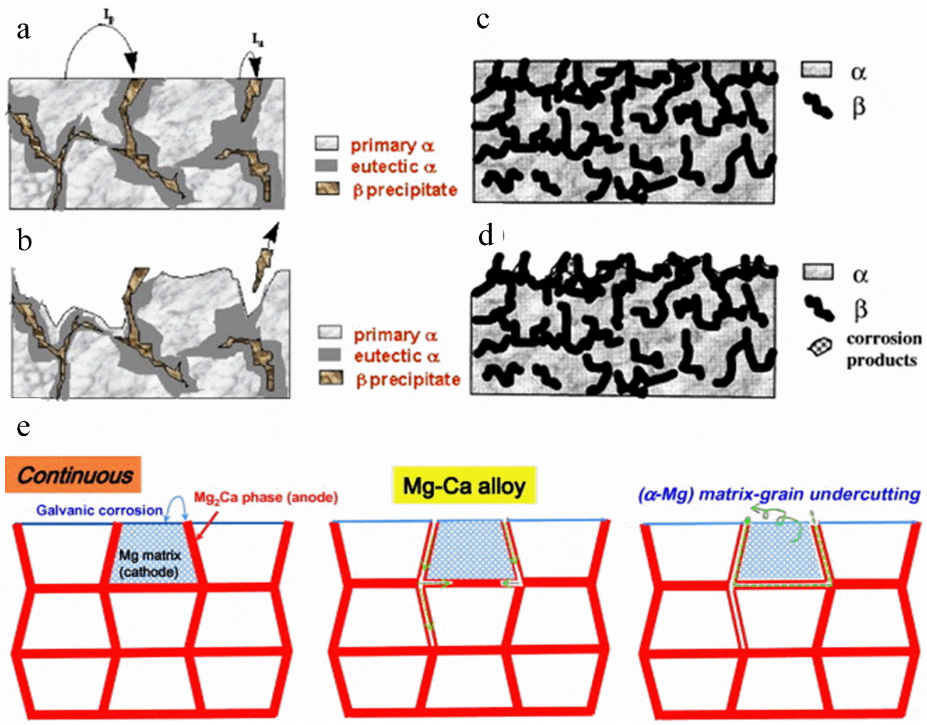

Fig. 2-6. Schematics of the galvanic corrosion in Mg-Al alloys between the β-$Mg_{17}Al_{12}$ phases and the α-matrix when the β-phases are (a, b) not continuous [78] and are (c, d) continuous [79], respectively; (e) schematics of the galvanic corrosion in Mg-Ca alloys between the Mg_2Ca phases and the α-matrix when the Mg_2Ca phases are continuous [15] (reproduced with permission from Elsevier)

2.2.3. Some alloy systems for biomedical applications

Mg-Al based alloys

Increasing Al content normally contributes to a lower corrosion rate due to the formation of a continuous network of $Mg_{17}Al_{12}$ phases [79] and/or the formation of insoluable Al_2O_3 layer which can enhance the protective character of the surface films [84]. However, high concentration of Al is not desired due to its biosafety concerns in human body (risk for Alzheimer's disease) [14, 85]. On the other hand, good biocompatibility is observed in anodised AZ31 and AZ91 alloys *in vitro* [86] and Mg-1Al alloy *in vivo* [87]. More *in vivo* studies are still needed to confirm the biocompatibility (especially in the long term) of Mg-Al based alloys and the addition limit of Al.

Mg-Ca based alloys

Ca is an important element in human bones since it is beneficial for the bone regeneration [15]. 99.5% of the total Ca in the body are distributed in the bones [88]. The addition of Ca can effectively strengthen the mechanical properties of Mg [89]. Li et al. [90] demonstrated good biocompatibility of Mg-1Ca alloy in rabbit femoral shafts for up to 3 months. However, one

concern of the Mg-Ca based alloys for biomedical applications is the fast degradation rates. For example, Mg-5Ca screws implanted in femoral condyle were completely dissolved within 2 weeks and the degradation volume of Mg-0.5Ca screws also reached 50% after 4 weeks [91]. The fast degradation of the implants may lead to the premature reduction in mechanical strengths. It is well known that the galvanic corrosion caused by potential difference between the intermetallic phases and the matrix is non-negligible in Mg alloys [45]. The optimal addition of Ca to Mg should be kept within 1 wt.% considering both the mechanical and corrosion properties [90, 92]. Kim et al. [93] and Zeng et al. [94] claimed that galvanic corrosion of Mg-Ca alloys occurred with the Mg_2Ca phase as the cathode and the Mg matrix as the anode. Mohedano et al. [95] pointed out that the Mg_2Ca phase presented a very small Volta potential difference compared to the Mg matrix (less than 10 mV), indicating inactive coupling on the Mg_2Ca/α-Mg interface. However, in recent years, a consensus in the literature has been reached that Mg_2Ca functions as the anode in the galvanic couple, which would be preferentially dissolved from the matrix [15, 80, 96-99]. Nonetheless, the conclusions were mostly drawn with the assistance of chromic acid to remove the corrosion products [15, 97-99]. Potentially, it is possible that chromic acid could remove Ca-rich precipitates. In order to rule out this possibility, further investigations are needed without only using this potentially interfering reagent.

Mg-RE (rare earth) based alloys

Temporarily the only Mg alloy with CE mark in the market is WE43 (Mg-4Y-3RE) due to its good corrosion resistance and mechanical properties [85]. Out of the 17 rare earth elements, Gd is one of the most widely-used alloying elemets in Mg alloys. The solubility of Gd in Mg is high (23.5 wt.% at the eutectic temperature), making it effective in strengthening Mg alloys [100]. With comparatively low additions of Gd (up to 10 wt.%), the corrosion rates of Mg-Gd alloys can be low due to the limited Mg_5Gd precipitates [100]. The corrosion rate of as-cast Mg-10Gd is about 5 mm/year in 0.5% NaCl solution [101] and that of as-extruded Mg-10Gd is around 0.15 mm/year in DMEM [102]. Arrabal et al. [103] reported the addition of Gd in AM50 would form Gd-containing intermetallics which could replace Al-Mn inclusions and $Mg_{17}Al_{12}$ phase. The Volta potentials of Gd-containing precipitates are lower than that of Al-Mn inclusion and higher than that of $Mg_{17}Al_{12}$ phase. If appropriate amount of Gd is added, the corrosion resistance is promoted due to the reduction of Al-Mn inclusions. Whereas higher corrosion rate would occur if more Gd is added and $Mg_{17}Al_{12}$ phase is reduced. Another common RE alloying element is Y, which has identical electrochemical potential (-2.37 V) and

similar crystal structure lattice parameters compared to those of Mg [30]. Liu et al. [104] found the precipitation of $Mg_{24}Y_5$ intermetallics could accelerate the corrosion rates of Mg-Y alloys. However, the oxidised Y (e.g. $Y(OH)_3$ and Y_2O_3) could also be incorporated in the corrosion layers and increase the protectiveness of the films [104]. Both of these two factors influence the corrosion behaviour of Mg-Y alloys and the domination of which is dependent on the addition amount of Y. Another possible mechanism that affect corrosion is the formation of continuous $Mg_{24}Y_5$ phases in Mg-15Y which form a barrier to prevent the corrosion [105], just like the case of $Mg_{17}Al_{12}$. However, the biosafety of the rare earth elements still need further investigations. Drynda et al. [106] reported rare earth elements in Mg alloys did not interfere with proliferation of smooth muscle cells but did induce the upregulation of inflammatory genes. Out of the most-widely added rare earth elements, Gd might accumulate in tissue leading to nephrogenic systemic fibrosis and kidney failure; Y gets distributed into plasma and leads to acute hepatic injury at a dose of 1 mg/kg for 144 days in rats [30].

Due to the biosafety concerns of Al [85] and RE [107] and the fast degradation of Mg-Ca alloys stated above, these systems will not be the focus of this work. Instead, Zn is one of the essential elements in the human body with more than 85% distributes in the muscles and bones. The daily requirement of Zn in the human body is around 15 mg [88]. Zn is also reported to strengthen Mg [108-110] and elevate the corrosion potential of Mg [111, 112]. Thus, Zn can be an interesting alloying element and a brief introduction to the Mg-Zn based alloys are shown in the next section.

2.2.4. Mg-Zn based alloys

Mg-Zn binary system

Research on Mg-Zn binary system is rather limited with disagreements still exist in the binary Mg-Zn phase diagram due to the complex intermetallics [113-115]. Song et al. [116, 117] named these phases as Mg_xZn_y for convenient description. Among the limited research on Mg-Zn binary system, the as-extruded Mg-6 wt.%Zn alloy attracted much attention. The cytotoxicity test and animal implant experiments indicated that the alloy had good biocompatibility *in vitro* and *in vivo* [111, 112, 118]. However, disagreements also exist on the role of Zn concentration on the corrosion performances of Mg-Zn alloys. Some researchers concluded a higher Zn addition promoted a better corrosion resistance [82, 114, 119], whereas others claimed that Zn content was inversely proportional to the corrosion performance [113, 120-122]. Liu et al. [123] reported that MgZn phase was a strong cathodic phase with 0.46 V

potential difference relative to the matrix and served as effective sites for localised corrosion. In the light of reducing galvanic corrosion to elevate the corrosion resistance, micro-alloying strategy and/or appropriate heat treatment should be considered.

Reviewing on the Mg-Zn binary system, the effects of Zn addition, heat treatment and the mechanical processing on the corrosion behaviour are summarised in **Table 2-1**. As can be seen, the systems with relatively high amount of Zn (more than 1 wt.%) attracted more attention. Although the solution treatment conditions varied, with annealing temperature ranging from 300-530 ℃ and time from 2-48 h, coincidently, almost all results pointed out that the corrosion resistance increased after solution treatment. Liu et al. [123] attributed this to the decreased amount of MgZn precipitates and Zn-rich segregation. Zhang et al. [124] explained that the grain boundaries which functioned as active areas for corrosion activation were reduced due to the grain growth during heat treatment. The only case that solution annealing weakened the corrosion property of Mg-Zn system was reported by Yan et al. [125]. The material was fabricated by powder metallurgy (sintered at 545 ℃) and then extruded at 350 ℃. Following that, the as-extruded bar was solution treated at 450 ℃ for 12 h. Heat treatment did reduce the intermetallic amounts whereas also caused micropores on the surface due to Kirkendall effect, which promoted localised corrosion. This does not apply to the traditional pore-free as-cast and as-wrought materials.

Table 2-1 Literature review on the corrosion behaviour of Mg-Zn binary systems. WL: weight loss; i_{corr}: corrosion current density; H_2: H_2 gas evolution

Alloy (wt.%) in initial state	Heat treatment	Mechanical treatment	Corrosion rate	Ref.
As-cast Mg-(1, 3)Zn	-	-	WL (mm/year) in 0.9% NaCl solution Mg-1Zn (1.3) < Mg-3Zn (2.5) < pure Mg (3.4)	[113]
As-cast Mg-(1.25, 2.5, 4)Zn	-	-	WL (mm/year) and i_{corr} ($\mu A/cm^2$) in Kokubo solution Mg-4Zn (2.1; 212) < Mg-2.5Zn (2.4; 242) < Mg-1.25Zn (3.1; 283) < pure Mg (4.8; 370)	[114]
As-cast Mg-(1, 5, 7)Zn	-	-	WL ($mg/cm^2/h$) and i_{corr} ($\mu A/cm^2$) in SBF with TRIS Mg-5Zn (0.025; 12) < Mg-1Zn (0.04; 23) < Mg-7Zn (0.063; 52) < pure Mg (0.69; 680)	[82]
As-extruded Mg-(2, 3, 4, 5)Zn	-	-	i_{corr} ($\mu A/cm^2$) in 3.5% NaCl solution Mg-2Zn (10) < Mg-3Zn (14) < Mg-4Zn (18) < Mg-5Zn (20)	[121]
As-cast Mg-(0.5, 1, 2, 3)Zn	-	-	i_{corr} ($\mu A/cm^2$) in SBF with TRIS Mg-3Zn (102) < Mg-2Zn (115) < Mg-1Zn (124) < Mg-0.5Zn (134) < pure Mg (190)	[119]
As-cast Mg-5Zn	T4: 300 °C 6 h + 500 °C 42 h, quenching	-	WL (mm/year) and i_{corr} ($\mu A/cm^2$) in 3.5% NaCl solution saturated with $Mg(OH)_2$	[126]

			T4 (6.5; 117) < as-cast (15.2; 340)	
As-cast Mg-(3, 6)Zn	T4: 340 °C 6, 12, 18 h, hot water quenching	-	WL (mm/year) and i_{corr} ($\mu A/cm^2$) in Kokubo solution As-cast: Mg-3Zn < Mg-6Zn Mg-3Zn T4 (1.9; 210-224) ≈ as-cast (2.0; 228) Mg-6Zn T4 (1.4; 191-205) < as-cast (3.5; 270)	[120]
As-cast Mg-3Zn	T4: 320 °C 10 h, hot water quenching; T6: (T4 + 200 °C 16 h, air cooling)	-	H_2 (mL/cm^2) and i_{corr} ($\mu A/cm^2$) in 0.1 mol/L NaCl solution T4 (2.4; 16) < T6 (2.8; 18) < as-cast (3.0; 24)	[123]
As-cast Mg-6Zn	T4: 350 °C 6, 12, 18, 24, 48 h, quenching	-	WL (mm/a) and i_{corr} ($\mu A/cm^2$) in SBF with TRIS 48 h (14; 180) < 24 h (15; 230) < 18 h (18; 360) < 12 h (21; 390) < 6 h (23; 630) < as-cast (36; 810)	[115]
As-extruded Mg-6Zn	T4: 350 °C 2 h; T6: (350 °C 2 h + 210 °C 12 h)	-	i_{corr} ($\mu A/cm^2$) in SBF T4 (4) < T6 (6) < as-extruded (8)	[124]
PM sintered then extruded Mg-(6, 14.5, 25.3, 40.3)Zn	T4: 450 °C 12 h, quenching; T5: 150 °C 24 h; T6: T4 + T5	-	i_{corr} ($\mu A/cm^2$) in Ringer's solution Mg-6Zn (16) < Mg-14.5Zn (54) < Mg-25.3Zn (80) < Mg-40.3Zn (132); Mg-6Zn T5 (9) < as-extruded (16) < T6 (17) < T4 (20)	[125]

As-cast Mg-(0.5, 1, 1.5, 2)Zn	T4: 530 °C10 h, hot water quenching	Preheated 420 °C 1h Extruded 420 °C	i_{corr} ($\mu A/cm^2$) in SBF with TRIS As-cast: Mg-0.5Zn (53) < Mg-1Zn (178) < Mg-1.5Zn (374) < Mg-2Zn (423); As-extruded: Mg-0.5Zn (20) < Mg-1Zn (47) < Mg-1.5Zn (57) < Mg-2Zn (59); Mg-XZn: as-extruded < as-cast	[122]
As-extruded Mg-6Zn	T4: 320 °C 8, 16, 24 h, quenching	-	H_2 (mL/cm^2) in 0.9% NaCl solution T4 (5) < as-extruded (17)	[127]
As-cast Mg-6Zn	T4: 350 °C 2 h, quenching	Extruded 250 °C	WL (mm/year) in 0.9% NaCl solution Mg-6Zn (0.2) < pure Mg (0.4)	[112]
As-extruded Mg-6Zn	-	-	WL (mm/year) and i_{corr} ($\mu A/cm^2$) in SBF Mg-6Zn (0.2; 45) < pure Mg (0.4; 60)	[111]
As-extruded Mg-5Zn	T4: 450 °C 2 h, quenching; T6: (T4 + 230 °C 4, 6, 10 h, air cooling)	-	WL ($g/m^2/h$) and i_{corr} ($\mu A/cm^2$) in 3.5% NaCl solution T4 (2.6; 23) < as-extruded (3.2; 26) < T6 (4.6; 51)	[116]
As-cast Mg-(0.5, 1, 2, 3)Zn	T6: (T4: 400 °C 24 h, hot water quenching + 200 °C 8, 16 h, air cooling)	-	i_{corr} ($\mu A/cm^2$) in 3.5% NaCl solution As-cast: Mg-0.5Zn (18) < Mg-1Zn (33) < Mg-2Zn (40) < Mg-3Zn (45); T6: Mg-3Zn (29) < Mg-2Zn (32) < Mg-1Zn (38) < Mg-0.5Zn (45); Mg-0.5Zn: Cast < T6	[128]

Besides the Mg-Zn binary system, some additional alloying elements are further added to see their modifications in microstructures and corrosion behaviour. In this work, some elements which were previously shown to possess positive effects on human health are selected to see their effects on the Mg-Zn binary alloy.

Mg-Zn-Ca

Mg-Ca and Mg-Zn systems are already shown above. It is reasonable to expect that with tailored additions of Zn and Ca, a Mg-Zn-Ca ternary system with good corrosion and mechanical performance could be obtained. Du et al. [81] found the addition of 2 wt.% Zn improved the mechanical strength, ductility and corrosion resistance of Mg-3Ca alloy. However, most of the literature focused on Mg-Zn-Ca alloys with a high addition of Ca (e.g. Mg-5Ca-(0.5~5)Zn [129]) and/or Zn (e.g. Mg-3Zn-2Ca [130], Mg-4Zn-0.2Ca [131], Mg-(1~5)Zn-0.3Ca [132]), which led to a high amount of intermetallic phases in the system. In recent years, there is a trend towards the development of micro-alloyed Mg-Zn-Ca systems. Bakhsheshi-Rad et al. [133] reported increased corrosion rate of Mg-0.5Ca-xZn alloys if the Zn content exceeded 1 wt.%. Zander et al. [134] pointed out that Mg-0.6Ca-0.8Zn alloy possessed the lowest corrosion rate compared to other systems with higher Ca or Zn content. Although Mg-Zn-Ca alloys are emerging materials for biomedical applications, most of the publications focused only on the general corrosion performance using electrochemical methods and mass loss and H_2 evolution during immersion [135-137]. As Mg_2Ca phase in Mg-Zn-Ca alloy is one of the few reported anodic precipitates, it would be interesting to see how the corrosion initiates and develops.

Mg-Zn-Sr

Sr shares the same group with Ca in the periodic table and is expected to promote bone regeneration and suppress bone resorption [16]. The human body contains approximately 320-400 mg Sr in bone and connective tissue [88]. Cheng et al. [138] reported that 0.2 wt.% Sr addition to the as-cast Mg-5Zn alloy was beneficial to the corrosion resistance in 0.9% NaCl and in Hank's solution due to the resulting finer grain size. Similar trend was also observed in Mg-4Zn-(0.15~1.5)Sr samples and the Mg, Zn and Sr ion concentration in the media after 48 h culture were within the therapeutic daily dosage ranges (Mg 24-40 mM, Zn 0.9 mM, Sr 5.9 mM) [139].

Mg-Zn-Ag

Tie et al. [17] reported the released Ag^+ ions from Mg-(2~6)Ag alloy in tryptic soy yeast extract medium reduced the viability of Staphylococcus aureus and Staphylococcus epidermidis, and the killing rates against the tested bacteria exceeded 90%. Ben-Hamu et al. [140] found that the addition of 1-3 wt.%Ag increased the corrosion rate of Mg-6Zn alloy in both as-cast and as-extruded states due to the precipitation of $Mg_{54}Ag_{17}$ phase. However, with a proper solution treatment and extrusion process, Mg-3Zn-0.2Ag alloy possessed higher corrosion resistance compared to Mg-3Zn probably due to the single phase microstructure and refined grains [141].

Mg-Zn-In

Indium (In) was commonly used in dental materials. However, scarce results can be found on Mg-In based system. Gu et al. [19] found similar evolved H_2 volumes from as-cast Mg-1Zn and Mg-1In alloys in SBF (10-14 ml/cm^2) and in Hank's solution (3-3.5 ml/cm^2) in 37 °C water bath after 10 days immersion. Likewise, the corresponding evolved H_2 volumes from as-rolled Mg-1In and Mg-1Zn alloys were also comparable in SBF (9-10 ml/cm^2) and in Hank's solution (3-3.5 ml/cm^2). Yu et al. [142] reported that Mg-Zn-In-Sn alloy (0.13 mg/cm^2/h) corroded slower than commercial AZ91 alloy (0.27 mg/cm^2/h) in 3.5% NaCl solution after 30 hours.

Mg-Zn-Cu

Cu is usually added in Mg to produce high strength alloys. Li et al. [18] found the corrosion rates of Mg-Cu alloys were proportional to the Cu contents (0.05-0.25 wt.%). Whereas Mg-0.25Cu exhibited the best antibacterial performance by inhibiting adhesions and biofilm formations from Escherichia coli, Staphylococcus epidermidis and methicillin-resistant Staphylococcus aureus. Lotfpour et al. [143] investigated the effect of Cu addition on the corrosion properties of as-cast Mg-2Zn alloy and found better performance with only 0.1 wt.% Cu addition. It turned out that the positive effect of grain refinement induced by Cu (from 1000 µm to 400 µm) overwhelmed the negative effect of the formation of few MgZnCu intermetallics. However, when the Cu addition increased to 1 wt.%, the corrosion rate of Mg-1Zn-1Cu derived from gravimetric test was almost 20 times higher than that of the Mg-1Zn alloy [144].

2.3. Effect of processing routes

A sketch of the processing routes of Mg alloys for biomedical applications is displayed in **Fig. 2-7** [88]. The properties of Mg alloys depend vastly on the processing techniques. Powder metallurgy is an approach to obtain material with desired composition and porosity by blending

the powders followed by sintering procedures, which however, is expensive [88] and might be corrosion susceptible due to its higher porosity level [125]. On the other hand, casting is more economical by melting the metals and then pouring the melts into the mould to solidify. After primary processing, the as-sintered and as-cast materials are subjected to hot/cold working processes such as rolling and extrusion to get the desired form such as rods, sheets, wires and tubes. However, due to the insufficient number of active deformation mechanisms, the workability of Mg at ambient temperature is low. Koh et al. [145] found the ductility and bendability of cold-rolled AZ31 sheets being rather limited compared to hot rolled ones. Thus processing at elevated temperature is often selected [146, 147].

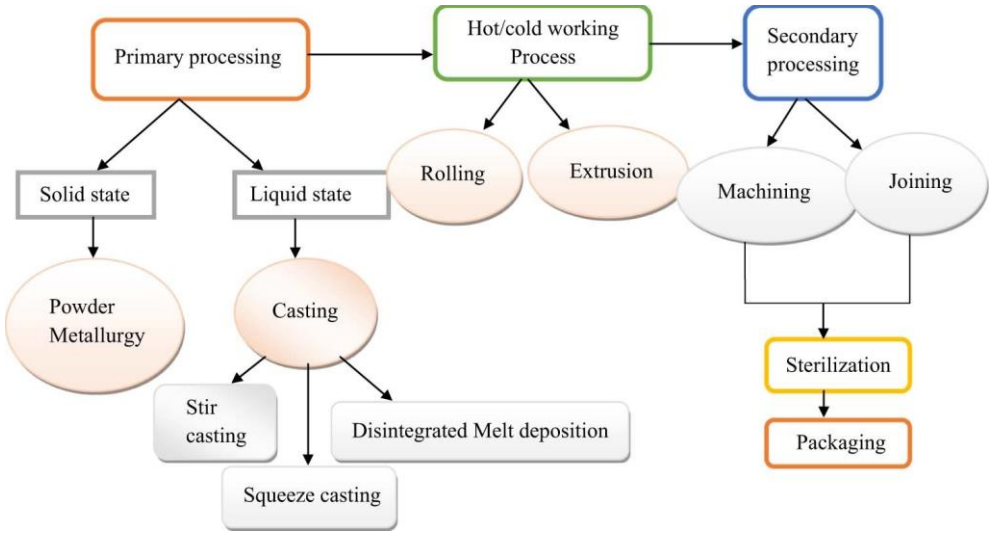

Fig. 2-7. Flow chart of processing sequences of biodegradable Mg alloys [88] under a creative commons license Attribution-NonCommercial-NoDerivatives 4.0 International (CC BY-NC-ND 4.0)

2.3.1. Heat treatment

To overcome the inherent corrosion problems of an as-received material, proper heat treatment might be an option. Generally the corrosion performance is improved after solution annealing due to the dissolution of the intermetallic phases [148]. Less amount of intermetallics contribute to less pronounced galvanic corrosion. Ageing is also a widely-used technique that enables the precipitation of the secondary phases in a homogeneously-distributed way, which is good for corrosion and mechanical properties [148]. The weight loss rate of an as-cast Mg-7Gd-3Y-0.4Zr alloy was almost 10 times higher than those of the solution-annealed and peak-aged samples [149]. However, the effect of grain growth brought by heat treatment can not be ignored too. Aung et al. [150] found that the corrosion performance of AZ31B alloy improved after heat treatment at 200-300 °C for 3 h (grain size 50-65 µm), whereas the corrosion resistance dropped after heat treated at 500 °C for 3 h (grain size 250 µm). The authors

attributed the loss in corrosion to the grain growth during treatment at elevated temperature. Cao et al. [126] performed systematic work on the corrosion characterisation of binary as-cast and solution-annealed Mg-X alloys, and they found the heat treatment decreased the corrosion rates of Mg-1Mn, Mg-5Sn, Mg-5Zn and Mg-0.1Zr whereas it accelerated the corrosion rates of Mg-0.3Ca, Mg-0.3Si, Mg-6Al and Mg-5Sr. The phenomena observed in the former 4 alloys were understandable due to the reduced galvanic corrosion. The corrosion loss in the latter 4 alloys were from some harmful particles precipitated during the solution heat treatment which was also proposed in [61].

2.3.2. Thermomechanical processing

Thermomechanical processings such as extrusion, equal channel angular pressing (ECAP) and rolling endow Mg alloys with finer grain sizes and better mechanical properties via dynamic and static recrystallization. Due to the inadequate mechanical properties of as-cast Mg alloy for biomedical applications, thermomechanical processing seems to be an approach to strengthen both the mechanical and the corrosion properties of the alloys. Ralston et al. [151] reported that grain refinement decreased the corrosion rate of Mg and Mg alloy (e.g. AZ system) and a Hall-Petch type-like relationship was observed between the grain size and the corrosion current density (i_{corr}) determined from potentiodynamic polarisation curves (**Equation 2-1**) [152]. A and B are material constants which differ according to the alloy compositions, impurities and corrosion environment, d is the average grain size. Alvarez-Lopez et al. [146] also observed that the corrosion resistance of as-rolled AZ31 alloy was higher after ECAP with the grain size reduced from 26 µm to 4 µm.

$$i_{corr} = A + Bd^{-0.5} \quad \textbf{(Equation 2-1)}$$

Cao et al. [147], however, found the corrosion rates of all Mg-X alloys (X = Gd, Ca, Al, Mn, Sn, Sr, Nd, La, Ce) decreased after hot rolling with the exception of Mg-0.1Zr and Mg-0.3Si. The authors claimed that there might be a higher sensitivity to Fe-containing particles precipitation during hot rolling, which caused the increase of corrosion rates. However, there was no direct evidence to prove this since the Fe-containing particles were too small. Another interesting study conducted by Ben-Haroush et al. [153] showed that the as-extruded AZ80 alloy had lower corrosion resistance compared to the as-cast counterpart by a factor of 60-80. The changes from continuous β-phase in the as-cast condition to non-continuous β-phase stringer in the as-extruded condition are the main reason for the different corrosion

performance (**Fig. 2-8**). In addition, higher dislocation density and twinning after extrusion might also cause higher susceptibility to corrosion [154, 155].

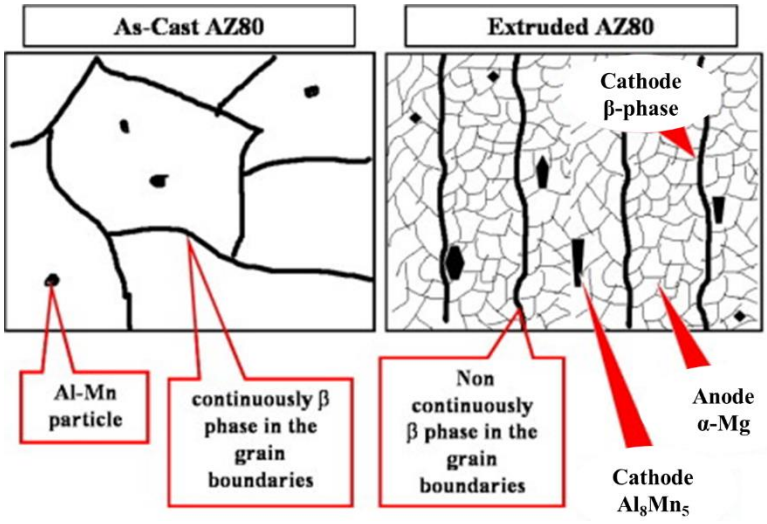

Fig. 2-8. Schematic of the β-phase distribution in as-cast and as-extruded AZ80 alloys [153] (reproduced with permission from Elsevier)

It is reported that the most corrosion resistant grains in as-cast Mg are near the (0001) orientation [156]. Likewise, Song et al. [157] and Xin et al. [158] found that the rolling surface (RS) of AZ31 Mg sheet which was dominated by the (0001) basal planes, exhibited a higher corrosion resistance than the transverse cross sectional surface (TS) which was dominated by the prismatic planes. The discrepancy in the corrosion performance between the TS and the RS might be ascribed to the higher atomic density and lower surface energy of (0001) than those of the $(11\bar{2}0)$ and $(10\bar{1}0)$ planes. However, Wang et al. [159] proposed the corrosion rate of the longitudinal cross-section (LS) was higher than that of the transverse cross-section (TS) in an as-extruded AZ31 bar. The main reason is that TS contains only $(10\bar{1}0)$ and $(11\bar{2}0)$ prism planes whereas LS contains (0001) basal planes and $(10\bar{1}0)$ and $(11\bar{2}0)$ prism planes. Galvanic corrosion also exist between different oriented planes due to their different electrochemical activities.

2.4. Effects of corrosive media

The corrosion performances of the same material differ greatly *in vivo* and *in vitro* [160, 161]. *In vitro* characterisations should be conducted for screening prior to the *in vivo* animal experiment. The corrosion resistances of Mg and Mg alloys are greatly affected by the corrosive media (e.g. solute concentration, pH, flow and temperature of the liquid). Cl^- has the tendency to activate the surface film and the corrosion rate of Mg increases with the increasing of Cl^- [162]. Jiang et al. [163] found $Mg(OH)_2$ was predominately formed in the corrosion

layers of Mg alloy after immersion in 0.9% NaCl solution prepared with deionised water. However, $Mg(OH)_2$ and $CaCO_3$ were formed after immersion in NaCl solution prepared with tap water (59 mg/L Ca^{2+}), which significantly improved the corrosion resistance. As can be seen in **Fig. 2-9**, the formations of corrosion products depend largely on the compositions of the corrosive media, which further influence the corrosion performances. Another important factor that dominates the corrosion products and corrosion behaviour is the pH value (**Fig. 2-9)**. WE43 suffered pitting corrosion in artificial plasma (pH = 7.4) [164] whereas no localised nor filiform corrosion features were observed after immersion in 3.5 wt.% NaCl solution saturated with $Mg(OH)_2$ (pH = 10.5) [165]. The corrosion rate of AZ91 in highly acidic 3.5% NaCl solution (pH = 2, 0.15 mm/year) is much higher than that in neutral and alkaline NaCl solution (pH = 7.2-12.0, 0.001 mm/year) [166]. Lévesque et al. [167] reported the flow rate of the corrosive media had a significant effect on the corrosion rate of Mg. For dynamic immersion condition, low corrosion rate is seen under slow flow rate due to the formation of passive film. Whereas faster degradation is observed if the flow rate increases due to the disruption of corrosion products and inhibition of local pH increase. The corrosion rate also increases with the temperature as the impurities become more active [1]. Baril et al. [168] investigated the corrosion performance of pure Mg in aerated and deaerated (degassed under Ar gas) Na_2SO_4 solution and concluded O_2 did not influence Mg corrosion. The different corrosion performances of Mg in these media could be attributed to the CO_2 dissolution in the aerated electrolyte which transformed into HCO_3^-.

To simulate the corrosive medium in biological body, various artificial physiological fluids are used which have ion concentrations nearly equal to that of the human blood plasma. 0.9% NaCl solution [104, 169, 170] is the simplest simulated body fluids (SBF) and its osmotic pressure is substantially equal to that of the human plasma. To imitate the inorganic components of the human plasma, Kokubo's SBF (c-SBF) [171], revised SBF (r-SBF) [172] and phosphate buffer solution (PBS) [173] were developed. Subsequently, organic components were also considered and Hank's balanced salt solution (HBSS) [174] and cell culture medium such as DMEM [175] under the cell culture conditions were also proposed as alternatives to the conventional SBFs. The chemical compositions of the commonly used SBFs are summarised in **Table 2-2**.

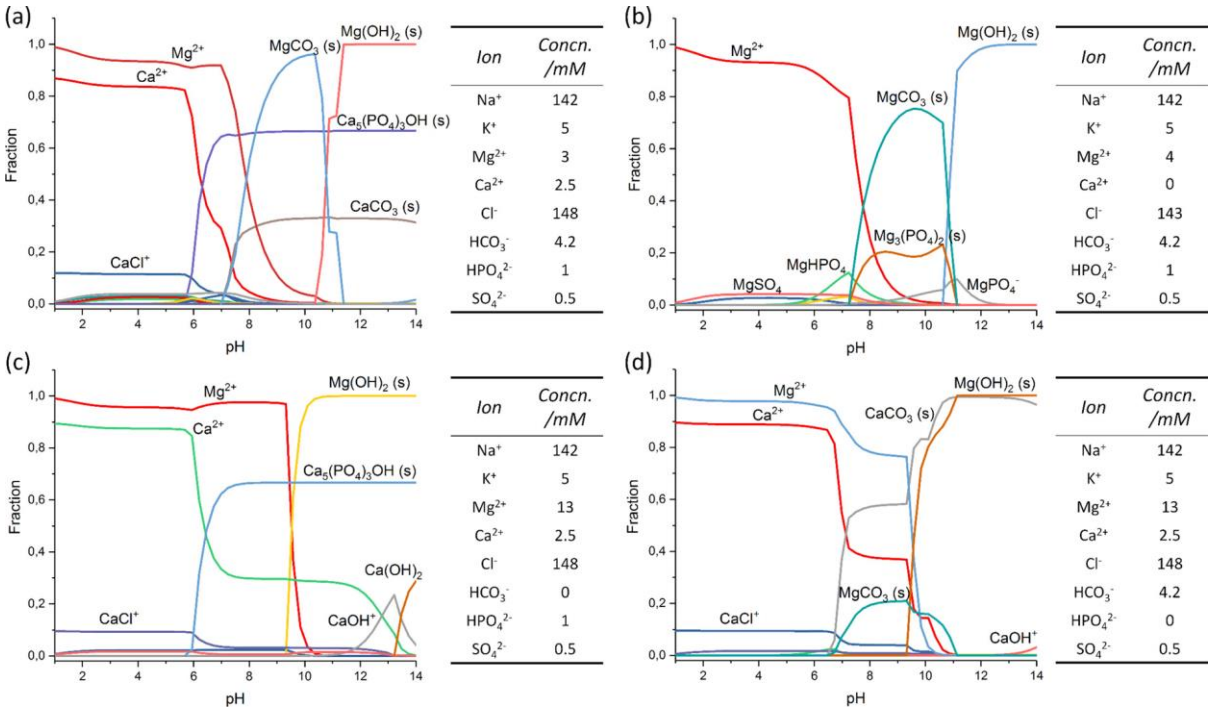

Fig. 2-9. Fraction of Ca^{2+} or Mg^{2+} species as a function of pH based on thermodynamicstability constants in different corrosive media (25 °C, simulated by Hydra-Medusa software) [176] (reproduced with permission from Elsevier)

Table 2-2 Chemical compositions of the commonly used SBFs [175, 177, 178]

		c-SBF	r-SBF	HBSS	PBS	NaCl	DMEM
mmol/L	Na^+	142	142	142	157	153	127.3
	K^+	5.0	5.0	5.9	4.1		5.3
	Ca^{2+}	2.5	2.5	1.3			1.8
	Mg^{2+}	1.5	1.5	0.8			0.8
	HCO_3^-	4.2	27	4.2			44.1
	Cl^-	147	103	145	140	153	90.8
	HPO_4^{2-}	1	1	0.8	11.5		0.9
	SO_4^{2-}	0.5	0.5	0.8			0.8
g/L	Glucose			1			4.5
	Amino acids						1.6

The corrosion performance of Mg alloys differ greatly in these media. Severe pitting corrosion was observed in AZ91 alloy after immersion in 0.9% NaCl solution for 4 days whereas no pitting corrosion appeared after immersion in PBS, HBSS and DMEM [175]. It was suggested that the synergistic effect of Ca^{2+}, Mg^{2+}, HPO_4^{2-} and HCO_3^- in solution promoted the formation of a protective layer on a Mg alloy surface [176]. The corrosion progress might be suppressed due to the co-precipitation of inorganic products (Ca-P and Ca-C) on the intermetallic and impurity particles [176], or even more complex interactions (e.g. adsorption/binding/chelating) relevant with organic molecules such as proteins (**Fig. 2-10**). For example, Hou et al. [179] found that proteins interacted with Ca^{2+}/PO_4^{3-} accelerating the formation of Ca-P salts in DMEM and impeding the degradation of Mg. In contrast, NaCl solution is much simpler. The corrosion products normally have an inner relatively dense MgO layer (thickness in nm), which transitioned to branched and filamentous $Mg(OH)_2$ in the outer layer (thickness in μm). Due to the thin MgO layer and porous nature of $Mg(OH)_2$, Cl^- will disrupt the protectiveness of $MgO/Mg(OH)_2$ [180]. With immersion in non-protective NaCl solution, more information from the material side (e.g. corrosion response to intermetallics and impurities) could be obtained, especially during the early stage of immersion [181].

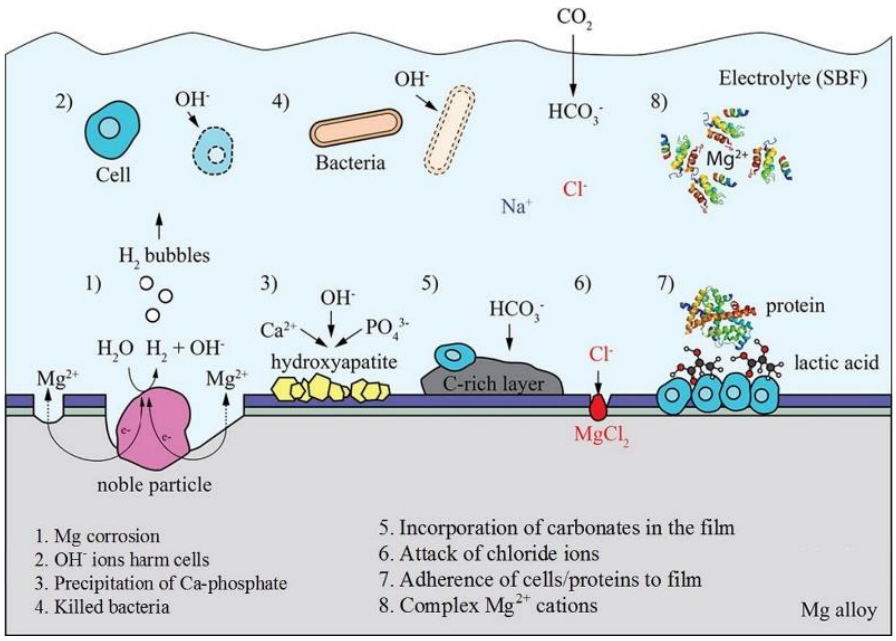

Fig. 2-10. Schematic of some possible interactions between Mg alloy and biological environment [10] under a creative commons license Attribution 4.0 International (CC BY 4.0)

2.5. Summary

As introduced above, the corrosion performances of Mg alloys are influenced by many factors which are summarised in **Fig. 2-11**. The main target of this work is to design a bare alloy with

superior corrosion performance, thus surface coating technology will not be focused. By selecting alloying elements with certain biofunctionality, the microstructures and corrosion performances of Mg-Zn(-X) alloys will be characterised and corelated. After material screening, the effects of further processing such as heat treatment and extrusion will be studied. As this study focuses more on the material part, influencing factors from the complex ingredients in SBFs will not be considered. Instead, a simple 0.9% NaCl solution is chosen as the corrosive medium so that this work can be related to studies with backgrounds of corrosion, biodegradation and metallurgy [182].

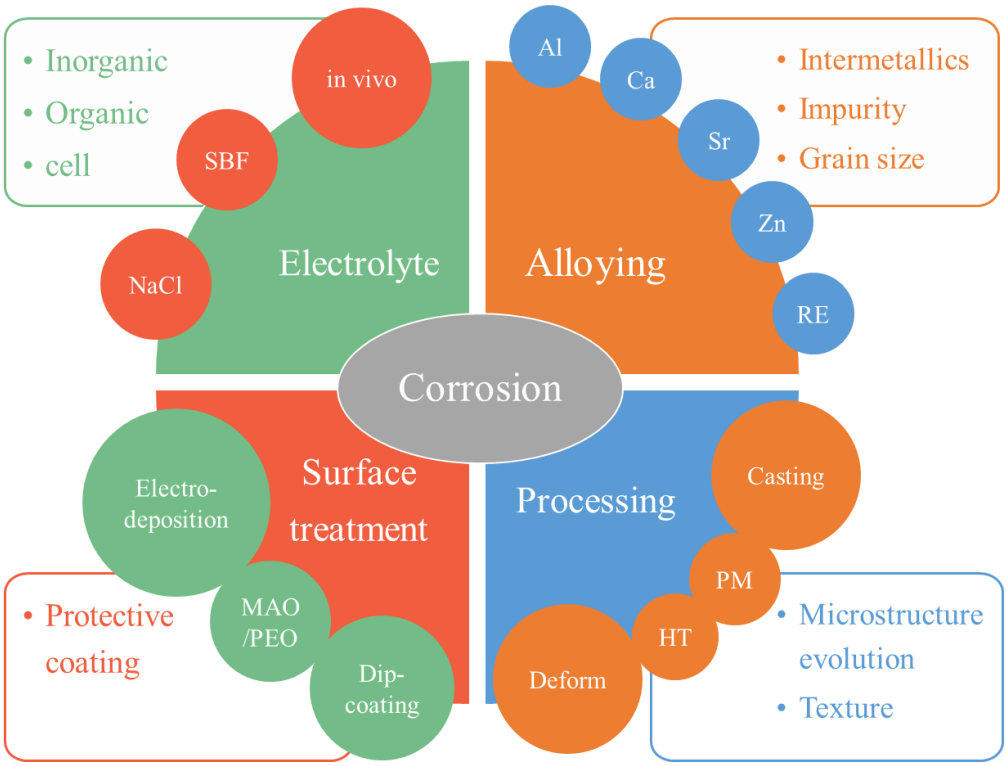

Fig. 2-11. Factors that influence the corrosion performances of Mg alloys. PM: powder metallurgy; HT: heat treatment; MAO: microarc oxidation; PEO: plasma electrolyte oxidation.

3. Motivation and objectives

As the most widely studied Mg-Al-Zn alloys are not appropriate for biomedical applications due to biosafety concerns of Al [14], in this work, alloying elements Ca, Sr, Ag, In and Cu are added to Mg-Zn to study their effects on microstructures and corrosion performances. These alloying elements are selected based on their potential functionality considerations in the body [15-19, 88] (see also in section 2.2.4). 0.5 wt.%Zn and 0.2 wt.%X are selected because low amounts of intermetallics would lead to reduced galvanic corrosion. The ultimate goal of this work is to develop a biodegradable Mg-Zn based alloy with low corrosion rate and additional biofunctionalities (e.g. bone regeneration, antibacterial). The objectives of this research aim at solving the following questions:

- What are the effects of micro additions of alloying elements X on the microstructure evolution of Mg-0.5Zn alloy i.e. grain size, intermetallics?
- Are there interactions between the alloying elements and impurities?
- How do the corrosion performances of Mg-0.5Zn(-0.2X) alloys respond to the modifications of the microstructural features?
- What are the effects of processing such as heat treatment or extrusion on the microstructures and corrosion performances of Mg-0.5Zn(-0.2X) alloys?
- What are the mechanisms for the beneficial or detrimental effects derived from processing? How to avoid the negative effect, if any, in the future research?

4. Materials and methods

4.1. Alloy preparations and compositions

4.1.1. Casting

The as-cast Mg-0.5Zn(-0.2X) alloys were prepared by direct-chill casting with pure Mg (99.95 wt.%, Magnesium Elektron Ltd., UK), Zn (99.99 wt.%, Wilhelm Grillo Handelsgesellschaft mbH, Germany) with or without the addition of Ca (99.51 wt.%, Alfa Aesar GmbH & Co. KG, Germany), Sr (99.9 wt.%, Alfa Aesar GmbH & Co. KG, Germany), Ag (99.99 wt.%, ESG Edelmetall-Handel GmbH & Co. KG, Germany), In (99.995 wt.%, Grirem Advanced Materials Co., Ltd., China) and Cu (99.99 wt.%, Alfa Aesar GmbH & Co. KG, Germany). The alloy melt was heated at 720 °C under Ar-3 Vol.% SF_6 protective atmosphere and stirred for 30 min with a speed of 200 rpm. Following that, the melt was cast into steel moulds which were coated with boron nitride and pre-heated up to 680 °C in a furnace (N 120/65SHA Nabertherm GmbH, Germany). The melt solidified in the moulds by water quenching and the final cylindrical casting ingots were 180 mm in length and 65 mm in diameter.

4.1.2. Solution annealing

The as-cast ingots were machined into 150 mm × 50 mm (length × diameter) billets for further use. To obtain a more homogeneous microstructure and to reduce the amount of intermetallic phases which might induce galvanic corrosion, solution annealing in a small resistance furnace (Vulcan™ A-550, DENTSPLY CERAMCO, USA) was performed. The heat treatment parameters for Mg-Zn(-X) systems (X=Ca, Sr, Ag, Cu) were derived from the phase diagrams calculated by Pandat software (CompuTherm LLC, USA) and that for Mg-Zn-In was from Mg-In binary phase diagram [183] (**Fig. 4-1**). The Mg-Zn binary system, Mg-Zn-Ag, Mg-Zn-In and Mg-Zn-Cu ternary systems were solution annealed at 400 ℃ for 16 h. According to the phase diagrams, the precipitates in Mg-Zn and Mg-Zn-Ag systems can be fully dissolved into the matrix at 400 °C, whereas the intermetallics in Mg-Zn-Cu system could not be fully dissolved. Nevertheless, the heat treatment parameters for Mg-Zn-Cu is the best practice to avoid the formation of liquid phase. Although In is not included in the PanMagnesium 2017 database in Pandat, 400 ℃ seems to be an appropriate temperature based on the information from the Mg-In binary phase diagram [183]. The Mg-Zn-Ca system was solution annealed at 450 ℃ for 16 h and the Mg-Zn-Sr system was solution annealed at 530 ℃ for 8 h under Ar protective gas due to safety considerations. All the solution-annealed ingots were water quenched to room temperature.

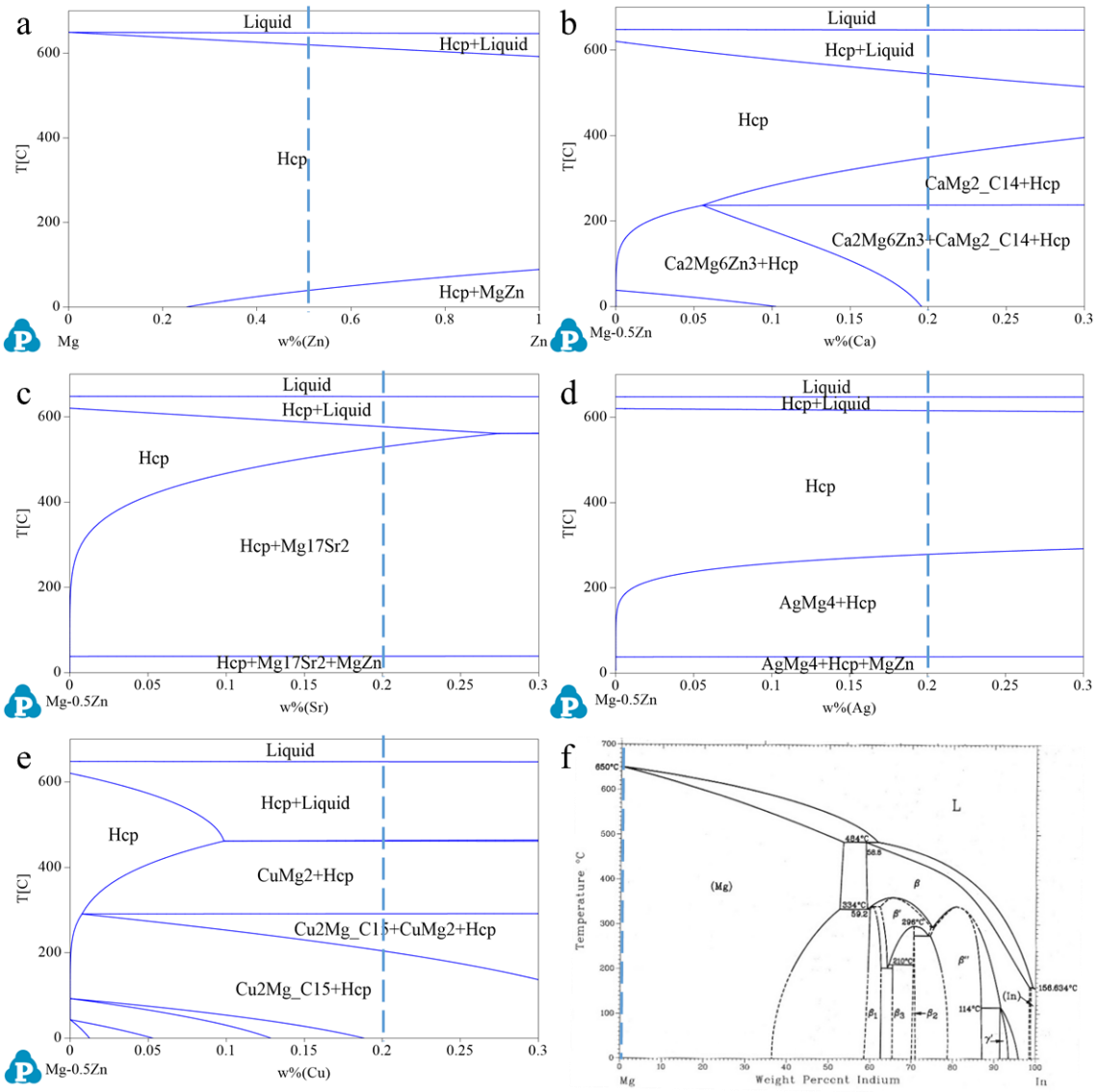

Fig. 4-1. Thermodynamic calculated phase diagrams of (a) Mg-0.5Zn, (b) Mg-0.5Zn-Ca, (c) Mg-0.5Zn-Sr, (d) Mg-0.5Zn-Ag and (e) Mg-0.5Zn-Cu system by PandatTM 2017 with PanMagnesium 2017 database; (f) Mg-In binary phase diagram referred from [183]. The blue dash line represents the exact composition of each system. CaMg2_C14 in (b) and Cu2Mg_C15 in (e) represents Mg_2Ca and $MgCu_2$ phase, respectively.

4.1.3. Extrusion

The solution-annealed billets were pre-heated in a furnace (N 120/65SHA Nabertherm GmbH, Germany) at 350 ℃ for 1 h, then hot extruded (Müller Engineering GmbH & Co. KG, Germany) immediately at 350 ℃ with an extrusion speed of 0.6 mm/s, 2.2 mm/s and 4.4 mm/s, respectively. The dies and press blocks were also pre-heated at 350 ℃ to avoid temperature gradient. The extrusion ratio (ϕ) of this indirect extrusion process was 25:1 which can be calculated as: $\phi = A_0/A_f$ (**Equation 4-1**), where A_0 and A_f are the transverse area of the

container and the profile, respectively. The as-extruded Mg-0.5Zn(-0.2X) bar with diameter of 10 mm and length of around 320 cm was cooled at room atmosphere. The first and last 70 cm of the extrusion bar were discarded and the in-between part was used for characterisation. During the extrusion process, only the middle part of the extrusion bar has a homogeneous microstructure whereas steady state is not guaranteed in the beginning and ending parts. Comparing to the direct extrusion process, indirect extrusion facilitates extrusion implemented at lower temperatures and higher speeds as friction between the billet and the container is avoided [184]. The microstructures of Mg alloys change significantly during extrusion because of dynamic recrystallization, static recrystallization (after exiting extrusion die), refinement of second phases and dynamic precipitation [185].

4.1.4. Composition analysis

To verify the compositions of the ingots (10 ingots for each alloy), Spark-Optical Emission Spectroscopy (Spark-OES, Spectrolab M9 Kleve, Germany) was conducted on the top part and bottom part of ingot No. 1, No. 5 and No. 10. Sample material is vaporized with the testing probe by an arc spark discharge. The atoms and ions contained in the atomic vapor are excited into emission of radiation. From the range of wavelengths emitted by each element, the most suitable line is measured. The radiation intensity (proportional to the element concentration) is calibrated and recalculated as percent concentration (**Fig. 4-2a**) [186]. Prior to the test, the top and bottom parts of the ingots were cut and ground with 200 grit SiC abrasive paper (WS flex 18 C SK, Hermes Schleifmittel GmbH, Germany). A photograph of an as-cast Mg-0.5Zn sample after Spark-OES measurements is shown in **Fig. 4-2b**. Calibration of the device was conducted using the supplied standards [187]. Chips from as-cast and as-extruded samples were also machined and carefully collected (**Fig. 4-2d**). Inductively Coupled Plasma-Optical Emission Spectroscopy measurements (ICP-OES, Thermo Fisher Scientific iCAP duo 6500, USA) were conducted at the Technische Universität Bergakademie Freiberg. The sample for ICP-OES measurement is typically liquid, which is introduced into the plasma (excitation source). The spectrometer is used to separate element-specific wavelengths of light and to focus the resolved light onto the detector as efficiently as possible. Then the derived signals are processed and shown as percent concentration (**Fig. 4-2c**) [188]. Prior to the analysis, the chips were digested with pure nitric acid (HNO_3) in order to receive a liquid solution that can be measured with ICP-OES. The contents of the examined elements were quantified using external calibration. The emission lines that were used for the evaluation of the elements were: Al 167.078 nm, 394.401 nm; Ag 328.068 nm; Be 234.861 nm; Ca 422.673 nm, 396.847 nm;

Cu 324.754 nm; Fe 238.204 nm, 239.562 nm; In 303.936 nm; Mn 257.611 nm; Ni 221.648 nm; Si 212.412 nm, 251.612 nm; Sr 421.552 nm; Zn 213.856 nm. All measurements were repeated 3-5 times to ensure the repeatability.

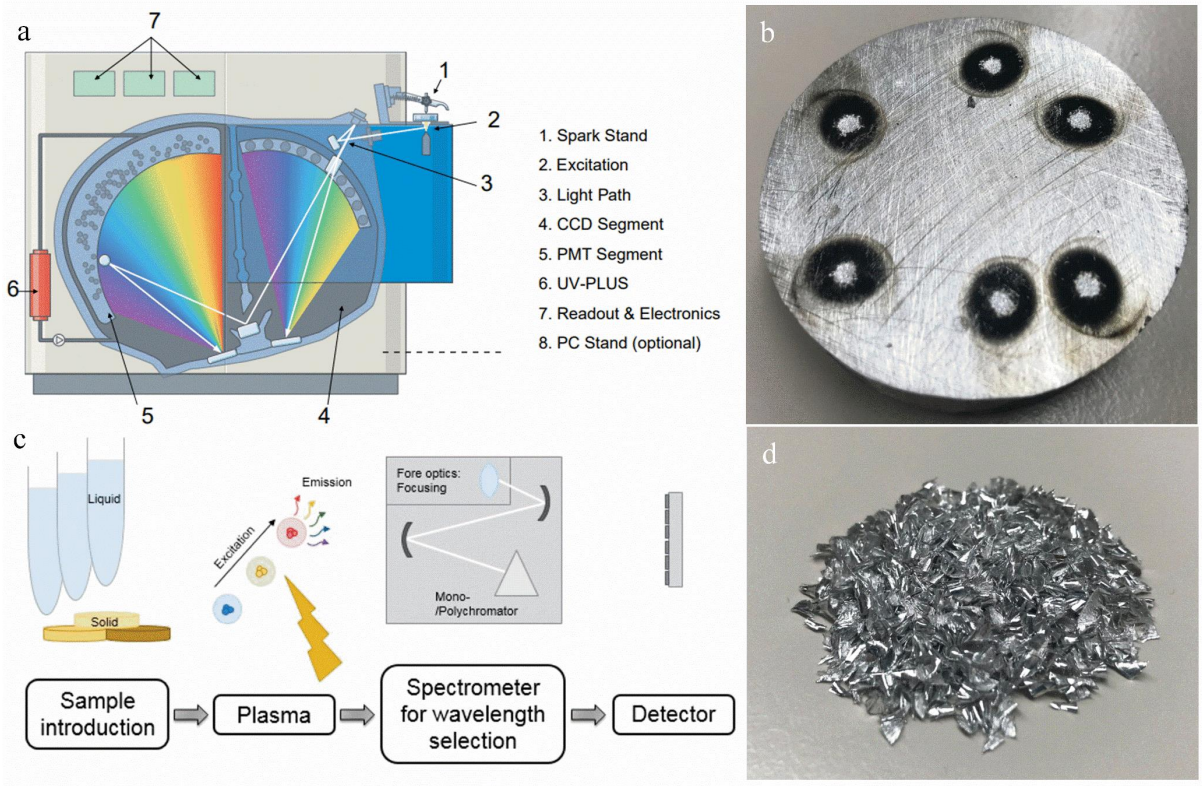

Fig. 4-2. (a) Principles of spark-OES analysis [186] and (b) images of as-cast sample after measurement; (c) Principles of ICP-OES analysis [188] and (d) images of as-extruded sample chips for measurement

4.2. Microstructure analysis

4.2.1. Metallography

The specimens were embedded in cold-curing epoxy composed of 2 parts powder and 1 part liquid (Demotec 30, Demotec Metallografie, Germany). After solidification, the samples were wet ground with SiC abrasive paper up to 2500 grit consecutively and polished with a mixture of water-free silica colloid (OPS^{TM}, Cloeren Technology GmbH), 1 µm diamond slurry and lubricant (1 part ethylene glycol and 10 part ethanol) using an automatic polishing machine (Kurth, Industrieservice Siegmund Bigott, Germany). To reveal the grain structure, the samples were treated by an etchant composed of 150 mL ethanol, 30 mL deionised water, 7 mL acetic acid and 8 g picric acid [189], followed by ethanol cleaning and air drying.

4.2.2. Microscopy

Optical microscopy (OM, Leica DM2500 M, Germany) was used to characterise the microstructure. The grain size was calculated using a line intercept method [190] embedded in the software analySIS pro 5.0 (Olympus Soft Imaging Solutions GmbH, Germany) with multiple measurements. The epoxy mounting surface was coated with carbon paste (N 650 Planocarbon, Plano GmbH, Germany) or the whole sample surface (including the alloy) was sputtered with gold to make it conductive for scanning electron microscopy (SEM, Tescan Vega3, Czech Republic) inspection. The compositions of intermetallic particles were determined by energy dispersive spectroscopy (EDS, IXRF Systems 550i, USA). Some high-magnification images of the precipitates were also obtained by field-emission SEM (Tescan Lyra 3, Czech Republic) with EDS (Oxford Instruments, UK). The overall area fraction of intermetallics was calculated by using software ImageJ (National Institutes of Health NIH, USA) [191]. In addition, some intermetallic analyses were also performed by transmission electron microscopy (TEM, Philips CM200, Netherlands) with accelerating voltage of 200 KV and EDS (Oxford Instruments, UK). The TEM samples were mechanically ground and punched into 100 µm thick 3 mm diameter foils. Further thinning was performed using twin-jet electropolishing with 1.5% perchloric acid solution in ethanol at -45 °C and a voltage of 50 V. Considering the Mg_2Ca phase was corroded during electropolishing (**Fig. S1**), focused ion beam (FIB)/SEM dual beam microscope (FEI NOVA200, USA) was additionally used to prepare some lamellae for further TEM investigations (**Fig. 4-3**).

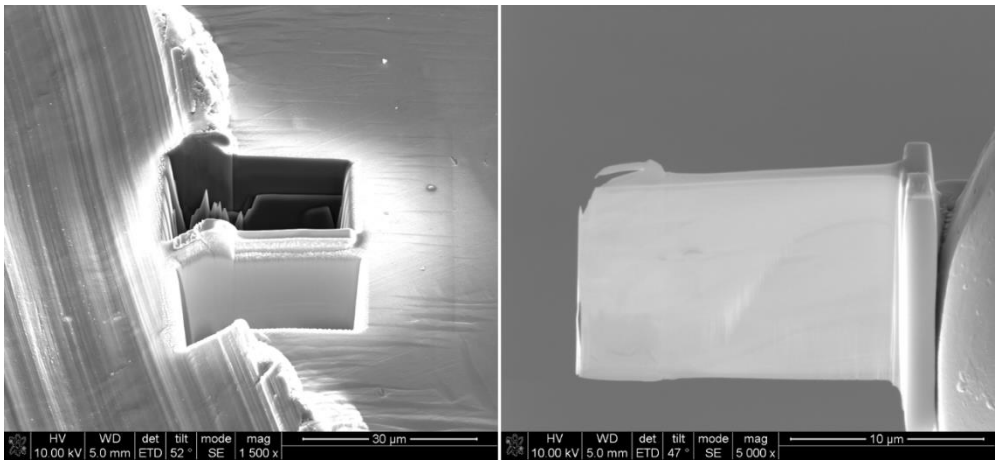

Fig. 4-3. SEM images of (a) as-cast Mg-Zn-Ca alloy during FIB cutting; (b) thinned foil of as-cast Mg-Zn-Ca alloy

4.2.3. Thermodynamic calculation

Pandat with the PanMagnesium 2017 database [192] was used to calculate the phase diagrams of Mg-Zn and Mg0.5Zn-X systems. In addition, considering the Si and Fe impurities in the systems, the phase diagrams of Mg0.5Zn-Si, Mg0.5Zn-Fe, Mg0.5Zn0.2X-Si and Mg0.5Zn0.2X-Fe systems were also calculated. The thermodynamic behaviour during the solidification process was calculated based on a Scheil model, which assumes that no diffusion takes place in the solid [193].

The Miedema model [194-196] is used to calculate the standard molar enthalpies of formation (ΔH) in the binary systems composed of elements i and j according to **Equation 4-2**:

$$\Delta H_{ij} = f_{ij}\frac{x_i(1+\mu_i x_j(\emptyset_i-\emptyset_j))x_j(1+\mu_j x_i(\emptyset_j-\emptyset_i))}{x_i V_i^{2/3}(1+\mu_i x_j(\emptyset_i-\emptyset_j))+x_j V_j^{2/3}(1+\mu_j x_i(\emptyset_j-\emptyset_i))} \quad \textbf{(Equation 4-2)}$$

$$f_{ij} = \frac{2pV_i^{2/3}V_j^{2/3}(q/p\left(\left(n_{ws}^{1/3}\right)_j-\left(n_{ws}^{1/3}\right)_i\right)^2-(\emptyset_i-\emptyset_j)^2-\alpha(\frac{r}{p}))}{\left(n_{ws}^{1/3}\right)_i^{-1}+\left(n_{ws}^{1/3}\right)_j^{-1}} \quad \textbf{(Equation 4-3)}$$

where x, V, Φ and n_{ws} stands for the molar fraction, molar volume, electronegativity and electron density of component i and j, respectively. μ, p, q, r and α are the empirical parameters [197]: r/p exists only when a transition metal is alloyed with a non-transition metal; q/p is 9.4, but p value differs for different alloy systems; μ depends on the element valence; α equals to 0.73 and 1 for liquid alloys and solid alloys, respectively.

4.2.4. Texture

A peak in a diffractogram represents the intensity of a certain (hkl) reflection in a certain orientation. By tilting and rotating the sample which is mounted onto a diffractometer, the intensity distribution of a reflection over the orientation sphere-a pole figure-can be recorded [198]. Texture measurements were carried out on the polished transverse cross section of the as-extruded samples using an X-ray diffractometer (X'Pert³ MRD, Malvern Panalytical GmbH, Germany). Six pole figures were measured with a Cu Kα radiation beam size of 1.5 mm x 1 mm and tilt angles from 0 to 70°. The inverse pole figures in extrusion direction were recalculated with the open-source code MTEX [199].

4.3. Characterisation of corrosion performance

All the corrosion tests were conducted in 0.9 wt.% NaCl solution at room temperature. The solution was prepared by dissolving 45.4 g NaCl (99.99 wt.%, Carl Roth GmbH Co.KG, Germany) in 5 L deionised water.

4.3.1. Electrochemical tests

The general corrosion behaviour of the Mg-0.5Zn(-0.2X) alloys were studied by potentiodynamic polarisation (PDP) and electrochemical impedance spectroscopy (EIS) measurements using a potentiostat (Gill AC, ACM Instruments, UK). Connected to the potentiostat was a three-electrode cell set-up with Ag/AgCl as reference electrode, platinum mesh as counter electrode and the specimen as working electrode (**Fig. 4-4a**). Typically, PDP is performed after certain exposure time where the open circuit potential (OCP) is recorded and stablised. Then voltage is swept at a controlled rate over a potential range by regulating the current between the working electrode and counter electrode. It is generally deemed that oxidation of Mg takes place in the anodic branch while water reduction and oxygen reduction take place in the cathodic branch. PDP can provide information on the kinetics of anodic and cathodic reactions. For example, it can be inferred from **Fig. 4-4b** that the addition of 2 wt.% Zr resulted in an increase in the cathodic kinetics and a retardation in the anodic kinetics over a range of potentials [200]. In this study, the PDP tests were started at -150 mV relative to the free corrosion potential and performed at a scanning rate of 0.2 mV/s after 30 min open circuit potential (OCP) measurement. By selecting the linear part of the cathodic branch that commenced about 50 mV from the corrosion potential with ACM Analysis software, the corrosion current density (i_{corr}) was estimated from its intercept with the vertical corrosion potential line. As for EIS analysis, the response of an electrode to a small amplitude sinusoidal potential perturbation at different frequencies is measured. EIS is non-destructive and can provide information on the impedance of a sample surface which is proportional to the corrosion resistance. For example, it is clear that pure Mg has a better corrosion resistance in HBSS than in NaCl solution (**Fig. 4-4c**) [200]. The electrochemical behaviour of systems can usually be interpreted by electrical equivalent circuits which compose of capacitors, resistors, inductors and other elements. In this work, after stabilising OCP for 5 min, the EIS measurements were carried out at OCP with an AC amplitude of ± 10 mV rms from 0.1 Hz to 30000 Hz after immersion for 0, 1, 2, 3, 6, 12, 24, 48 and 72 h, respectively. The EIS spectra were fitted with Zview (Scribner Associates Inc., USA). Prior to the PDP and EIS test, all samples were ground until 1200 grit SiC abrasive paper. The exposed sample area and the electrolyte volume were 0.5 cm^2 and 330 mL, respectively. During measurement, a magnetic stirrer at 200 rpm constantly agitated the electrolyte. All tests were repeated four times to guarantee the reliability of the results.

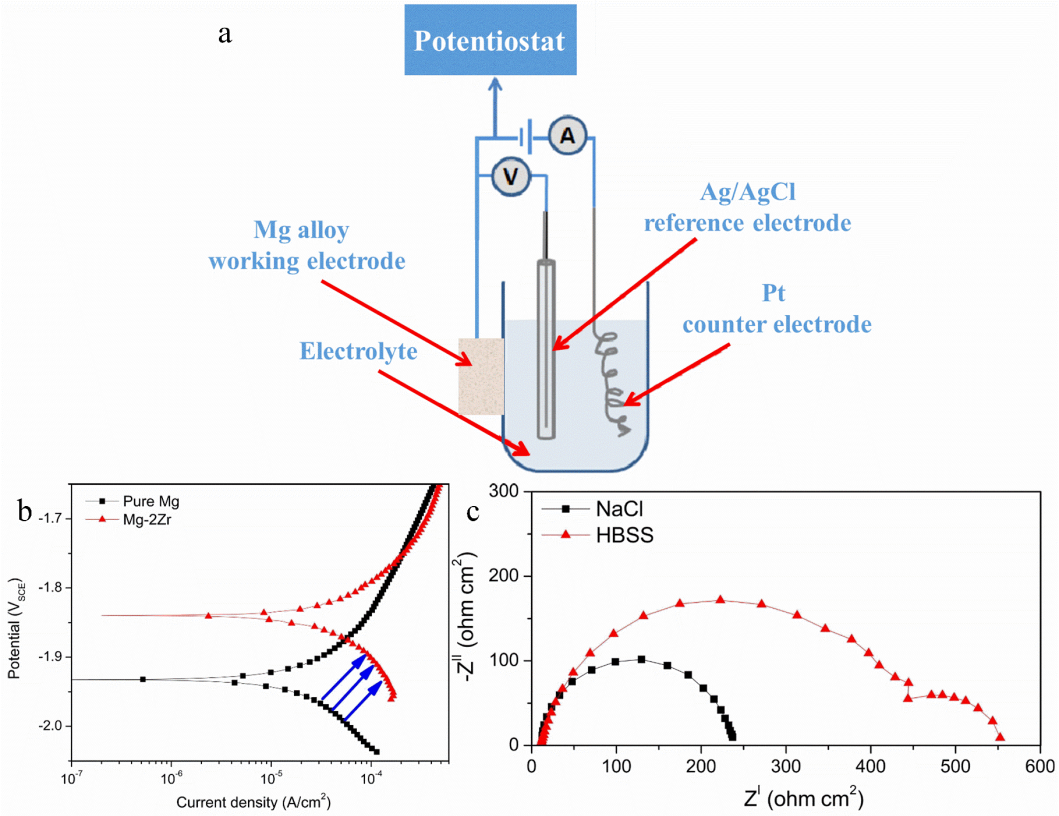

Fig. 4-4. (a) Schematic of a three-electrode electrochemical cell set-up; (b) Polarization curves of pure Mg and Mg-2Zr in HBSS with arrows indicating cathodic shift and (c) Nyquist plots of pure Mg in 1% NaCl solution and HBSS after 2 h immersion [200] (reproduced with permission from Elsevier)

4.3.2. Hydrogen evolution test

The corrosion performance was also evaluated by measuring the hydrogen gas (H_2) evolution at room temperature without agitation. The as-cast specimen was cuboid with a size of 20 mm × 20 mm × 5 mm cut by electrical discharge machine (AW3SL, AMS Technology Co., Ltd., Taiwan). Since the outmost surface of the wrought material is impurity-enriched [70, 71], the 10 mm diameter as-extruded bar was machined into 9 mm diameter rod. The as-extruded specimen for the hydrogen evolution test was cylindrical with a diameter of 9 mm and length of 20 mm. To further eliminate the deleterious effect of contamination from cutting, further slight grinding on each surface was performed with 2500 grid SiC emery paper followed by ethanol degreasing. Prior to the test, the dimensions of all samples were recorded so that the exposed surface areas can be calculated. To avoid the sample surface in direct contact with the glass beaker, the sample was hanged in the medium with a fishing wire (**Fig. 4-5**). Due to the pressure of the evolved H_2 gas in the burette, the electrolyte was pumped back to the beaker and the H_2 volume was recorded after certain time periods. The total volume of the electrolyte was kept constant at 350 mL with the aid of Parafilm (Bemis Company, Inc., USA) sealing to

avoid evaporation. Due to the higher specific heat capacity of water than air at room temperature (25 °C) [201], the beaker was placed in a water bath at room temperature to minimise the possible temperature deviation.

The corrosion rates of the Mg alloys can be calculated using **Equation 4-4** [6]:

$$CR = \frac{8.76*10^4*\Delta g}{A*t*\rho} \quad \textbf{(Equation 4-4)}$$

where CR is the corrosion rate (mm/year), Δg is the weight change (g), A is the initial surface area (cm^2), t is the immersion time (h), ρ is the sample density (g/cm^3), 8.76×10^4 is the factor to convert the unit to CR in mm/year. Based on the hydrogen evolution reaction:

$$Mg + 2H_2O \rightarrow H_2 + Mg(OH)_2 \quad \textbf{(Equation 4-5)}$$

1 mol corroding Mg (24.31 g) will produce 1 mol hydrogen gas (24.5 L) at room temperature (25 °C). The corrosion rate derived from weight loss P_w (mm/year) is determined as: $P_w = 2.10\Delta W$ (**Equation 4-6**) [202] and the corrosion rate derived from H_2 volume P_H (mm/year) can be calculated as: $P_H = 2.088V_H$ (**Equation 4-7**) [203]. At least 3 specimens were tested for each alloy.

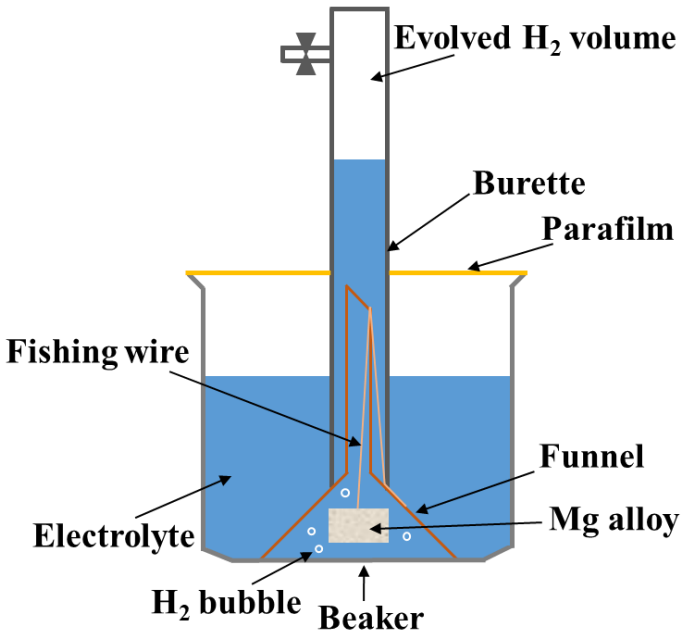

Fig. 4-5. Schematic of a hydrogen evolution test set-up

4.3.3. Immersion test

Quasi-in situ corrosion observation

The quasi-in situ corrosion observation was only conducted on the Mg-0.5Zn-0.2Ca alloy. The samples were ground and polished following the procedures in section 4.2.1. They were

carefully marked so that the exact same position could be tracked before and after the corrosion process. A titanium tweezer was slightly applied on the sample surface to mark a small cross as a reference. A titanium tweezer rather than a steel tweezer was chosen to guarantee that no iron residuals remained on the surface during the marking process. The distance between the targeted intermetallic particles and the cross mark was 0.92 ± 0.07 mm. The intermetallics and the surrounding matrix were observed with SEM in back scattered electron (BSE) and secondary electron (SE) mode. Prior to the corrosion test, the sample was carefully polished again to further reduce the effects of marking and electron exposure during SEM imaging on the corrosion performance. After immersion for a specific time, i.e. 0.5 min, 10 min, 30 min, 1 h, 3 h, 6 h, 12 h or 24 h, respectively, the corroded samples were rinsed with deionised water and ethanol to remove NaCl and poorly attached corrosion products. Then, the same positions were observed again by SEM in BSE and SE mode directly after immersion as well as after the removal of the corrosion products. Reviewing literature, chromic acid was used by most researchers to remove the corrosion products and they claimed that only negligible effect was caused to the alloys [200, 204]. However, fresh chromic acid cleaning (180 g/L in distilled water, VWR International GmbH, Germany) was found to etch the Mg-0.5Zn-0.2Ca samples heavily (**Fig. S2a,b**). Even the diluted one (~1.5 g/L) corroded the Mg_2Ca phase after 5 min cleaning (**Fig. S2c,d**). Inspired by Novoselov and Geim [205], repeated peeling by scotch tape was considered. The mechanical exfoliation process together with diluted chromic acid cleaning were applied to remove the corrosion products to better visualise the corrosion process development.

Short immersion test

Due to the fine and scarce amount of intermetallics in system like as-cast Mg-Zn, the quasi-in situ corrosion observation described above is not applicable. Therefore, some short immersion test is applied to see the corrosion development in macroscale. The as-polished samples were immersed in 60 mL 0.9% NaCl solution in a Parafilm sealed beaker for different periods (e.g. 2 min, 5 min, 30 min, 1 h, 2 h, 6 h, 12 h and 24 h). After immersion, the corroded samples were rinsed with deionised water and ethanol to remove the remaining NaCl and samples with the corrosion products were characterised by SEM. The corrosion morphology was further observed with SEM after the removal of the corrosion products using chromic acid. Cross section of the specimen after immersion (with corrosion products) were characterised by SEM and the compositions were analysed by EDS mapping and point analysis.

5. Results

5.1. As-cast Mg-0.5Zn(-0.2X) alloys

5.1.1. Composition and microstructure

According to the results from Spark-OES, the concentrations of alloying elements and impurities in the top part and bottom part of the casting ingots are comparable, showing a homogeneous distribution of the elements without sedimentation. The alloying element and impurity concentrations detected by ICP-OES are displayed here in **Table 5-1** and those by Spark-OES are shown in **Table S1**. The amounts of alloying elements agree with the stoichiometric of alloys. Although small differences exist in the results from these two methods, generally Fe is less than 30 ppm and Cu and Ni are less than 20 ppm. Particularly, it is noteworthy that Si is present in all systems with concentration range from 70 to 160 ppm.

Table 5-1 Main alloying element and impurity concentrations of the as-cast Mg-0.5Zn(-0.2X) alloys determined by ICP-OES (published in Materials & Design [206])

	Mg-0.5Zn	Mg-0.5Zn-0.2Ca	Mg-0.5Zn-0.2Sr	Mg-0.5Zn-0.2Ag	Mg-0.5Zn-0.2In	Mg-0.5Zn-0.2Cu
Zn (wt.%)	0.49 ± 0.02	0.52 ± 0.02	0.49 ± 0.02	0.50 ± 0.02	0.48 ± 0.02	0.49 ± 0.02
X (wt.%)	-	0.20 ± 0.02	0.19 ± 0.02	0.19 ± 0.02	0.19 ± 0.02	0.20 ± 0.01
Mn (ppm)	177 ± 5	193 ± 5	188 ± 5	193 ± 5	173 ± 5	172 ± 5
Si (ppm)	76 ± 4	145 ± 4	164 ± 4	157 ± 4	77 ± 4	70 ± 4
Al (ppm)	47 ± 5	43 ± 5	162 ± 5	123 ± 5	102 ± 5	48 ± 5
Fe (ppm)	14 ± 6	21 ± 6	18 ± 6	14 ± 6	12 ± 6	8 ± 6
Cu (ppm)	< 3	< 3	< 3	< 3	< 3	-
Ni (ppm)	< 3	< 3	< 3	< 3	< 3	< 3
Be (ppm)	< 3	< 3	< 3	< 3	< 3	< 3

With the additions of alloying element X, different grain structures are observed in **Fig. 5-1**. The grains in Mg-Zn, Mg-Zn-In and Mg-Zn-Cu are coarse (in millimetre range) and the grain sizes can not be revealed with statistical accuracy. With a slight addition (0.2 wt.%) of Ca, Sr and Ag to the Mg-0.5Zn binary system, the average grain size of Mg-Zn-Ca, Mg-Zn-Sr and Mg-Zn-Ag is refined to 147 ± 8 μm, 238 ± 10 μm and 378 ± 55 μm, respectively. Ca is found to exhibit the highest grain refinement efficiency compared to the other alloying elements in this study. Whereas no grain refining effect is observed after the addition of In and Cu. Dendritic microstructures are observed in all as cast Mg-Zn(-X) alloys (**Fig. 5-2**). The

intermetallics of Mg-Zn-Ca, Mg-Zn-Sr and Mg-Zn-Cu are distributed both along the grain boundary and within the grains, whereas intermetallics can be barely seen in Mg-Zn, Mg-Zn-Ag and Mg-Zn-In. Some segregations are found in the interdendritic spacings of all these samples.

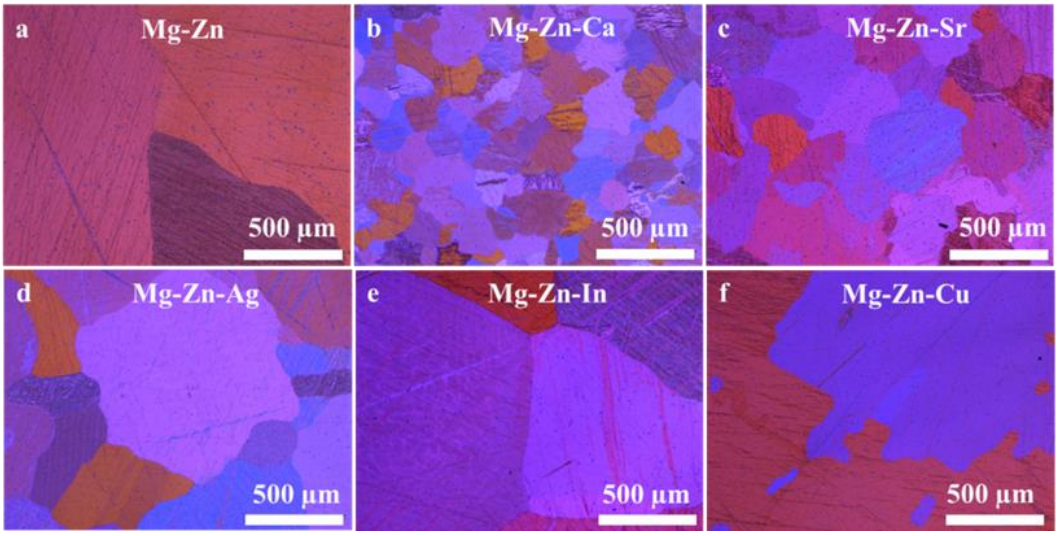

Fig. 5-1. OM micrographs of the as-cast Mg-0.5Zn(-0.2X) systems (published in Materials & Design [206])

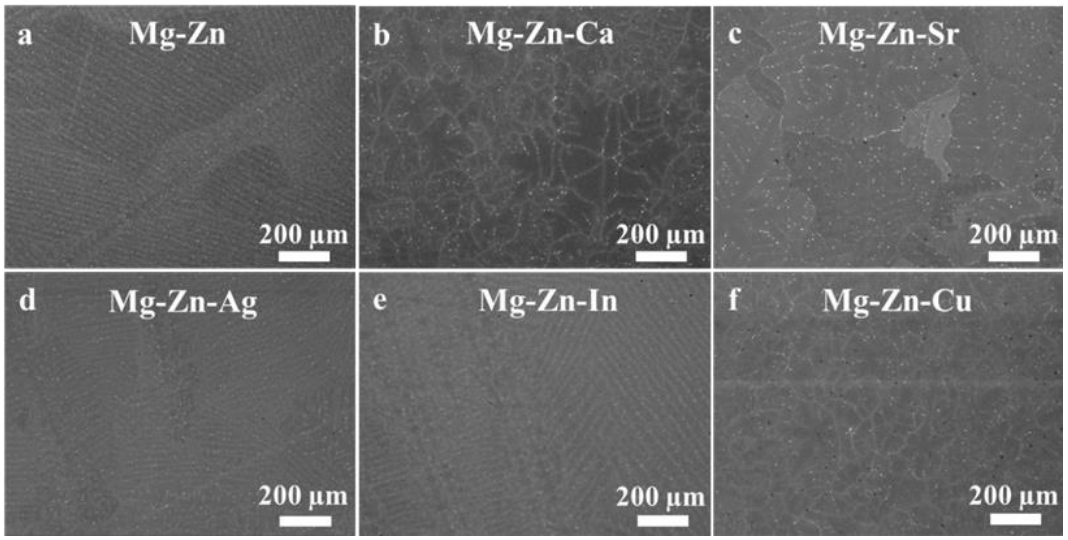

Fig. 5-2. BSE SEM micrographs of the as-cast Mg-0.5Zn(-0.2X) systems (published in Materials & Design [206])

The compositions of the intermetallics (marked in orange) and matrix (marked in green) were analysed by EDS point analysis in **Fig. 5-3**. According to the energy table for EDS analysis [207], the interaction volume in Mg under accelerating voltage of 15 kV is around 4 µm. Considering the size of the precipitates, a large volume of the Mg matrix will be detected in the EDS point analysis. Mg-Zn (**Fig. 5-3a**) and Mg-Zn-In (**Fig. 5-3e**) shared similar

microstructures and coexisting intermetallic particles (CE-IMP) could be seen. The darker part (spot 3 in **Fig. 5-3a** and **Fig. 5-3e**) had higher contents of Si while the brighter part (spot 1, 2) had higher contents of Zn. Indium (In) seemed to be totally dissolved into the Mg matrix and was not segregated in the precipitates. The sizes of the precipitates in Mg-Zn and Mg-Zn-In ranged from submicron to 2 µm. Three types of intermetallics were identified in Mg-Zn-Ca (**Fig. 5-3b**). Two distinct phases were visible in CE-IMP with clear contrast differences, i.e. Mg/Ca with high Zn content (spot 1) and Mg/Ca with low Zn content (spot 2), respectively. The part with higher Zn was also brighter in the BSE SEM image. The CE-IMPs in Mg-Zn-Ca were usually in round or stretched shape and located within the grains. In addition, a Mg/Ca/Si containing phase was discretely distributed within the grains or along the grain boundaries (spot 3). The precipitates in Mg-Zn-Sr were all Mg/Si/Sr/Zn-containing (**Fig. 5-3c**). Within CE-IMP, one part with similar amounts of Si and Sr (spot 2, 4) and another part with high Sr low Si concentrations (spot 1, 3) could be observed. The former one seemed to be brighter and was encapsulated by the latter one which was comparatively darker. In the CE-IMP in Mg-Zn-Ag (**Fig. 5-3d**), higher amounts of Zn and Ag existed in the brighter part (spot 2, 3) and higher amount of Si existed in the darker part (spot 1). Similarly, the darker part of CE-IMP in Mg-Zn-Cu is enriched in Si while the brighter part had higher contents of Zn and Cu (**Fig. 5-3f**). It could be assumed that there existed element gradient within CE-IMPs in Mg-Zn(-X) alloys. Put aside the precipitates formed by the alloying elements (Zn and X), Si also participated in the precipitate formation in all Mg-0.5Zn(-0.2X) systems, although its concentration was only between 70 and 160 ppm. The intermetallic area fractions of the Mg-Zn-Sr, Mg-Zn-Ca, Mg-Zn-Cu and Mg-Zn-Ag alloys calculated by ImageJ are 0.98 ± 0.12%, 0.29 ± 0.05%, 0.20 ± 0.03% and 0.04 ± 0.01%, respectively. Mg-Zn-Sr, Mg-Zn-Ca and Mg-Zn-Cu are found to be with higher amount of intermetallics among all materials, whereas the limited quantities in Mg-Zn and Mg-Zn-In defy quantification.

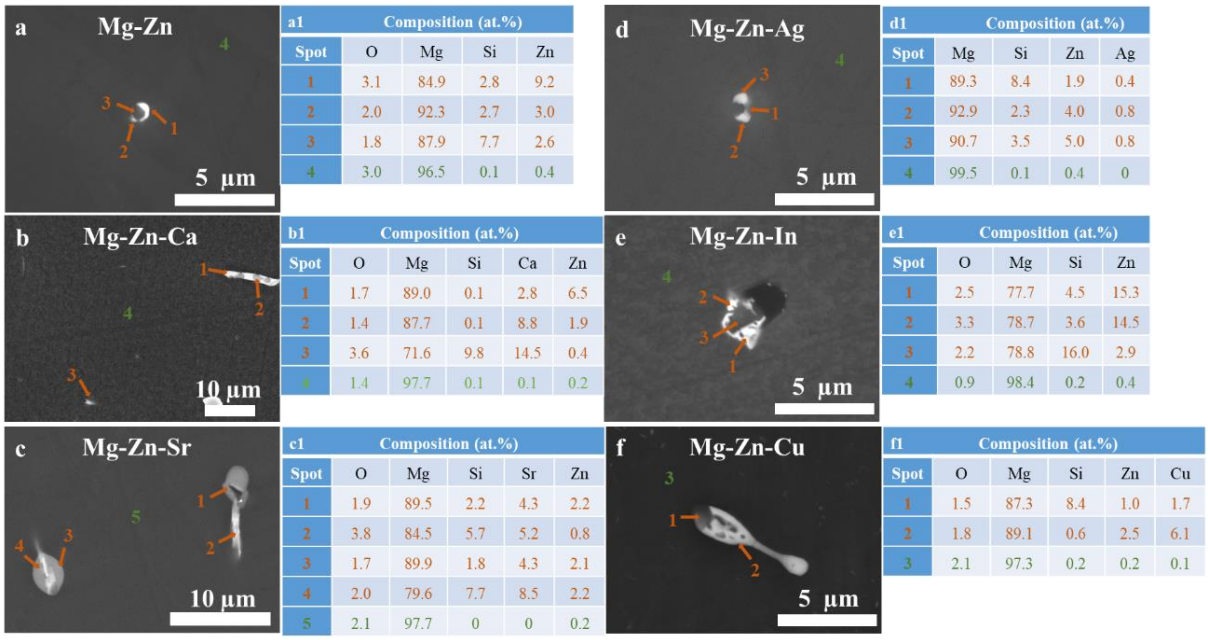

a1 Composition (at.%)

Spot	O	Mg	Si	Zn
1	3.1	84.9	2.8	9.2
2	2.0	92.3	2.7	3.0
3	1.8	87.9	7.7	2.6
4	3.0	96.5	0.1	0.4

d1 Composition (at.%)

Spot	Mg	Si	Zn	Ag
1	89.3	8.4	1.9	0.4
2	92.9	2.3	4.0	0.8
3	90.7	3.5	5.0	0.8
4	99.5	0.1	0.4	0

b1 Composition (at.%)

Spot	O	Mg	Si	Ca	Zn
1	1.7	89.0	0.1	2.8	6.5
2	1.4	87.7	0.1	8.8	1.9
3	3.6	71.6	9.8	14.5	0.4
4	1.4	97.7	0.1	0.1	0.2

e1 Composition (at.%)

Spot	O	Mg	Si	Zn
1	2.5	77.7	4.5	15.3
2	3.3	78.7	3.6	14.5
3	2.2	78.8	16.0	2.9
4	0.9	98.4	0.2	0.4

c1 Composition (at.%)

Spot	O	Mg	Si	Sr	Zn
1	1.9	89.5	2.2	4.3	2.2
2	3.8	84.5	5.7	5.2	0.8
3	1.7	89.9	1.8	4.3	2.1
4	2.0	79.6	7.7	8.5	2.2
5	2.1	97.7	0	0	0.2

f1 Composition (at.%)

Spot	O	Mg	Si	Zn	Cu
1	1.5	87.3	8.4	1.0	1.7
2	1.8	89.1	0.6	2.5	6.1
3	2.1	97.3	0.2	0.2	0.1

Fig. 5-3. (a-f) Intermetallics (marked in orange) and matrix (marked in green) in the Mg-0.5Zn(-0.2X) systems indicated by BSE SEM images; (a1-f1) corresponding compositions measured by EDS point analysis (published in Materials & Design [206])

5.1.2. Corrosion performance

The corrosion performance of the as-cast alloys is evaluated by hydrogen evolution test and the evolved hydrogen volumes are plotted against the immersion time in **Fig. 5-4a**. Mg-Zn-Ca generates the least amount of H_2 during the entire immersion with a value of 0.36 ml/cm^2 after 7 days. The evolved H_2 volumes of Mg-Zn (0.16 ml/cm^2), Mg-Zn-Sr (0.22 ml/cm^2), Mg-Zn-Ag (0.19 ml/cm^2) and Mg-Zn-In (0.29 ml/cm^2) are similar during the first 24 h immersion, which increase steadily reaching 0.77, 1.00, 2.95, 1.77 ml/cm^2, respectively after 7 days. Astonishingly, the H_2 volume of Mg-Zn-Cu skyrockets to 1.81 ml/cm^2 after 6 h immersion and increases continuously to a high value of 49.63 ml/cm^2 after 7 days, which is more than 130 times higher than that in Mg-Zn-Ca. Based on **Equation 4-7**, the calculated corrosion rate of Mg-Zn, Mg-Zn-Ca, Mg-Zn-Sr, Mg-Zn-Ag, Mg-Zn-In and Mg-Zn-Cu after 7 days is 0.25, 0.12, 0.33, 0.97, 0.58 and 16.67 mm/year, respectively (**Fig. 5-4b**).

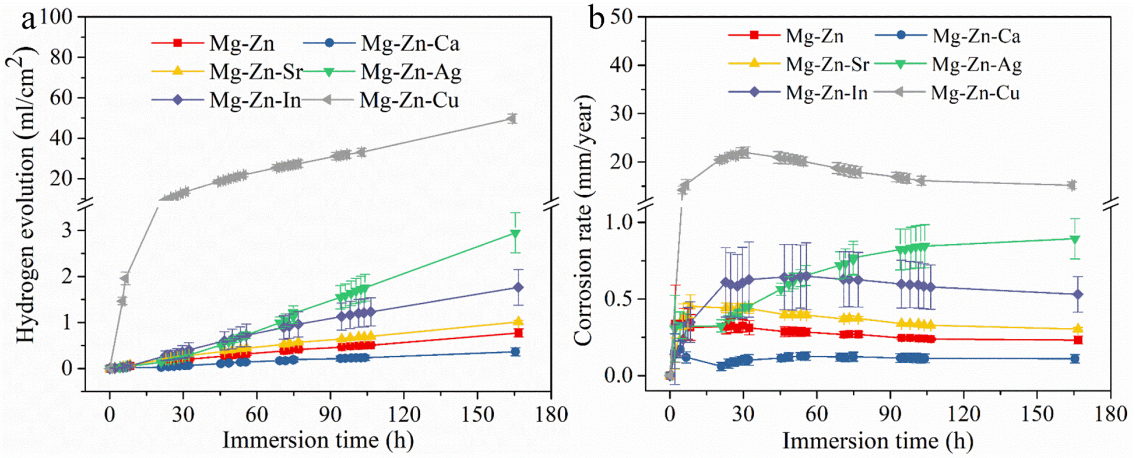

Fig. 5-4. (a) Evolved hydrogen volumes and (b) corresponding corrosion rate of the as-cast Mg-0.5Zn(-0.2X) alloys during 7 days hydrogen evolution test (published in Materials & Design [206])

Compared to Mg-Zn, the additions of Ca and In lead to slight cathodic shift of the corrosion potentials whereas pronounced anodic shifts are seen after adding Ag and Cu (**Fig. 5-5a**). The corrosion potential of Mg-Zn-Sr is similar to that of Mg-Zn. The corrosion current density (i_{corr}) of Mg-0.5Zn(-0.2X) shows a slight variation among each other with the exception of Mg-Zn-Cu. A fivefold increase of the i_{corr} of Mg-Zn-Cu is seen compared to that of Mg-0.5Zn (**Fig. 5-5b**).

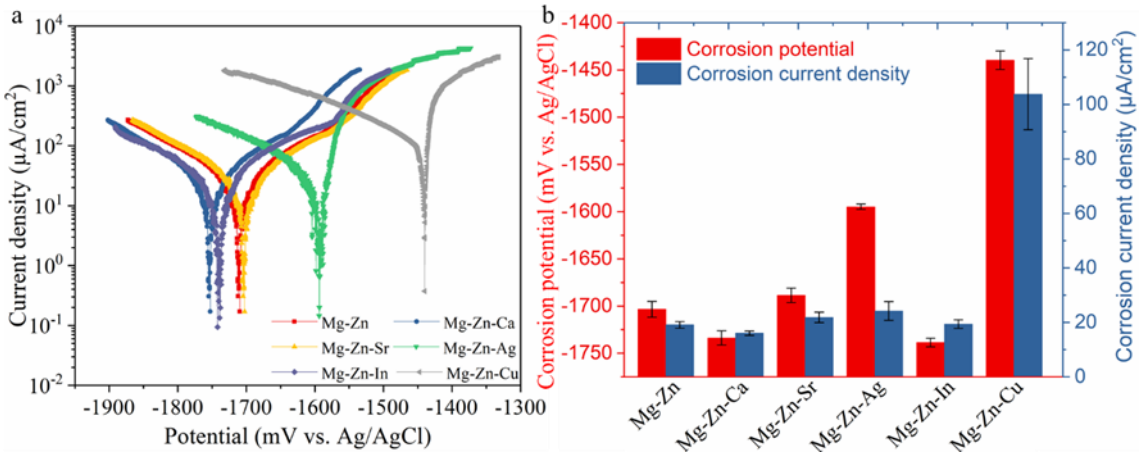

Fig. 5-5. (a) Potentiodynamic polarisation curves and (b) corrosion potential and corrosion current density of the as-cast Mg-0.5Zn(-0.2X) alloys (published in Materials & Design [206])

The Nyquist plots of Mg-0.5Zn(-0.2X) samples are shown in **Fig. 5-6** with the fitted results as solid lines. For better observation, the spectra after 2 h and 3 h immersion are not shown. Two equivalent circuit models are used to fit the EIS data depending on the characteristics of the measured spectra during immersion. The model in **Fig. 5-7a** is used if two capacitive components are observed. The high frequency capacitive loop results from the oxide film (film resistance R_f and film capacitance CPE_f) present on the surface of alloy and the one at middle

frequencies is responsible for charge transfer process (charge transfer resistance R_{ct} and electric double layer capacitance CPE_{dl}). R_s represents the solution resistance between the working electrode and the reference electrode. On the other hand, the middle frequency capacitive loop might reduce in some cases with some scattering points in the low frequency which might be related to non-stationarity during measurements [208], then the model in **Fig. 5-7b** is used. Only the capacitive components are fitted and compared in this study. The general corrosion performance of the Mg-0.5Zn(-0.2X) samples are indicated by the sum of resistances ($R_{sum} = R_f + R_{ct}$) as displayed in **Fig. 5-7c**.

It is found that R_{sum} of Mg-Zn increases during the first 6 h of immersion (1665 Ωcm^2) and drops to a minimum (386 Ωcm^2) at 12 h followed by another raise. A similar trend can also be observed in Mg-Zn-Ca with a steady increase in the first 6 h (1504 Ωcm^2) and a minimum at 12 h (772 Ωcm^2). Mg-Zn-Sr shows an increase until 3 h (1580 Ωcm^2) followed by a reduction until 12 h (656 Ωcm^2), indicating that its first corrosion resistance loss seems to occur earlier than those of Mg-Zn and Mg-Zn-Ca. In a similar manner, the R_{sum} of Mg-Zn-In peaks within 3-6 h (1335 Ωcm^2) then declines gradually or becomes stable afterwards (676 Ωcm^2), depending on the inhomogeneity among different samples. On the contrary, the R_{sum} of Mg-Zn-Ag tops at 1 h (776 Ωcm^2) and then decreases subsequently (307 Ωcm^2) although a slight increase within the time frame of 6-12 h (380 Ωcm^2) is observed in some samples. Although there is a comparatively smaller deviation of the R_{sum} for Mg-Zn-Cu, the sample reaches the minimum value at 1 h (153 Ωcm^2) and stays low until the end of the measurement (194 Ωcm^2). Mg-Zn-Cu possesses only one obvious capacitive component throughout the whole immersion process. Although the R_{sum} is changing during immersion, it is generally found that the corrosion resistance of Mg-Zn, Mg-Zn-Ca, Mg-Zn-Sr and Mg-Zn-In are comparable within 24 h immersion, whereas higher resistance is observed in Mg-Zn-Ca in the later stage of immersion (1771 Ωcm^2). Mg-Zn becomes more prone to corrosion with the addition of Ag and Cu.

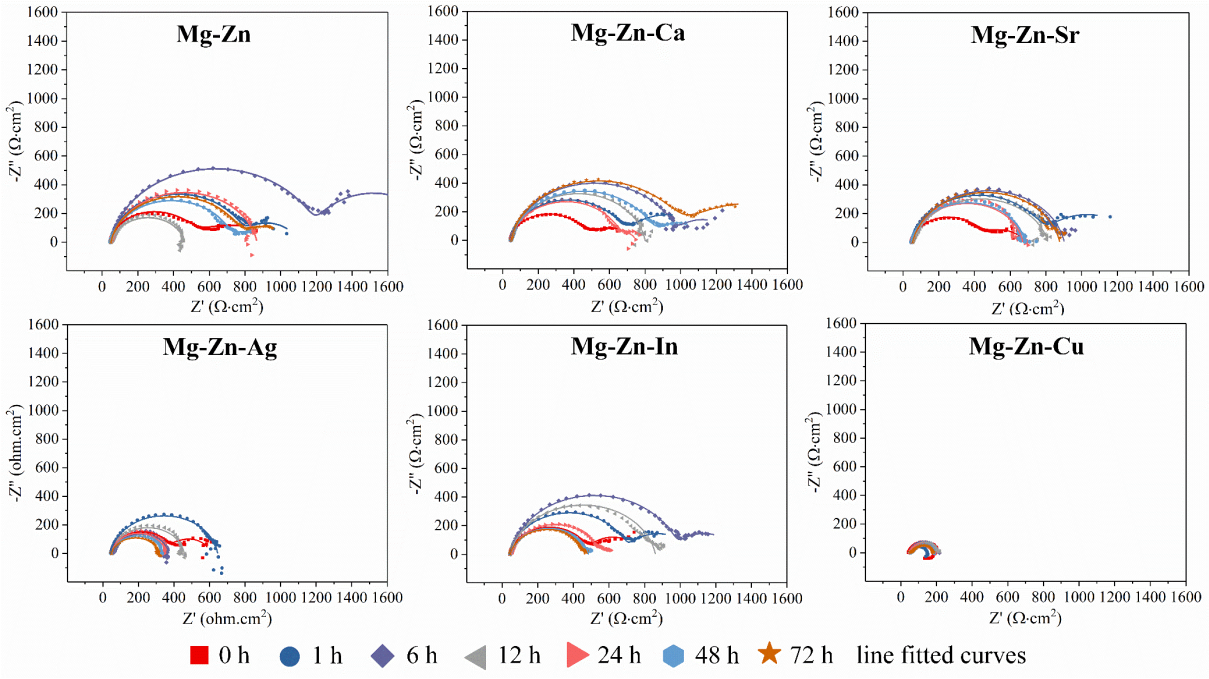

Fig. 5-6. EIS Nyquist diagrams of the as-cast Mg-0.5Zn(-0.2X) alloys after 3 days immersion in 0.9% NaCl solution. The original data are shown as the scatter points and the fitted data are shown as the lines (published in Materials & Design [206])

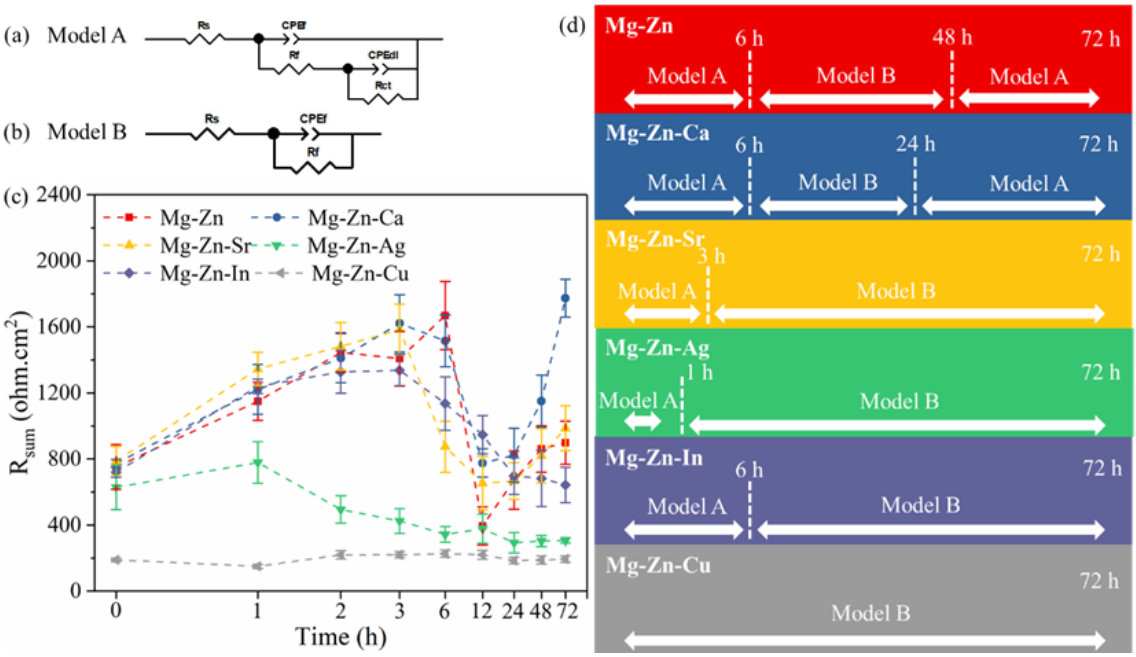

Fig. 5-7. (a-b) Equivalent circuits used to fit the impedance spectra of Mg-0.5Zn(-0.2X) alloys exposed in 0.9 wt.% NaCl solution; (c) the fitted sum of the resistance of Mg-0.5Zn(-0.2X) alloys during the 3 days measurement (the X axis is in log10 scale for better perception); (d) selection of the models for EIS spectra at different immersion periods (published in Materials & Design [206])

The corrosion morphologies of the Mg-0.5Zn(-0.2X) alloys after immersion for different durations are illustrated in **Fig. 5-8**. Filiform-like corrosion occurs on the surface of Mg-Zn

after 12 h immersion. However, scratches from grinding can still be seen on the rest of the sample surface, indicating the corrosion is not that severe in this area. The filiform-like corrosion spreads to a larger area after 24 h. The cracks in the corrosion layers are derived from the dehydration process after immersion. Similarly, slight corrosion is observed in Mg-Zn-Ca during the first 6 h immersion with the corrosion products align along the grinding patterns. However, with prolonged exposure, the corrosion layers become less compact after 12 h and 24 h and the gaps in between are also larger. No filiform-like corrosion is observed in Mg-Zn-Ca during 24 h immersion. As for Mg-Zn-Sr, localised corrosion is seen after 6 h (in white circle) which develops into filiform-like corrosion after 24 h. However, filiform corrosion in Mg-Zn-Sr is not as significant as that in Mg-Zn. Similarly, localised corrosion occurs after 1 h and develops into filiform corrosion after 6 h in Mg-Zn-Ag, which is already much more severe than that in Mg-Zn and Mg-Zn-Sr after 24 h. In addition, the corrosion products are loose and hundred micrometre-sized corrosion pits (in white circle) can be found. In a similar but faster way, Mg-Zn-Cu also exhibits filiform corrosion after 1 h and pitting corrosion (in white circle) after 6 h. Comparatively uniform corrosion is observed in Mg-Zn-In during the first 6 h, just like the case in Mg-Zn-Ca. However, the corrosion products seem to be denser in Mg-Zn-Ca than those in Mg-Zn-In.

Cross sections of the corrosion products of the Mg-0.5Zn(-0.2X) alloys after 24 h immersion are presented in **Fig. 5-9**. Mg-Zn and Mg-Zn-Sr generally exhibit uniform corrosion with some localised corrosion sites. This is consistent with the filiform corrosion observed in some areas in **Fig. 5-8**. For Mg-Zn-Ca and Mg-Zn-In, the arc-shaped corrosion products in the cross section view are in accordance with the wide-gap corrosion products in the top view (**Fig. 5-8**). The corrosion products are more compact in Mg-Zn-Ca than those in Mg-Zn-In. Localised corrosion is observed in Mg-Zn-Ag and Mg-Zn-Cu and the pits are deeper in the case of Mg-Zn-Cu (as deep as 40 μm).

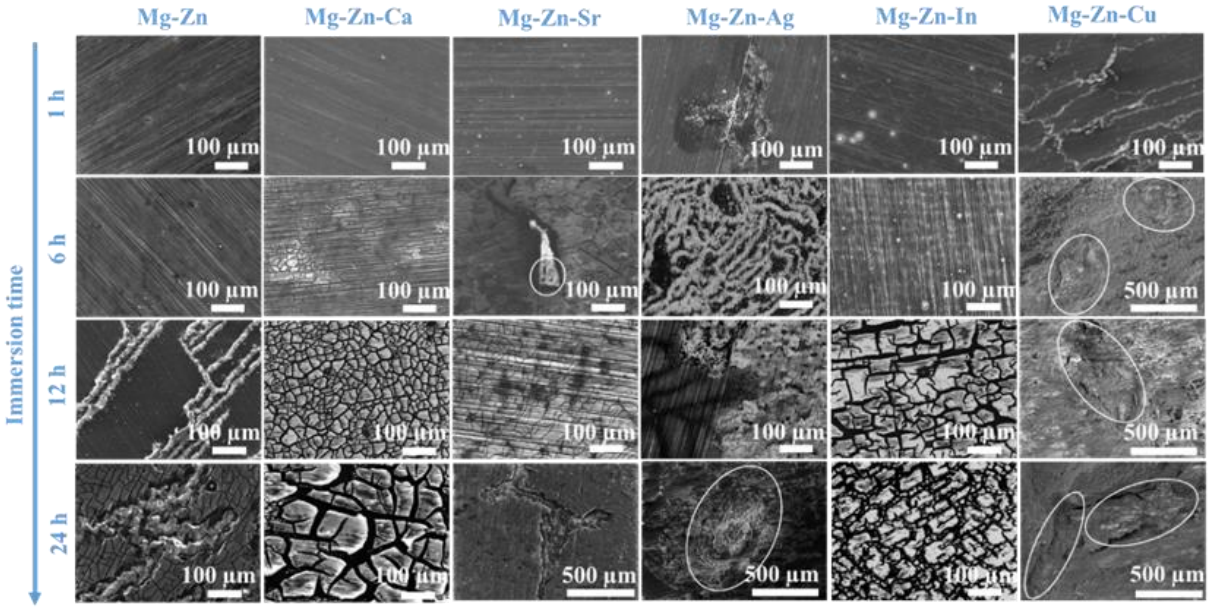

Fig. 5-8. Corrosion morphology (with corrosion products) of the as-cast Mg-0.5Zn(-0.2X) alloys after immersion in 0.9% NaCl solution for 1, 6, 12 and 24 h (published in Materials & Design [206])

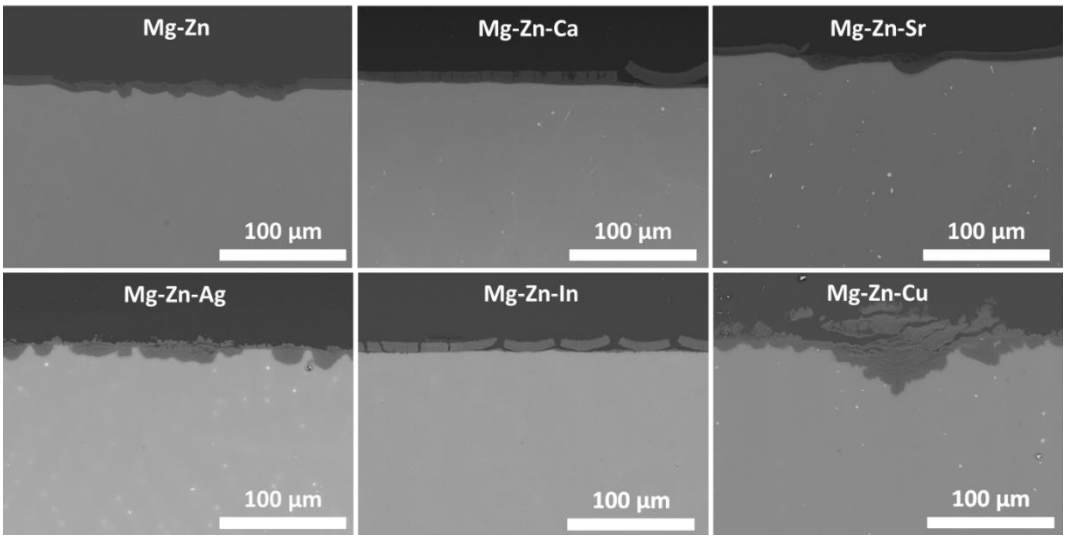

Fig. 5-9. Cross section of the corrosion products of the as-cast Mg-0.5Zn(-0.2X) alloys after 24 h immersion in 0.9% NaCl solution (published in Materials & Design [206])

Although the general thickness of the corrosion products in Mg-Zn(-X) are in the range of 10-20 µm, the corrosion layers of Mg-Zn-Ag and Mg-Zn-Cu are obviously thicker and looser than those in the other systems (**Fig. 5-10**). To obtain information about the compositions of the corrosion products, EDS point analysis were carried out on the cross sections of the corrosion products and matrices. The main signals coming from the corrosion layers were Mg and O, indicating the corrosion products were mainly composed of oxides and/or hydroxides which were only partially protective. Alloying elements X were not found in the corrosion products whereas slight contents of Zn could be detected. Particularly, higher content of Zn (~ 2 at.%)

existed in the outer layer of the corrosion products in Mg-Zn-Sr ((**Fig. 5-10c**). As displayed in the EDS mapping in **Fig. 5-11a**, Zn and O are enriched in the outer layer of the corrosion products, hinting Zn/O composite is formed during degradation in 0.9% NaCl solution. On the other hand, the corrosion products of the other systems are just composed of Mg and O (Mg-Zn-Ca as an example in **Fig. 5-11b**).

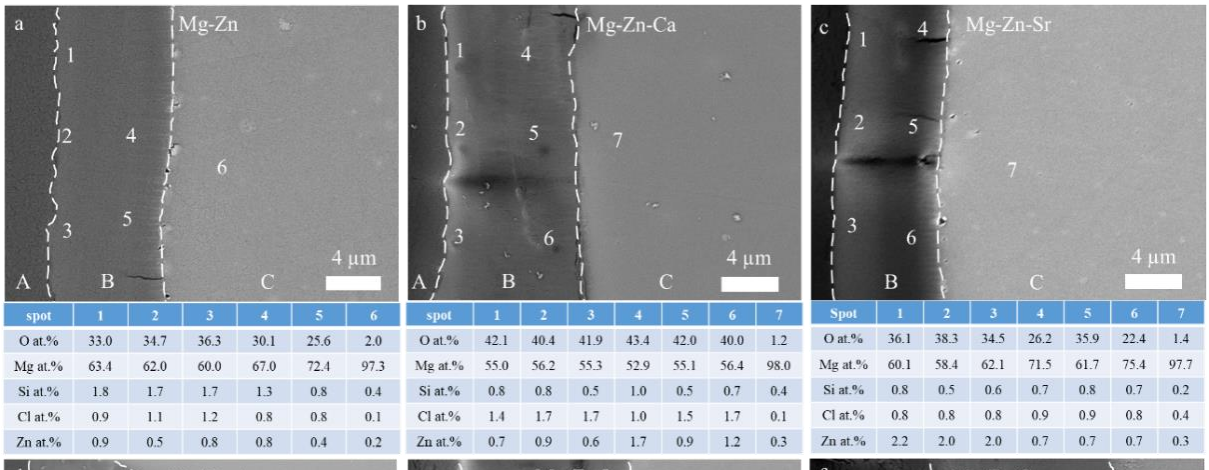

spot	1	2	3	4	5	6
O at.%	33.0	34.7	36.3	30.1	25.6	2.0
Mg at.%	63.4	62.0	60.0	67.0	72.4	97.3
Si at.%	1.8	1.7	1.7	1.3	0.8	0.4
Cl at.%	0.9	1.1	1.2	0.8	0.8	0.1
Zn at.%	0.9	0.5	0.8	0.8	0.4	0.2

spot	1	2	3	4	5	6	7
O at.%	42.1	40.4	41.9	43.4	42.0	40.0	1.2
Mg at.%	55.0	56.2	55.3	52.9	55.1	56.4	98.0
Si at.%	0.8	0.8	0.5	1.0	0.5	0.7	0.4
Cl at.%	1.4	1.7	1.7	1.0	1.5	1.7	0.1
Zn at.%	0.7	0.9	0.6	1.7	0.9	1.2	0.3

Spot	1	2	3	4	5	6	7
O at.%	36.1	38.3	34.5	26.2	35.9	22.4	1.4
Mg at.%	60.1	58.4	62.1	71.5	61.7	75.4	97.7
Si at.%	0.8	0.5	0.6	0.7	0.8	0.7	0.2
Cl at.%	0.8	0.8	0.8	0.9	0.9	0.8	0.4
Zn at.%	2.2	2.0	2.0	0.7	0.7	0.7	0.3

spot	1	2	3	4	5	6	7
O at.%	35.1	31.6	30.5	32.3	28.1	35.1	1.4
Mg at.%	63.4	67.0	68.3	65.7	69.5	63.3	97.9
Si at.%	0.8	0.6	0.6	0.9	1.0	0.9	0.4
Cl at.%	0.5	0.6	0.4	0.6	0.7	0.5	0.1
Zn at.%	0.2	0.2	0.2	0.5	0.7	0.2	0.2

spot	1	2	3	4	5	6	7
O at.%	41.7	41.2	42.3	42.3	40.8	41.1	2.6
Mg at.%	56.0	56.1	55.0	55.6	57.3	56.8	96.7
Si at.%	0.6	1.1	1.1	0.8	0.5	0.6	0.4
Cl at.%	1.1	1.1	1.0	0.9	0.9	1.0	0.1
Zn at.%	0.6	0.5	0.6	0.4	0.5	0.5	0.2

spot	1	2	3	4	5	6	7
O at.%	42.2	39.5	40.0	43.0	45.5	44.5	1.8
Mg at.%	56.5	59.1	58.5	55.7	53.5	54.3	97.5
Si at.%	0.8	0.8	0.8	0.5	0.4	0.4	0.3
Cl at.%	0.3	0.4	0.4	0.5	0.4	0.6	0.2
Zn at.%	0.2	0.2	0.3	0.3	0.3	0.2	0.2

Fig. 5-10. EDS point analysis on the cross sections of the corrosion products and the matrices in Mg-0.5Zn(-0.2X) alloys. A, B, C regions separated by the dash lines represent epoxy resin, corrosion layer and matrix, respectively (published in Materials & Design [206])

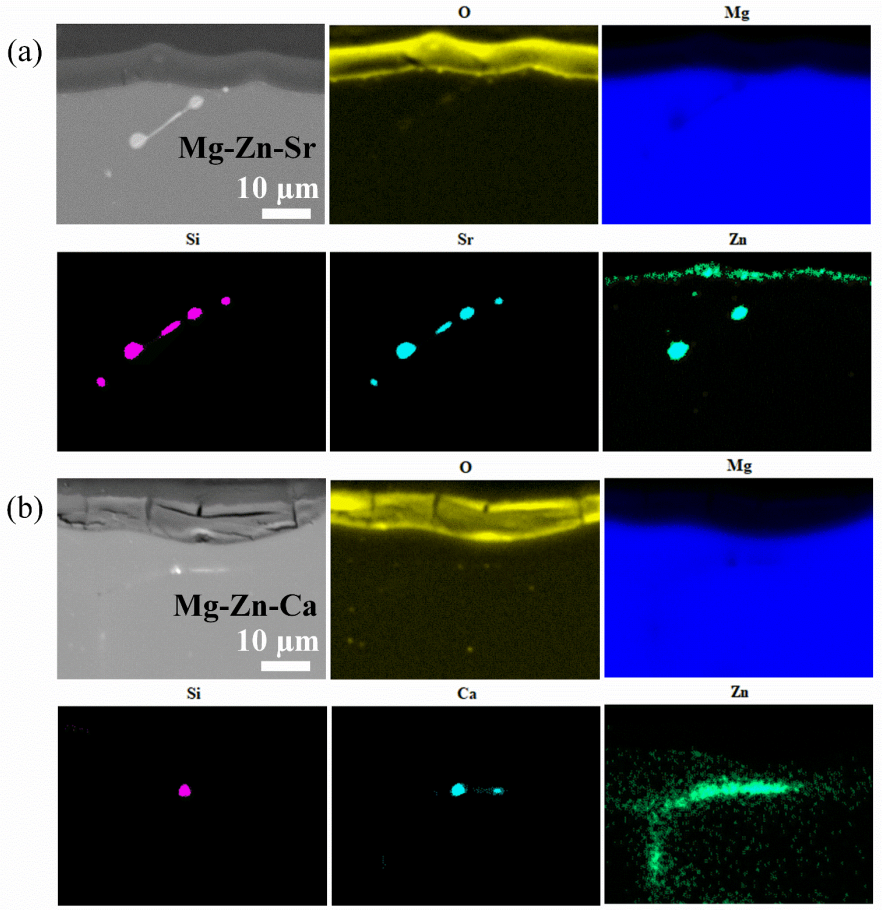

Fig. 5-11. EDS element mapping of the cross section of corrosion products of (a) Mg-0.5Zn-0.2Sr and (b) Mg-0.5Zn-0.2Ca alloys (published in Materials & Design [206])

5.1.3. Summary

(1) The micro additions of alloying elements X influence the microstructure of Mg-0.5Zn refenrence material significantly. The grain size of Mg-0.5Zn is refined with the addition of Ca, Sr and Ag. Considerable amounts of intermetallics are formed in Mg-Zn-Sr, Mg-Zn-Ca and Mg-Zn-Cu. Moreover, Si impurity participates actively in the formation of precipitates in all Mg-Zn(-X) systems.

(2) Different corrosion performances of Mg-Zn(-X) alloys are observed due to the different microstructural features. Mg-Zn-Ca exhibits the lowest corrosion rate while Mg-Zn-Cu exhibits the highest corrosion rate. The corrosion rate of Mg-Zn is comparable to that of Mg-Zn-Sr. Slight deterioration in the corrosion resistance is observed after adding In and Ag. Except for Mg-Zn-Cu, the corrosion rates of all the other as-cast alloys are less than 1 mm/year after 7 days immersion.

5.2. Effects of solution treatment

As stated in section 3, the goal of this work is to develop a biodegradable Mg-Zn based alloy with low corrosion rate and additional functionalities. The as-wrought alloys usually exhibit better corrosion and mechanical properties compared to the as-cast counterpart [90, 209]. Most of the studies in literature conduct solution treatment prior to extrusion [209] and rolling [90]. Thus, the effects of solution annealing are described in this section. Particularly, Mg-Zn-Ca is selected as it has the highest corrosion resistance among the as-cast Mg-Zn(-X) alloys. Moreover, the potentially formed Mg_2Ca phase is reported as the anodic intermetallics in literature [80, 97] which is different to the precipitates in other Mg-Zn(-X) systems. Thus, it would be interesting to see how the microstructure changes during annealing and how the corrosion performance responds. On the other hand, Mg-Zn serves as the reference and limited intermetallics (potentially cathodic MgZn phase [123]) are present in the system. The different responses of Mg-Zn and Mg-Zn-Ca to solution annealing, if any, would also be appealing.

5.2.1. Mg-0.5Zn alloy

The Mg-0.5Zn samples are solution treated at 400 ℃ for 2 h and 16 h to see the effect of heat treatment. These samples are shortened as HT-2 h and HT-16 h, respectively. As the precipitates in Mg-0.5Zn are too small and too scarce, the quasi-in situ corrosion observation approach used in Mg-Zn-Ca is not appropriate in the case of Mg-Zn.

Microstructure

Microstructures of the as-cast and solution-treated Mg-0.5Zn are shown in **Fig. 5-12a-c**. The as-cast sample exhibits a dendritic microstructure which is barely seen after heat treated at 400 ℃. The grain sizes of all samples are in millimetre range. According to the EDS element mapping (**Fig. 5-12d**), Zn is segregated between the dendritic arms in the as-cast sample. Zn and Si signals can be simultaneously detected in some spots due to the formations of CE-IMP (possibly MgZn and Mg_2Si phases). However, after heat treated for 2-16 h, Zn-rich segregation is reduced and a more homogeneous microstructure is obtained (the HT-16 h sample as an example in **Fig. 5-12e**). The assumed MgZn phase dissolves during annealing while Mg_2Si phase still remains. In addition, it is noteworthy that some submicron-sized precipitates containing certain amounts of Fe and Si can also be observed in these as-cast and solution-annealed samples (**Fig. 5-13a-c**). The concentration of Zn in the matrix (rectangular area) of the as-cast sample is slightly higher than those of the heat treated samples possibly due to the presence of segregations.

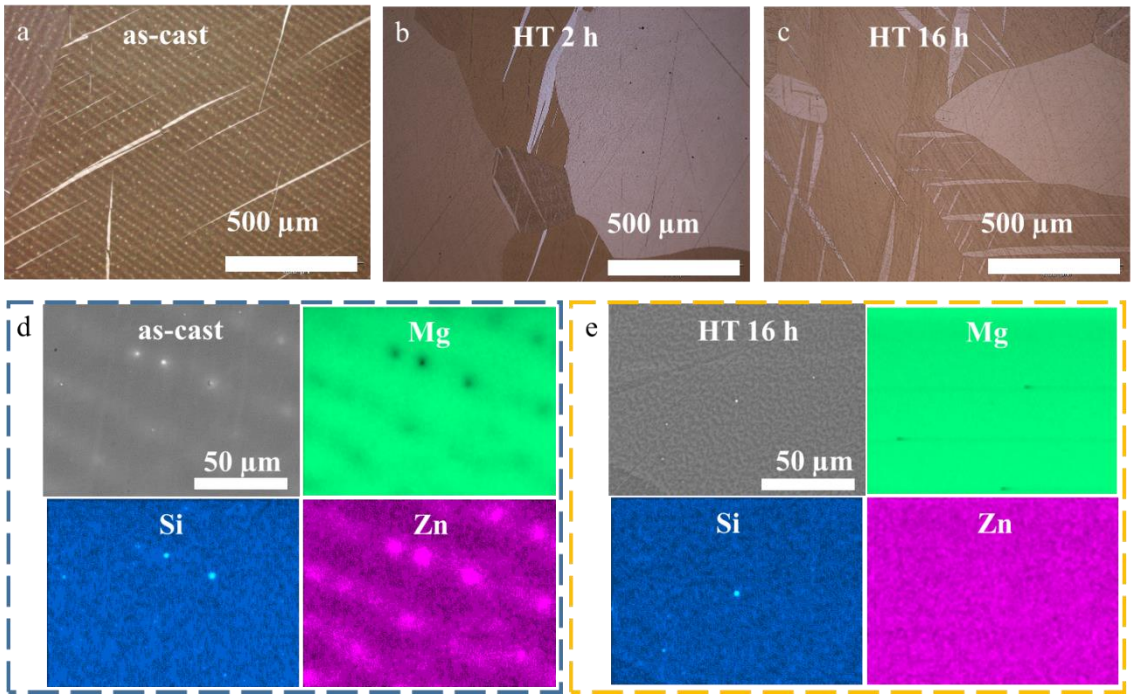

Fig. 5-12. (a-c) OM images of as-cast, HT-2 h and HT-16 h Mg-0.5Zn; BSE SEM images and EDS element mappings of (d) as-cast and (e) HT-16 h samples

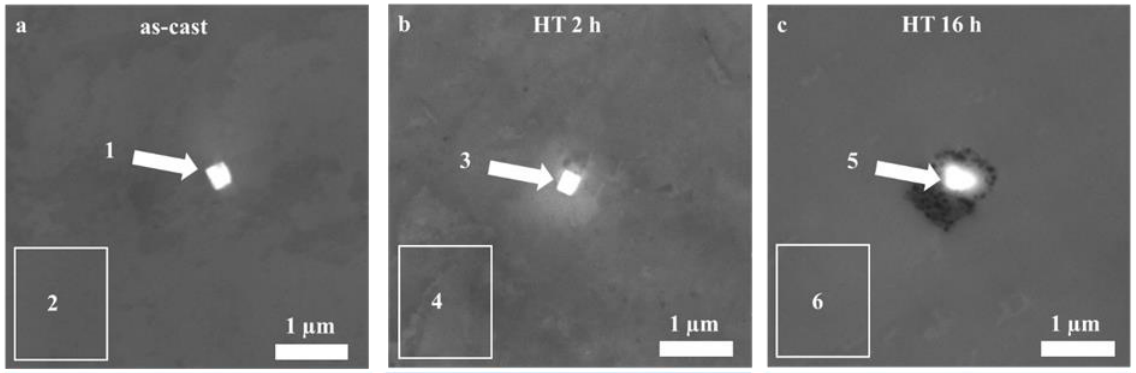

a1	Composition (at. %)				
	O	Mg	Si	Fe	Zn
1	1.65	90.92	3.64	3.79	
2	0.48	99.28			0.24

b1	Composition (at. %)				
	O	Mg	Si	Fe	Zn
3	1.69	87.85	3.38	7.08	
4	0.53	99.27			0.20

c1	Composition (at. %)				
	O	Mg	Si	Fe	Zn
5	2.18	87.01	4.06	6.75	
6	0.53	99.29			0.18

a2	Composition (wt. %)				
	O	Mg	Si	Fe	Zn
1	1.04	86.66	4.01	8.30	
2	0.32	99.04			0.64

b2	Composition (wt. %)				
	O	Mg	Si	Fe	Zn
3	1.02	80.50	3.58	14.91	
4	0.35	99.11			0.54

c2	Composition (wt. %)				
	O	Mg	Si	Fe	Zn
5	1.32	80.09	4.32	14.28	
6	0.35	99.17			0.48

Fig. 5-13. BSE SEM images of the precipitates in (a) as-cast, (b) HT-2 h and (c) HT-16 h Mg-0.5Zn samples; (a1-c1) (a2-c2) corresponding compositions of the precipitates and the matrices indicated by EDS

To understand the changes of Fe-Si particles during heat treatment, EDS point analyses are carried out on about 50 randomly selected particles in each Mg-0.5Zn sample (**Fig. 5-14**). The majority of the Fe-Si particles in the as-cast state contain less than 0.5 at.% Fe as indicated in

the bottom-left of **Fig. 5-14a**. However, after solution treatment for 2 h, the fractions of Fe-Si particles with Fe in the range of 0.5-2 at.% increase significantly (**Fig. 5-14b**). With a prolongation of the solution treatment to 16 h, the number of particles with Fe higher than 2 at.% is further promoted (**Fig. 5-14c**). Although it is difficult to statistically calculate the overall number of Fe-Si particles in each sample, the amount of Fe-Si particles containing higher concentration of Fe is seemingly increasing with the heat treatment duration. It is important to mention here that the changes of Fe concentrations during annealing rather than the exact Fe contents in the Fe-Si precipitates are the focus of this section. The EDS measurements of Fe concentrations depend vastly on the microscopy, image magnification, etc. All the data points in **Fig. 5-14** are measured at identical conditions (same microscopy, same 5000× magnification), so that these results can be statistically compared.

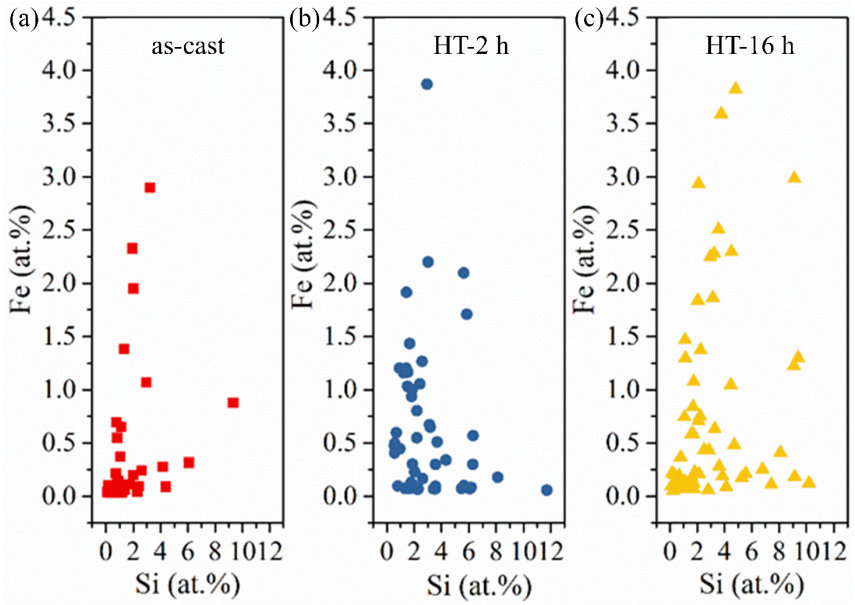

Fig. 5-14. Fe and Si concentrations in Fe-Si particles in the (a) as-cast, (b) HT-2 h and (c) HT-16 h Mg-0.5Zn samples

Corrosion performance

After immersion in 0.9% NaCl solution for 5 min, uniform corrosion is initiated in the as-cast sample with some black spots on the surface (**Fig. 5-15a**). As the immersion prolongs, more black spots occur in a uniform manner (**Fig. 5-15b-d**). Similar to the as-cast sample, corrosion is not obvious in the first 30 min for the HT-2 h sample (**Fig. 5-15e-f**). Whereas more corrosion spots appear after 2 h and the filiform corrosion filaments develop almost all over the surface after 6 h (**Fig. 5-15g-h**). Distinctively, localised corrosion can already be recognised on the HT-16 h sample after 5 min exposure (**Fig. 5-15i**). Corrosion develops as the filament propagates. Corrosion (the black areas) almost covers the whole specimen surface after 2 h and

a big pit with a diameter of almost 1 mm can be identified after 6 h (**Fig. 5-15j-l**). Generally, localised corrosion seems to develop at earlier exposure times and become more significant after heat treatment.

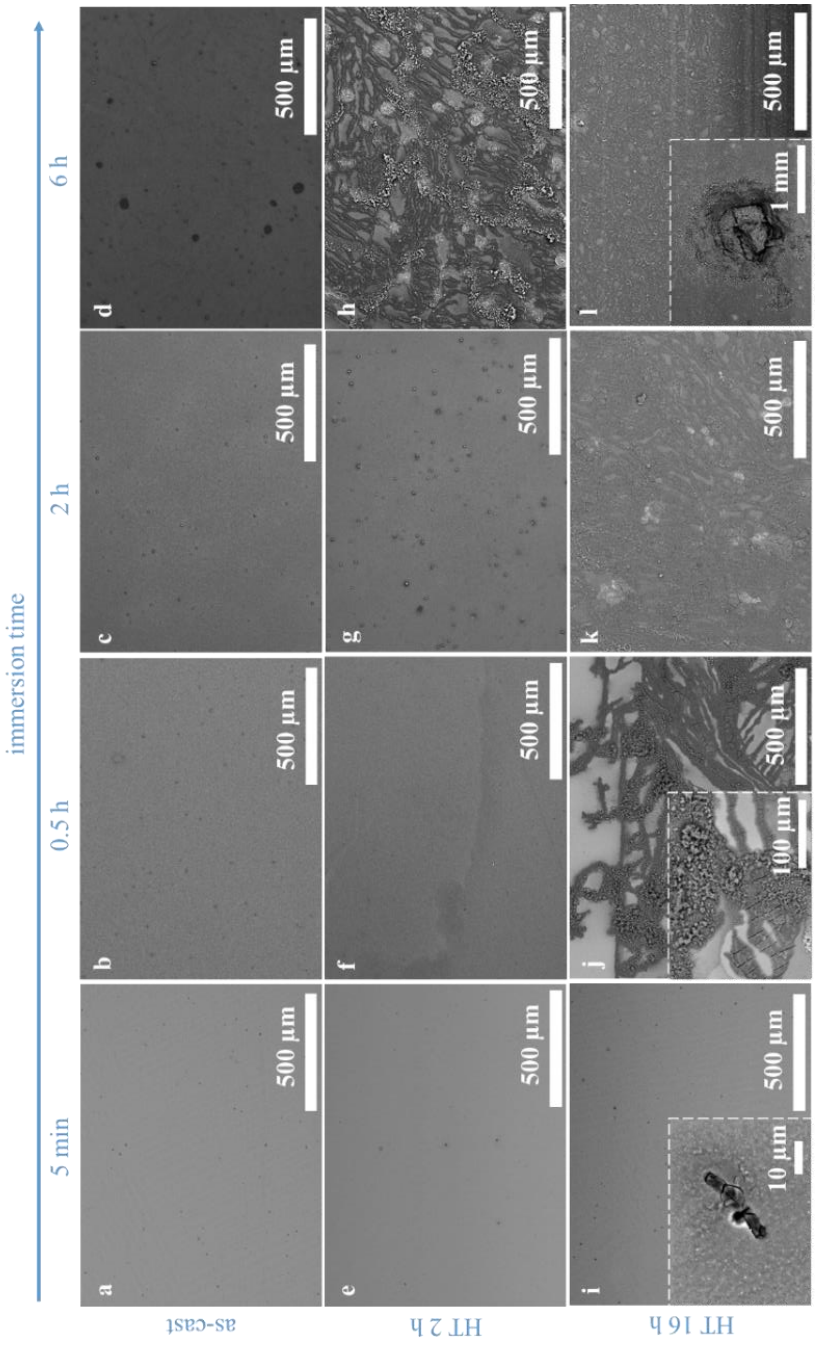

Fig. 5-15. Corrosion morphologies of (a-f) as-cast, (e-h) HT-2 h and (i-l) HT-16 h Mg-0.5Zn samples after immersion for 5 min, 0.5 h, 2 h and 6 h, respectively

The deteriorated corrosion performance after solution treatment is contradictory to most of the studies in literature claiming solution treatments enhance the corrosion resistances of binary Mg-Zn systems (**Table 2-1**). To understand the mechanism, corrosion initiations of the samples are studied. Slight corrosion initiates around the Fe-Si particles in the as-cast sample (**Fig. 5-16a**) after 2 min immersion. Additionally, the corrosion products near Fe-Si particles (spot

2, 3) are thicker (O at. % is higher) than those near Mg_2Si particle (spot 1). As the Fe-Si particles may alter during the heat treatment (**Fig. 5-14**), 2 min short immersion is also conducted on the HT-16 h sample as an example (**Fig. 5-16b**). Thicker corrosion products are detected near the particles with higher Fe concentrations (spot 1, 2) than those around the particles with higher Si and lower Fe contents (spot 3). Moreover, severe localised corrosion is also found in the same HT-16 h sample (**Fig. 5-16c**). It is worth noting that the Fe concentration is as high as 32 at. % in spot 1 while Si is almost negligible. Furthermore, the sizes of the Fe particles in these areas seem to be larger than those near the slightly-corroded areas.

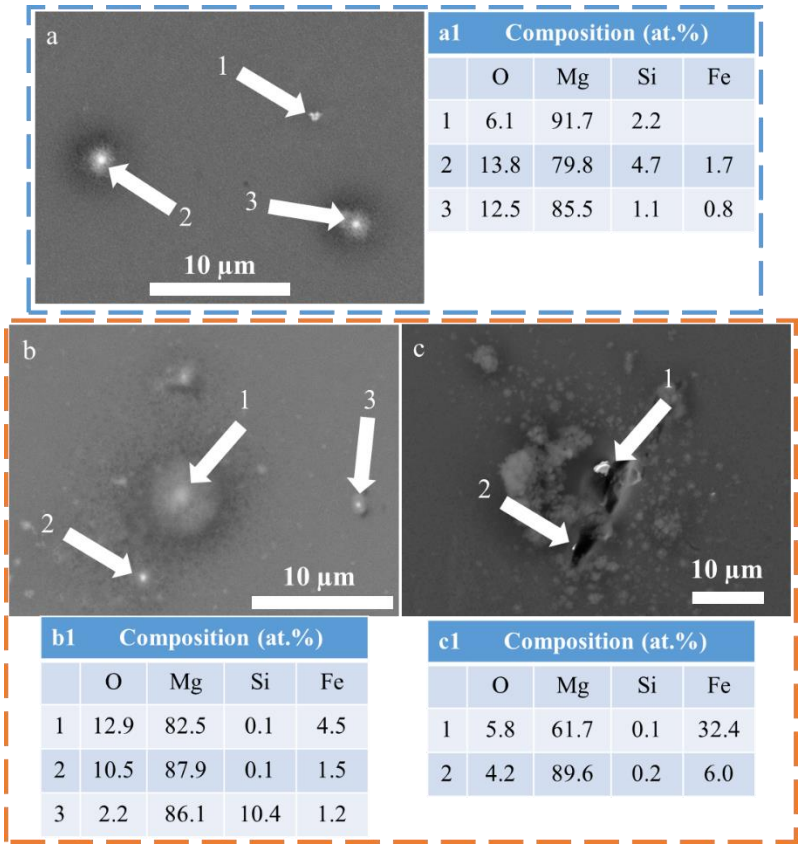

a1	Composition (at.%)			
	O	Mg	Si	Fe
1	6.1	91.7	2.2	
2	13.8	79.8	4.7	1.7
3	12.5	85.5	1.1	0.8

b1	Composition (at.%)			
	O	Mg	Si	Fe
1	12.9	82.5	0.1	4.5
2	10.5	87.9	0.1	1.5
3	2.2	86.1	10.4	1.2

c1	Composition (at.%)			
	O	Mg	Si	Fe
1	5.8	61.7	0.1	32.4
2	4.2	89.6	0.2	6.0

Fig. 5-16. Corrosion morphologies of the (a) as-cast and (b-c) HT-16 h Mg-0.5Zn samples after immersion for 2 min; (a1-c1) the corresponding particle compositions indicated by EDS

After 5 min immersion, corrosion develops slowly in the as-cast sample (**Fig. 5-17a**). The area around the Fe-Si particle (spot 1) corrodes faster than that near the CE-IMP containing Mg_2Si and MgZn (spot 2). However, pitting corrosion (**Fig. 5-16c**) in HT-16 h sample develops into filiform corrosion after 5 min (**Fig. 5-17b**). It appears that corrosion tends to initiate around the Fe rich particles rather than the Fe-Si particles. For some reasons, the HT-16 h sample has more Fe rich particles than the as-cast counterpart. An example of the corroded sample surface without corrosion products is shown in **Fig. 5-18**. The corroded area has vertically aligned

parallel thin layers and the material between the adjacent layers are corroded away. As indicated by the arrows, the directions of the uncorroded thin layers are dependent on the grains. The Fe-Si and Fe particles play a decisive role in the initiation and development of localised corrosion in Mg-0.5Zn alloy.

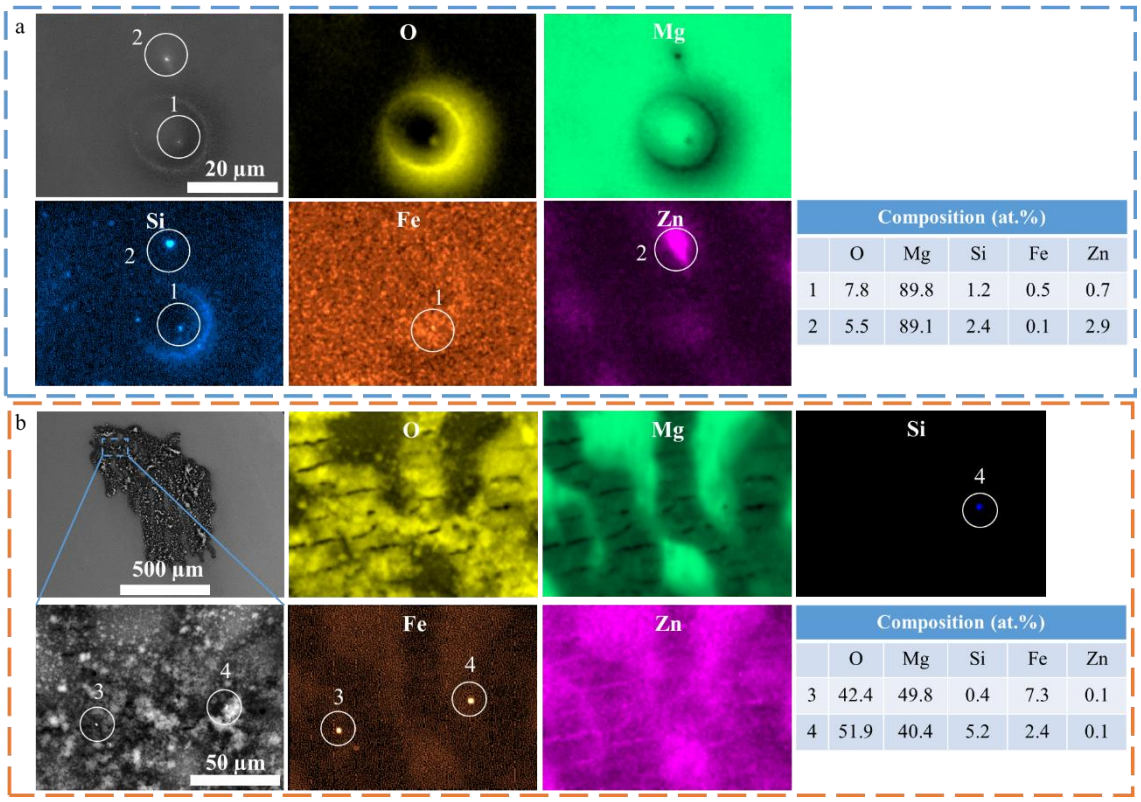

Composition (at.%)

	O	Mg	Si	Fe	Zn
1	7.8	89.8	1.2	0.5	0.7
2	5.5	89.1	2.4	0.1	2.9

Composition (at.%)

	O	Mg	Si	Fe	Zn
3	42.4	49.8	0.4	7.3	0.1
4	51.9	40.4	5.2	2.4	0.1

Fig. 5-17. Corrosion morphologies and EDS element mapping of (a) as-cast and (b) HT-16 h Mg-0.5Zn samples after immersion for 5 min

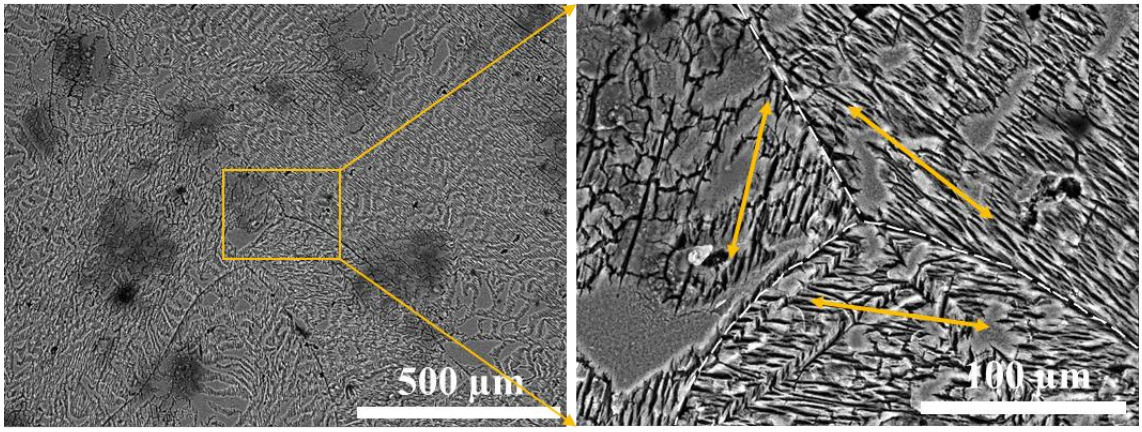

Fig. 5-18. Example of the corroded HT-16 h sample surface after the removal of corrosion products with chromic acid

PDP curves of the as-cast and solution-treated samples are collectively shown in **Fig. 5-19a**. The corrosion potential of Mg-0.5Zn shifts continuously towards the positive direction with

increasing the solution treatment time. A 170 mV potential difference is seen after 16 h heat treatment. The positively shifted OCP is most possibly due to the increased impurity-rich particles with high Fe content, which results in accelerated kinetics of cathodic reaction. The i_{corr} of the as-cast sample increases from 12 μA/cm^2 to 70 μA/cm^2 after heat treated for 16 h (**Fig. 5-19b**).

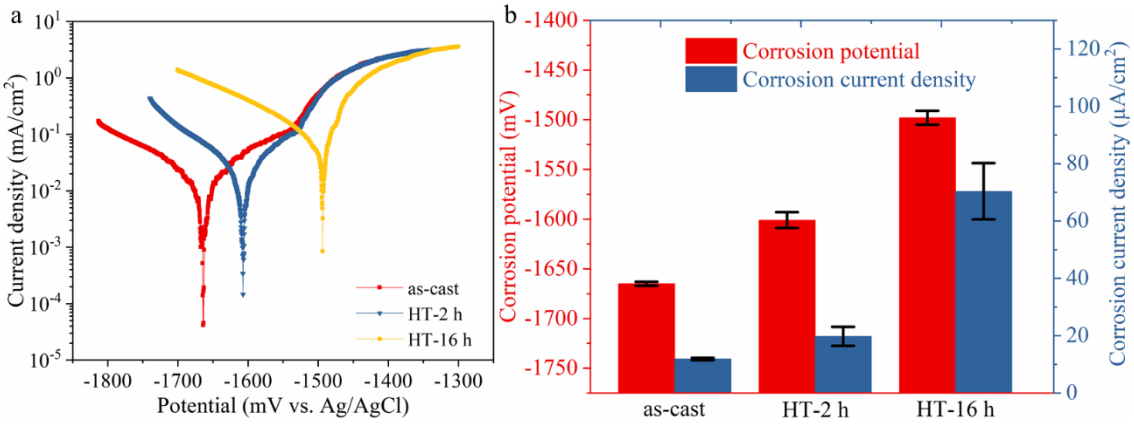

Fig. 5-19. (a) PDP curves of as-cast, HT-2 h and HT-16 h Mg-0.5Zn samples; (b) the corresponding corrosion potential and corrosion current density

The EIS Nyquist plots of the Mg-0.5Zn samples are displayed in **Fig. 5-20a-c**. Due to the strong overlapping of the spectra, the results measured after 2, 3 and 48 h immersion are not shown here. The EIS data is fitted with the equivalent circuit models in **Fig. 5-7** and the corresponding R_{sum} values are shown in **Fig. 5-20d**.

Two time constants can be observed in the Nyquist plots of as-cast sample during the entire immersion period. Though R_{sum} values slightly fluctuate, the increasing and then stable trend indicates that corrosion is developed uniformly and the corrosion products are formed steadily. Similar increasing tendency of R_{sum} is seen in the first 3 h immersion of HT-2 h sample, followed by a distinct decrease at 6 h, which is consistent with the corrosion morphologies in **Fig. 5-15h**. In contrast, only one capacitive loop is recognised for the HT-16 h sample. It undergoes severe localised corrosion after being held at OCP for 5 min as indicated by the low R_{sum} value, which is stable in the initial 6 h and then increases gradually with longer immersion. Although R_{sum} values of the samples vary during immersion due to the dynamic process of alloy dissolution and corrosion products formation, it is evident that R_{sum} of Mg-0.5Zn becomes much lower after 16 h solution treatment. In addition, it seems that the occurrence of localised corrosion shifts to an earlier time spot with the prolongation of the solution treatment duration (e.g. 6 h for HT-2 h, 5 min for HT-16 h).

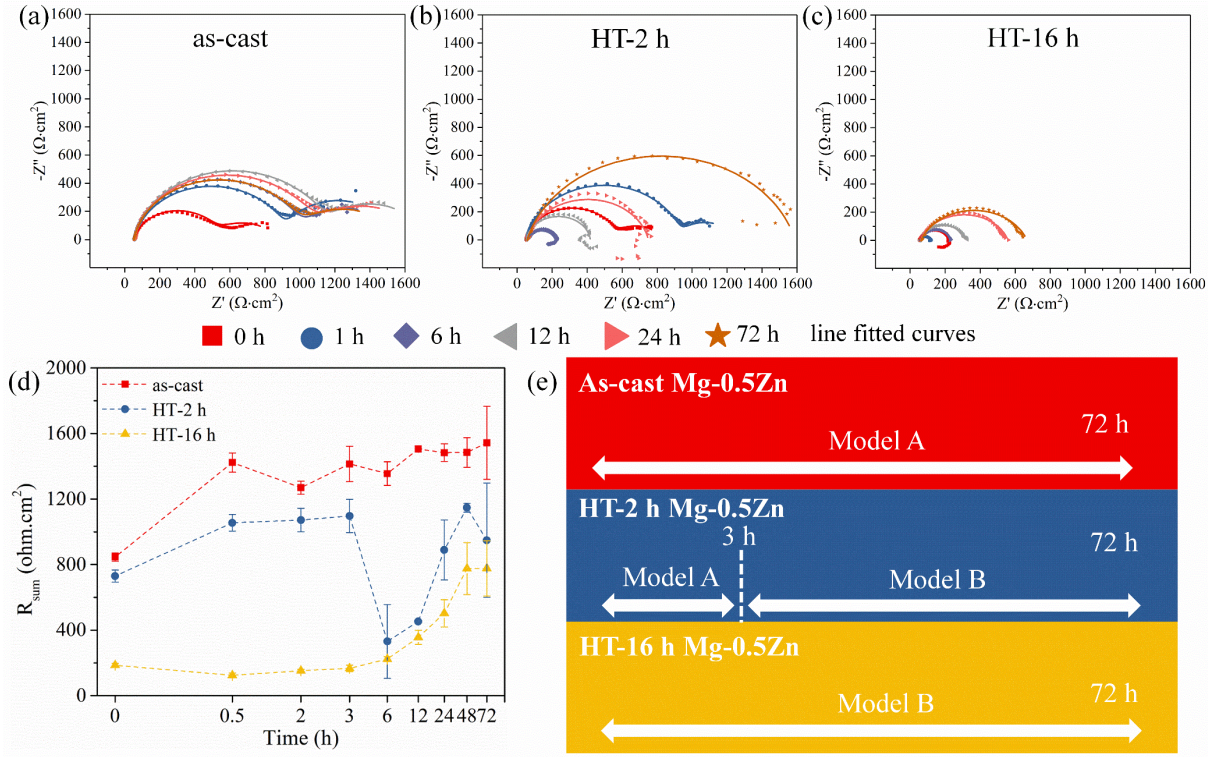

Fig. 5-20. EIS Nyquist plots of the (a) as-cast, (b) HT-2 h and (c) HT-16 h Mg-0.5Zn samples during 3 days measurement; (d) the fitted corresponding sum of resistances R_{sum} (the X axis is in log10 scale for better perception); (e) selection of the models for EIS spectra at different immersion periods

After 3 days EIS measurement, the corrosion products of the samples are characterised by SEM. The oxide film on the as-cast sample is compact especially in area A, indicating its higher corrosion resistance (**Fig. 5-21a**). However, as the solution treatment progresses, the oxide layers become looser with the presence of some pits in area A (**Fig. 5-21b-c**). The existence of Fe-Si particles with higher Fe concentrations after heat treatment lead to the corrosion initiation in **Fig. 5-16c** and **Fig. 5-17b** and might ultimately lead to the reduced protectiveness of the film.

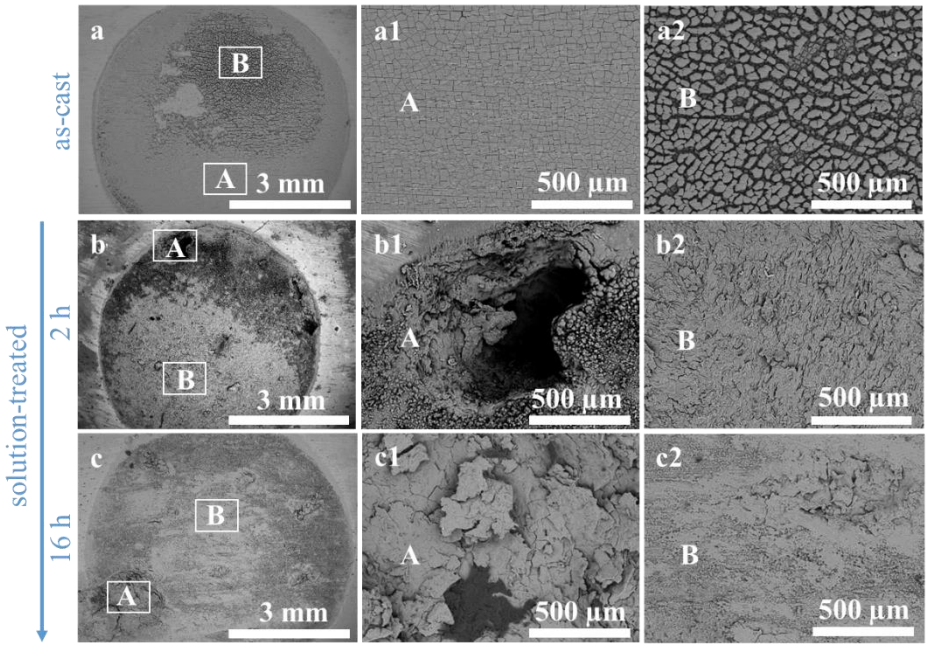

Fig. 5-21. BSE-SEM images of the characteristic corrosion morphologies of (a) as-cast, (b) HT-2 h and (c) HT-16 h samples after 3 days immersion. Images a1 and a2 are the selected areas of image a at higher magnifications.

5.2.2. Mg-0.5Zn-0.2Ca alloy

Microstructure

The as-cast Mg-0.5Zn-0.2Ca alloy reveals a dendritic microstructure with intermetallics present along the grain boundary and within the grains (**Fig. 5-2b**). Zn is enriched in the interdendritic arms and grain boundaries (**Fig. 5-22**). The average grain size is 147 ± 8 µm. By analysing the morphologies and compositions of numerous precipitates via SEM and EDS, three types of secondary phases are identified in the alloys (**Fig. 5-23a, b**). The Mg/Ca/Si-containing phases have either spherical or elongated shape, which are distributed within grains and along grain boundaries. CE-IMPs are composed of Mg/Ca with high Zn (brighter part) and Mg/Ca with low Zn (darker part), which are located within grains. In addition, a limited amount of isolated Mg/Zn/Ca-containing particles can also be observed. Although the shape and brightness of the isolated Mg/Zn/Ca- and Mg/Ca/Si-containing particles are similar in BSE image, clear discrepancy can be seen in SE image.

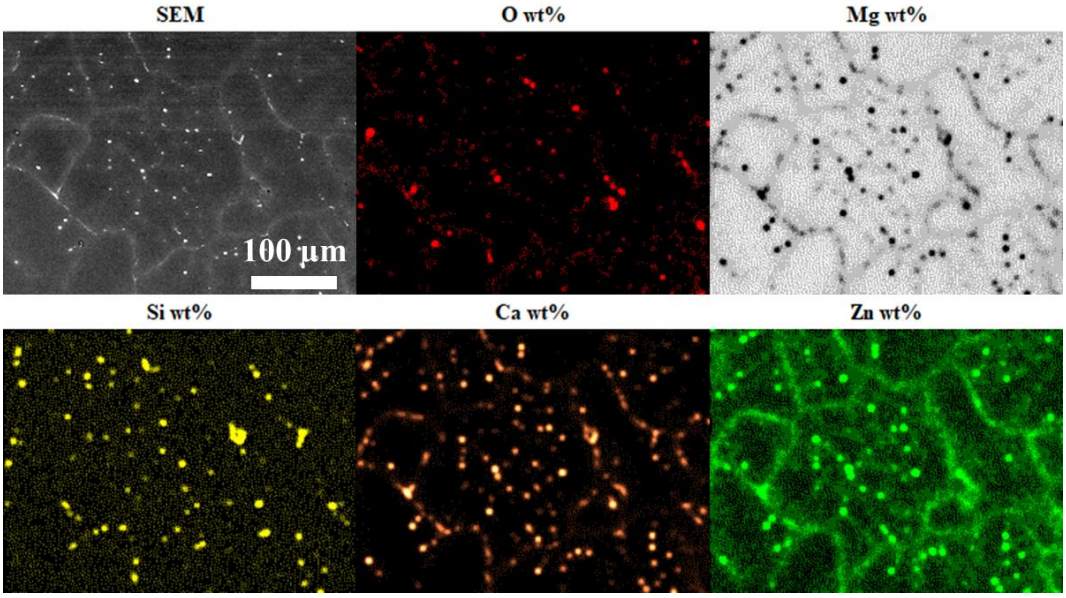

Fig. 5-22. EDS element mapping of the as-cast Mg-0.5Zn-0.2Ca alloy (published in Corrosion Science [181])

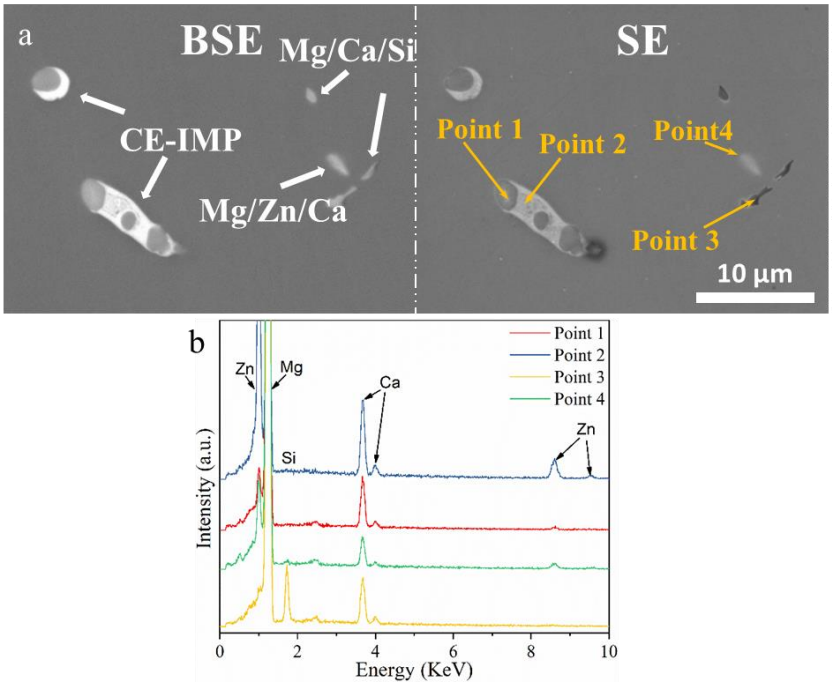

Fig. 5-23. (a) Intermetallic phases in as-cast Mg-0.5Zn-0.2Ca alloy indicated by SEM images in BSE and SE mode; (b) corresponding EDS spectra conducted on point 1-4 (published in Corrosion Science [181])

The average compositions of the intermetallics in the as-cast sample are listed in **Table 5-2**. The values are based on multiple measurements from 10-20 particles of the same phase via EDS measurements. The relative atomic ratio of Ca/Si in the Mg/Ca/Si-containing phase is 0.8 ± 0.1 indicating it is potentially a MgCaSi phase [210]. The Zn/Ca (atomic ratio) in the brighter

part of CE-IMP is 1.6 ± 0.4, revealing it is possibly a $Ca_2Mg_6Zn_3$ phase [130]. Compared to the brighter part, higher Ca contents and lower Zn contents are seen in the darker part of CE-IMP, meaning it is perhaps a Mg_2Ca phase. The average Zn concentration in Mg_2Ca is approximately 3 at.%, which is probably detected from the neighboured $Ca_2Mg_6Zn_3$. The overall area fraction of the intermetallics in the as-cast state is calculated to be 0.29 ± 0.05% by ImageJ. However, it is difficult to measure the fraction of every single phase since the sizes of the intermetallics are just several microns. For the main precipitates in the system, the quantity fraction of CE-IMP and MgCaSi phases is 45.6 ± 4.8% and 54.5 ± 4.8%, respectively.

Table 5-2 Average compositions of the intermetallics in as-cast Mg-0.5Zn-0.2Ca alloy via EDS measurements (published in Corrosion Science [181])

	as-cast		
Intermetallic particles	Mg/Ca/Si-containing	brighter part of CE-IMP	darker part of CE-IMP
O at.%	1.9 ± 1.0	1.8 ± 0.5	3.2 ± 4.6
Mg at.%	86.2 ± 6.6	81.2 ± 5.4	82.9 ± 5.4
Si at.%	6.4 ± 3.5	0.2 ± 0.1	0.1 ± 0.1
Ca at.%	5.1 ± 2.6	6.6 ± 2.2	10.9 ± 4.9
Zn at.%	0.4 ± 0.2	10.2 ± 3.4	2.9 ± 1.0
Zn/Ca	-	1.6 ± 0.4	-
Ca/Si	0.8 ± 0.1	-	-

To confirm the crystal structures of the intermetallics, selected area electron diffraction (SAED) analysis of MgCaSi and CE-IMP are also conducted in TEM. Both phases in CE-IMP possess an hcp crystal structure with two distinct lattice spacing. The hcp phase with a larger lattice spacing in reciprocal space (**Fig. 5-24a**) corresponds to Mg_2Ca phase and the hcp phase with a smaller lattice spacing in reciprocal space (**Fig. 5-24b**) corresponds to $Ca_2Mg_6Zn_3$ phase. MgCaSi phase possesses a primitive orthorhombic crystal structure (**Fig. 5-24c**). TEM EDS spot analyses (**Fig. 5-24d**) on Mg_2Ca part (x1) and $Ca_2Mg_6Zn_3$ part (x2) in CE-IMP, and MgCaSi (x3) are consistent with the SEM EDS results **(Fig. 5-23b)**. Cu signal is detected from the TEM sample holder.

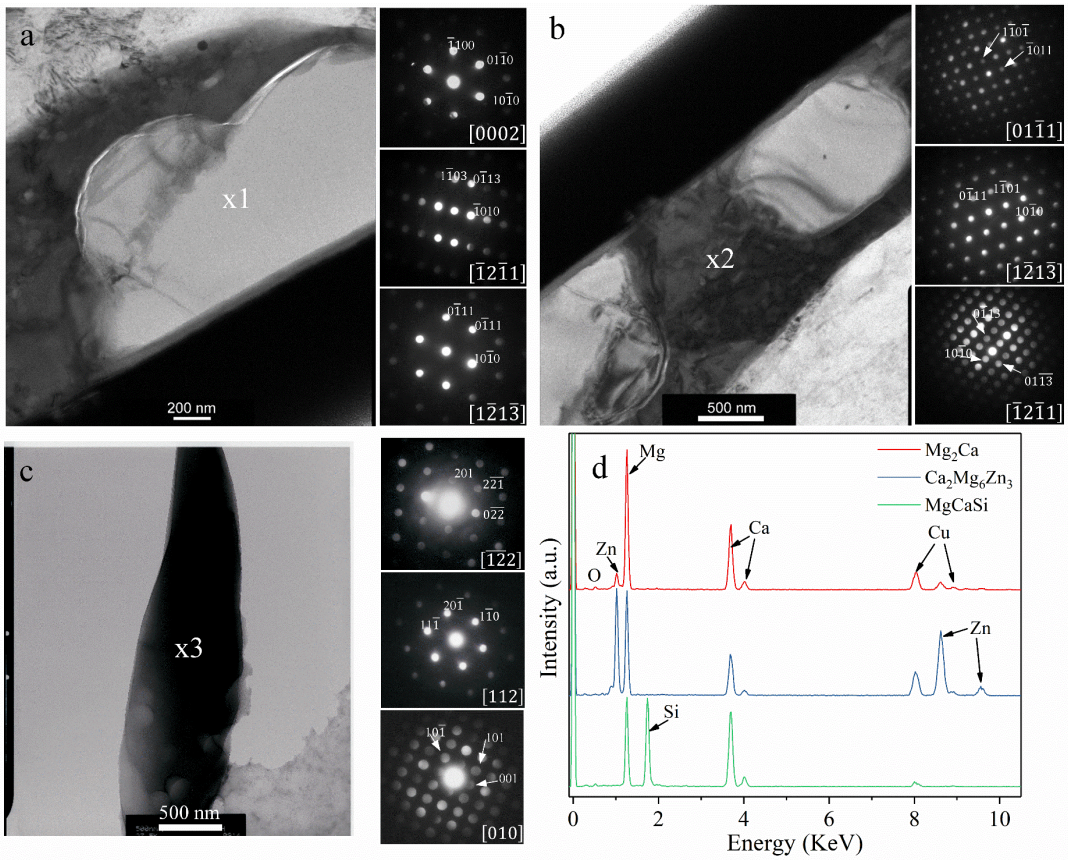

Fig. 5-24. TEM SAED patterns of (a) Mg_2Ca, (b) $Ca_2Mg_6Zn_3$ in CE-IMP and (c) MgCaSi phase in the as-cast Mg-0.5Zn-0.2Ca alloy; (d) TEM EDS spectra of spot x1 (Mg_2Ca), x2 ($Ca_2Mg_6Zn_3$), x3 (MgCaSi) in (a-c) (published in Corrosion Science [181])

After solution annealing at 450 °C for 16 h, the microstructure becomes more homogeneous. The average grain size slightly increases to 164 ± 3 µm and no segregation of Zn can be detected (**Fig. 5-25a, b**). According to the EDS results which are based on multiple measurements (**Table 5-3**), the $Ca_2Mg_6Zn_3$ phase and the Mg_2Ca phase from CE-IMP cannot be recognised and only Mg/Ca/Si-containing particles can be detected after solution annealing (**Fig. 5-25c, d**). The atomic ratio of Ca/Si in these precipitates (0.8 ± 0.1) are identical as that in the as-cast counterpart. Therefore, MgCaSi prevails as the dominant secondary phase in the solution-annealed Mg-0.5Zn-0.2Ca alloy with an area fraction of 0.15 ± 0.02%.

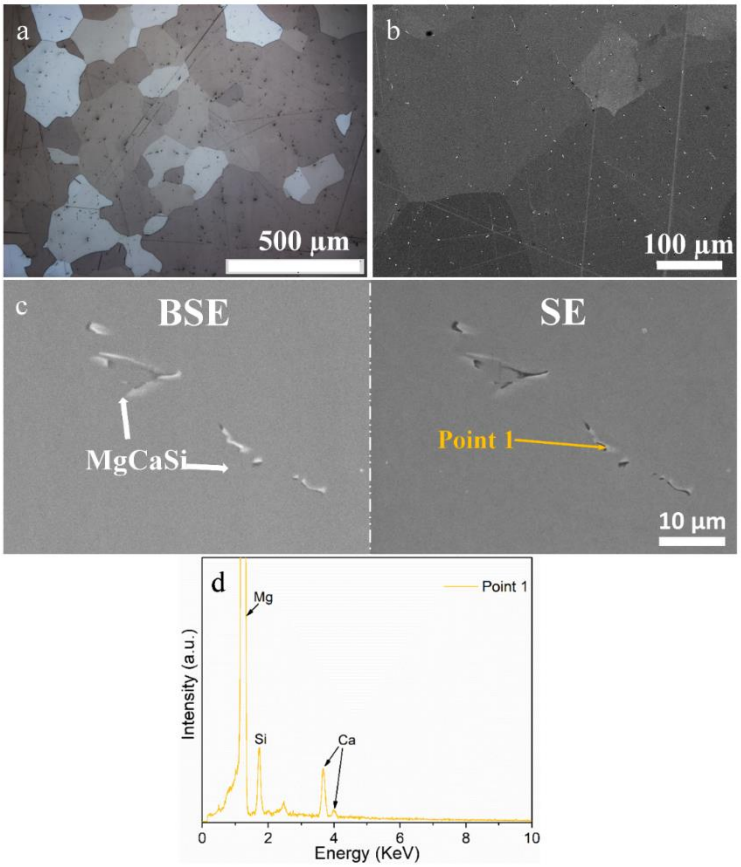

Fig. 5-25. Microstructure of the solution-annealed Mg-0.5Zn-0.2Ca alloy indicated by (a) OM image and (b) BSE SEM image; (c) MgCaSi precipitates indicated by SEM images in BSE and SE mode; (d) corresponding EDS spectrum conducted on point 1 (published in Corrosion Science [181])

Table 5-3 Average compositions of the intermetallics in the solution-annealed Mg-0.5Zn-0.2Ca alloy via EDS measurements (published in Corrosion Science [181])

Particles	O at.%	Mg at.%	Si at.%	Ca at.%	Zn at.%	Ca/Si
MgCaSi	1.3 ± 1.1	87.3 ± 4.7	6.1 ± 2.0	4.8 ± 1.7	0.5 ± 0.2	0.8 ± 0.1

General corrosion performance

PDP and EIS are employed to characterise and compare the general corrosion performances of the as-cast and solution-annealed Mg-Zn-Ca samples.

According to the PDP curves, the corrosion potential moves towards the positive direction after solution annealing (**Fig. 5-26**). The pitting potential shows the likelihood of localised corrosion, and a more positive value implies a less likely localised corrosion [81, 211]. It is visible from the polarisation curves that the pitting potential of the solution annealed sample is more positive than that of the as-cast sample, revealing a more compact or protective layer on the surface after solution annealing.

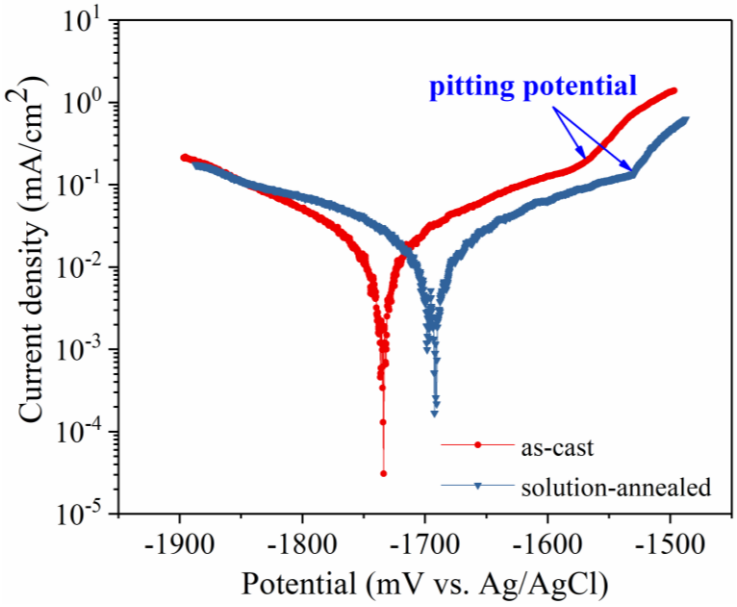

Fig. 5-26. PDP of the as-cast and solution-annealed Mg-0.5Zn-0.2Ca alloy (published in Corrosion Science [181])

In order to see the EIS curves more clearly, only the results after 0, 1, 6, 12, 24 and 72 h immersion are presented here. For as-cast Mg-0.5Zn-0.2Ca alloy, two time constants are observed during the first 6 h immersion, as indicated by the Nyquist plot (**Fig. 5-27a**). After 12 h and 24 h, only one capacitive loop is observed with some scattered points in the low frequency range, indicating active mass transport that happens on the sample surface. With further immersion, two time constants can be seen again. In contrast, two time constants are present during the entire immersion period for the solution annealed state (**Fig. 5-27b**). R_{sum} is the sum of hydroxide layer resistance R_f and charge transfer resistance R_{ct} (**Fig. 5-27c**). For as-cast Mg-0.5Zn-0.2Ca, the R_{sum} value increases steadily from 670 Ωcm^2 to 1320 Ωcm^2 upon immersion until 6 h, demonstrating the densification and thickening of the semi-protective corrosion product layer. After that, R_{sum} drops sharply at 12 h implying the alloy suffers from localised corrosion attack. With prolonged exposure until 72 h, an increase in R_{sum} can be observed again, which is possibly due to the precipitation of corrosion products dominates over the dissolution of the alloy. During this comparatively longer time interval (1 measurement per day), the samples are covered with thicker and more protective corrosion product layers. For solution-annealed sample, R_{sum} increases steadily until 12-24 h and suffers a little loss afterwards. The distinct loss of R_{sum} value in the as-cast sample is not observed in the solution annealed counterpart. Although there is a slight decline after 24 h possibly due to localised corrosion or dissolution of the hydroxide film, the respective time of occurrence is also delayed. By

comparing the R_{sum} values of the two states, the solution-annealed sample exhibits a better corrosion resistance during the entire immersion process.

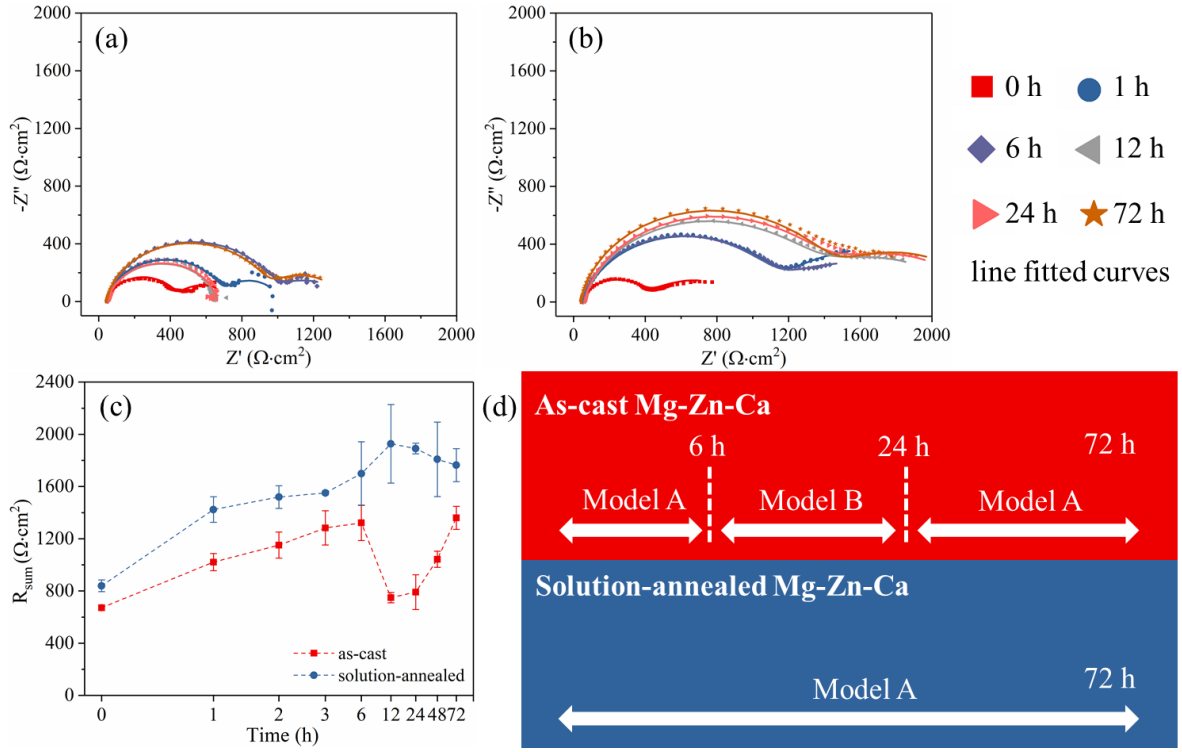

Fig. 5-27. Nyquist plots of the (a) as-cast and (b) solution annealed Mg-0.5Zn-0.2Ca alloy; (c) corresponding fitted sum of resistance $R_{sum} = R_f + R_{ct}$ with the X axis in log10 scale for better perception; (d) selection of the models for EIS spectra at different immersion periods (adapted from Corrosion Science [181])

After removing the corrosion layers, the corrosion morphologies of the two samples after 24 h immersion are compared. It seems that corrosion near the grain boundary in the as-cast sample (**Fig. 5-28a**) is more pronounced than that in the solution-annealed sample (**Fig. 5-28b**). Due to the segregation of Zn, the Volta potential at the grain boundary area is more positive than that of the inner grain area, thus causing galvanic corrosion at the grain boundary interface. In contrast, Zn is uniformly distributed in the solution-annealed sample and corrosion develops homogeneously.

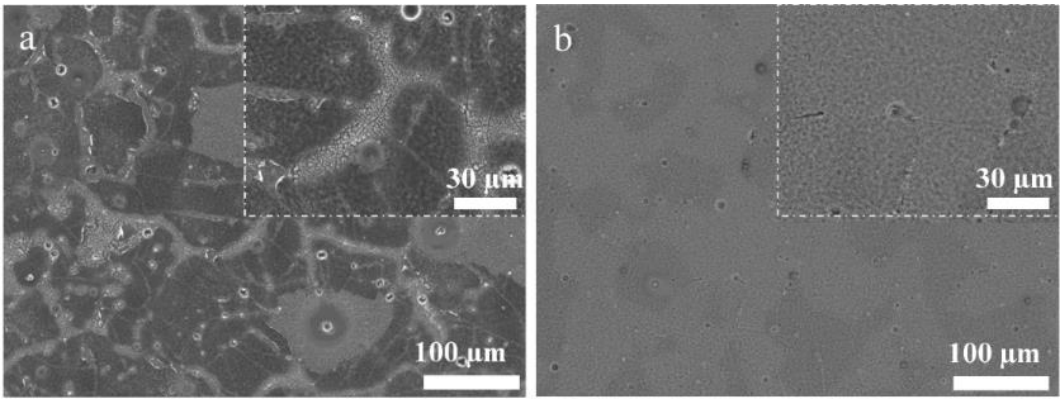

Fig. 5-28. SEM images in BSE mode of (a) as-cast and (b) solution-annealed Mg-0.5Zn-0.2Ca alloy after immersion for 24 h (adapted from Corrosion Science [181])

Quasi-in situ corrosion observation

The quasi-in situ corrosion observation (described in section 4.3.3) is a useful method to investigate the initiation of corrosion on a microscopic scale [176, 212]. To explain the general corrosion performance described above and to elucidate the corrosion mechanism of Mg-0.5Zn-0.2Ca alloy, this approach is adopted.

After only 30 s exposure to 0.9% NaCl solution, there are already discernible thin corrosion products forming on both the matrix and the IMPs (**Fig. 5-29a, d, g**). With prolonged exposure for 10 min and 30 min, the corrosion products become thicker but the inherent contrast in CE-IMP can still be observed (**Fig. 5-29b, e, h**), which demonstrates that the intermetallics are at least not fully corroded. CE-IMPs are entirely covered with the corrosion products that blur the phase contrast subsequent to 1 h immersion (**Fig. 5-29c, f**). After being peeled off by scotch tape, it is discovered that the greyish part which used to be the Mg_2Ca phase is no longer present, whereas the brighter part which used to be $Ca_2Mg_6Zn_3$ phase still remains (**Fig. 5-29i**). According to the EDS point analysis (**Fig. 5-29j**), trace amount of Ca can be detected in Point 1, which hints that the Mg_2Ca phase is dissolved. The slight Zn and Ca signals are possibly from the $Ca_2Mg_6Zn_3$ in the vicinity or from the Mg_2Ca phase residuals underneath. In contrast, evident Zn and Ca signals are captured in Point 2. This result can be a direct evidence that corrosion is inclined to take place initially in the CE-IMP area, and out of which, the Mg_2Ca phase is preferentially dissolved within 1 h immersion leaving $Ca_2Mg_6Zn_3$ phase uncorroded.

As revealed in **Fig. 5-29i**, the corrosion products cannot be thoroughly removed by the tape-peeling process. More complete removal of the corrosion layer is needed to understand the corrosion mechanism of Mg-Zn-Ca. Although Mg_2Ca can be corroded by diluted chromic acid (**Fig. S2c-d**), Mg_2Ca precipitates are already fully dissolved after 1 h immersion. Considering

the facts that $Ca_2Mg_6Zn_3$ and MgCaSi phases are not affected by diluted chromic acid cleaning, the corrosion products are removed with diluted chromic acid after immersion longer than 1 h. According to **Fig. 5-30**, similar corrosion morphologies are observed after the removal of corrosion layers by diluted chromic acid cleaning and tape-peeling.

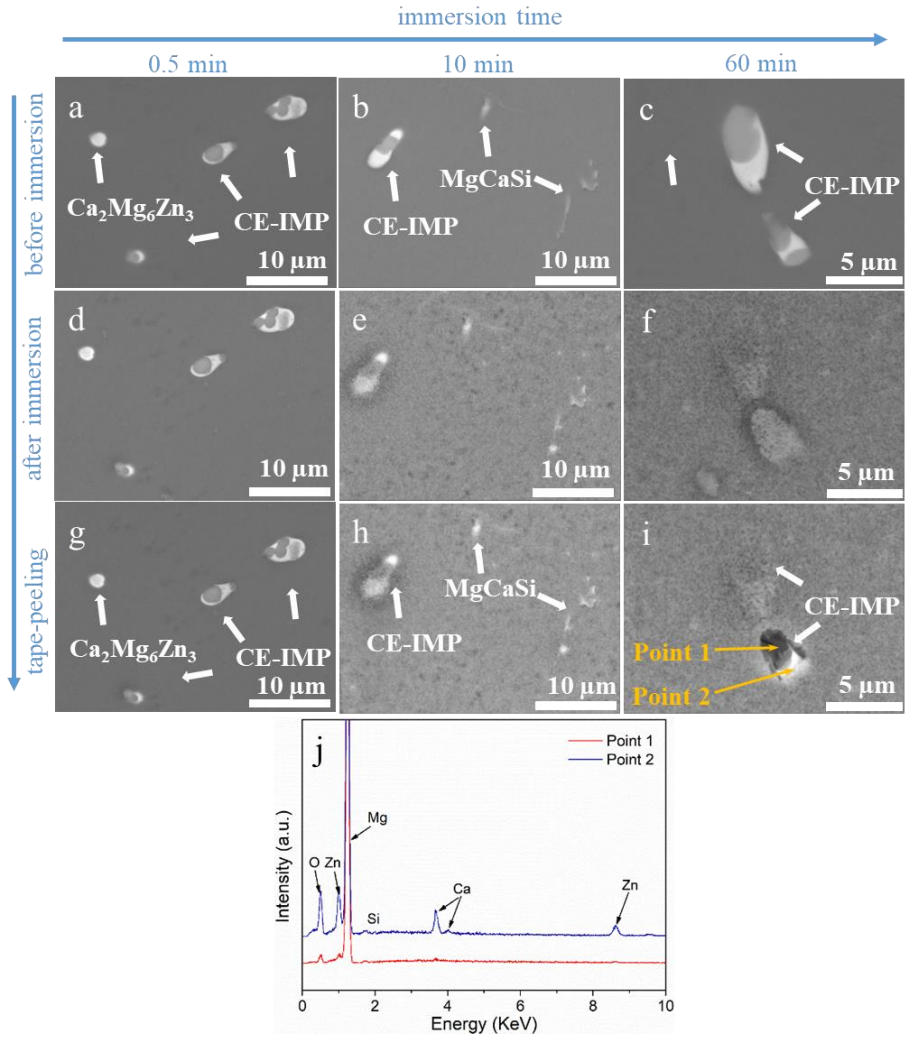

Fig. 5-29. SEM images in BSE mode of the as-cast Mg-0.5Zn-0.2Ca alloy (a-c) before immersion, (d-f) after immersion for 0.5 min, 10 min and 60 min, respectively; (g-i) after tape-peeling process to remove the corrosion products; (j) corresponding EDS spectra of point 1 and 2 (published in Corrosion Science [181])

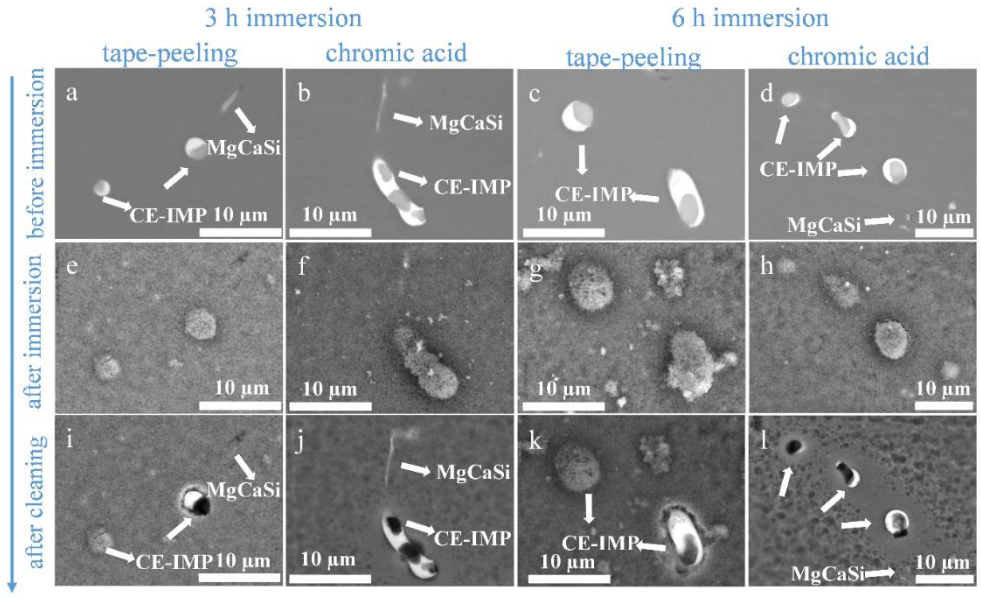

Fig. 5-30. SEM images in BSE mode of the as-cast Mg-0.5Zn-0.2Ca alloy (a)(b)(c)(d) before immersion; after immersion for (e)(f) 3 h and (g)(h) 6 h, respectively; after (i)(k) tape-peeling process and (j)(l) diluted chromic acid to remove the corrosion products (published in Corrosion Science [181])

CE-IMPs are completely covered and MgCaSi are partially covered with the corrosion products subject to 1 h immersion (**Fig. 5-31f**), implying that the corrosion kinetics of Mg/CE-IMP galvanic coupling is faster than that of Mg/MgCaSi. After cleaning, the corrosion products and Mg_2Ca phase are removed whereas $Ca_2Mg_6Zn_3$ and MgCaSi phases remain (**Fig. 5-31k**). After 3 h, the Mg matrix near the CE-IMP starts to be undermined while the matrix in the vicinity of the isolated $Ca_2Mg_6Zn_3$ or MgCaSi shows comparatively less corrosion (**Fig. 5-31g, l**). This correlates with the larger Volta potential difference of $Mg_2Ca/Ca_2Mg_6Zn_3$ and Mg/CE-IMP than those of $Mg/Ca_2Mg_6Zn_3$ and Mg/MgCaSi, which drive more intense oxidation-reduction reactions at the respective interface. The undermined Mg matrix area becomes even larger after 6 h. Galvanic corrosion would terminate only if the $Ca_2Mg_6Zn_3$ phase in position II would be detached (**Fig. 5-31c, h, m**). With 12 h and 24 h exposure, cracks are found in the much thicker corrosion layers due to the dehydrating process. Although the pit size and surface roughness increase, the majority of $Ca_2Mg_6Zn_3$ and MgCaSi phases are still present on the sample surface (**Fig. 5-31n, o**), indicating a continuous galvanic corrosion at the specific interface.

The same procedure is also applied to the solution-annealed sample with only Mg/MgCaSi galvanic couples present in the system. With 1 h exposure, only moderate corrosion attack occurs at the interface (**Fig. 5-32k**) and Mg matrix surrounding MgCaSi phase corrodes slightly. After 3 h, MgCaSi is fully covered with the corrosion products (**Fig. 5-32l**) and some places start to be undermined subject to 6 h immersion (**Fig. 5-32m**). After 12 h and longer immersion

durations, the corrosion products become thicker (**Fig. 5-32i, j**). Cracks are formed along the intermetallics possibly due to the active interaction at the interface. The degradation of matrix becomes more severe with increasing immersion time (**Fig. 5-32n, o**).

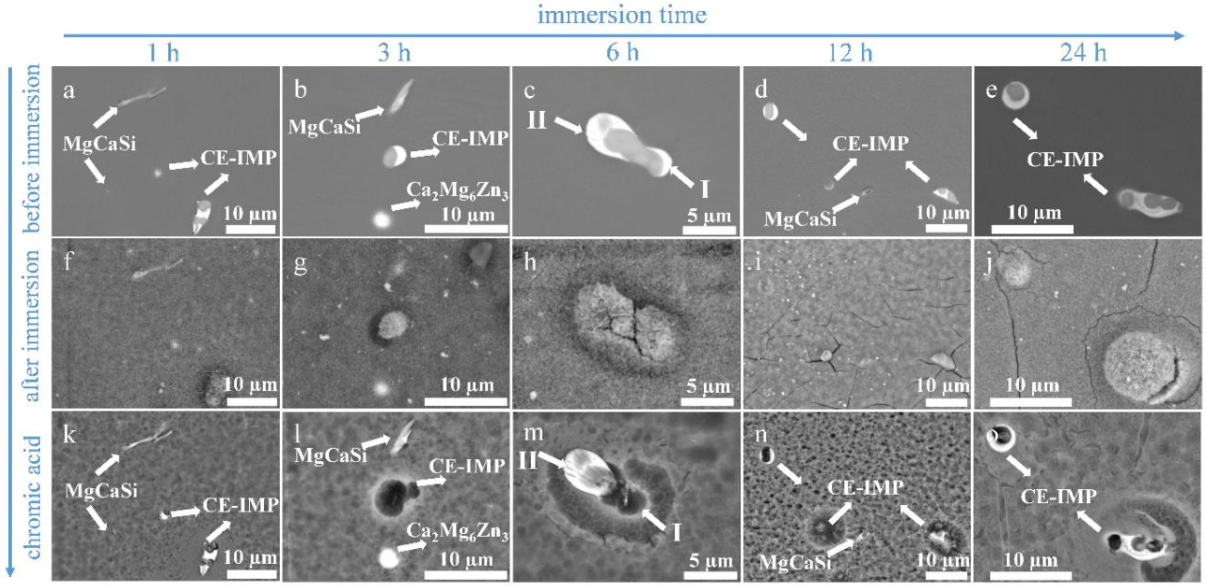

Fig. 5-31. SEM images in BSE mode of as-cast Mg-0.5Zn-0.2Ca alloy (a-e) before immersion; after immersion for (f) 1 h, (g) 3 h, (h) 6 h, (i) 12 h and (j) 24 h, respectively; (k-o) after diluted chromic acid to remove the corrosion products (published in Corrosion Science [181])

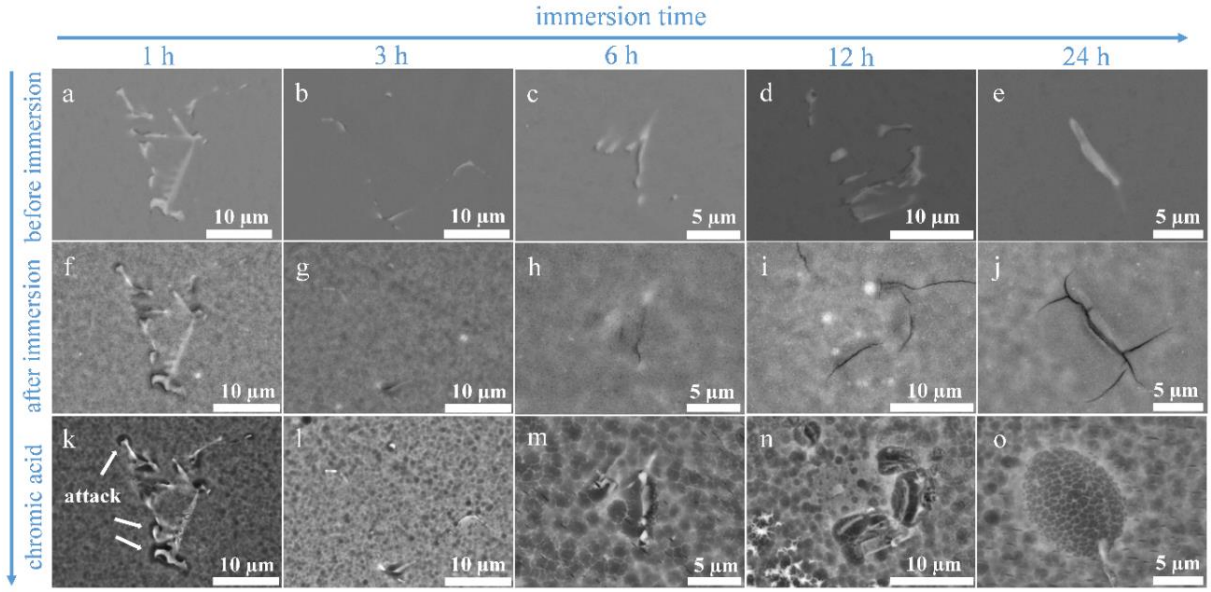

Fig. 5-32. SEM images in BSE mode of solution-annealed Mg-0.5Zn-0.2Ca alloy (a-e) before immersion; after immersion for (f) 1 h, (g) 3 h, (h) 6 h, (i) 12 h and (j) 24 h, respectively; (k-o) after diluted chromic acid to remove the corrosion products (published in Corrosion Science [181])

5.2.3. Summary

(1) In as-cast Mg-Zn-Ca, anodic Mg_2Ca is preferentially corroded within 1 h whereas cathodic $Ca_2Mg_6Zn_3$ and MgCaSi phases remain even after 24 h immersion. In the solution annealed Mg-Zn-Ca sample, MgCaSi is the only remaining precipitate. Higher corrosion resistance is observed in the solution annealed sample.

(2) The Fe concentrations in the Fe-Si particles increase as the heat treatment duration prolongs. Uniform corrosion in as-cast Mg-Zn changes into localised corrosion in the heat treated sample. The corrosion resistance of Mg-Zn is significantly deteriorated after solution annealing.

5.3. As-extruded Mg-0.5Zn(-0.2X) alloys

As seen in section 5.1, the microstructure and corrosion behaviour of as-cast Mg-0.5Zn change with the addition of alloying element X. It would be interesting to study also the effects of extrusion on these alloys. Moreover, the corrosion response to heat treatment differ in different systems (section 5.2). Can the deteriorated corrosion performance of solution annealed Mg-0.5Zn be compensated by extrusion?

5.3.1. Composition and microstructure

The alloying element and impurity concentrations of the as-extruded Mg-0.5Zn(-0.2X) alloys measured by ICP-OES are shown in **Table 5-4**, which are similar to those of the as-cast state in **Table 5-1**. Those measured by Spark-OES (**Table S2**) have lower impurity levels compared to those in as-cast state (**Table S1**). This might be due to the experimental setup as the diameter of the holder is similar to that of the extruded bar, making the Spark-OES analysis for the as-extruded alloys less accurate. Nevertheless, the compositions do not change much after heat treatment and extrusion according to the ICP-OES measurement.

The solution-annealed billets are pre-heated and extruded at 350 °C with an extrusion speed of 0.6 mm/s, 2.2 mm/s and 4.4 mm/s, respectively. The microstructures of the as-extruded alloys are shown in **Fig. 5-33**. The grains are mostly equiaxed and recrystallized in all cases with only minor areas of Mg-Zn-Ca/Ag/In extruded at 0.6 mm/s are non-fully recrystallized. The recrystallized grains are generally uniform although some comparatively big grains near the small ones can also be observed. An example of the non-fully recrystallized microstructure in Mg-Zn-Ca is displayed in **Fig. 5-34**. However, the exact area fractions of these elongated grains are difficult to measure quantitatively as their amounts are too low. Although the grain sizes of the as-extruded alloys are generally proportional to the extrusion speeds, the grain sizes do not

change much with the adopted extrusion speeds except for Mg-Zn-Ca (**Table 5-5**). Mg-Zn-Cu extruded at 4.4 mm/s has a slightly coarser grain size than the other alloys. The effect of grain size on the corrosion performance of Mg alloy is still under debate [124, 151, 213]. To exclude the effect of grain size so that the corrosion behaviour of different systems can be compared, the samples with similar grain sizes (around 30 µm, hereafter referred as as-extruded Mg-Zn(-X) alloys) are selected for further study (e.g. Mg-0.5Zn and Mg-0.5Zn-0.2Cu extruded at 2.2 mm/s and Mg-0.5Zn-0.2Ca/Sr/Ag/In extruded at 4.4 mm/s). The influence of the non-fully recrystallized microstructures on the corrosion performance can also be avoided by using the selected fully recrystallized samples mentioned above.

Table 5-4 Main alloying element and impurity concentrations of as-extruded Mg-0.5Zn(-0.2X) alloys determined by ICP-OES

	Mg-0.5Zn	Mg-0.5Zn-0.2Ca	Mg-0.5Zn-0.2Sr	Mg-0.5Zn-0.2Ag	Mg-0.5Zn-0.2In	Mg-0.5Zn-0.2Cu
Zn (wt.%)	0.49 ± 0.02	0.51 ± 0.02	0.48 ± 0.02	0.50 ± 0.02	0.49 ± 0.02	0.47 ± 0.02
X (wt.%)	-	0.18 ± 0.02	0.19 ± 0.02	0.19 ± 0.02	0.19 ± 0.02	0.20 ± 0.01
Mn (ppm)	169 ± 5	200 ± 5	186 ± 5	168 ± 5	171 ± 5	174 ± 5
Si (ppm)	67 ± 4	137 ± 4	154 ± 4	140 ± 4	57 ± 4	59 ± 4
Al (ppm)	32 ± 5	52 ± 5	130 ± 5	146 ± 5	81 ± 5	55 ± 5
Fe (ppm)	13 ± 6	22 ± 6	13 ± 6	13 ± 6	12 ± 6	7 ± 6
Cu (ppm)	< 3	< 3	< 3	< 3	< 3	-
Ni (ppm)	< 3	< 3	< 3	< 3	< 3	< 3
Be (ppm)	< 3	< 3	< 3	< 3	< 3	< 3

As texture always exists in the wrought Mg alloy after plastic deformation and can as well influence the degradation behaviour, textures of the as-extruded Mg-0.5Zn(-0.2X) alloys are measured. According to the inverse pole figures in **Fig. 5-35**, all the as-extruded Mg-0.5Zn(-0.2X) alloys have fibre texture (c-axes of the grains perpendicular to the extrusion direction) with the exception of Mg-Zn-Ca. The texture intensity of Mg-0.5Zn is greatly reduced with the addition of Ca and a “rare earth” component can be observed. The “rare earth” component is commonly found in rare earth or Ca containing Mg alloys [214], typically characterised by intensities with tilt out of the arc between the $\langle 10\bar{1}0 \rangle$ and $\langle 11\bar{2}0 \rangle$ poles toward the $\langle 0001 \rangle$ pole. The addition of Cu seems to increase the texture intensity of Mg-Zn.

Table 5-5 Influence of extrusion speeds on the grain sizes of as-extruded Mg-0.5Zn(-0.2X) alloys

Speed / Alloy	0.6 mm/s	2.2 mm/s	4.4 mm/s
Mg-0.5Zn	26 ± 1 μm	30 ± 1 μm	31 ± 1 μm
Mg-0.5Zn-0.2Ca	7 ± 1 μm	20 ± 1 μm	30 ± 2 μm
Mg-0.5Zn-0.2Sr	23 ± 2 μm	26 ± 0 μm	31 ± 1 μm
Mg-0.5Zn-0.2Ag	24 ± 0 μm	26 ± 0 μm	29 ± 1 μm
Mg-0.5Zn-0.2In	24 ± 0 μm	27 ± 2 μm	30 ± 2 μm
Mg-0.5Zn-0.2Cu	22 ± 1 μm	32 ± 1 μm	37 ± 1 μm

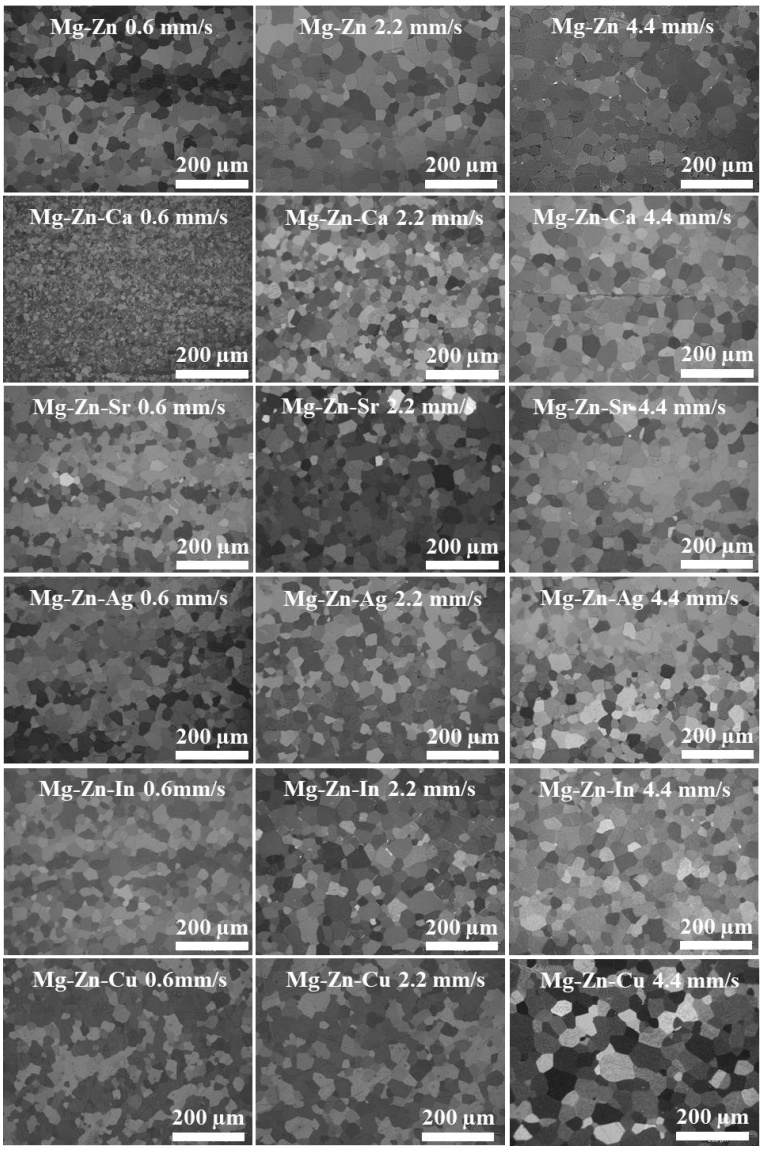

Fig. 5-33. OM microstructures of as-extruded Mg-0.5Zn(-0.2X) alloys with extrusion speed of 0.6 mm/s, 2.2 mm/s and 4.4 mm/s at 350 °C, respectively

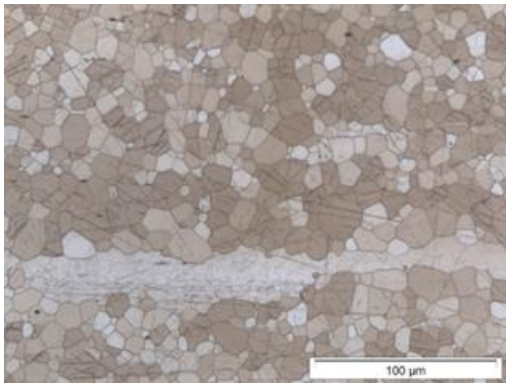

Fig. 5-34. OM image of a non-fully recrystallized microstructure of Mg-0.5Zn-0.2Ca extruded at 350 ℃ with a speed of 0.6 mm/s

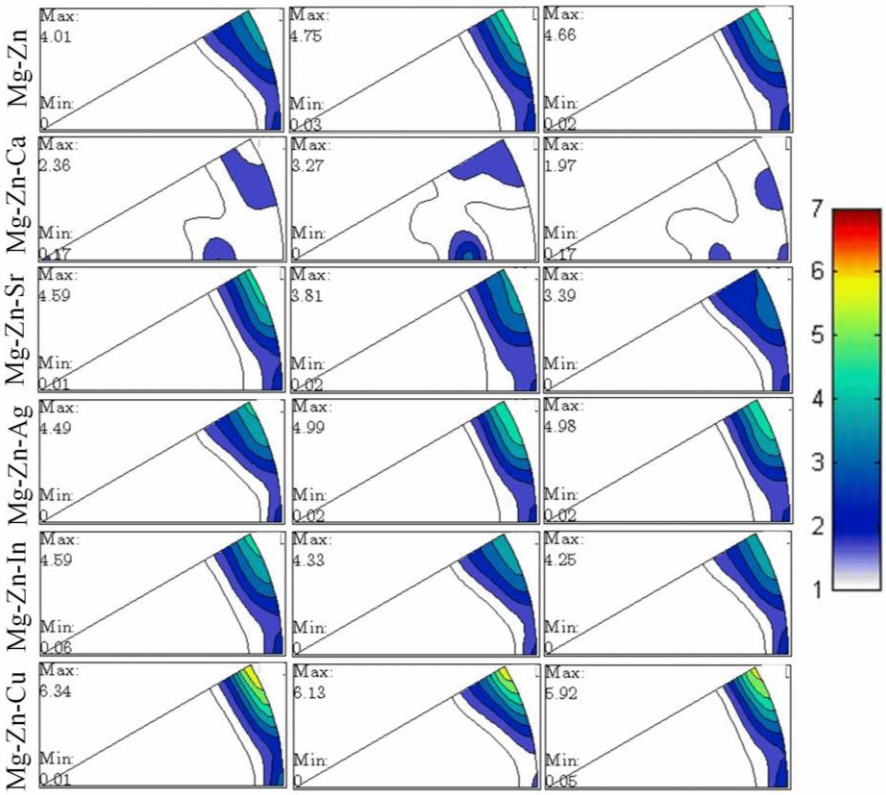

Fig. 5-35. Inverse pole figures of the as-extruded Mg-0.5Zn(-0.2X) alloys with extrusion speed of 0.6 mm/s, 2.2 mm/s and 4.4 mm/s, respectively. Bottom left ⟨0001⟩ pole, bottom right ⟨$10\bar{1}0$⟩ pole and top right ⟨$11\bar{2}0$⟩ pole. Max and Min are the maximum and minimum pole density in multiples of random distribution, respectively.

The dendritic microstructures in as-cast Mg-0.5Zn(-0.2X) alloys (**Fig. 5-2**) are dissolved after heat treatment and extrusion. Moreover, Zn segregations existing between the dendritic arms also vanish accordingly (**Fig. 5-36**). Although solution annealing is applied to reduce the amount of intermetallics prior to the extrusion process, there are still intermetallics remaining in some systems. From higher magnification SEM images, the as-extruded Mg-Zn, Mg-Zn-Ag

and Mg-Zn-In samples exhibit analogous microstructures with the presences of CE-IMP containing Fe-Si and Mg_2Si precipitates (**Fig. 5-37a, d, e**). The Fe-Si particles are usually submicron sized and Mg_2Si are a little bigger (1-2 µm). Sometimes isolated Mg_2Si phase can also be seen (spot 3 in **Fig. 5-37a**). There are a few precipitates containing Mg, Ca and Si in the as-extruded Mg-Zn-Ca sample (**Fig. 5-37b**). Ocassionally, small amounts of Fe are also incorporated in these MgCaSi particles (spot 2). The intermetallics in as-extruded Mg-Zn-Sr are Mg/Si/Sr-containing particles (**Fig. 5-37c**). Interestingly, put aside the particles with Si < Sr and Si ≈ Sr observed in the as-cast state, precipitates with Si > Sr (spot 3) can also be observed in the as-extruded sample. Fe is sometimes incorporated in these Mg/Si/Sr particles (spot 4). The precipitates differ significantly in sizes and tend to distribute in parallel to the extrusion direction. Similarly, both larger (~5 µm) and smaller (hundreds nm) precipitates can be observed in as-extruded Mg-Zn-Cu (**Fig. 5-37f**). The particles (especially the big ones) have high Cu concentrations (10-20 at.%). Ocassionally, CE-IMP with Mg/Cu (spot 1) and Mg_2Si (spot 2) particles can be observed. In addition, Fe tends to exist in the Mg_2Si part in CE-IMP (spot 4). The Zn containing intermetallics in the as-cast alloys are generally found to be dissolved into the matrix after solution annealing and extrusion, whereas the Si-containing intermetallics can still be detected indicating the relative high stability of these particles even at elevated temperatures. The particle sizes are generally refined after extrusion. The intermetallic area fractions of the longitudinal cross sections of the as-extruded Mg-Zn-Cu, Mg-Zn-Sr and Mg-Zn-Ca alloys are calculated to be 0.26 ± 0.01, 0.23 ± 0.01 and 0.10 ± 0.01, respectively. Mg-Zn-Sr, Mg-Zn-Cu and Mg-Zn-Ca have larger amounts of intermetallics, whereas the low amounts of intermetallics in the rest of the alloys defy quantification.

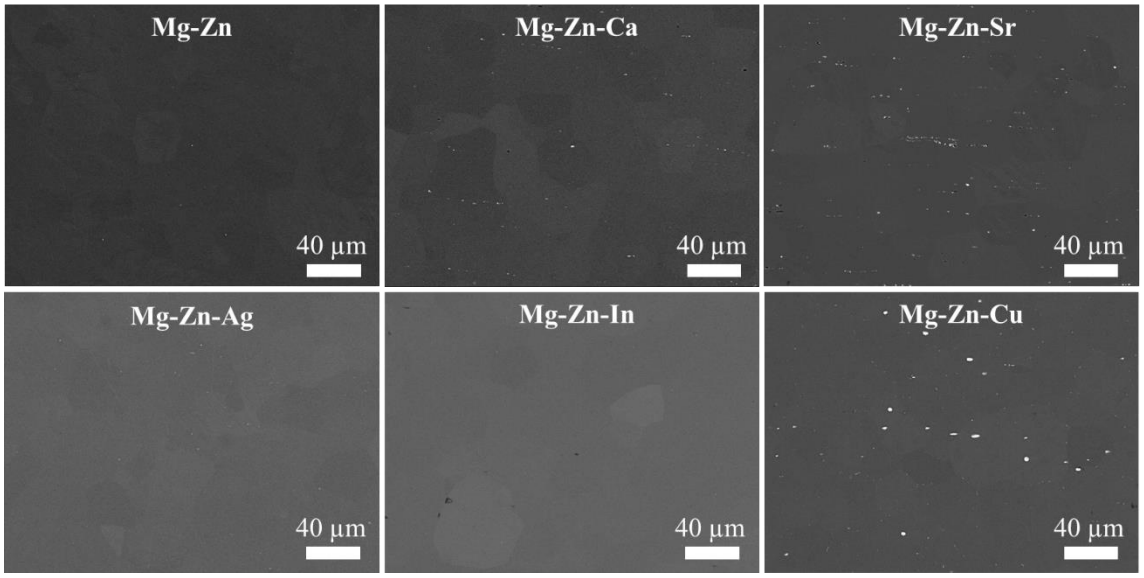

Fig. 5-36. Microstructures of the as-extruded Mg-0.5Zn(-0.2X) systems indicated by BSE SEM images

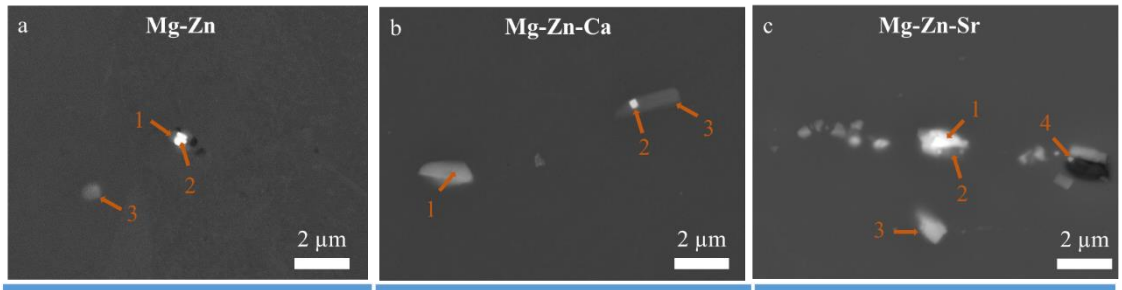

a1	Composition (at. %)				
Spot	O	Mg	Si	Fe	Zn
1	1.7	95.9	2.1	0.2	0.1
2	1.4	87.5	4.9	6.1	0.1
3	1.2	92.0	6.5	0.1	0.2

b1	Composition (at. %)					
Spot	O	Mg	Si	Ca	Fe	Zn
1	1.6	82.0	9.1	7.1		0.2
2	0.6	89.6	3.8	1.5	4.2	0.3
3	1.4	93.0	3.2	2.0		0.4

c1	Composition (at. %)					
Spot	O	Mg	Si	Fe	Zn	Sr
1	2.2	74.9	7.3		0.4	15.2
2	1.2	92.6	2.9		0.2	3.1
3	4.1	80.3	9.8		0.2	5.6
4	3.4	92.1	2.2	1.2	0.2	0.9

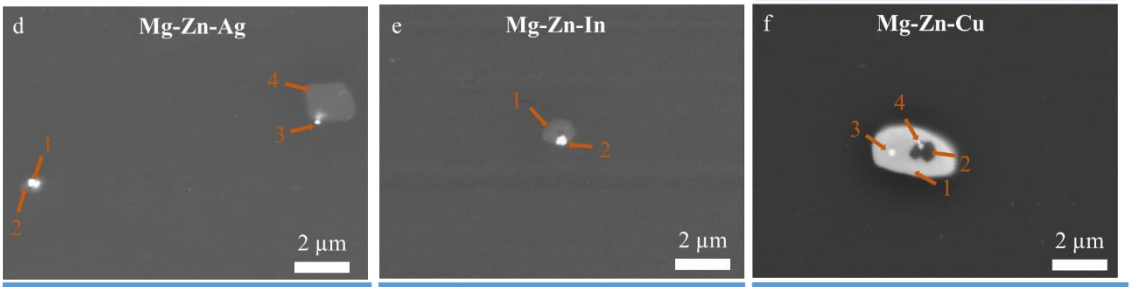

d1	Composition (at. %)				
Spot	O	Mg	Si	Fe	Zn
1	3.0	87.0	4.3	5.5	0.2
2	0.4	94.5	4.5	0.2	0.4
3	0.6	88.8	9.2	1.1	0.3
4	1.4	82.2	16.0	0.1	0.3

e1	Composition (at. %)				
Spot	O	Mg	Si	Fe	Zn
1	1.2	92.3	6.2	0.1	0.2
2	1.2	89.2	5.2	4.1	0.3

f1	Composition (at. %)					
Spot	O	Mg	Si	Fe	Cu	Zn
1	0.9	80.7	0.4		17.4	0.6
2	1.2	76.8	9.4		12.2	0.4
3	1.5	73.9	0.6		22.6	1.4
4	2.1	75.5	7.7	1.8	12.5	0.4

Fig. 5-37. (a-f) Intermetallics in the as-extruded Mg-0.5Zn(-0.2X) systems indicated by BSE SEM images; (a1-f1) corresponding intermetallic compositions measured by EDS point analysis

5.3.2. Corrosion performance

The PDP curves (**Fig. 5-38a**) show that the corrosion potentials of as-extruded Mg-Zn-Ca and Mg-Zn-Sr are the most and second most negative, respectively, while the values of as-extruded Mg-Zn, Mg-Zn-Ag, Mg-Zn-In and Mg-Zn-Cu are similar (~-1500 mV). Mg-Zn-Ca and Mg-Zn-Sr also possess the lowest i_{corr} followed by Mg-Zn-Ag (**Fig. 5-38b**), while the i_{corr} values of Mg-Zn, Mg-Zn-In and Mg-Zn-Cu are similar (90-100 µA/cm^2).

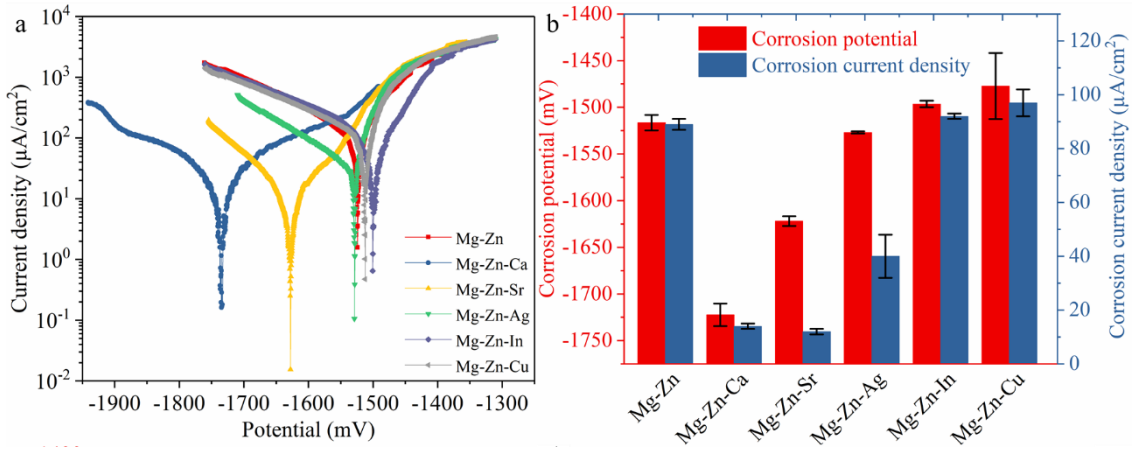

Fig. 5-38. (a) Potentiodynamic polarisation curves and (b) corrosion potential and corrosion current density of the as-extruded Mg-0.5Zn(-0.2X) alloys.

The Nyquist plots of the as-extruded Mg-0.5Zn(-0.2X) alloys are shown in **Fig. 5-39** and the EIS data is fitted with the equivalent circuit models in **Fig. 5-7**. Mg-Zn and Mg-Zn-In suffer severe corrosion attacks at the beginning of immersion (160-170 Ωcm^2) with clear inductive loops in the low frequency ranges. The R_{sum} values decrease to the minimum (98-103 Ωcm^2) at 1 h and then increase steadily afterwards (Mg-Zn 622 Ωcm^2, Mg-Zn-In 535 Ωcm^2) possibly due to the accumulation of the corrosion products. The steadily-raising R_{sum} in Mg-Zn-Ca implies the progressively build-up of corrosion products in the first 24 h (1459 Ωcm^2) although it suffers slight decline at 72 h (1328 Ωcm^2). The R_{sum} of Mg-Zn-Sr increases during the first 1 h (956 Ωcm^2) followed by a decline until 6 h (416 Ωcm^2) possibly due to some localised corrosion from oxides film breakdown. The highest R_{sum} value occurs after 72 h immersion (1058 Ωcm^2). The R_{sum} of Mg-Zn-Ag reaches the maximum value (595 Ωcm^2) at the very beginning of the test (5 min). Afterwards, R_{sum} decreases to the minimum (112 Ωcm^2) at 1 h and then gradually increases again. R_{sum} maintains low (150 Ωcm^2) during the entire immersion period in Mg-Zn-Cu, indicating the precipitated corrosion products on Mg-Zn-Cu are not compact or protective. The low R_{sum} of Mg-Zn, Mg-Zn-In and Mg-Zn-Cu after 5 min hint that active reactions already take place at the interface during the early stage of immersion.

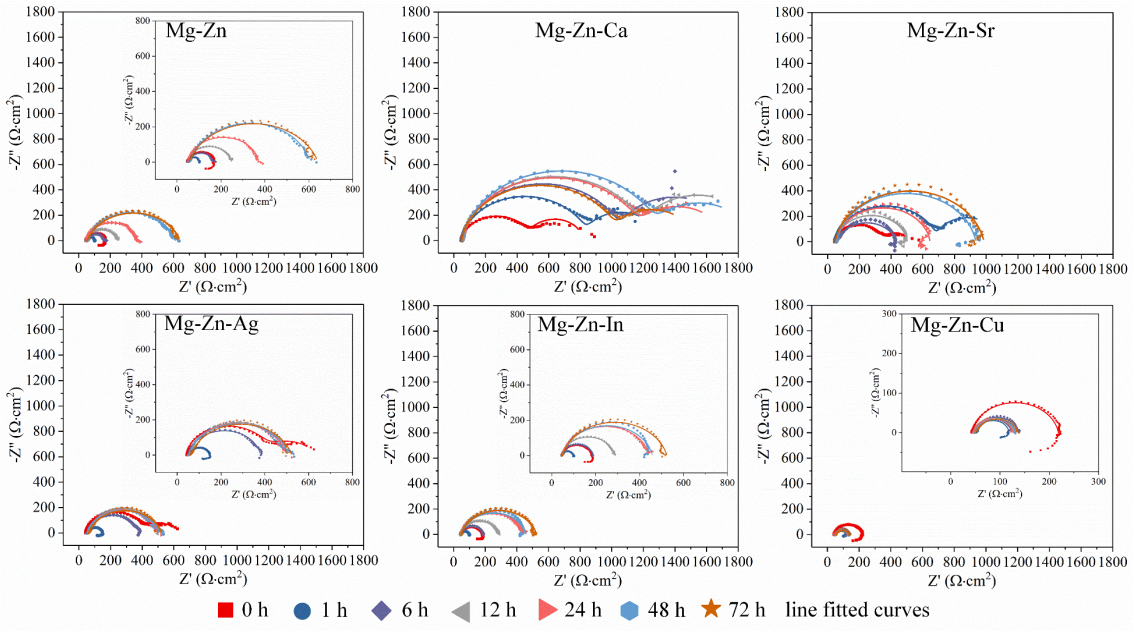

Fig. 5-39. EIS Nyquist plots of the as-extruded Mg-0.5Zn(-0.2X) alloys during 3 days immersion in 0.9% NaCl solution

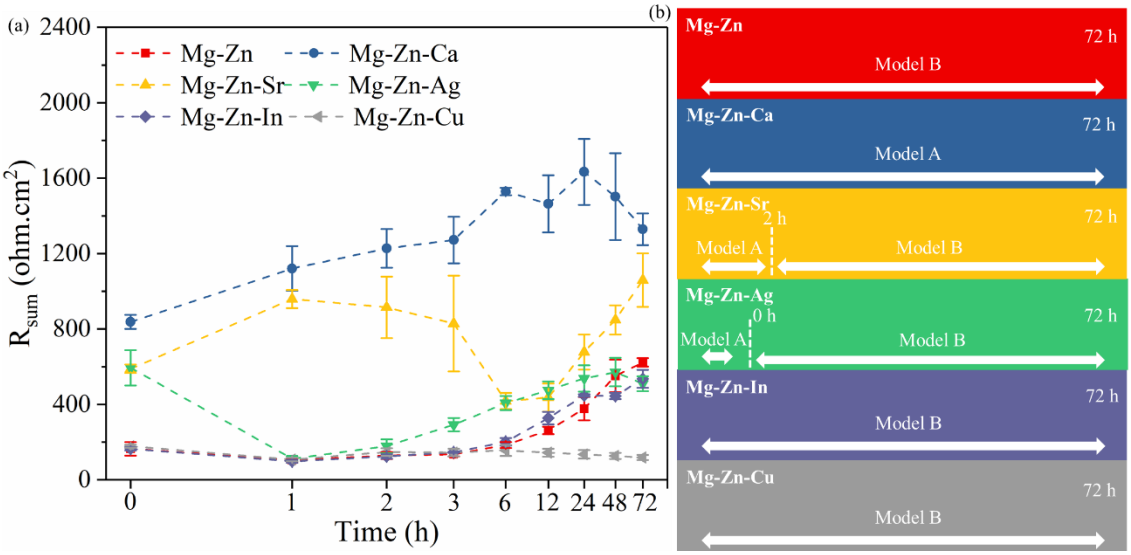

Fig. 5-40. (a) The fitted sum of the resistance of as-extruded Mg-0.5Zn(-0.2X) alloys during the 3 days measurement ($R_{sum} = R_f + R_{ct}$) (the X axis is in log10 scale for better perception); (b) selection of the models for EIS spectra at different immersion periods

Hydrogen evolution test is further conducted on the as-extruded Mg-0.5Zn(-0.2X) alloys for 7 days (**Fig. 5-41**). Only slight corrosion takes place in as-extruded Mg-Zn-Ca with the H_2 generation efficiency being 0.16 ml/cm^2 after 7 days immersion. The evolved H_2 volumes from Mg-Zn-Sr increase steadily to 2.71 ml/cm^2 at 7 days. In contrast, H_2 is generated vigorously in Mg-Zn, Mg-Zn-Ag, Mg-Zn-In and Mg-Zn-Cu, especially during the early stage of immersion (i.e. 0-10 h). The final evolved H_2 volumes from Mg-Zn, Mg-Zn-Ag, Mg-Zn-In and Mg-Zn-

Cu are 9.29, 11.38, 7.19, 52.49 ml/cm^2, respectively. Based on **Equation 4-7**, the calculated corrosion rate of Mg-Zn, Mg-Zn-Ca, Mg-Zn-Sr, Mg-Zn-Ag, Mg-Zn-In and Mg-Zn-Cu after 7 days is 3.07, 0.05, 0.90, 3.71, 2.37 and 17.19 mm/year, respectively.

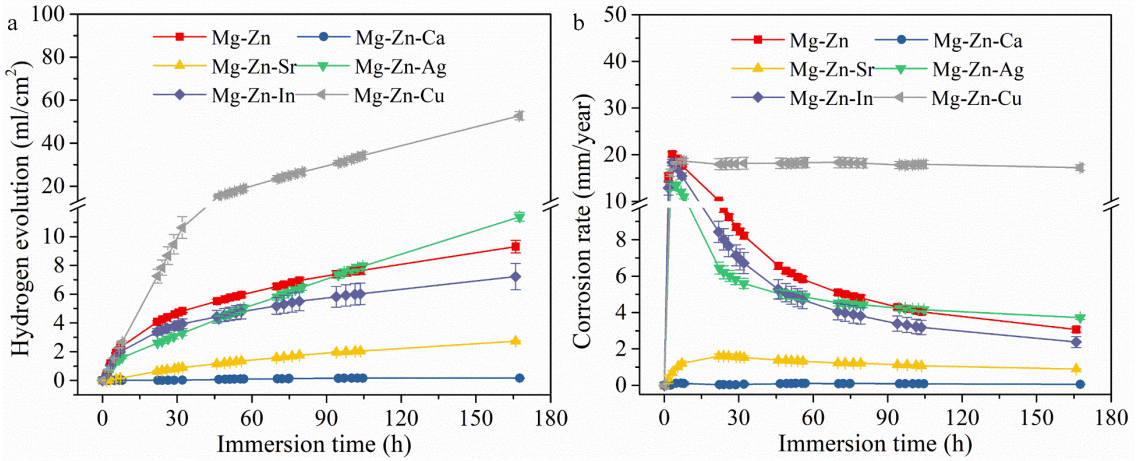

Fig. 5-41. (a) Evolved hydrogen volumes and (b) corresponding corrosion rates of the as-extruded Mg-0.5Zn(-0.2X) alloys during 7 days hydrogen evolution test

The corrosion morphologies of the alloys after 7 days hydrogen evolution test are shown in **Fig. 5-42**. Slight corrosion occurs in as-extruded Mg-Zn-Ca, whereas the most severe corrosion takes place in Mg-Zn-Cu. The as-extruded Mg-Zn, Mg-Zn-Ag and Mg-Zn-In samples also suffer severe localised corrosion such as pitting and selective dissolution. Filiform-like corrosion can be seen on the surface of the as-extruded Mg-Zn-Sr sample with some places being preferentially corroded.

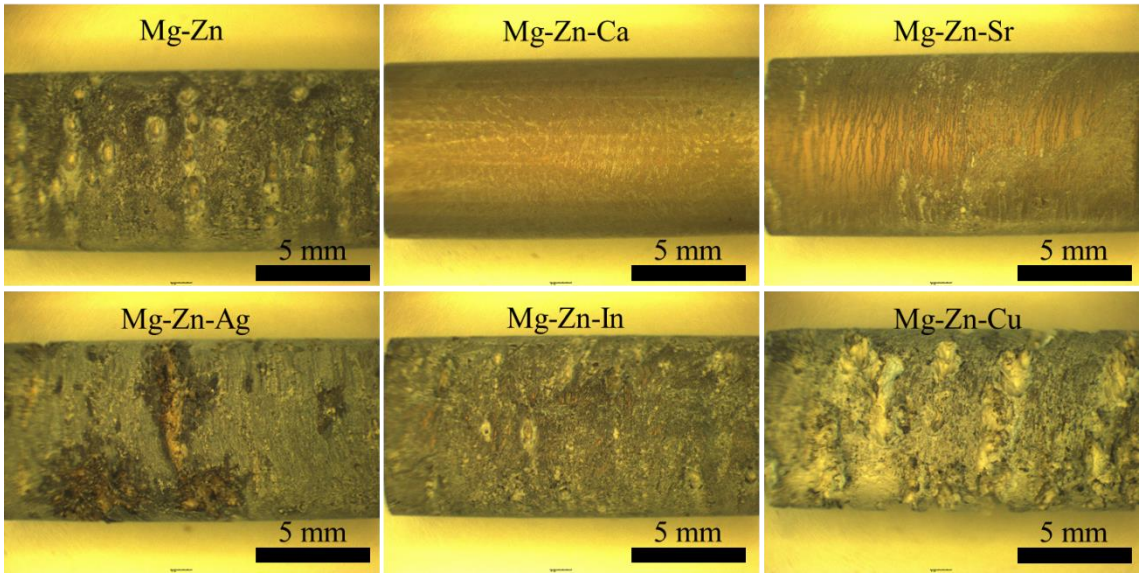

Fig. 5-42. Corrosion morphologies (with corrosion products) of the as-extruded Mg-0.5Zn(-0.2X) alloys after 7 days hydrogen evolution test

Similar to the cases in the as-cast states, Mg-Zn-Ca possesses the highest corrosion resistance and Mg-Zn-Cu possesses the lowest corrosion resistance among the as-extruded alloys. The R_{sum} value of as-extruded Mg-Zn-Ca is comparable to that of the as-cast sample with the occurance and scale of R_{sum} loss being postponed and reduced. The corrosion rate derived from hydrogen evolution test (0.05 mm/year) is even lower than that of the as-cast sample (0.12 mm/year). Similar corrosion rates are observed in as-cast and as-extruded Mg-Zn-Cu (16-17 mm/year). In contrast, the corrosion performances of as-extruded Mg-Zn, Mg-Zn-Ag and Mg-Zn-In are significantly deteriorated compared to the as-cast samples. Particularly, the R_{sum} of as-extruded Mg-Zn is not higher than that of the HT 16 h sample, indicating the deteriorated corrosion performance of solution annealed Mg-0.5Zn cannot be compensated by extrusion. Since solution annealing would decrease the corrosion resistance of Mg-0.5Zn and deformation seems to be essential to enhance the mechanical and corrosion properties, one may wonder what measures should/should not be done to alleviate the negative effects incurred by annealing. Is annealing really a necessary procedure prior to deformation?

5.3.3. Necessity of heat treatment before extrusion

It is widely accepted that as-cast Mg alloys are not mechanically suitable for biomedical implants and as-wrought alloys are preferred due to better corrosion and mechanical properties [90, 209]. Prior to the mechanical deformation, heat treatments on the alloys are widely used (**Table 2-1**). To evaluate the necessity of heat treatment, the as-cast Mg-0.5Zn sample is directly extruded at the same extrusion conditions (350 ℃, 2.2 mm/s). The corrosion performance of which is compared to that of the as-extruded Mg-0.5Zn sample described in section 5.3.2. For simplicity, the solution-treated (400 ℃ 16 h) and then extruded Mg-0.5Zn is shortened as HT16 h-extruded sample while the as-cast and then directly extruded Mg-0.5Zn is shortened as as cast-extruded sample. As expected, both the extruded samples show fully-recrystallized microstructures with average grain sizes of around 30 μm (**Fig. 5-43**).

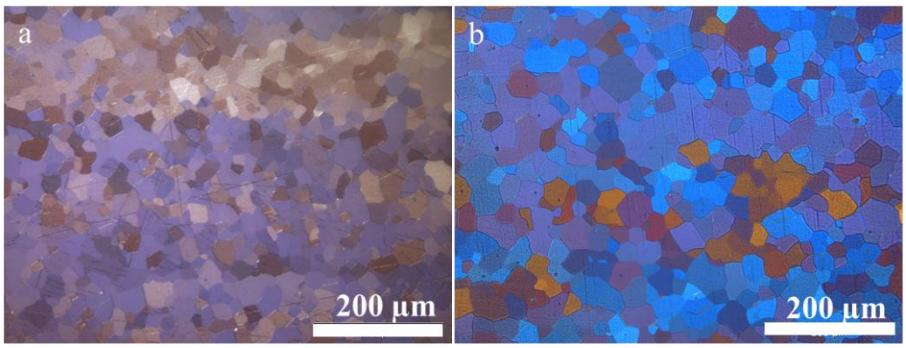

Fig. 5-43. OM images of (a) as cast-extruded and (b) HT16 h-extruded Mg-0.5Zn samples

The corrosion performances of these two extruded samples are characterised by Nyquist plots (**Fig. 5-44a-b**). The EIS data is fitted with the equivalent circuit models in **Fig. 5-7** and the R_{sum} values are displayed in **Fig. 5-44c**. During the whole immersion period, two capacitive loops can be seen in the as cast-extruded sample whereas only one capacitive loop is present in the HT16 h-extruded sample. After only 5 min immersion, R_{sum} of as cast-extruded Mg-0.5Zn (725 Ωcm^2) is already much higher than that of the HT16 h-extruded sample (160 Ωcm^2). With prolonged immersion, R_{sum} of as cast-extruded Mg-0.5Zn increases steadily until 6 h (1535 Ωcm^2) and becomes stable afterwards. In addition, the corrosion morphologies after 3 days immersion show that uniform corrosion occurs in the as cast-extruded sample (**Fig. 5-44a1**). Whereas severe localised corrosion with corrosion pits ranging from 500 µm to 2 mm are observed in the HT16 h-extruded specimen (**Fig. 5-44b1**). The as cast-extruded sample exhibits a much higher corrosion resistance than the HT16 h-extruded specimen, hinting mechanical deformation cannot necessarily compensate the detrimental effects derived from heat treatment. Moreover, it seems heat treatment is not an indispensable procedure to be carried out before deformation.

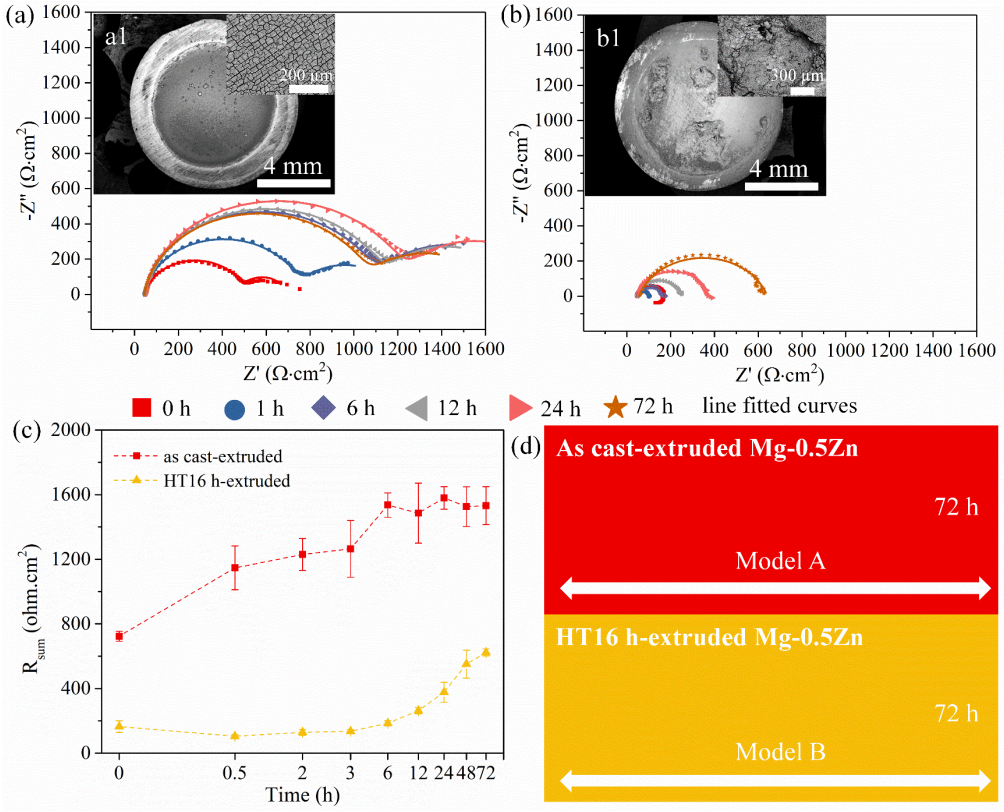

Fig. 5-44. EIS Nyquist plots of (a) as cast-extruded and (b) HT16 h-extruded Mg-0.5Zn samples; (a1-b1) corresponding corrosion morphologies after 3 days immersion; (c) the fitted sum of resistance $R_{sum} = R_f + R_{ct}$ (the X axis is in log10 scale for better perception); (d) selection of the models for EIS spectra at different immersion periods

5.3.4. Summary

(1) Zn segregations and Zn containing precipitates dissolve into the matrix while Si containing precipitates still remain in the as-extruded Mg-Zn(-X) alloys. Fe impurity tends to exist with Si.

(2) Corrosion test results indicate that as-extruded Mg-Zn-Ca exhibits the lowest corrosion rate whereas as-extruded Mg-Zn-Cu possesses the highest corrosion rate. Similarly low corrosion resistances are found in as-extruded Mg-Zn, Mg-Zn-Ag and Mg-Zn-In alloys. The corrosion rates of which are significantly higher than their as-cast counterparts.

(3) The as cast-extruded Mg-Zn sample has a much higher corrosion resistance than the HT16 h-extruded specimen, hinting it is not necessary, at least not for all Mg alloys, to conduct heat treatment before extrusion.

5.4. Comparisons between the as-cast and as-extruded samples

For easier comparisons of the as-cast and as-extruded Mg-Zn(-X) alloys and to understand the effects of solution treatment and hot extrusion, results of microstructure and corrosion are collectively shown here.

As displayed in **Table 5-6**, Zn dissolves after solution treatment and extrusion. Moreover, Fe, together with Si are found in the precipiates in the as-extruded systems. Although Fe-Si particles are also observed in the as-cast state (e.g. **Fig. 5-13a**), the Fe-Si particles dominate the precipitates especially in as-extruded Mg-Zn, Mg-Zn-Ag and Mg-Zn-In. Fe is also discerned in the Mg/Ca/Si and Mg/Sr/Si precipitates in as-extruded Mg-Zn-Ca and Mg-Zn-Sr.

Table 5-6 Summary of the compositions of the intermetallic particles formed in the as-cast and as-extruded Mg-0.5Zn(-0.2X) alloys

	Alloy	IMP compositions	Alloy	IMP compositions
as-cast	Mg-Zn	Mg/Si/Zn	Mg-Zn-Ca	Mg/Ca/high Zn, Mg/Ca/low Zn, Mg/Ca/Si
as-extruded		Mg/Si, Fe/Si		Mg/Ca/Si/(Fe)
as-cast	Mg-Zn-Sr	Mg/Zn/Sr/Si (Si < Sr) Mg/Zn/Sr/Si (Si ≈ Sr)	Mg-Zn-Ag	Mg/Zn/Ag/Si
as-extruded		Mg/Sr/Si(Fe)		Mg/Si, Fe/Si
as-cast	Mg-Zn-In	Mg/Si/Zn	Mg-Zn-Cu	Mg/Zn/Cu/Si
as-extruded		Mg/Si, Fe/Si		Mg/Cu, Mg/Si(Fe)

Corrosion results of the as-cast and as-extruded samples are shown in **Table 5-7**. The amounts of H_2 generated by Mg-Zn, Mg-Zn-Ag and Mg-Zn-In are significantly promoted after solution treatment and extrusion. Especially during the early stage of immersion (6 h), these as-extruded samples corrode 35-55 times faster than their as-cast counterparts. After solution treatment and extrusion, corrosion is also slightly accelerated in Mg-Zn-Sr while Mg-Zn-Cu maintains the high dissolution rate. In contrast, as-extruded Mg-Zn-Ca generates the least amount of H_2 among all materials. The electrochemical characterisations also corroborate the results of H_2 evolution test. The i_{corr} of Mg-Zn, Mg-Zn-Ag and Mg-Zn-In increase significantly after solution treatment and extrusion. In addition, compared to the as-cast counterparts, the corrosion potentials of the as-extruded alloys experience shifts to the positive direction except Mg-Zn-Ca and Mg-Zn-Cu. Significant reductions in R_{sum} from EIS are observed in as-extruded Mg-Zn and Mg-Zn-In after 6 h until the end of test.

Table 5-7 Comparisons of the evolved H_2 volumes, corrosion potential (E_{corr}) and corrosion current density (i_{corr}) from PDP, R_{sum} from EIS between the as-cast and as-extruded Mg-Zn(-X) samples.

Alloy		Evolved H_2 volume (ml/cm^2)				E_{corr} (mV)	i_{corr} (μA/cm^2)	R_{sum} (Ωcm^2) in EIS		
		6 h	24 h	72 h	168 h			6 h	24 h	72 h
Mg-Zn	as-cast	0.04 ± 0.01	0.16 ± 0.02	0.38 ± 0.03	0.77 ± 0.09	-1703 ± 8	19 ± 1	1668 ± 206	672 ± 176	898 ± 130
	as-extruded	1.92 ± 0.04	4.25 ± 0.08	6.67 ± 0.19	9.31 ± 0.43	-1516 ± 8	89 ± 2	185 ± 15	377 ± 62	623 ± 22
Mg-Zn-Ca	as-cast	0.02 ± 0.00	0.04 ± 0.01	0.17 ± 0.04	0.36 ± 0.09	-1733 ± 7	16 ± 1	1515 ± 157	823 ± 163	1773 ± 115
	as-extruded	0.02 ± 0.01	0.02 ± 0.01	0.12 ± 0.02	0.16 ± 0.02	-1722 ± 12	14 ± 1	1528 ± 20	1633 ± 175	1329 ± 84
Mg-Zn-Sr	as-cast	0.04 ± 0.01	0.22 ± 0.01	0.52 ± 0.02	1.01 ± 0.04	-1688 ± 8	22 ± 2	874 ± 154	666 ± 110	986 ± 136
	as-extruded	0.10 ± 0.00	0.70 ± 0.06	1.64 ± 0.05	2.73 ± 0.06	-1622 ± 5	12 ± 1	417 ± 42	677 ± 92	1059 ± 141
Mg-Zn-Ag	as-cast	0.04 ± 0.01	0.18 ± 0.01	1.05 ± 0.14	2.95 ± 0.44	-1594 ± 3	24 ± 3	344 ± 47	293 ± 62	307 ± 16
	as-extruded	1.48 ± 0.06	2.72 ± 0.16	5.96 ± 0.23	11.37 ± 0.30	-1527 ± 1	40 ± 8	407 ± 37	537 ± 69	509 ± 39
Mg-Zn-In	as-cast	0.03 ± 0.01	0.29 ± 0.10	0.89 ± 0.26	1.76 ± 0.39	-1738 ± 4	19 ± 2	1135 ± 162	697 ± 112	642 ± 107
	as-extruded	1.68 ± 0.06	3.50 ± 0.26	5.30 ± 0.62	7.22 ± 0.91	-1496 ± 4	92 ± 1	201 ± 20	447 ± 7	535 ± 47
Mg-Zn-Cu	as-cast	1.96 ± 0.14	10.58 ± 0.34	26.48 ± 1.69	49.72 ± 2.25	-1439 ± 10	104 ± 13	227 ± 22	186 ± 20	194 ± 20
	as-extruded	2.26 ± 0.03	7.85 ± 0.54	24.13 ± 1.45	52.75 ± 1.91	-1477 ± 35	97 ± 5	156 ± 29	135 ± 22	117 ± 13

6. Discussion

6.1. Influence of alloying elements on the as-cast alloys

6.1.1 Microstructure

The grain structures of Mg-0.5Zn differed greatly with the additions of different alloying elements (**Fig. 5-1** and **Fig. 5-2**). The grain sizes of Mg-Zn, Mg-Zn-In and Mg-Zn-Cu are in millimetre range while that of Mg-Zn-Ca, Mg-Zn-Sr and Mg-Zn-Ag are refined. The roles of solutes in the grain refinement of Mg alloys were extensively studied in literature [215] and a growth restriction factor (GRF) or Q value is proposed. The Q value is relevant to the rate of establishing constitutional supercooling zone. During solidification, the solute segregations ahead of the advancing solid/liquid interface cause constitutional supercooling, which would restrict the growth of dendrite/grain and promote nucleation [215]. Higher Q value normally corresponds to higher possibility to build up constitutional supercooling zone and higher grain refinement efficiency. The Q value can be described as:

$$Q = mC_0(k-1) \quad \textbf{(Equation 6-1)}$$

where m is the slope of the liquidus line, C_0 is the solute composition (wt.%) of the alloy and k is the equilibrium partition coefficient of the element [216]. The calculated Q value of each alloying element in this study is shown in **Table 6-1**. However, this equation is only valid for binary systems. When it comes to ternary systems, the addition of a tertiary element to a binary alloy should lead to an increase in the Q value in the system, which in turn led to finer grains [217, 218]. This is in agreement with the observations in **Fig. 5-1** and **Fig. 5-2** that the additions of 0.2 wt.% Ca, Sr and Ag decrease the grain size of reference Mg-0.5Zn alloy and the grain refinement extent is proportional to the corresponding Q value. The grain refining effects of Ca [89], Sr [16] and Ag [141] were also reported elsewhere although the base material was not necessarily Mg-Zn. Indium, with a Q value of 0.4, is significantly lower in the grain refining effect than those of the other alloying elements. Indeed, the grain size does not change much after the addition of 0.2 wt.% In. Surprisingly, Zn and Cu have high Q values (next to that of Ca among the selected elements) whereas grains are not refined in this work. For example, the grain size of Mg-0.5Zn is similar to that reported in literature (1 mm for Mg-2Zn [143], 1.5-3 mm for Mg-0.5Zn [219]). The coarse grains are related to the low supercooling degree during solidification as the additions of the alloying elements are rather limited. Blawert et al. [220] reported the grain size of AZ91 reduced from 500 µm to 200 µm after adding 2 wt.% Cu, whereas no grain refining effect was noticed if the Cu content was less than 0.5 wt.%. Cai et

al. [82] also found grain refinement effect of Zn was significant only if its addition was in the range of 1-5 wt.%. Mg-Zn and Mg-Zn-Cu are expected to show finer grains if the additions of Zn and/or Cu are higher. In addition, the formation of intermetallics (e.g. Ca-Si [221], Sr-Si [222], Mg-Sr [215]) can also contribute to the grain refinement. These elements have high affinities with each other and will be pushed to the front of solid/liquid interface forming the relevant precipitates during solidification. These thermostable phases are distributed on the dendrite/grain boundaries (**Fig. 5-2**) which could further impede the grain growth of Mg-Zn-Ca and Mg-Zn-Sr by pinning effect.

Table 6-1 Q value [216] and solubility limit in Mg [183, 223] of the alloying elements and corresponding grain size of Mg-Zn(-X) system (published in Materials & Design [206])

Element	Zn	Ca	Sr	Ag	In	Cu	Si	Mg
Q value (-)	5.3	11.9	3.5	2.7	0.4	5.3	-	-
Grain size of Mg-Zn(-X) in this work	mm level	147 µm	238 µm	378 µm	mm level	mm level	-	-
Maximal solubility in Mg (wt.%)	6.2	1.34	0.11	15	53	0.034	0.003	-
Solubility in Mg at RT (wt.%)	2	~0	~0	~0	35	~0	~0	-

Due to the different solubility of the alloying elements and impurities in Mg [183, 223], different intermetallics are formed in the alloys. Similar microstructure and Mg/Zn/Si containing intermetallics are observed in Mg-Zn and Mg-Zn-In (**Fig. 5-3a, e**). Only MgZn and Mg_2Si phases were reported in the Mg-Zn-Si systems and no ternary phases were detected [108, 224]. The brighter and darker part of CE-IMP could be determined as MgZn and Mg_2Si, respectively. Due to the lower enthalpy of formation of Mg_2Si (-25.9 kJ/mol·atom) [225] than that of MgZn (-15 kJ/mol·atom) [226], Mg_2Si is preferentially formed. Thus, Mg_2Si can act as a nucleation site for MgZn during solidification. Due to the high solubility of In, no In-rich secondary phase is formed. Similar precipitate free microstructures were also observed in Mg-(1~7)In [227].

As for Mg-Zn-Ca, the relative atomic ratio of Ca/Si in the Mg-Ca-Si-containing phase is 0.8 ± 0.1 (**Table 5-2**). Carbonneau et al. [210] reported the atomic fraction among Mg, Ca and Si was close to a stoichiometric value of one-third in the ternary MgCaSi phase. In this case, the atomic ratio of Ca/Si is near 1, indicating that the Mg-Ca-Si-containing phase is potentially a

MgCaSi phase. The atomic ratio of Zn/Ca in Mg-Zn-Ca part in CE-IMP is 1.6 ± 0.4 (**Table 5-2**), which indicates that the Mg-Zn-Ca part in CE-IMP is possibly $Ca_2Mg_6Zn_3$ [130]. Since only one IMP forms between Mg and Ca, it could be assumed that the Mg-Ca part in CE-IMP is the Mg_2Ca phase [228]. With further assistance of TEM diffration patterns within CE-IMP (**Fig. 5-24**), the hcp phase with smaller lattice parameters is Mg_2Ca phase [229] and the hcp phase with larger lattice parameters is $Ca_2Mg_6Zn_3$ phase [230]. In addition, the isolated MgCaSi phase possesses a primitive orthorhombic crystal structure [210]. The SAED patterns confirm with the literature that conducted on these phases [231-237]. Similar CE-IMP structure can be found in Ref. [81, 130, 232] and the presence of MgCaSi is also reported in Ref. [236, 238]. According to the solidification simulation by Pandat^{TM}2017 (database PanMagnesium 2017) [192] using a Scheil model [193] (**Fig. 6-1**), α-Mg starts to form at 647.26 °C followed by the precipitation of MgCaSi at 634.89 °C. This suggests that MgCaSi phase solidifies at an early stage between the dendrite arms while α-Mg grains are forming. The precipitation of $Ca_2Mg_6Zn_3$ begins at 393.88 °C and the last drop of liquid exhausts at 393.82 °C. With further cooling at 393.80 °C, Mg_2Ca starts to precipitate. Due to the similar solidification temperatures of $Ca_2Mg_6Zn_3$ and Mg_2Ca phases (less than 0.1 °C difference), it can be inferred that they solidify almost simultaneously and $Ca_2Mg_6Zn_3$ acts as a nucleation site when Mg_2Ca starts to precipitate. This is in accordance with the present distribution in as-cast state in which $Ca_2Mg_6Zn_3$ embraces Mg_2Ca in CE-IMP (**Fig. 5-23c**). The detection of Mg_2Ca and MgCaSi are consistent with the claim of Gil-Santos et al. [239] that these phases would form if Ca/Si wt.% > 1.7 (13.8 in this study). The formation of $Ca_2Mg_6Zn_3$ also agrees well with literature [240] that α-Mg + $Ca_2Mg_6Zn_3$ phase would precipitate when Zn/Ca at.% > 1.2 (1.6 in this study).

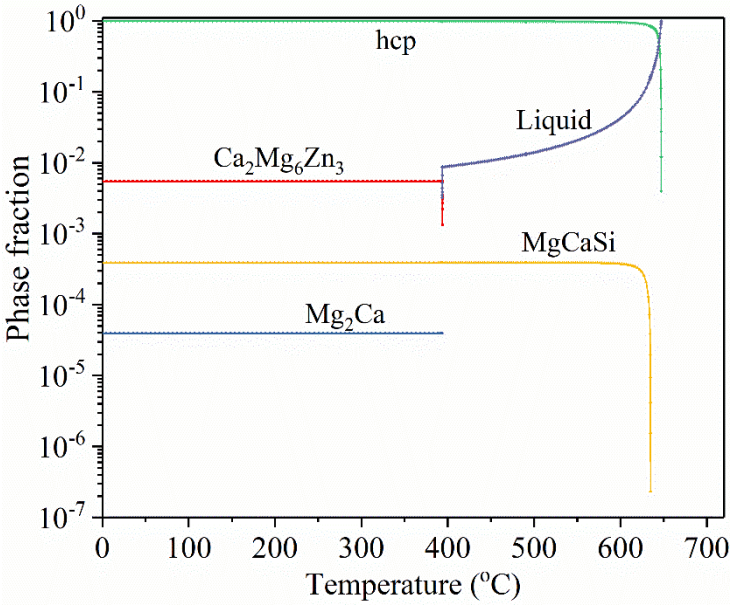

Fig. 6-1. Phase fractions of intermetallics, hcp Mg and liquid of the as-cast Mg-0.5Zn-0.2Ca alloy in dependence of temperature using a Scheil model by Pandat™2017 with PanMagnesium 2017 database (published in Corrosion Science [181])

Two types of intermetallics Mg/Zn/Sr/Si (Si < Sr) and Mg/Zn/Sr/Si (Si ≈ Sr) are observed in Mg-Zn-Sr sysyem (**Fig. 5-3c**). A $Mg_{11}Zn_4Sr_3$ ternary phase is found in Mg-5Zn if the Sr addition is higher than 0.6 wt.% [138]. However, the Zn/Sr ratio (4/3) in $Mg_{11}Zn_4Sr_3$ is not consistent with the results in this study (Zn < Sr, **Fig. 5-3c**). The Zn contents in CE-IMPs in Mg-Zn-Sr (1.4 ± 0.6 at.% for the brighter part and 1.7 ± 0.7 at.% for the darker part) are lower than those of MgZn phase in Mg-Zn, Mg-Zn-Ag and Mg-Zn-In, indicating Zn might be dissolved in the Mg/Si/Sr particles. Gil-Santos et al. [241] reported the presence of differnet phases in Mg-Sr-Si systems depending on the addition amounts of Si and Sr: $Mg_{17}Sr_2$ + MgSiSr + $MgSi_2Sr$ are formed if 0.05 < Si/Sr wt.% < 0.2; $Mg_{17}Sr_2$ + MgSiSr are formed if 0.35 < Si/Sr wt.% < 0.5; Mg_2Si + $MgSi_2Sr$ are formed if 0.7 < Si/Sr wt.% < 2. The Si/Sr weight ratio in Mg-Zn-Sr in this study is 0.03 which is out of the range given above. However, the observed Mg/Zn/Sr/Si (Si ≈ Sr) particle should be MgSiSr phase with some dissolution of Zn (shortened as MgSiSr(Zn)). Moreover, the Sr/Si atomic ratio in the observed Mg/Zn/Sr/Si (Si < Sr) particle is around 2 (**Fig. 5-3c**), which agrees with the $SiSr_2$ phase indicated in the phase diagram (**Fig. 6-2c**). $MgSi_2Sr$ phase is formed in Ref. [241] due to the high additions of Si (0.5-5 wt.%) in the system. With the low contents of Si (160 ppm) and Si/Sr wt.% ratio (0.03) in this study, $SiSr_2$(Zn) phase is formed.

The precipitates in Mg-Zn-Ag alloy contain Mg/Zn/Ag/Si (**Fig. 5-3d**) which are different to the reported $Mg_{51}Zn_{20}$ + $Mg_{54}Ag_{17}$ [140, 242] or MgZn + Mg_4Ag [243] in literature. The Zn/Ag

at.% (~5) in the precipitates (**Fig. 5-3d,** spot 2 and 3) are also not consistent with that of $Mg_4Zn_4Ag_8$ ternary phase (Zn/Ag = 0.5) proposed by Lu et al. [244]. The most common Zn-Ag precipitates are Zn_3Ag and Zn_8Ag_5 which however still don't match with the Zn/Ag at.% (~5) in **Fig. 5-3d**. The presence of Zn_5Ag phase was only mentioned in [245], which still needs further validation by TEM. Zn_5Ag can nucleate on Mg_2Si during solidification.

As for Mg-Zn-Cu, CE-IMP was never reported in the literature. The Cu/Zn atomic ratio in the brighter side is around 2 (**Fig. 5-3f1**), which is also consistent with the composition of MgZnCu phase [246, 247]. Si is much higher in the darker side, indicating it is Mg_2Si phase. The low intensities of Zn and Cu in Mg_2Si are detected from the surrounding MgZnCu phase.

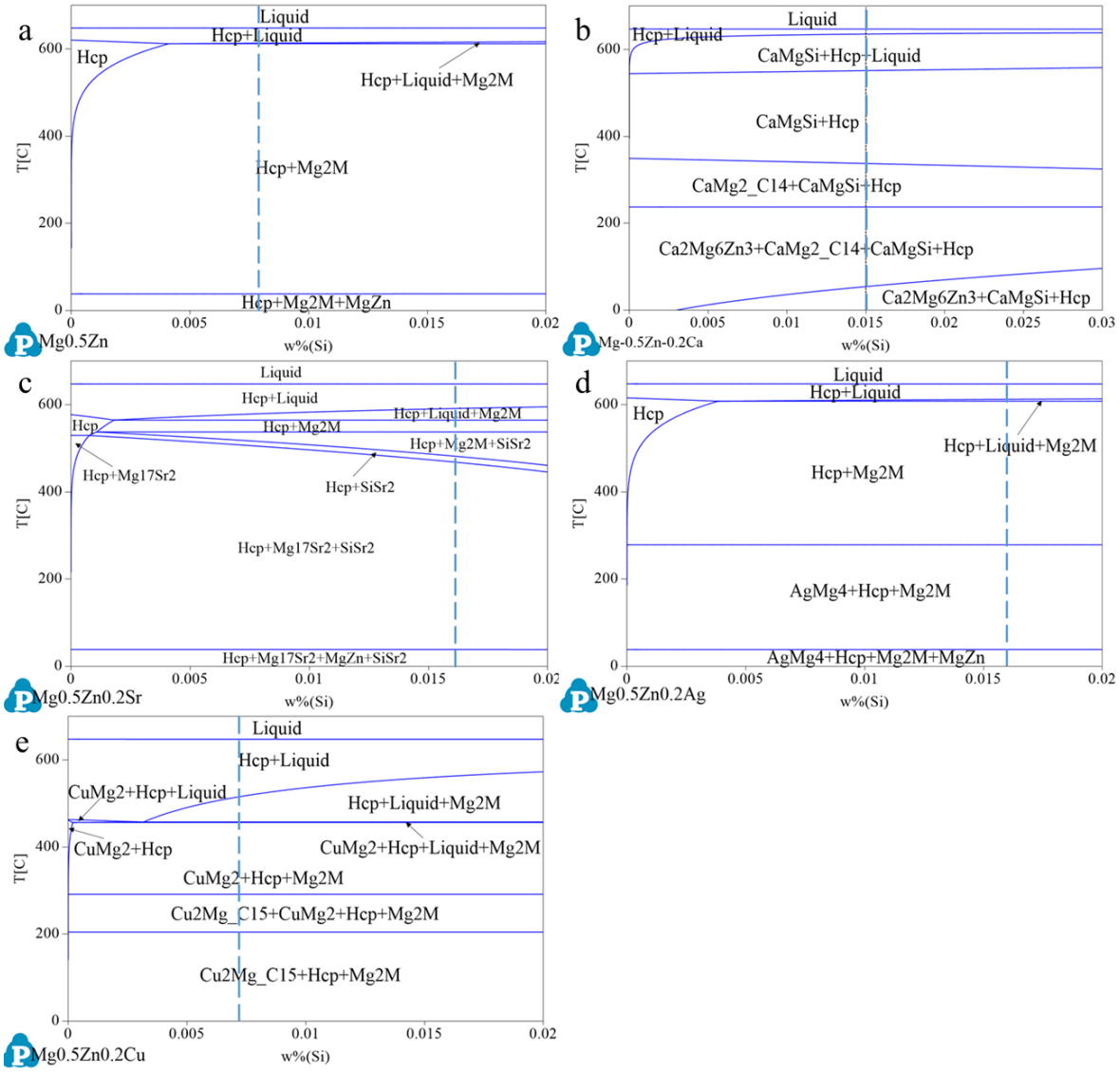

Fig. 6-2. Thermodynamic calculated phase diagrams of (a) Mg0.5Zn-Si and (b-e) Mg-0.5Zn(0.2X)-Si systems (X: (b) Ca, (c) Sr, (d) Ag, (e) Cu) by PandatTM 2017 with PanMagnesium 2017 database. The blue dash line represents the exact composition of each system. Mg_2M in (a) (c) (d) (e) represent Mg_2Si phase. CaMg2_C14 in (b) and Cu2Mg_C15 in (e) represents Mg_2Ca and $MgCu_2$ phase, respectively.

Table 6-2 Summary of the possible intermetallics formed in the as-cast Mg-0.5Zn(-0.2X) alloys (published in Materials & Design [206])

Alloy	Intermetallics
Mg-0.5Zn	Mg_2Si, MgZn
Mg-0.5Zn-0.2Ca	Mg_2Ca, $Ca_2Mg_6Zn_3$, MgCaSi
Mg-0.5Zn-0.2Sr	MgSrSi(Zn), $SiSr_2$(Zn)
Mg-0.5Zn-0.2Ag	Mg_2Si, Zn_5Ag
Mg-0.5Zn-0.2In	Mg_2Si, MgZn
Mg-0.5Zn-0.2Cu	Mg_2Si, MgZnCu

It is found that Fe, Cu and Ni impurities (**Table 5-1**) which are well-known as detrimental to the corrosion properties are within the tolerance limits [76]. Notably, Si, which was sometimes not considered in the compositional analysis in literature [81, 98, 136, 204] falls in the range of 70 to 160 ppm. The source of this slight Si inclusion might be related to the Mg production process (Pidgeon process [248]) with the overall reaction described as:

$$2MgO + 2CaO + Fe(Si) \rightarrow 2Mg(g) + Ca_2SiO_4(s) + Fe \quad \textbf{(Equation 6-2)}$$

The ferrosilicon functions as a reducing agent against MgO. It is evident that Si plays an active role in the intermetallics formation in this study (**Fig. 5-3**). However, no Si containing particles are reported although the Si contents (320 ppm in Mg-1In [227], 310-400 ppm in Mg-0.5Ca-(0.5~9)Zn [133], 440-610 ppm in Mg-(4~6)Zn-(0.2~2)Sr [249]) are much higher than those in this study. It is reasonable to speculate that the Si concentration should be limited at least below 70 ppm or even further (e.g. 50 ppm [250]) to reduce the formation of unwanted Si containing intermetallics. Further endeavours are still needed to understand the role of Si inclusion in microstructure modification.

6.1.2 Corrosion performance

As mentioned above, the grain size of alloy depends largely on the alloying element. Although discrepancies still exist regarding the effect of grain size on corrosion performance, most studies mainly focused on the corrosion behaviour of the same material under different treatment conditions [124, 151, 213]. It is difficult to separately discuss the effect of grain size in different alloying systems. Nevertheless, in this study, Mg-Zn (with mm grain size) has a comparable corrosion rate with respect to Mg-Zn-Sr (238 μm) (**Fig. 5-4**), indicating grain size is not the only factor that affects the corrosion behaviour and other effects such as intermetallics and impurity contents should also be considered.

The Volta potential difference of intermetallics relative to the matrix (ΔE) is known as one of the main criteria that affect the corrosion performance [251, 252]. Although scanning kelvin probe force microscopy (SKPFM) measurements are not carried out in this study, based on the possible precipitates discussed in section 6.1.1, ΔE of some relevant phases are summarised in **Table 6-3**. However, it is noteworthy that the ΔE of the same phase may deviate widely due to the different systems and testing environments. ΔE of $MgZn_2$ and MgZn are reported to be 460-551 mV [123, 253, 254], while that of Mg_2Si is 96 mV [253]. The possible precipitates in Mg-Zn and Mg-Zn-In are Mg_2Si and MgZn. Although ΔE of MgZn is high, the corrosion resistances of Mg-Zn and Mg-Zn-In are comparatively high in the first 6 h (**Fig. 5-7c**) due to the limited amount of these particles. Filiform corrosion occurs in Mg-Zn after 12 h (**Fig. 5-8**), which is commonly observed on bare Mg alloy surfaces exposed to NaCl solution [47, 255]. Instead of filiform corrosion, corrosion is more uniform with the addition of In. However, the R_{sum} of Mg-Zn-In become lower after 12 h, which might be related to the sparse corrosion products within this time frame. The addition of In enhances the anodic reaction kinetics (**Fig. 5-5a**) which results in sparser and looser corrosion products. The gaps in between the corrosion products are getting wider after 24 h.

Three types of precipitates are recognised in Mg-Zn-Ca (**Fig. 5-23**). Slight corrosion attack is observed in Mg-Zn-Ca after 6 h immersion (**Fig. 5-8**). As determined by SKPFM, ΔE of Mg_2Ca and $Ca_2Mg_6Zn_3$ were -126 mV and 396 mV [251]. However, Buzolin et al. [256] claimed ΔE of $Ca_2Mg_6Zn_3$ was less than 100 mV and Moreno et al. [257] showed ΔE of Mg_2Ca was only -15 mV. Moreover, MgCaSi is reported to be 200-400 mV more positive to the matrix [95, 253]. Considering the complex precipitates in Mg-Zn-Ca with significant potential differences, galvanic corrosion should be severe at the interface of the precipitates and matrix (**Fig. 5-31**). However, the R_{sum} values of Mg-Zn-Ca are comparable to that of Mg-Zn in the initial 6 h due to the refined grains and limited precipitates (area fraction being 0.29%). With longer immersion, the R_{sum} value remains low during 12-24 h (**Fig. 5-7c**). Similar to the case of Mg-Zn-In, the corrosion products are also getting sparser within this time period and Cl^- can easily penetrate through to accelerate the dissolution of Mg.

With the addition of Sr, slight localised corrosion is observed after 6 h (**Fig. 5-8**) which contributes to the R_{sum} decrease (**Fig. 5-7c**). Considering the much higher ΔE of MgCaSi [95, 253] than that of Mg_2Ca [251], there is a possibility that the ΔE of MgSrSi(Zn) and $SiSr_2$(Zn) phases in Mg-Zn-Sr are higher than that of $Mg_{17}Sr_2$ (100 mV [250]). Moreover, the dissolution of Zn would further increase the potential due to the significant ΔE of MgZn (~500 mV) [253,

258]. Galvanic corrosion also exists at the interface between MgSrSi(Zn) and $SiSr_2$(Zn). Although with the highest fraction of precipitates (0.98%), Mg-Zn-Sr had low corrosion rate due to the refined grain structures and the Zn/O layer in the corrosion products. Higher contents of Zn are detected in the corrosion layers of Mg-Zn-Sr (**Fig. 5-10** and **Fig. 5-11**) due to the less strong segregation of Zn in the alloy. The matrix in the vicinity of segregations is prone to corrosion due to potential differences [54]. The dissolved Zn precipitate on the sample surface as the solubility product constant (K_{sp}) of $Zn(OH)_2$ (3×10^{-17}) is lower than that of $Mg(OH)_2$ (5.6×10^{-12}) [259]. Although the exact composition of Zn/O containing layer could not be confirmed due to its low concentration, this Zn/O layer might improve the corrosion resistance due to the Pilling-Bedworth ratio[1] of ZnO (R_{PB} = 1.58) [260]. Leleu et al. [261] also found the corrosion performance of WE43 was superior to that of pure Mg due to the enrichment of Y_2O_3 (R_{PB} = 1.39) in the corrosion products. The oxide with higher R_{PB} would be thinner and possess higher coverage ability. This is consistent with the claim that the corrosion resistance of Mg-Sr improved after addition of Zn [262].

Earlier occurrence of filiform-like corrosion and pitting corrosion are observed with the addition of Ag (**Fig. 5-8**). Pitting corrosion in Mg-Zn-Ag is also reported elsewhere [141]. Faster degradation of Mg-Zn with the addition of Ag is expected due to the presence of some Mg_2Si and Zn_5Ag particles. Ag is a nobler element than Mg, with the standard electrode potential (0.8 V) being much more positive than that of Mg (-2.38 V) [263]. A reduced corrosion resistance of Mg-Zn or pure Mg with the addition of Ag is also reported due to the existence of Mg_4Ag or $Mg_{54}Ag_{17}$ [17, 140]. However, information on the Volta potential of Mg-Ag intermetallics in literature is still missing. Due to the pitting tendency of Mg-Zn-Ag, considerable ΔE of Zn_5Ag is expected.

Pilling-Bedworth ratio[1]

In addition to the Pilling-Bedworth ratio used to describe the oxidation resistance at elevated temperature in air, Zeng et al. [174] proposed a novel Pilling-Bedworth ratio based on the chemical compounds or reaction products during corrosion:

$$R_{PB} = \frac{V_{com}}{V_M}$$

where V_{com} and V_M are the volumes of the chemical compounds and the metal, respectively. Then based on the R_{PB} value, the compactness of the corrosion layers can be used to elucidate the corrosion mechanism.

Likewise, the addition of Cu also promotes the filiform-like corrosion and pitting corrosion (**Fig. 5-8**). Pitting corrosion of Mg-Cu is also reported in literature [264, 265]. ΔE of MgZnCu particle is about 680 mV [258] and strong galvanic corrosion occurs at the interface of MgZnCu/α-Mg and MgZnCu/Mg_2Si. However, the corrosion resistance of Mg-Zn based alloys are reported to suffer only slight loss [266, 267] or even got strengthened [143] with the addition of 0.1-0.2 wt.% Cu due to the competitive mechanism between grain refinement and MgZnCu precipitation. The corrosion rate of Mg-Zn-Cu is much higher thanthat of reference Mg-Zn in this study (**Fig. 5-4**) due to the absence of grain refinement, which possibly derived from the limited alloying additions.

Table 6-3 Summary of the Volta potential difference of intermetallics in different systems (published in Materials & Design [206])

Alloy	Intermetallics type	Volta potential difference (ΔE) respect to α-Mg (mV)	Ref.
Mg-1Ca-1Mn	Mg_2Ca	-126	[251]
Mg-0.8Ca		< 10	[95]
Mg-0.6Ca		< -50	[257]
Mg-4Zn-0.34Zr-CaO	$Ca_2Mg_6Zn_3$	50	[256]
Mg-4Zn-1Ca-1Mn		396	[251]
Mg-6Zn-5Si-1Mn-0.8Ca	MgCaSi	408 ± 26	[253]
Mg-0.8Ca		200	[95]
Mg-1Zn-1Mn-1.5Sr	$Mg_{17}Sr_2$	100	[250]
Mg-6Zn-5Si-1Mn-0.8Ca	$MgZn_2$	551 ± 78	[253]
Mg-2Zn-0.6Zr	MgZn	550	[254]
Mg-3Zn		460	[123]
Mg-6Zn-5Si-1Mn- 0.8Ca	Mg_2Si	96 ± 22	[253]
Mg-6Zn-0.5Zr-1Cu	MgZnCu	680	[258]

To compare the corrosion performances of Mg-0.5Zn(-0.2X) alloys in this study (TS) and some relevant systems from literature, the results from corrosion tests are summarised in **Table S3** for easier comparison. In 0.9% NaCl solution (**Fig. 6-3a**), Mg-0.5Zn (TS) has lower evolved H_2 volume and i_{corr} than Mg-2Zn [268], Mg-4Zn [269] and Mg-6Zn [127, 270]. The corrosion rate of Mg-0.5Zn-0.2Ca (TS) calculated from H_2 evolution is 0.08 mm/year while that of Mg-4Zn-0.56Ca derived from mass loss was 2.4 mm/year [271] after 24 h immersion. The low i_{corr} (0.17 μA/cm^2) of Mg-1Zn-0.5Ca might come from the refined grains after extrusion [272]. The

corrosion rate of Mg-0.5Zn-0.2Ca (TS) calculated from H_2 evolution is 0.08 mm/year while that of Mg-4Zn-0.56Ca derived from mass loss is 2.4 mm/year [271] after 24 h immersion. Mg-0.5Zn-0.2Sr (TS) shows lower i_{corr} than Mg-5Zn-0.2Sr [138]. The corrosion rate of Mg-0.5Zn-0.2In calculated from H_2 evolution is 0.57 mm/year while that of Mg-1In derived from mass loss is 0.45 mm/year [227] after 7 days immersion. The i_{corr} of Mg-Zn-Cu (TS) is lower than that of Mg-0.1Cu [273]. Corrosion characterisation of relevant systems of Mg-Zn-Ag in 0.9% NaCl solution cannot be found in literature. Due to the lower amounts of precipitates, the micro-alloyed Mg-Zn, Mg-Zn-Ca, Mg-Zn-Sr systems exhibited higher corrosion resistances than the highly-alloyed systems in 0.9% NaCl solution.

However, most of the Mg alloys used for biomedical applications are tested in media like SBFs (**Table 2-2**). As the corrosion behaviour of Mg alloys depends greatly on the corrosion media [175], direct comparisons of systems in this study to those in SBFs in literature would be difficult. However, Mei et al. [274] found the corrosion rates of Mg and Mg-0.8Ca in 0.85% NaCl solution were 10 times and 2 times higher than those in SBF (without TRIS), respectively. Similar phenomenon is also observed in WE43 [275] and Mg-1Zn-(0.2~1)Ca [272]. Normally Ca^{2+}, Mg^{2+}, HPO_4^{2-} and HCO_3^- in SBFs promotes the formation of protective layers on Mg alloy surface [176] whereas Cl^- promotes pitting effect [276]. If the corrosion results of the systems (TS) in 0.9% NaCl solution are lower than those protective media in literature (e.g. SBFs), then these systems (TS) are also expected to exhibit superior corrosion resistance in SBFs and can be candidates for biomedical applications. The evolved H_2 volume and i_{corr} of Mg-0.5Zn (TS) are lower than those of Mg-2Zn in 0.1M NaCl [277], Mg-1Zn [19] and Mg-6Zn [278] in HBSS and Mg-6Zn in SBF [111] (**Fig. 6-3b**). The evolved H_2 volume and i_{corr} of Mg-0.5Zn-0.2Ca (TS) are much lower than those of Mg-5Ca-1Zn in HBSS [279], Mg-2Zn-0.2Ca in Ringer's solution [177], Mg-6Zn-1Ca in 1 × PBS [280] and Mg-0.5Ca-0.25Zn-0.25Mn in c-SBF [281]. The evolved H_2 volumes of Mg-0.5Zn-0.2Ag (TS) and Mg-0.5Zn-0.2In (TS) after 7 days exposure are 2.9 ml/cm^2 and 1.8 ml/cm^2, respectively, which is lower than that of Mg-1Ag (4.7 ml/cm^2) and Mg-1In (2.8 ml/cm^2) in HBSS [19]. The corrosion resistances of micro-alloyed Mg-Zn, Mg-Zn-Ca, Mg-Zn-Ag and Mg-Zn-In systems (TS) in 0.9% NaCl solution are better than the relevant highly-alloyed systems in SBFs.

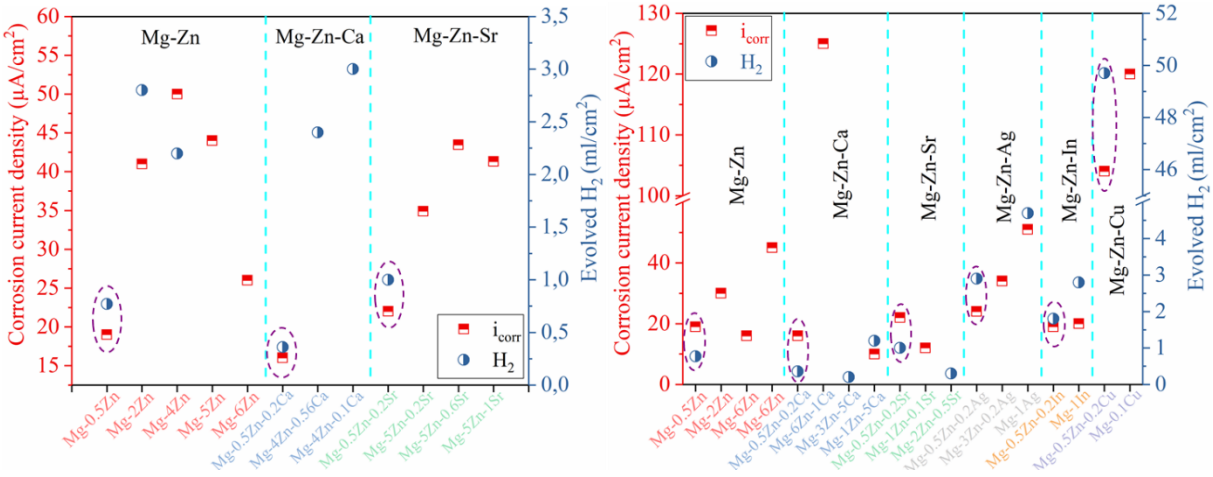

Fig. 6-3. Comparisons of i_{corr} and evolved H_2 volumes of (a) Mg-Zn(-X) in this study and relevant systems in literature in 0.9% NaCl solution; (b) Mg-Zn(-X) in this study and relevant systems in literature in SBF. The values in this study are circled.

With the exception of Mg-Zn-Cu, the corrosion rates of Mg-0.5Zn(-0.2X) (**Fig. 5-4**) are well below the threshold of 1.2-1.5 mm/year for biomedical applications [214]. Specifically, the corrosion rates of Mg-Zn, Mg-Zn-Ca and Mg-Zn-Sr match the desired degradation during the bone repair progress (0.2-0.5 mm/year) [32]. It is expected these systems could exhibit higher corrosion resistances in the protective physiological media. From the corrosion results in this study and literature, some suggestions are made here for the further design and development of these systems. The coarse grains of Mg-Zn, Mg-Zn-In and Mg-Zn-Cu can be refined with higher additions of Zn. The possibility of increased corrosion rate with the increasing Zn addition should also be noted. Indium addition (up to 1 wt.%) was poor in strengthening the corrosion and mechanical properties of Mg-In alloys [227], thus higher addition of Zn would be favoured. In respect of corrosion resistance, the addition of 0.2 wt.% Cu in Mg-0.5Zn is already too much. Lower content of Cu should be considered (e.g. below 0.1 wt.% [273, 282]) in order to minimise pitting corrosion. Ca, Sr and Ag can effectively refine the grains of Mg-0.5Zn. Ag concentration should be limited to less than 0.2 wt.% to avoid strong galvanic corrosion. Moreover, heat treatment should be conducted to reduce the pitting tendency [141]. Although the optimal additions/ratios of Zn, Ca and Sr are still unclear, Mg-0.5Zn-0.2Ca and Mg-0.5Zn-0.2Sr have comparatively high corrosion resistances in 0.9% NaCl solution. A higher Zn addition in Mg-Zn-Sr might realise the formation of compact Zn/O layer in the corrosion products. Further heat treatment is also suggested to reduce the localised corrosion [181, 283]. Considerable amounts of Si containing precipitates are formed (MgCaSi, MgSrSi(Zn), $SiSr_2$(Zn)) due to the strong bonding strengths of Ca-Si and Sr-Si. Si impurities should be controlled to low levels especially in Ca containing and Sr containing Mg alloys.

6.2. Intermetallic and impurity changes during heat treatment

6.2.1. Mg-0.5Zn-0.2Ca alloy

Various galvanic couples exist in the as-cast sample. $Ca_2Mg_6Zn_3$ phase remains while Mg_2Ca phase dissolves preferentially after 1 h immersion (**Fig. 5-29i**), indicating that $Ca_2Mg_6Zn_3$ acts as the cathode following **Equation 6-3** and Mg_2Ca acts as the anode following **Equation 6-4**:

$$2H_2O + 2e^- \rightarrow H_2 + 2OH^- \quad \textbf{(Equation 6-3)}$$

$$Mg_2Ca_{(s)} \rightarrow 2Mg^{2+} + Ca^{2+} + 6e^- \quad \textbf{(Equation 6-4)}$$

The strongest galvanic coupling during this period should be $Mg_2Ca/Ca_2Mg_6Zn_3$. One may argue that Mg_2Ca/Mg also participates in the corrosion process. However, the corrosion products on $Ca_2Mg_6Zn_3$ are much thicker than that on Mg matrix (**Fig. 5-29e, f**), revealing a stronger coupling of $Mg_2Ca/Ca_2Mg_6Zn_3$ than Mg_2Ca/Mg. This is in good agreement with the reported order of the Volta potential: 0 > $Ca_2Mg_6Zn_3$ > Mg > Mg_2Ca [81]. The phase in negative direction of the Volta potential series is more inclined to be corroded which functions as the anode in the galvanic couple, thus the high potential difference between Mg_2Ca and $Ca_2Mg_6Zn_3$ drives fast corrosion kinetics. CE-IMP acts as the cathode in overall following **Equation 6-3** and its surrounding Mg matrix functions as the anode according to **Equation 6-5**:

$$Mg \rightarrow Mg^{2+} + 2e^- \quad \textbf{(Equation 6-5)}$$

Moreover, the MgCaSi phase with a positive Volta potential difference relative to the Mg matrix also serves as an effective site for localised corrosion initiation [108, 253]. The intense galvanic corrosion between $Ca_2Mg_6Zn_3$ and Mg_2Ca in CE-IMP weakens due to the consumption of the Mg_2Ca phase after 1 h immersion (**Fig. 5-31a, f, k**). The Mg matrix around CE-IMP is not severely corroded within 1 h immersion (**Fig. 5-31k**) whereas some parts of the matrix are already undermined after 3 h (**Fig. 5-31l**). Although with the continuously presenting of $Mg/Ca_2Mg_6Zn_3$ and Mg/MgCaSi galvanic couples during immersion, the corrosion layer is built up gradually within the first 6 h (**Fig. 5-31f, g, h**), which corresponds well with the steady increase of R_{sum} value from the EIS results (**Fig. 5-27c**). After 12 h, the galvanic corrosion of $Mg/Ca_2Mg_6Zn_3$ and Mg/MgCaSi proceed and selective corrosion of the matrix develops into larger scale, which destroy the integrity of the corrosion film. Cl^- ions can penetrate through the loose corrosion layers and react with the Mg matrix underneath. This is in accordance with the significant decrease of R_{sum} value at 12 h (**Fig. 5-27c**). The majority of

the cathodic $Ca_2Mg_6Zn_3$ and MgCaSi phases remain after 24 h immersion, revealing that the galvanic corrosion derive from $Ca_2Mg_6Zn_3$/Mg and MgCaSi/Mg couples will continue. A sketch of the corrosion behaviour of the as-cast Mg-0.5Zn-0.2Ca sample is shown in **Fig. 6-4**.

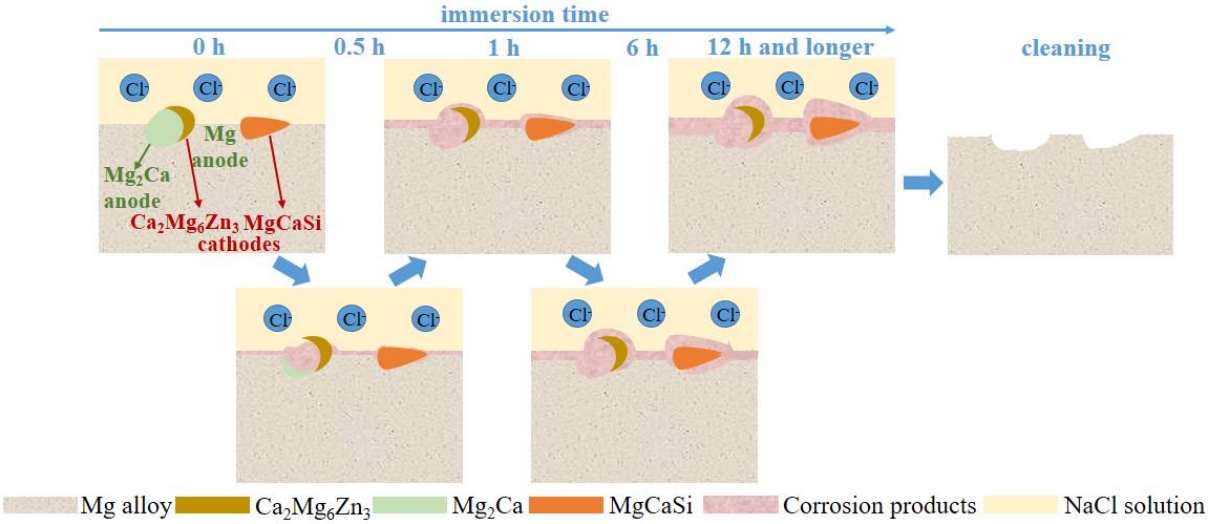

Fig. 6-4. Sketch of the corrosion behaviour of the as-cast Mg-0.5Zn-0.2Ca alloy during immersion (adapted from Corrosion Science [181])

The solution annealing parameters (450 °C, 16 h) are chosen based on the thermodynamic calculated phase diagrams of Mg0.5Zn-Ca (**Fig. 6-5a**) and Mg0.5Zn0.2Ca-Si systems (**Fig. 6-5b**) and some studies in literature [280, 284-287]. It is predicted that the MgCaSi phase cannot be dissolved under the selected annealing condition. MgCaSi possesses a low diffusion efficiency in the Mg matrix [210]. In contrast, the $Ca_2Mg_6Zn_3$ and Mg_2Ca phases from CE-IMP cannot be recognised after the solution annealing (**Table 5-3**), which is consistent with literature [130] and thermodynamic calculations. Zn from the $Ca_2Mg_6Zn_3$ phase and Ca from the $Ca_2Mg_6Zn_3$ and Mg_2Ca phases dissolve into the Mg matrix during solution annealing. It is also possible that Ca atoms from $Ca_2Mg_6Zn_3$ and Mg_2Ca is absorbed into the surrounding precipitates [130] (as in this case MgCaSi). However, the Ca content in MgCaSi in as-cast state (5.1 ± 2.6 at.%) stays at the same level after solution annealing (4.8 ± 1.7 at.%).

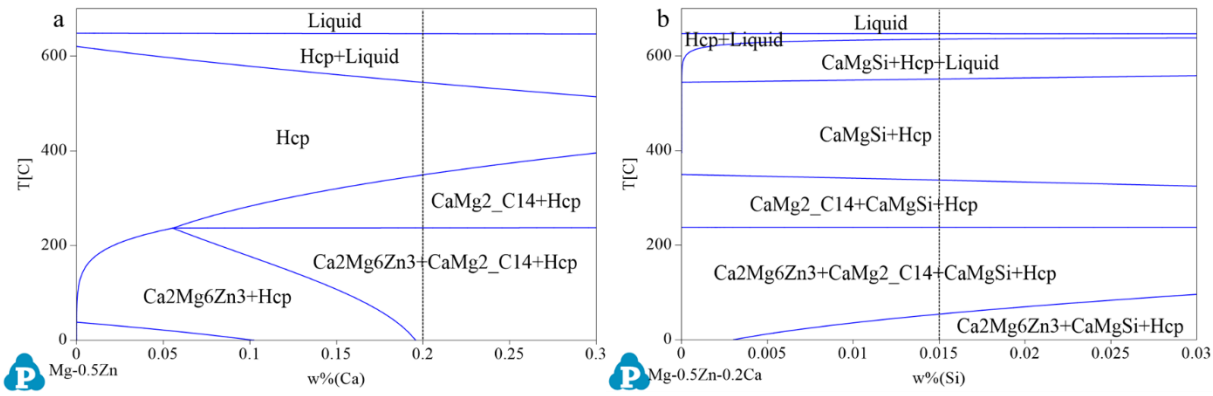

Fig. 6-5. Thermodynamic calculated phase diagrams of (a) Mg0.5Zn-Ca and (b) Mg0.5Zn0.2Ca-Si systems by PandatTM 2017 with PanMagnesium 2017 database. CaMg2_C14 represents Mg_2Ca phase. (published in Corrosion Science [181])

For the solution annealed sample (**Fig. 6-6**), reduced amounts of intermetallics (only MgCaSi) contribute to less pronounced galvanic corrosion between the matrix and the precipitates. In addition, with the dissolution of Zn segregations at the grain boundaries, the homogeneous microstructure results in a more uniform corrosion behaviour. All these lead to a higher R_{sum} value for the solution annealed sample during immersion (**Fig. 5-27c**).

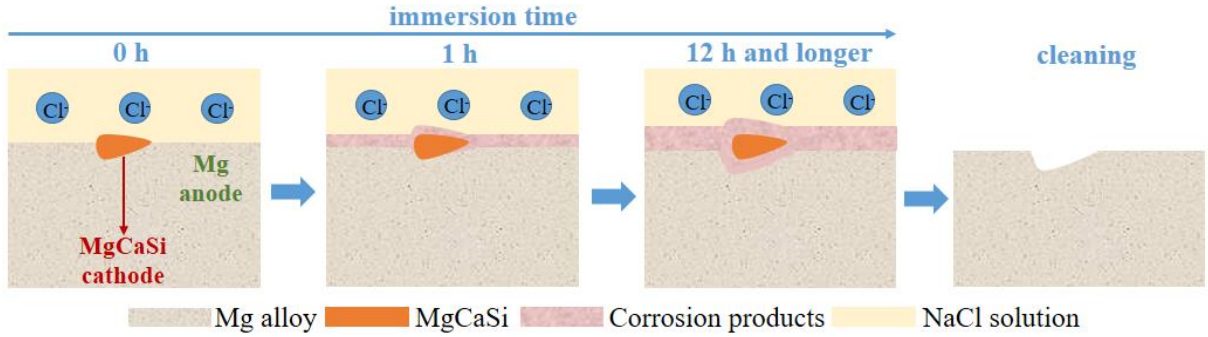

Fig. 6-6. Sketch of the corrosion behaviour of the solution-annealed Mg-0.5Zn-0.2Ca alloy during immersion (adapted from Corrosion Science [181])

6.2.2. Mg-0.5Zn alloy

According to the EDS results (Fig. **5-13**), Mg, Zn, Si and Fe are the four elements of interest in forming precipitates. ΔH of the respective binary systems are shown in **Fig. 6-7**. The parameters of each element used for calculation (**Equation 4-2** and **Equation 4-3**) are referred from Ref. [195]. A lower ΔH suggests a higher thermal stability of the compound. In this case, Si-Fe system possesses the lowest ΔH among all binary systems, indicating Si reacts preferentially with Fe to form compounds. This is further confirmed by some studies in literature claiming the discoveries of Fe-Si particles [46, 73]. Although ΔH of Mg-Si and Mg-

Zn are not so negative as that of Fe-Si, Mg_2Si and MgZn precipitates can also form during solidification which are corroborated in **Fig. 5-3a**.

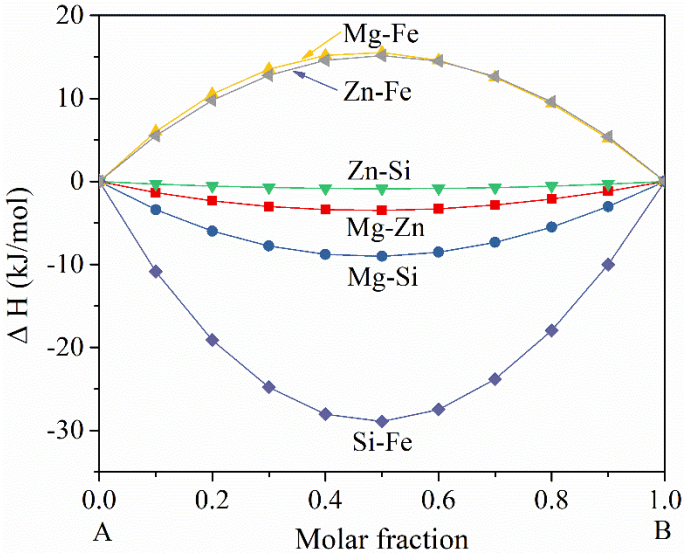

Fig. 6-7. Thermodynamic calculation of the formation enthalpies of Mg-Zn, Mg-Si, Mg-Fe, Zn-Si, Zn-Fe, Si-Fe binary systems (A-B binary systems)

As the solution annealing time extends, Fe-Si particles with increased Fe concentrations are observed (**Fig. 5-14**). To understand this, the phase diagrams of Mg-Fe (**Fig. 6-8**) and Mg0.5Zn-Fe (**Fig. 6-9a**) systems are calculated via Pandat. It is noticeable that the solidification interval from liquid to α-Mg in Mg-Fe system is very narrow (less than 0.1 ℃), whereas it expands to 14 ℃ in the Mg0.5Zn-Fe system. The liquid starts to solidify at 648 ℃ and the composition line (red) intersects with the solubility line of Fe (line ABC) at 634 ℃. The solubility of Fe decreases fast with the cooling process, which would lead to Fe precipitation. However, due to the fast cooling rate during quenching, Fe diffusion is depressed. Considering the smaller radius of Fe atom (126 pm) compared to that of Mg (160 ppm) [288], Fe can be supersaturated in Mg matrix in the as-cast Mg-0.5Zn sample. In addition, as mentioned in **Fig. 6-7**, Fe tends to coexist with Si due to their low enthalpy of formation. In contrast, when the sample is heat-treated at 400 ℃ for a certain duration, precipitation of Fe from α-Mg will take place as its solubility in Mg is only 0.1 ppm (at 400 ℃). The treatment time needed for the thorough precipitation of the supersaturated Fe is not clear yet. Nevertheless, the presences of Fe-Si particles with increased Fe concentrations after heat treatment could be the synergistic results from Fe precipitation and diffusion. Liu et al. [61] and Yang et al. [73] also proved the Fe tolerance limit in pure Mg dropped from 180 ppm in the as-cast state to 5-10 ppm in the heat treated state using calculated Mg-Fe phase diagram. According to the lever rule[1], the estimated fraction of the Fe containing particles heat treated

at 400 ℃ is (0.0015-0.00001)/(100-0.00001) = 0.0015%. The schematics illustrating the microstructure and Fe-Si particles change during solidification and solution treatment are shown in **Fig. 6-9b**.

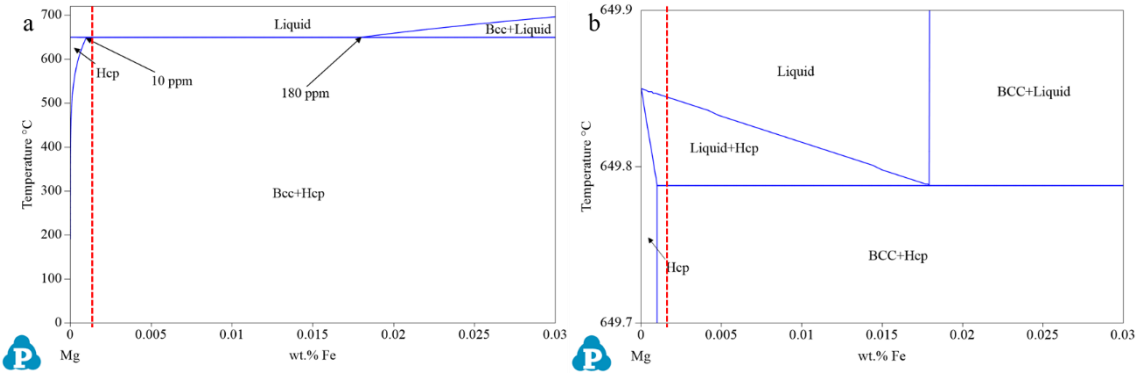

Fig. 6-8. (a) Calculated phase diagram of Mg-Fe system via Pandat and (b) its enlarged section. The red lines represent the Fe content being 14 ppm. Bcc represents Fe.

The heat treatment parameters (400 ℃ for 2 h, 16 h) for Mg-0.5Zn in this work are more efficient than the one in literature (Mg-3Zn, 320 ℃ for 10 h) [123], which did not completely dissolve the Zn segregations due to the high Zn additions and relatively low annealing temperature. The grain boundary area with element enrichment (in this case, Zn segregations) should suffer corrosion attack preferentially due to the Volta potential difference (validated also in **Fig. 5-28a**) [54]. In this sense, the diminishment of segregations in Mg-0.5Zn after heat treatment principally should lead to a better corrosion resistance. However, based on the PDP (**Fig. 5-19**), EIS (**Fig. 5-20**) and corrosion morphology observation (**Fig. 5-15**), the merits derived from homogenisation seem to disappear due to the promoted Fe contents in Fe-Si particles.

---

[1] Lever rule [289]

The lever rule is a rule used to determine the fraction of each phase in a binary equilibrium phase diagram. In an alloy or a mixture with two phases (α and β), which themselves contain two elements (A and B), the lever rule states that the mass fraction of the α phase can be calculated as:

$$W^{\alpha} = \frac{W_B - W_B^{\beta}}{W_B^{\alpha} - W_B^{\beta}}$$

where W_B^{α} is the mass fraction of element B in the α phase, W_B^{β} is the mass fraction of element B in the β phase, W_B is the mass fraction of element B in the entire alloy or mixture.

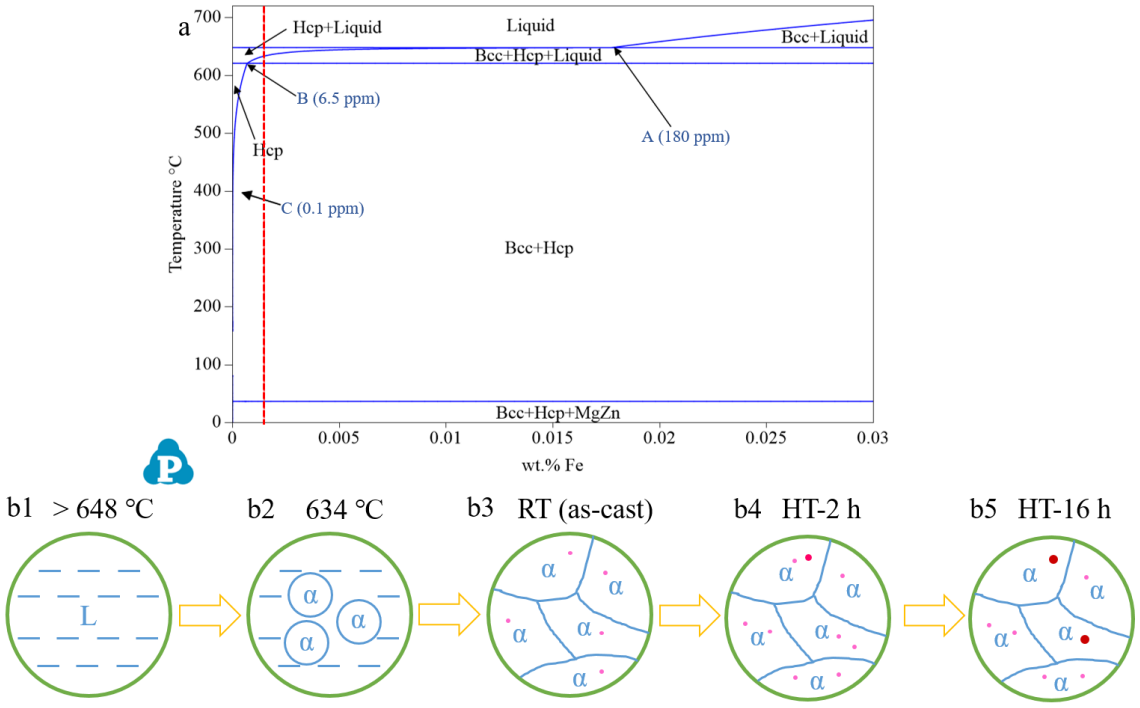

Fig. 6-9. (a) Calculated phase diagrams of Mg0.5Zn-Fe system via Pandat; (b1-b5) schematics of the changes in microstructures and Fe containing particles during solidification and solution treatment. The red line in (a) represents the exact Fe content in the system (14 ppm). The red dots in (b) stand for the Fe containing particles. The Fe concentrations in the particles are promoted (dots getting darker) during heat treatment. Bcc represents Fe.

Corrosion is observed near the Fe-Si particles in the as-cast sample after 2 min immersion (**Fig. 5-16a**). The Fe-Si particle acts as the cathode following **Equation 6-3** and its surrounding Mg matrix behaves as the anode following **Equation 6-5** due to the Volta potential difference [290]. Pawar et al. [291] found pure Fe particles in AZ31 (70 ppm Fe in total) and measured the ΔE of Fe particle being 650 ± 95 mV. Woo et al. [292] reported Fe_3Si particles in high purity Mg (19 ppm Fe and 19 ppm Si in total) and found the ΔE of which was 239 mV. In contrast, Mg_2Si phase is reported to exert no significant influence on the corrosion performance due to its relatively low ΔE (~100 mV) [253, 293].

For the heat treated samples, corrosion is initiated around the Fe-Si particles (**Fig. 5-16b-c**). The existence forms of Fe impurity affect the corrosion performances of Mg greatly. For example, although with similar overall Fe contents, one Mg sample corrodes significantly faster than the other one due to the presences of highly-concentrated Fe inclusions [46]. The promoted Fe contents in Fe-Si (**Fig. 5-14**) after annealing would increase the corrosion rate of Mg-Zn obviously. In addition, filiform corrosion is developed in the heat treated samples during the early stage of immersion (**Fig. 5-15**). Filiform corrosion is commonly found on bare

Mg alloy surfaces exposed to NaCl solution [47, 255]. The propagations of the corrosion filaments are affected by the amounts and sizes of the intermetallics. If considerable amounts of intermetallics exist, the corrosion filament will initiate from one corrosion site and terminate at the coarse intermetallics [294]. However, due to the fine and limited precipitates in the heat treated Mg-0.5Zn sample, the corrosion filaments can easily go through the grain boundaries and develop continuously all over the surface. One may argue the precipitates in as-cast Mg-0.5Zn are also small whereas no filiform corrosion occurs. This might be related to the delayed and less severe corrosion initiation in the as-cast sample as the Fe contents in Fe-Si particles are comparatively lower (**Fig. 5-14**). As indicated by the arrows in **Fig. 5-18**, some planes in the grains are preferentially corroded after immersion while other plans are less attacked. This preferred crystallographic pitting corrosion is reported to be initiated by the Fe impurities and developed along certain planes in Mg with coarse grain size [74, 295]. Similar corrosion morphology was also reported in Mg [64, 296] and other hcp metals (e.g. Be and Zn [297]). After 3 days immersion, the oxide layers in HT 2 h and HT 16 h Mg-0.5Zn samples are loose with the presence of some corrosion pits in area A (**Fig. 5-21b-c**). The Fe-Si particles with higher Fe concentrations after heat treatment have stronger driving force accelerating corrosion. It is anticipated that particles with considerable Fe contents exist in area A, making the oxide film around these precipitates more active (presence of more imperfections) during corrosion [121]. However, neither the quasi-in situ corrosion observation (peeling process) nor chromic acid cleaning is appropriate to see the Fe-Si particles after immersion as they are too small in sizes.

Normally, a more homogeneous microstructure results in a better corrosion resistance [119, 298] and the refined grain structure might help to induce more compact and protective corrosion layers [299]. For biodegradable Mg based implants with sufficient mechanical properties, deformation such as extrusion and rolling might be inevitable. However, it is obvious that the HT16 h-extruded Mg-0.5Zn sample is not appropriate for biomedical applications owing to its inadequate corrosion resistance (**Fig. 5-44b**). The merits derived from homogenisation and grain refinement seem to be totally balanced by the Fe-Si particles. Fe precipitation during heat treatment might be universal to all systems due to its low solubility (maximum 10 ppm in Mg [10]). The effects of solution annealing on the corrosion performances of the alloys are related to the competitive mechanisms between Fe precipitation and intermetallic dissolutions. When there are substantial intermetallics in the system, the corrosion performance depends more on the alloy microstructure. The enhanced corrosion

resistance after heat treatment (e.g. Mg-5Zn [126], Mg-6Zn [115]) is due to the diminishment of galvanic couples between the matrix and intermetallics. However, the impurities might play even more decisive roles if the amounts of intermetallics are limited. Together with some literature [61, 73], it is suggested for micro-alloying Mg systems, heat treatment should be conducted cautiously or even omitted, when scarce amount of precipitates and considerable Fe and Si contents exist in the system. For example, the as cast-extruded Mg-0.5Zn alloy exhibits superior corrosion performance compared to the HT16 h-extruded sample in this study (**Fig. 5-44c**). As for the appropriate heat treatment parameters, a shorter duration might be aimed. One may also argue that Fe precipitation could be less if the heat treatment is conducted at a higher temperature (higher solubility of Fe). However, the detrimental effects from potential overheating on the mechanical and corrosion performances have also to be considered [300, 301]. Furthermore, for the micro-alloyed Mg alloys and pure Mg, fast solidification velocity is suggested to minimise Fe precipitation. However, this still needs validation by further research.

6.2.3. Fe precipitation, a universal phenomenon?

The Mg0.5Zn-Fe phase diagram calculated by Pandat is used to explain Fe precipitation during heat treatment in **Fig. 6-9**. In comparison, the calculated phase diagrams of Mg0.5Zn0.2X-Fe systems (X = Ca, Sr, Ag and Cu) are also shown in **Fig. 6-10**. Similar to the case of Mg-0.5Zn, the Fe solubilities in Mg-0.5Zn-0.2X systems are also very low at the heat treatment temperatures (450 ℃ for Mg-Zn-Ca, 530 ℃ for Mg-Zn-Sr, 400 ℃ for Mg-Zn-Ag and Mg-Zn-Cu). With sufficient solution annealing time, Fe precipitations from α-Mg would also take place in these systems which corroborate with **Fig. 5-37**.

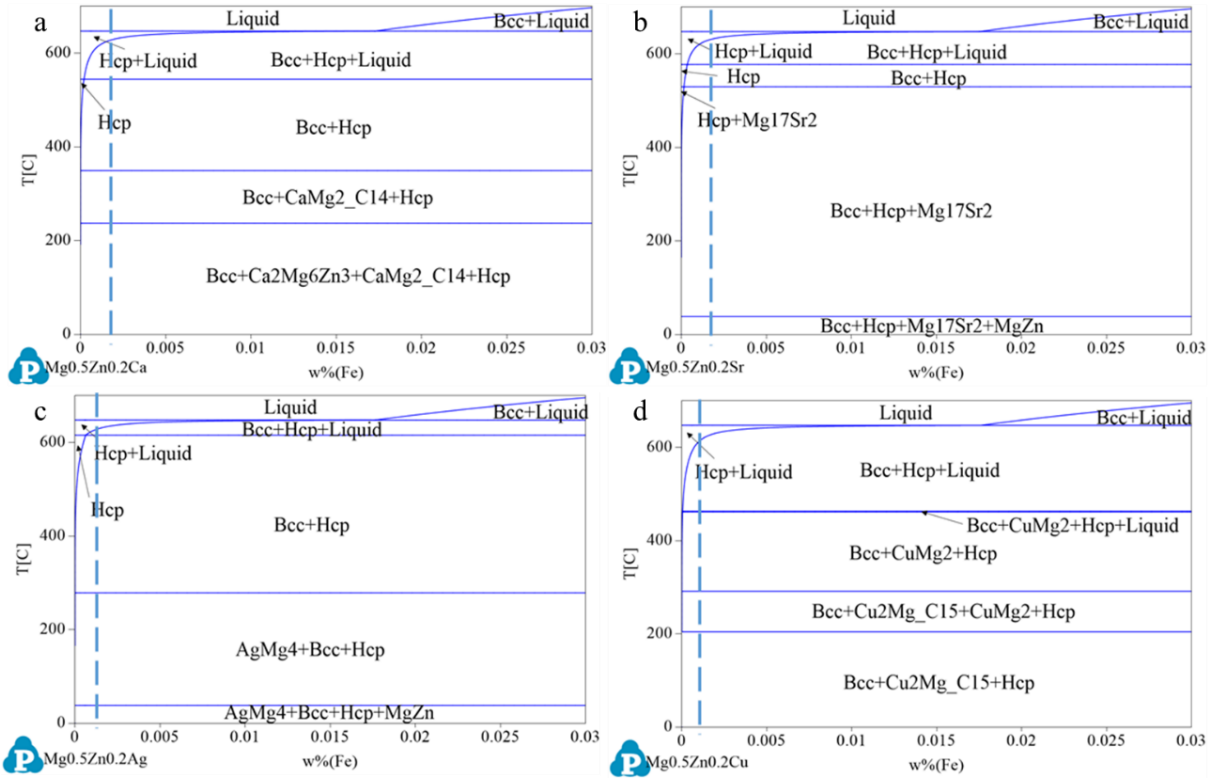

Fig. 6-10. Calculated phase diagrams of Mg0.5Zn0.2X-Fe systems by Pandat. X: (a) Ca, (b) Sr, (c) Ag and (d) Cu. The blue lines represent the Fe contents in the respective systems. Bcc represents Fe. CaMg2_C14 in (a) and Cu2Mg_C15 in (d) represents Mg_2Ca and $MgCu_2$ phase, respectively.

Although only Mg-0.5Zn and Mg-0.5Zn-0.2Ca are characterised in the solution annealed states in section 5.2, all the as-extruded samples experience heat treatment (solution annealing plus hot extrusion). However, the corrosion rates of as-extruded Mg-0.5Zn, Mg-0.5Zn-0.2Ag and Mg-0.5Zn-0.2In are strongly accelerated compared to their as-cast counterparts whereas those of as-cast and as-extruded Mg-0.5Zn-0.2Ca are comparable. As stated in sections 5.2, 5.3 and 6.2.2, the different corrosion behaviour after heat treatment/extrusion might be partly related to the distributions of impurities. To understand this, thermodynamic calculations of the ΔH of A-B binary systems in Mg-Zn-X alloys are collectively shown in **Fig. 6-11a-e**. Those of Mg-Zn, Mg-Si, Mg-Fe, Zn-Si, Zn-Fe are already calculated in **Fig. 6-7**. Si could form compounds with Mg and alloying element X with the exceptions of Zn and In. In addition, the ΔH values of Si-Ca and Si-Sr are the lowest in Mg-Zn-Ca and Mg-Zn-Sr, respectively, which corroborate with the formations of MgCaSi, MgSrSi, $SiSr_2$ phases in the respective systems (**Fig. 5-3**). As for Fe impurity, it interacts preferentially only with Si with the ΔH values of Fe-Mg, Fe-Zn and Fe-X being either positive or near 0. The ΔH of Si-Fe is the lowest in Mg-Zn, Mg-Zn-Ag, Mg-Zn-In and Mg-Zn-Cu alloys whereas it is higher than those of Si-Ca and Si-Sr in Mg-Zn-Ca and Mg-Zn-Sr alloys. The alloying systems have tendencies to transfer to the lower ΔH

values aiming for higher stabilities. During solution annealing, the elements have thorough time to diffuse and homogenise. For Mg-Zn, Mg-Zn-Ag and Mg-Zn-In alloys, Si-Fe is the most stable and will remain during heat treatment. Moreover, the supersaturated Fe in the matrix can also precipitate in the Fe-Si and Mg_2Si particles during heat treatment as Si and Fe have strong bonding strengths. As the ΔE of Mg_2Si phase is low [253, 293], the incorporation of Fe [291] or Fe_3Si [292] would promote the overall ΔE value significantly and lead to accelerated corrosion rate. In contrast, Si-Ca and Si-Sr in Mg-Zn-Ca and Mg-Zn-Sr are more stable than Si-Fe. Thus, the supersaturated Fe in the matrix can precipitate in MgCaSi and Si/Sr particles during heat treatment. The influence of Fe or Fe_3Si included in MgCaSi is not as great as that incorporated in Mg_2Si as MgCaSi has much higher ΔE [253] than Mg_2Si. Although the ΔE of Si/Sr particles are still unavailable in literature, they are also expected to be higher than that of Mg_2Si (similar to the case of MgCaSi). Particularly, only few Fe containing precipitates can be seen in the as-extruded Mg-Zn-Sr sample (**Fig. 5-37c**), which can also be attributed to the higher annealing temperatures. The higher solubility of Fe in Mg-Zn-Sr (1.6 ppm at 530 °C) than those of the other alloys (0.1-0.3 ppm at lower temperatures) leads to less Fe precipitation.

The maximal solubility of Fe and Si in Mg is only 10 and 30 ppm, respectively [10, 288]. The Si/Fe-ratio tolerance limits in the common high purity Mg alloys are still not clear. Even traces of Si could significantly decrease the tolerance limit of Fe in Mg and accelerate the corrosion rate [73]. It is suggested the Si content should be limited especially when the alloy is not extra-high purity (e.g. less than 2 ppm Fe) [69, 203]. However, as the accessibility of extra-high purity Mg is very limited, corrosion issues related to Fe and Si inclusions are still waiting to be resolved. As stated above, the corrosion rate depends largely on the Fe distribution in the system. Apart from the high quenching velocity and high annealing temperatures mentioned above, some suggestions on alloy designs are also made here.

Mn is the most common alloying element to balance the detrimental effect of Fe in Mg. Although Fe and Mn has almost no tendency to form compound ($\Delta H \approx 0$, **Fig. 6-11f**), Mn has a high affinity to Fe which makes the Mn encapsulated Fe particle a less active cathodic site than pure Fe [295]. However, the α-Mn particles will dissolve or become smaller after solutionisation [302] and extrusion [303] which may make Fe encapsulation less effective. For the alloys with certain amount of Fe and limited intermetallics, Fe precipitation during heat treatment cannot be ignored. To suppress the incurred negative effects, some restriction should be met (with Mg-X-Fe as an example). Firstly, the formation of enthalpy should be in the following order: ΔH (Mg-X) < ΔH (Fe-X) < η (η is a negative value which ensures the strong

bonding of Fe-X), so that the supersaturated Fe can precipitate in Mg/X intermetallics during heat treatment. However, this is not the full story. Mg/X must also have an appreciable ΔE so that the corrosion rate of Mg-X alloy is not significantly promoted. For example, Si might capture Fe to form FeSi particles [292] which have lower potential difference relevant to the matrix than pure Fe [291]. In this sense, Si acts as a "Fe scavenger" to elevate the corrosion resistance. However, due to ΔH (Mg-Si) > ΔH (Fe-Si) and ΔE of Mg_2Si is small, Fe precipitation would increase the corrosion rate hugely. When it comes to ternary or even more complex systems (e.g. Mg-X-Y-Fe), Mg does not necessarily participate in the intermetallic formation and thus the restrictions can be adjusted as ΔH (X-Y) < ΔH (Fe-X) < η and ΔE (X/Y) is not small. When adding Mn in Al containing alloys, the formed Al_8Mn_5 phase is reported to encapsulate Fe [304]. According to **Fig. 6-11f**, ΔH (Al-Mn) < ΔH (Al-Fe) << 0. In addition, Al_8Mn_5 has a high ΔE value (340 mV [251], 385 mV [305], 487 mV [293]), thus Fe incorporation in Al_8Mn_5 will not accelerate the corrosion rate significantly. For the Al free alloys in this study, certain amounts of Si exist in the systems (e.g. Mg-0.5Zn, Mg-0.5Zn-0.2Ag and Mg-0.5Zn-0.2In). Although around 200 ppm Mn exist, the content is too low to prevent the damage caused by Fe [61]. It is expected the additions of Mn in these systems would also reduce the negative effects of Fe precipitation due to ΔH (Mn-Si) < ΔH (Si-Fe) << 0 (**Fig. 6-11f**) and the notable ΔE of Mn_5Si_3 (428 ± 148 mV) [253].

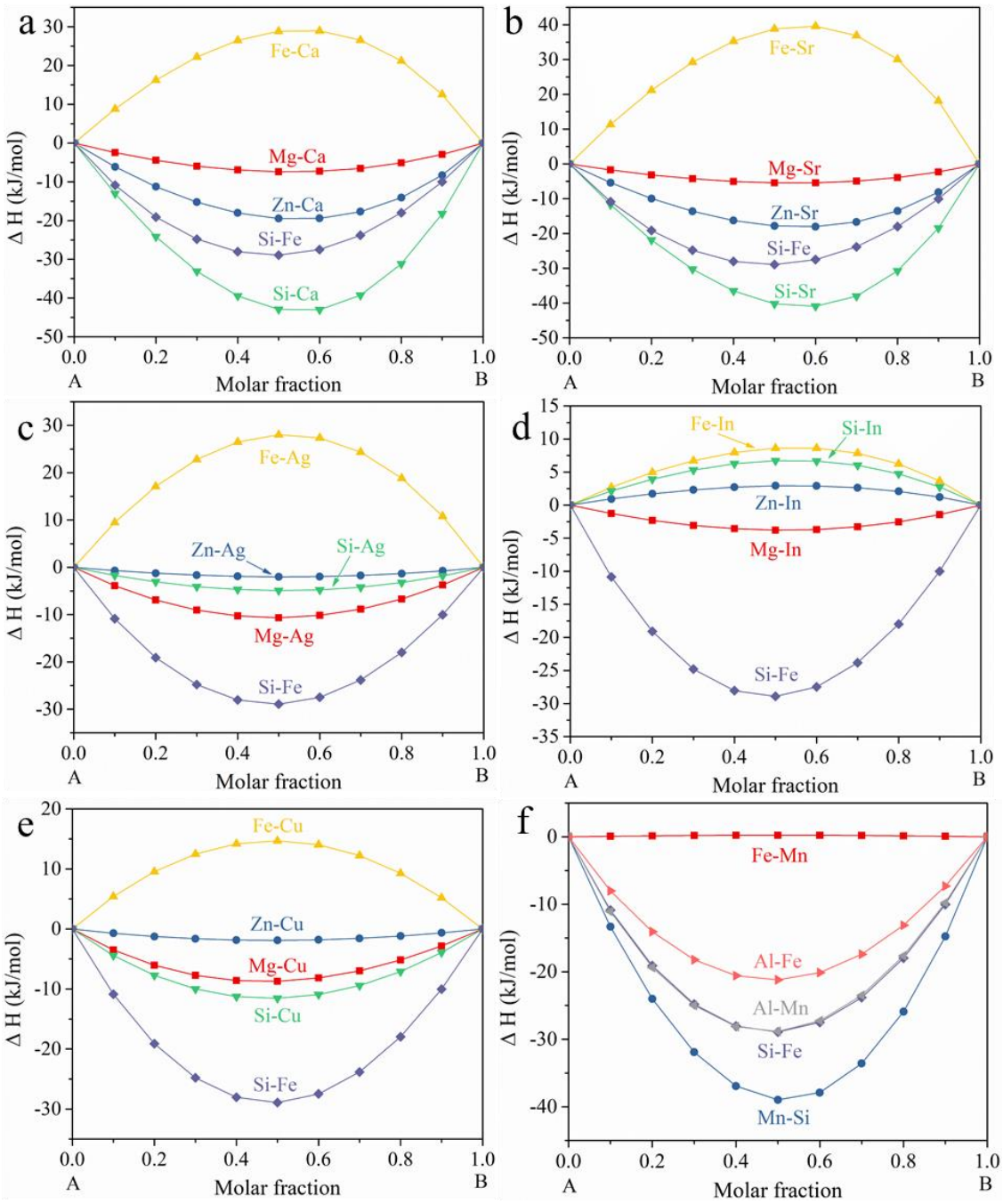

Fig. 6-11. Thermodynamic calculation of the formation enthalpies of A-B binary systems in (a) Mg-Zn-Ca, (b) Mg-Zn-Sr, (c) Mg-Zn-Ag, (d) Mg-Zn-In, (e) Mg-Zn-Cu and (f) Fe-Mn-Si systems. Those of Mg-Zn, Mg-Si, Mg-Fe, Zn-Si, Zn-Fe are already calculated in Fig. 6-7

6.3. Synergistic influence of solution annealing plus extrusion

The possibility of defects pickup during the deformation process is reported in literature [306]. However, as inferred from the similar element concentrations in the as-cast (**Table 5-1**) and as-extruded state (**Table 5-4**), the potential effect of contamination during solution annealing and extrusion on the corrosion performance can be excluded in this study.

6.3.1 Microstructure

Grain structure and texture

The average dynamic recrystallized grain sizes ($\bar{d}_{DRX}$) of the as-extruded Mg-0.5Zn(-0.2X) alloys increase with the increase of extrusion speed (**Table 5-5**). The Zener-Hollomon (*Z*) parameter [307] is found important in relating the $\bar{d}_{DRX}$ of Mg alloys to the parameters of hot deformation process, which can be described as:

$$\bar{d}_{DRX} = AZ^{-n} \quad \textbf{(Equation 6-6)}$$

$$Z = \dot{\varepsilon} * \exp(Q_a/RT) \quad \textbf{(Equation 6-7)}$$

where n and A is approximately 0.12 and 232, respectively, Q_a is the activation energy for deformation (135 kJ/mol for Mg alloys) [308], R is the gas constant, T is the absolute temperature (K), and $\dot{\varepsilon}$ is the metal flow rate which can be calculated by:

$$\dot{\varepsilon} = \frac{6D_B^2 V_R \ln ER}{D_B^3 - D_E^3} \quad \textbf{(Equation 6-8)}$$

where D_B and D_E is the diameter of billet and extrudate, respectively, V_R is the extrusion speed and ER is the extrusion ratio. From these equations, it can be inferred that the $\bar{d}_{DRX}$ is proportional to the extrusion temperature and inversely proportional to the extrusion speed. Indeed, Watanabe et al. [309] found the grain size of AZ31 decreased when the true strain rate increased at 573 K, which is contradictory to the results in this study (**Table 5-5**). This phenomenon can be explained by the increased exit temperature due to the higher deformation heating at a higher extrusion speed [214]. The grain growth effect derived from higher temperature exceeds the grain refinement effect derived from higher metal flow rate as the extrusion speed increases. Similar observations are also reported in [310, 311].

It is worth noting that Mg-Zn-Ca has the smallest grain size of the DRXed (dynamic recrystallized) region among the alloys under the extrusion speeds of 0.6 and 2.2 mm/s. One explanation is that fine precipitates formed at the grain boundary can reduce the grain boundary mobility and hinder the grain growth. Ca containing precipitates (200-300 nm) [312] and co-segregation of Zn and Ca atoms (~5 nm in width) [313] at the grain boundaries are reported in Mg-Zn-Ca system, which would reduce the grain boundary energy and ultimately lead to a pinning effect. Another possibility is the grain size of as-cast Mg-Zn-Ca is the smallest among the Mg-Zn(-X) alloys (**Fig. 5-2**), as the $\bar{d}_{DRX}$ is also dependent on the initial grain size before extrusion [314]. Moreover, the texture intensity of Mg-Zn is greatly reduced after the addition

of Ca (**Fig. 5-35**). The texture weakening is commonly found in RE [315] or Ca [316] containing Mg alloys. Although the exact mechanism of RE and Ca on texture modification is still unclear, mainly two reasons are widely adopted for explanation, i.e. particle-stimulated nucleation (PSN) and solid solubility of the alloying element [316]. Precipitates are reported to assist recrystallization during deformation due to the accumulating dislocations in the grains (PSN) and the recrystallized grains exhibit more random textures [317]. According to the phase diagram of Mg0.5Zn0.2Ca-Si (**Fig. 6-2b**), the formed MgCaSi phases are thermostable under the extrusion temperature (350 °C). These precipitates can facilitate nucleation and recrystallization, thus contributing to texture weakening. Apart from the PSN effect, Ca solid solution in Mg matrix may also play a role in the texture weakening [318]. Mg_2Ca and $Ca_2Mg_6Zn_3$ phases dissolve into the matrix after solution annealing and extrusion (**Fig. 5-37b**). Ca (197.4 pm) has a bigger atomic radius than Mg (159.9 pm) [288] and the dissolved Ca can decrease the stacking fault energy [316] and axial ratio (c/a) [314], which will contribute to the activation of non-basal slip and then weaken the texture characteristics.

Except Mg-Zn-Ca, the textures of the as-extruded Mg-0.5Zn(-0.2X) alloys exhibit typical fibre textures (**Fig. 5-35**), namely, the c-axis of most grains is perpendicular to the extrusion direction while few is perpendicular to the transverse direction. The texture intensity is also a little weakened with the addition of Sr, but the influence is not as strong as that from Ca. PSN effect is also applicable in Mg-Zn-Sr as Si-Sr containing precipitates are stable at the extrusion temperature (**Fig. 6-2c**). However, the solubility of Sr is much lower than that of Ca (**Table 6-1**) and thus only limited amount of Sr can dissolve into the Mg matrix. In this way, the texture intensity of Mg-Zn-Sr is higher than that of Mg-Zn-Ca. One may argue why the texture intensity of Mg-Zn-Cu is strengthened rather than weakened, although the precipitates are also stable (**Fig. 6-2e**). This might be due to the coarser DRXed grains in Mg-Zn-Cu compared to the other systems. The grains with a predominant orientation of fiber texture are grown in the extruded bar [246], causing a stronger texture intensity. As for Mg-Zn, Mg-Zn-Ag and Mg-Zn-In systems, the Fe-Si particles are too small and too scarce for PSN. It is well recognized that only the coarse particles with sizes greater than 1 μm or clusters of small particles can contribute to the nucleation of recrystallized grains [318].

Intermetallics

Zn containing intermetallics are generally dissolved into the matrix after solution annealing and extrusion for all Mg-Zn(-X) alloys (**Fig. 5-37**), which are in accordance with literature [123, 130]. MgZn phase from as-cast Mg-Zn and Mg-Zn-In, Zn_5Ag phase from as-cast Mg-

Zn-Ag and Zn segregations are not identified in the as-extruded counterparts. Instead, only Mg_2Si and Fe-Si particles are observed in these systems. Some Fe-Si particles are found to distribute on the Mg_2Si particles which significantly deteriorate the corrosion resistances of these alloys. The mechanism of Fe precipitation is already discussed in section 6.2.2 and 6.2.3.

Mg_2Ca, $Ca_2Mg_6Zn_3$ and MgCaSi are the main precipitates in as-cast Mg-Zn-Ca (**Fig. 5-24**). However, MgCaSi is the only intermetallics in the solution annealed sample (**Fig. 5-25**) and as-extruded sample (**Fig. 5-37b**), which is consistent with the phase diagram (**Fig. 6-2b**) and the strong bonding of Ca-Si (**Fig. 6-11a**). MgCaSi is a thermodynamically and mechanically stable phase [319]. Fe precipitation takes place in the MgCaSi phase (spot 2, **Fig. 5-37b**) due to the low ΔH of Si-Fe (**Fig. 6-11a**).

MgSrSi and $SiSr_2$ phases with certain Zn dissolution exist in the as-cast Mg-Zn-Sr sample (**Fig. 5-3c**). Zn dissolves into the matrix after solution annealing and extrusion while Si and Sr still remain (**Fig. 5-37c**). In contrast, some Mg/Zn/Sr containing phases were reported in the solution annealed Mg-Zn-Sr alloys in literature due to the synergistic effects of processing parameters [320], Zn concentration [321] and Zn/Sr atomic ratio [322]. The amounts of $SiSr_2$ phases are reduced significantly with some remaining $SiSr_2$ (spot 1, **Fig. 5-37c**) distribute on the MgSrSi phase (spot 2). MgSrSi is still one of the main precipitates after annealing and extrusion, revealing its high thermostability. In addition, the Si/Sr atomic ratio in spot 3 is near 2, indicating it is a Si_2Sr phase. The ΔH of α-Si_2Sr (-42.7 kJ/mol) and β-Si_2Sr (-40.3 kJ/mol) are lower comparted to that of $SiSr_2$ (-39.7 kJ/mol) [323]. Thus, the $SiSr_2$(Zn) phase in the as-cast state either dissolves into the matrix or transforms into Si_2Sr phase during homogenisation and extrusion. Some Fe containing Si_2Sr or MgSrSi particles are also observed (spot 4) due to the low ΔH of Si-Fe (**Fig. 6-11b**).

Zn from the MgZnCu phase in as-cast Mg-Zn-Cu mostly dissolves into the matrix after solution treatment and extrusion. The main precipitates (spot 1 in **Fig. 5-37f**) have high Cu concentrations, indicating they are Mg_2Cu phase which is corroborated with the phase diagram (**Fig. 6-2e**). Some brighter spots with higher Zn contents (spot 3) exists on Mg_2Cu, revealing MgZnCu phase is not completely dissolved. Certain amounts of Zn (0.4-1 at.%) are also found in the Mg_2Cu particles. The stability of MgZnCu phase (withstands the homogenisation and extrusion processes) is also reported in literature [246, 324]. Some Mg_2Si precipitates (spot 2) form CE-IMP together with Mg_2Cu. Like the cases of Mg-Zn, Mg-Zn-Ag and Mg-Zn-In, Fe-Si particles (spot 4) are found on Mg_2Si due to the low ΔH of Si-Fe (**Fig. 6-11e**). It is noteworthy that the area fractions of the intermetallics are not reduced after annealing and

extrusion (from 0.20% to 0.26%). The annealing temperature is important for the dissolution of the precipitates. Acccroding to the phase diagrams (**Fig. 4-1e**, **Fig. 6-2e**), the precipitates in Mg-Zn-Cu cannot be fully dissolved at 400 °C and liquid phase might form at a higher temperature. However, Yan et al. [264, 325, 326] claimed more Mg_2Cu particles in Mg-Cu systems dissolved at higher annealing temperature (510-540 °C) than at lower one (450 °C) although the former one already exceeded the eutectic temperature (485 °C). Thus, the solution treatment temperature for Mg-Zn-Cu alloy should be high enough or repeated heat treatment should be performed [282] to dissolve the MgZnCu and Mg_2Cu phases. The possible intermetallics formed in the as-extruded Mg-0.5Zn(-0.2X) alloys are summarised in **Table 6-4**. The distribution of Fe impurity is also shown.

Table 6-4 Summary of the possible intermetallics formed in the as-extruded Mg-0.5Zn(-0.2X) alloys

Alloy	Intermetallics	Form of Fe impurity
Mg-0.5Zn	Mg_2Si	Fe-Si
Mg-0.5Zn-0.2Ca	MgCaSi	MgCaSi(Fe)
Mg-0.5Zn-0.2Sr	MgSrSi, Si_2Sr	MgSrSi(Fe), Si_2Sr(Fe)
Mg-0.5Zn-0.2Ag	Mg_2Si	Fe-Si
Mg-0.5Zn-0.2In	Mg_2Si	Fe-Si
Mg-0.5Zn-0.2Cu	Mg_2Cu, Mg_2Si, MgZnCu	Fe-Si

6.3.2 Corrosion performance

The fraction of dynamic recrystallized area (f_{DRX}) of Mg alloys increases with the extrusion speed. The unDRXed (not dynamic recrystallized) region contained coarse grains and large amounts of dislocations [327]. Dislocations are matrix defects which will encourage the corrosion process [153]. To exclude these potential effects, only the fully-recrystallized alloys with similar grain sizes (~30 μm) are selected for comparison. The corrosion performances of these selected as-extruded alloys differ greatly. Few intermetallics exist in as-extruded Mg-Zn, Mg-Zn-Ag and Mg-Zn-In, which theoretically should lead to limited galvanic corrosion. However, due to the presence of Fe-Si precipitates, the corrosion resistances of these alloys are significantly deteriorated after heat treatment and extrusion as discussed in section 6.2.2 and 6.2.3. Furthermore, the relatively small R_f of these samples (**Fig. 5-39**) indicate that the oxide layers are not protective. The refined grains after extrusion are accompanied with higher grain boundary density. The grain boundaries serve as the metallographic defects and are reported to be prone to corrosion. Thus, if no passivity exist, higher grain boundary density will accelerate the corrosion rate [152, 155, 328].

The amounts of precipitates in Mg-Zn-Ca are reduced after solution annealing and extrusion. From the observations in **Fig. 5-31**, MgCaSi/Mg galvanic couple is electrochemically less active than CE-IMP/Mg. Thusly, the diminishment of CE-IMP and Zn segregations lead to a higher corrosion resistance of the as-extruded sample. In addition, the sample undergoes "passivation" somehow with a corrosion rate of 0.06 mm/year after 7 days immersion (**Fig. 5-41**). The grain boundary in this case will facilitate the passivation process and build compact corrosion layers, thereby reduce the corrosion rate [129, 152, 155, 284, 328]. As-extruded Mg-Zn-Ca possesses higher corrosion resistance than other Mg-Zn(-X) alloys. Although Fe precipitation also takes place during heat treatment, the Fe-Si particles are encapsulated by MgCaSi in the as-extruded sample which is less detrimental to the corrosion resistance. Another contribution can be explained in terms of texture weakening. With the exception of Mg-Zn-Ca, the as-extruded alloys exhibit typical fibre textures (**Fig. 5-35**), which are commonly found in the extruded bars [102, 154]. With the addition of Ca, the maximum texture intensity is greatly reduced to 1.97. Similar texture weakening effects after adding Ca are also reported in literature [214, 316, 329]. Lower fibre texture intensity means a higher possibility of (0001) basal plane lying in parallel to the sample surface. The dissolution rate of (0001) plane is much lower than those of the $(10\bar{1}0)$ and $(11\bar{2}0)$ planes due to its higher in-plane atomic density and lower surface energy [330, 331]. Therefore, the weakened fibre texture intensity further contributes to the higher corrosion resistance of Mg-Zn-Ca. Similar beneficial effect of texture weakening on the corrosion performance is also reported elsewhere [332].

The corrosion performance of as-extruded Mg-Zn-Sr is similar to or slightly worse than that of the as-cast state from EIS and hydrogen evolution tests, respectively. The different results between these two measurements might be partially related to the different exposed sample surfaces. The size and area fraction of the intermetallics are reduced after extrusion, which should lead to a higher corrosion resistance [283, 321, 333]. However, due to the presence of Si impurity and the strong bonding of Sr-Si, MgSrSi and Si_2Sr phases withstand annealing and extrusion and some "stringer-like" particles occur. These primary precipitates accumulate in some areas, leading to more severe galvanic corrosion as the accumulated particles are normally bigger than those in the as-cast state [334]. The precipitates in the as-extruded sample are not as homogeneous as those in the as-cast sample. Other than the stringers, the distances among the precipitates are longer in the as-extruded sample, contributing to a relatively less continuous corrosion layer [335, 336]. Fe is incorporated in the MgSrSi and Si_2Sr paticles, exerting milder effect on the corrosion property. Additionally, the slightly weakened texture of

Mg-Zn after adding Sr (from 4.75 to 3.39, **Fig. 5-35**) also helps to improve the corrosion resistance.

The corrosion resistances of the as-cast and as-extruded Mg-Zn-Cu are comparably low. Most MgZnCu phase changes to Mg_2Cu phase after annealing and extrusion with the overall area fractions of the precipitates similar. Information on the ΔE of Mg_2Cu phase is still missing in literature. Nevertheless, the corrosion potential of Mg_2Cu (-1 V_{SCE}) is much nobler than that of pure Mg (-1.68 V_{SCE}) [337], indicating accelerated galvanic corrosion would take place.

7. Summaries and perspectives

In this work, the effects of micro additions of the selected alloying elements (X: Ca, Sr, Ag, In, Cu) on the microstructure and corrosion behaviour of as-cast Mg-0.5Zn alloy are systematically studied. The corrosion performance is evaluated based on electrochemical methods, H_2 evolution test and corrosion morphology observations and is related to the microstructure, mainly in the aspects of grain size, intermetallics and impurities. Additions of Ca, Sr and Ag (0.2 wt.%) promote grain refinement in Mg-0.5Zn due to the higher Q values of the solutes and precipitates pinning effect. Whereas no grain refinement effect is seen with the additions of In and Cu due to the limited additions of the alloying elements. Scarce amounts of Mg_2Si and MgZn exist in Mg-0.5Zn and Mg-0.5Zn-0.2In, leading to comparatively high corrosion resistance in the early stage of immersion. The lower corrosion resistance of Mg-Zn-In in the later immersion periods can be attributed to the enhanced anodic reaction kinetics which results in sparser and looser corrosion products. Likewise, the addition of Ca also slightly promotes anodic reaction kinetics, leading to looser corrosion products in some areas. However, the refined grain structures and limited precipitates contribute to the highest corrosion resistance of Mg-0.5Zn-0.2Ca. The generally low corrosion rate of Mg-0.5Zn-0.2Sr derives from the refined microstructures and formation of Zn/O layer in the corrosion products. The additions of Ag and Cu induce filiform corrosion and pitting corrosion due to the formation of noble precipitates (Zn_5Ag and MgZnCu). The Ag and Cu additions are suggested to be less than 0.2 wt.% to minimise pitting tendency. With the exception of Mg-Zn-Cu, the micro-alloying systems designed in this study are promising candidates for biomedical applications as their corrosion performances are comparable to the highly-alloyed systems. Although the Si concentrations in Mg-0.5Zn(-0.2X) are 70-160 ppm, Si participates actively in the formation of precipitates in all systems. The Si content should be limited to avoid the formation of relevant intermetallics.

The corrosion behaviour of Mg-0.5Zn-0.2Ca are further studied as it has the highest corrosion resistance among the alloys. The corrosion sequences of the intermetallics are unveiled via quasi-in situ corrosion observation (mechanical exfoliation combined with diluted chromic acid cleaning). Mg_2Ca is the most anodic phase in respect to the matrix and other precipitates. Mg_2Ca will be corroded preferentially within 1 h immersion in 0.9% NaCl solution, whereas $Ca_2Mg_6Zn_3$ and MgCaSi are cathodes which remain even after 24 h. The nature of IMPs and their corresponding corrosion time are not only beneficial for understanding the corrosion

mechanism, but also helpful for the design and development of new lifetime-scalable implant material.

Furthermore, effects of solution treatment on the microstructures and corrosion performances of Mg-0.5Zn-0.2Ca and Mg-0.5Zn are investigated. Mg-Zn-Ca is selected as it has the highest corrosion resistance while Mg-Zn is selected as a reference. After annealing, Mg_2Ca and $Ca_2Mg_6Zn_3$ dissolve into the matrix and MgCaSi(Fe) phase is the only remaining precipitate in Mg-Zn-Ca. The homogeneous microstructure and reduced galvanic couples contribute to a higher corrosion resistance. In contrast, Mg_2Si and Fe-Si are the main precipitates in solution annealed Mg-0.5Zn and its corrosion resistance is significantly deteriorated compared to the as-cast state. In fact, the scale of loss in the corrosion resistance is positively correlated with the treatment duration. Higher concentrations of Fe in the Fe-Si particles are observed in the longer treated Mg-Zn sample due to Fe precipitation during heat treatment. The Si and Fe contents should be restricted to lower levels. In order to supress the precipitation of Fe containing particles, the solidification rate of the casting melts should also be fast. For Mg-X-Y system with some Fe impurities, Fe precipitation might not induce severe corrosion if the enthalpies of formation are in the following order: ΔH (X-Y) < ΔH (Fe-X) < η and considerable Volta potential difference of X/Y precipitate to the matrix exists.

By adjusting the extrusion parameters, Mg-0.5Zn(-0.2X) alloys with similar grain sizes are obtained. The corrosion performances of as-extruded Mg-Zn, Mg-Zn-Ag and Mg-Zn-In deteriorate significantly compared to the as-cast counterpart due to Fe precipitation during solution treatment. The corrosion resistance of as-extruded Mg-0.5Zn is as poor as the solution-treated sample. On the other hand, the as-extruded Mg-0.5Zn sample without prior heat treatment possesses much better corrosion resistance than the annealed and extruded sample. It is suggested that prior to a mechanical deformation, the widely-adopted heat treatment process should be conducted cautiously. Shorter treatment duration or cold working should be considered in the case of micro-alloying Mg systems. The fine grain size, weakened fibre texture and limited intermetallics contribute to the highest corrosion resistance of as-extruded Mg-Zn-Ca. The corrosion rate of Mg-Zn-Sr is slightly increased after annealing and extrusion due to the rearrangement of intermetallics. The corrosion rate of as-extruded Mg-Zn-Cu is as high as that of the as-cast one due to the presence of Mg_2Cu precipitates.

Apart from these, some clarifications are made here and still some points await to be accomplished in the future research:

- ✓ Although each alloy in this work is from the same batch (10 ingots per alloy) and the impurities level are checked by the 1st, 5th and 10th ingots, the corrosion behaviour of as-cast Mg-0.5Zn described in section 5.1.2 is not the same as that described in section 5.2.1. However, this does not change the main conclusions as the same ingot is used in each section. Further studies are still needed to see whether the different corrosion behaviour is related to the inhomogeneity among the samples. Also natural ageing effect in Mg-Zn based systems should also be considered [338].
- ✓ Si and Fe influence the microstructures and they might interact with the alloying elements. It would be important to investigate/simulate the threshold/tolerance limits of Si/Fe impurities in Mg alloys.
- ✓ As the solution annealing deteriorates the corrosion performance of Mg-0.5Zn, appropriate heat treatment conditions (e.g. solution annealing temperature/time) for more micro-alloyed Mg alloys should be studied.
- ✓ Setting up the database regarding the ΔH and ΔE of the precipitates and impurities. Without conducting experiments, maybe it is already predictable to see whether heat treatments have major negative effects on the corrosion performances of the alloys via methods such as artificial neural networks [11].
- ✓ Studying the corrosion behaviour of the alloys in media which are more similar to the physiological environments such as SBFs.

References

[1] G. Song, A. Atrens, Understanding magnesium corrosion-a framework for improved alloy performance, Adv. Eng. Mater., 5 (2003) 837-858.
[2] M.T. Andani, N. Shayesteh Moghaddam, C. Haberland, D. Dean, M.J. Miller, M. Elahinia, Metals for bone implants. Part 1. Powder metallurgy and implant rendering, Acta Biomater., 10 (2014) 4058-4070.
[3] M.P. Staiger, A.M. Pietak, J. Huadmai, G. Dias, Magnesium and its alloys as orthopedic biomaterials: A review, Biomaterials, 27 (2006) 1728-1734.
[4] F. Witte, The history of biodegradable magnesium implants: A review, Acta Biomater., 6 (2010) 1680-1692.
[5] F. Feyerabend, H.-P. Wendel, B. Mihailova, S. Heidrich, N.A. Agha, U. Bismayer, R. Willumeit-Römer, Blood compatibility of magnesium and its alloys, Acta Biomater., 25 (2015) 384-394.
[6] L. Yang, Y. Huang, F. Feyerabend, R. Willumeit, C. Mendis, K.U. Kainer, N. Hort, Microstructure, mechanical and corrosion properties of Mg–Dy–Gd–Zr alloys for medical applications, Acta Biomater., 9 (2013) 8499-8508.
[7] B.P. Zhang, Y. Wang, L. Geng, Research on Mg-Zn-Ca alloy as degradable biomaterial, in: R. Pignatello (Ed.) Biomaterials - physics and chemistry, IntechOpen, 2011.
[8] H.Y. Ang, Y.Y. Huang, S.T. Lim, P. Wong, M. Joner, N. Foin, Mechanical behavior of polymer-based vs . metallic-based bioresorbable stents, Journal of Thoracic Disease, 9 (2017) S923-S934.
[9] J. Vormann, Magnesium: nutrition and metabolism, Molecular Aspects of Medicine, 24 (2003) 27-37.
[10] M. Esmaily, J.E. Svensson, S. Fajardo, N. Birbilis, G.S. Frankel, S. Virtanen, R. Arrabal, S. Thomas, L.G. Johansson, Fundamentals and advances in magnesium alloy corrosion, Prog. Mater. Sci., 89 (2017) 92-193.
[11] R. Willumeit, F. Feyerabend, N. Huber, Magnesium degradation as determined by artificial neural networks, Acta Biomater., 9 (2013) 8722-8729.
[12] H. Hornberger, S. Virtanen, A.R. Boccaccini, Biomedical coatings on magnesium alloys – A review, Acta Biomater., 8 (2012) 2442-2455.
[13] S. Agarwal, J. Curtin, B. Duffy, S. Jaiswal, Biodegradable magnesium alloys for orthopaedic applications: A review on corrosion, biocompatibility and surface modifications, Mater. Sci. Eng. C, 68 (2016) 948-963.
[14] P.C. Ferreira, K.d.A. Piai, A.M.M. Takayanagui, S.I. Segura-Muñoz, Aluminum as a risk factor for Alzheimer's disease, Revista Latino-Americana de Enfermagem, 16 (2008) 151-157.
[15] Y.S. Jeong, W.J. Kim, Enhancement of mechanical properties and corrosion resistance of Mg–Ca alloys through microstructural refinement by indirect extrusion, Corrosion Sci., 82 (2014) 392-403.
[16] Y. Li, C. Wen, D. Mushahary, R. Sravanthi, N. Harishankar, G. Pande, P. Hodgson, Mg–Zr–Sr alloys as biodegradable implant materials, Acta Biomater., 8 (2012) 3177-3188.
[17] D. Tie, F. Feyerabend, W.-D. Mueller, R. Schade, K. Liefeith, K.U. Kainer, R. Willumeit, Antibacterial biodegradable Mg-Ag alloys, European cells & materials, 25 (2013) 284-298.
[18] Y. Li, L. Liu, P. Wan, Z. Zhai, Z. Mao, Z. Ouyang, D. Yu, Q. Sun, L. Tan, L. Ren, Z. Zhu, Y. Hao, X. Qu, K. Yang, K. Dai, Biodegradable Mg-Cu alloy implants with antibacterial activity for the treatment of osteomyelitis: In vitro and in vivo evaluations, Biomaterials, 106 (2016) 250-263.
[19] X. Gu, Y. Zheng, Y. Cheng, S. Zhong, T. Xi, In vitro corrosion and biocompatibility of binary magnesium alloys, Biomaterials, 30 (2009) 484-498.

[20] B. Heublein, R. Rohde, V. Kaese, M. Niemeyer, W. Hartung, A. Haverich, Biocorrosion of magnesium alloys: a new principle in cardiovascular implant technology?, Heart, 89 (2003) 651-656.
[21] A. Chaya, S. Yoshizawa, K. Verdelis, N. Myers, B.J. Costello, D.-T. Chou, S. Pal, S. Maiti, P.N. Kumta, C. Sfeir, In vivo study of magnesium plate and screw degradation and bone fracture healing, Acta Biomater., 18 (2015) 262-269.
[22] H. Hermawan, D. Dubé, D. Mantovani, Developments in metallic biodegradable stents, Acta Biomater., 6 (2010) 1693-1697.
[23] D. Zhao, F. Witte, F. Lu, J. Wang, J. Li, L. Qin, Current status on clinical applications of magnesium-based orthopaedic implants: A review from clinical translational perspective, Biomaterials, 112 (2017) 287-302.
[24] R. Erbel, C. Di Mario, J. Bartunek, J. Bonnier, B. de Bruyne, F.R. Eberli, P. Erne, M. Haude, B. Heublein, M. Horrigan, C. Ilsley, D. Böse, J. Koolen, T.F. Lüscher, N. Weissman, R. Waksman, Temporary scaffolding of coronary arteries with bioabsorbable magnesium stents: a prospective, non-randomised multicentre trial, The Lancet, 369 (2007) 1869-1875.
[25] H.-S. Han, S. Loffredo, I. Jun, J. Edwards, Y.-C. Kim, H.-K. Seok, F. Witte, D. Mantovani, S. Glyn-Jones, Current status and outlook on the clinical translation of biodegradable metals, Materials Today, 23 (2019) 57-71.
[26] J.-M. Seitz, A. Lucas, M. Kirschner, Magnesium-based compression screws: a novelty in the clinical use of implants, JOM, 68 (2016) 1177-1182.
[27] J.-W. Lee, H.-S. Han, K.-J. Han, J. Park, H. Jeon, M.-R. Ok, H.-K. Seok, J.-P. Ahn, K.E. Lee, D.-H. Lee, S.-J. Yang, S.-Y. Cho, P.-R. Cha, H. Kwon, T.-H. Nam, J.H.L. Han, H.-J. Rho, K.-S. Lee, Y.-C. Kim, D. Mantovani, Long-term clinical study and multiscale analysis of in vivo biodegradation mechanism of Mg alloy, Proceedings of the National Academy of Sciences, 113 (2016) 716-721.
[28] D. Zhao, S. Huang, F. Lu, B. Wang, L. Yang, L. Qin, K. Yang, Y. Li, W. Li, W. Wang, S. Tian, X. Zhang, W. Gao, Z. Wang, Y. Zhang, X. Xie, J. Wang, J. Li, Vascularized bone grafting fixed by biodegradable magnesium screw for treating osteonecrosis of the femoral head, Biomaterials, 81 (2016) 84-92.
[29] C. Li, C. Guo, V. Fitzpatrick, A. Ibrahim, M.J. Zwierstra, P. Hanna, A. Lechtig, A. Nazarian, S.J. Lin, D.L. Kaplan, Design of biodegradable, implantable devices towards clinical translation, Nature Reviews Materials, 5 (2020) 61-81.
[30] Y. Ding, C. Wen, P. Hodgson, Y. Li, Effects of alloying elements on the corrosion behavior and biocompatibility of biodegradable magnesium alloys: a review, Journal of Materials Chemistry B, 2 (2014) 1912-1933.
[31] M.H. Song, W.J. Yoo, T.-J. Cho, Y.K. Park, W.-J. Lee, I.H. Choi, In Vivo Response of Growth Plate to Biodegradable Mg-Ca-Zn Alloys Depending on the Surface Modification, International journal of molecular sciences, 20 (2019) 3761.
[32] Y. Yang, C. He, E. Dianyu, W. Yang, F. Qi, D. Xie, L. Shen, S. Peng, C. Shuai, Mg bone implant: Features, developments and perspectives, Mater. Des., 185 (2020) 108259.
[33] G. Song, Control of biodegradation of biocompatable magnesium alloys, Corrosion Sci., 49 (2007) 1696-1701.
[34] E. Willbold, A.A. Kaya, R.A. Kaya, F. Beckmann, F. Witte, Corrosion of magnesium alloy AZ31 screws is dependent on the implantation site, Materials Science and Engineering: B, 176 (2011) 1835-1840.
[35] F. Witte, V. Kaese, H. Haferkamp, E. Switzer, A. Meyer-Lindenberg, C.J. Wirth, H. Windhagen, In vivo corrosion of four magnesium alloys and the associated bone response, Biomaterials, 26 (2005) 3557-3563.

[36] X. Zhang, G. Yuan, L. Mao, J. Niu, W. Ding, Biocorrosion properties of as-extruded Mg–Nd–Zn–Zr alloy compared with commercial AZ31 and WE43 alloys, Materials Letters, 66 (2012) 209-211.
[37] J. Liu, B. Zheng, P. Wang, X. Wang, B. Zhang, Q. Shi, T. Xi, M. Chen, S. Guan, Enhanced in vitro and in vivo performance of Mg–Zn–Y–Nd alloy achieved with APTES pretreatment for drug-eluting vascular stent application, ACS Applied Materials & Interfaces, 8 (2016) 17842-17858.
[38] J. Hofstetter, M. Becker, E. Martinelli, A.M. Weinberg, B. Mingler, H. Kilian, S. Pogatscher, P.J. Uggowitzer, J.F. Löffler, High-strength low-alloy (HSLA) Mg–Zn–Ca alloys with excellent biodegradation performance, JOM, 66 (2014) 566-572.
[39] P. Zartner, R. Cesnjevar, H. Singer, M. Weyand, First successful implantation of a biodegradable metal stent into the left pulmonary artery of a preterm baby, Catheterization and Cardiovascular Interventions, 66 (2005) 590-594.
[40] X. Zhang, Z. Ba, Q. Wang, Y. Wu, Z. Wang, Q. Wang, Uniform corrosion behavior of GZ51K alloy with long period stacking ordered structure for biomedical application, Corrosion Sci., 88 (2014) 1-5.
[41] Standard guide for development and use of a galvanic series for predicting galvanic corrosion performance, in, ASTM International, West Conshohocken, PA, 2014.
[42] G. Song, B. Johannesson, S. Hapugoda, D. StJohn, Galvanic corrosion of magnesium alloy AZ91D in contact with an aluminium alloy, steel and zinc, Corrosion Sci., 46 (2004) 955-977.
[43] A.E. Coy, F. Viejo, P. Skeldon, G.E. Thompson, Susceptibility of rare-earth-magnesium alloys to micro-galvanic corrosion, Corrosion Sci., 52 (2010) 3896-3906.
[44] M.F. Hurley, C.M. Efaw, P.H. Davis, J.R. Croteau, E. Graugnard, N. Birbilis, Volta potentials measured by scanning kelvin probe force microscopy as relevant to corrosion of magnesium alloys, Corrosion, 71 (2015) 160-170.
[45] G.L. Song, A. Atrens, Corrosion mechanisms of magnesium alloys, Adv. Eng. Mater., 1 (1999) 11-33.
[46] S.V. Lamaka, B. Vaghefinazari, D. Mei, R.P. Petrauskas, D. Höche, M.L. Zheludkevich, Comprehensive screening of Mg corrosion inhibitors, Corrosion Sci., 128 (2017) 224-240.
[47] R. Zeng, Z. Yin, X. Chen, D. Xu, Corrosion types of magnesium alloys, in: Tomasz Tański, W. Borek, M. Król (Eds.) Magnesium alloys - selected issue, IntechOpen, 2018.
[48] O. Lunder, T.K. Aune, K. Nisancioglu, Effect of Mn additions on the corrosion behavior of mould-cast magnesium ASTM AZ91, Corrosion, 43 (1987) 291-295.
[49] R. Zeng, W. Qi, H. Cui, F. Zhang, S. Li, E. Han, In vitro corrosion of as-extruded Mg–Ca alloys—The influence of Ca concentration, Corrosion Sci., 96 (2015) 23-31.
[50] D.K. Xu, E.H. Han, Effect of quasicrystalline phase on improving the corrosion resistance of a duplex structured Mg–Li alloy, Scripta Materialia, 71 (2014) 21-24.
[51] Y. Song, D. Shan, R. Chen, E.-H. Han, Corrosion characterization of Mg–8Li alloy in NaCl solution, Corrosion Sci., 51 (2009) 1087-1094.
[52] O. Lunder, J.E. Lein, S.M. Hesjevik, T.K. Aune, K. Nişancioğlu, Corrosion morphologies on magnesium alloy AZ 91, Mater. Corros., 45 (1994) 331-340.
[53] S. Heise, S. Virtanen, A.R. Boccaccini, Tackling Mg alloy corrosion by natural polymer coatings—A review, Journal of Biomedical Materials Research Part A, 104 (2016) 2628-2641.
[54] Y. Song, D. Shan, E.-H. Han, Pitting corrosion of a rare earth Mg alloy GW93, J. Mater. Sci. Technol., 33 (2017) 954-960.
[55] R. Zeng, K.U. Kainer, C. Blawert, W. Dietzel, Corrosion of an extruded magnesium alloy ZK60 component—The role of microstructural features, J. Alloy. Compd., 509 (2011) 4462-4469.

[56] M. Bobby Kannan, W. Dietzel, C. Blawert, A. Atrens, P. Lyon, Stress corrosion cracking of rare-earth containing magnesium alloys ZE41, QE22 and Elektron 21 (EV31A) compared with AZ80, Mater. Sci. Eng. A, 480 (2008) 529-539.
[57] D. Höche, C. Blawert, S.V. Lamaka, N. Scharnagl, C. Mendis, M.L. Zheludkevich, The effect of iron re-deposition on the corrosion of impurity-containing magnesium, Physical Chemistry Chemical Physics, 18 (2016) 1279-1291.
[58] R.W. Revie, Uhlig's Corrosion Handbook 2nd edition, John Wiley & Sons Ltd, New York, USA, 2000.
[59] J.D. Hanawalt, C.E. Nelson, J.A. Peloubet, Corrosion studies of magnesium and its alloys, Trans. AIME, 147 (1942) 273-299.
[60] C. Scharf, A. Ditze, Iron pickup of AZ91 and AS31 magnesium melts in steel crucibles, Adv. Eng. Mater., 9 (2007) 566-571.
[61] M. Liu, P.J. Uggowitzer, A.V. Nagasekhar, P. Schmutz, M. Easton, G.-L. Song, A. Atrens, Calculated phase diagrams and the corrosion of die-cast Mg–Al alloys, Corrosion Sci., 51 (2009) 602-619.
[62] D.S. Gandel, M.A. Easton, M.A. Gibson, N. Birbilis, Influence of Mn and Zr on the corrosion of Al-free Mg alloys: Part 2—impact of Mn and Zr on Mg alloy electrochemistry and corrosion, Corrosion, 69 (2013) 744-751.
[63] C. Blawert, D. Fechner, D. Höche, V. Heitmann, W. Dietzel, K.U. Kainer, P. Živanović, C. Scharf, A. Ditze, J. Gröbner, R. Schmid-Fetzer, Magnesium secondary alloys: Alloy design for magnesium alloys with improved tolerance limits against impurities, Corrosion Sci., 52 (2010) 2452-2468.
[64] Z. Qiao, Z. Shi, N. Hort, N.I. Zainal Abidin, A. Atrens, Corrosion behaviour of a nominally high purity Mg ingot produced by permanent mould direct chill casting, Corrosion Sci., 61 (2012) 185-207.
[65] F. Cao, G.-L. Song, A. Atrens, Corrosion and passivation of magnesium alloys, Corrosion Sci., 111 (2016) 835-845.
[66] A. Prasad, P.J. Uggowitzer, Z. Shi, A. Atrens, Production of high purity magnesium alloys by melt purification with Zr, Adv. Eng. Mater., 14 (2012) 477-490.
[67] F. Pan, X. Chen, T. Yan, T. Liu, J. Mao, W. Luo, Q. Wang, J. Peng, A. Tang, B. Jiang, A novel approach to melt purification of magnesium alloys, J. Magnes. Alloy., 4 (2016) 8-14.
[68] J. Hofstetter, E. Martinelli, A.M. Weinberg, M. Becker, B. Mingler, P.J. Uggowitzer, J.F. Löffler, Assessing the degradation performance of ultrahigh-purity magnesium in vitro and in vivo, Corrosion Sci., 91 (2015) 29-36.
[69] J. Hofstetter, E. Martinelli, S. Pogatscher, P. Schmutz, E. Povoden-Karadeniz, A.M. Weinberg, P.J. Uggowitzer, J.F. Löffler, Influence of trace impurities on the in vitro and in vivo degradation of biodegradable Mg–5Zn–0.3Ca alloys, Acta Biomater., 23 (2015) 347-353.
[70] U.C. Nwaogu, C. Blawert, N. Scharnagl, W. Dietzel, K.U. Kainer, Influence of inorganic acid pickling on the corrosion resistance of magnesium alloy AZ31 sheet, Corrosion Sci., 51 (2009) 2544-2556.
[71] U.C. Nwaogu, C. Blawert, N. Scharnagl, W. Dietzel, K.U. Kainer, Effects of organic acid pickling on the corrosion resistance of magnesium alloy AZ31 sheet, Corrosion Sci., 52 (2010) 2143-2154.
[72] M.M. Gawlik, B. Wiese, A. Welle, J. González, V. Desharnais, J. Harmuth, T. Ebel, R. Willumeit-Römer, Acetic acid etching of Mg-xGd alloys, Metals, 9 (2019) 117.
[73] L. Yang, X. Zhou, S.-M. Liang, R. Schmid-Fetzer, Z. Fan, G. Scamans, J. Robson, G. Thompson, Effect of traces of silicon on the formation of Fe-rich particles in pure magnesium and the corrosion susceptibility of magnesium, J. Alloy. Compd., 619 (2015) 396-400.

[74] G. Han, J.-Y. Lee, Y.-C. Kim, J.H. Park, D.-I. Kim, H.-S. Han, S.-J. Yang, H.-K. Seok, Preferred crystallographic pitting corrosion of pure magnesium in Hanks' solution, Corrosion Sci., 63 (2012) 316-322.
[75] H. Matsubara, Y. Ichige, K. Fujita, H. Nishiyama, K. Hodouchi, Effect of impurity Fe on corrosion behavior of AM50 and AM60 magnesium alloys, Corrosion Sci., 66 (2013) 203-210.
[76] M. Liu, G.-L. Song, Impurity control and corrosion resistance of magnesium–aluminum alloy, Corrosion Sci., 77 (2013) 143-150.
[77] N. Hort, Y. Huang, K.U. Kainer, Intermetallics in magnesium alloys, Adv. Eng. Mater., 8 (2006) 235-240.
[78] A. Atrens, M. Liu, N.I. Zainal Abidin, Corrosion mechanism applicable to biodegradable magnesium implants, Materials Science and Engineering: B, 176 (2011) 1609-1636.
[79] G. Song, A. Atrens, M. Dargusch, Influence of microstructure on the corrosion of diecast AZ91D, Corrosion Sci., 41 (1998) 249-273.
[80] A.D. Südholz, N.T. Kirkland, R.G. Buchheit, N. Birbilis, Electrochemical properties of intermetallic phases and common impurity elements in magnesium alloys, Electrochem. Solid-State Lett, 14 (2011) C5-C7.
[81] H. Du, Z. Wei, X. Liu, E. Zhang, Effects of Zn on the microstructure, mechanical property and bio-corrosion property of Mg–3Ca alloys for biomedical application, Materials Chemistry and Physics, 125 (2011) 568-575.
[82] S. Cai, T. Lei, N. Li, F. Feng, Effects of Zn on microstructure, mechanical properties and corrosion behavior of Mg–Zn alloys, Mater. Sci. Eng. C, 32 (2012) 2570-2577.
[83] L.G. Bland, N. Birbilis, J.R. Scully, Exploring the effects of intermetallic particle size and spacing on the corrosion of Mg-Al alloys using model electrodes, J. Electrochem. Soc., 163 (2016) C895-C906.
[84] M. Esmaily, D.B. Blücher, J.E. Svensson, M. Halvarsson, L.G. Johansson, New insights into the corrosion of magnesium alloys — The role of aluminum, Scripta Materialia, 115 (2016) 91-95.
[85] J. Chen, L. Tan, X. Yu, I.P. Etim, M. Ibrahim, K. Yang, Mechanical properties of magnesium alloys for medical application: A review, Journal of the Mechanical Behavior of Biomedical Materials, 87 (2018) 68-79.
[86] L. Pompa, Z.U. Rahman, E. Munoz, W. Haider, Surface characterization and cytotoxicity response of biodegradable magnesium alloys, Mater. Sci. Eng. C, 49 (2015) 761-768.
[87] C. Miura, Y. Shimizu, Y. Imai, T. Mukai, A. Yamamoto, Y. Sano, N. Ikeo, S. Isozaki, T. Takahashi, M. Oikawa, H. Kumamoto, M. Tachi, In vivo corrosion behaviour of magnesium alloy in association with surrounding tissue response in rats, Biomedical Materials, 11 (2016) 025001.
[88] R. Radha, D. Sreekanth, Insight of magnesium alloys and composites for orthopedic implant applications – a review, J. Magnes. Alloy., 5 (2017) 286-312.
[89] Y. Wan, G. Xiong, H. Luo, F. He, Y. Huang, X. Zhou, Preparation and characterization of a new biomedical magnesium–calcium alloy, Mater. Des., 29 (2008) 2034-2037.
[90] Z. Li, X. Gu, S. Lou, Y. Zheng, The development of binary Mg–Ca alloys for use as biodegradable materials within bone, Biomaterials, 29 (2008) 1329-1344.
[91] P. Makkar, S.K. Sarkar, A.R. Padalhin, B.-G. Moon, Y.S. Lee, B.T. Lee, In vitro and in vivo assessment of biomedical Mg–Ca alloys for bone implant applications, Journal of Applied Biomaterials & Functional Materials, 16 (2018) 126-136.
[92] N. Erdmann, N. Angrisani, J. Reifenrath, A. Lucas, F. Thorey, D. Bormann, A. Meyer-Lindenberg, Biomechanical testing and degradation analysis of MgCa0.8 alloy screws: A comparative in vivo study in rabbits, Acta Biomater., 7 (2011) 1421-1428.
[93] W.-C. Kim, J.-G. Kim, J.-Y. Lee, H.-K. Seok, Influence of Ca on the corrosion properties of magnesium for biomaterials, Materials Letters, 62 (2008) 4146-4148.

[94] R. Zeng, W. Qi, F. Zhang, H. Cui, Y. Zheng, In vitro corrosion of Mg–1.21Li–1.12Ca–1Y alloy, Progress in Natural Science: Materials International, 24 (2014) 492-499.
[95] M. Mohedano, B.J.C. Luthringer, B. Mingo, F. Feyerabend, R. Arrabal, P.J. Sanchez-Egido, C. Blawert, R. Willumeit-Römer, M.L. Zheludkevich, E. Matykina, Bioactive plasma electrolytic oxidation coatings on Mg-Ca alloy to control degradation behaviour, Surf. Coat. Technol., 315 (2017) 454-467.
[96] N.T. Kirkland, N. Birbilis, J. Walker, T. Woodfield, G.J. Dias, M.P. Staiger, In-vitro dissolution of magnesium–calcium binary alloys: Clarifying the unique role of calcium additions in bioresorbable magnesium implant alloys, Journal of Biomedical Materials Research Part B: Applied Biomaterials, 95B (2010) 91-100.
[97] J.W. Seong, W.J. Kim, Development of biodegradable Mg–Ca alloy sheets with enhanced strength and corrosion properties through the refinement and uniform dispersion of the Mg2Ca phase by high-ratio differential speed rolling, Acta Biomater., 11 (2015) 531-542.
[98] E. Zhang, L. Yang, Microstructure, mechanical properties and bio-corrosion properties of Mg–Zn–Mn–Ca alloy for biomedical application, Mater. Sci. Eng. A, 497 (2008) 111-118.
[99] M. Deng, D. Höche, S.V. Lamaka, L. Wang, M.L. Zheludkevich, Revealing the impact of second phase morphology on discharge properties of binary Mg-Ca anodes for primary Mg-air batteries, Corrosion Sci., 153 (2019) 225-235.
[100] N. Hort, Y. Huang, D. Fechner, M. Störmer, C. Blawert, F. Witte, C. Vogt, H. Drücker, R. Willumeit, K.U. Kainer, F. Feyerabend, Magnesium alloys as implant materials – Principles of property design for Mg–RE alloys, Acta Biomater., 6 (2010) 1714-1725.
[101] M.d.R. Silva Campos, C. Blawert, C.L. Mendis, M. Mohedano, T. Zimmermann, D. Proefrock, M.L. Zheludkevich, K.U. Kainer, Effect of Heat Treatment on the Corrosion Behavior of Mg-10Gd Alloy in 0.5% NaCl Solution, Frontiers in Materials, 7 (2020).
[102] J. Harmuth, B. Wiese, J. Bohlen, T. Ebel, R. Willumeit-Römer, Wide range mechanical customization of Mg-Gd alloys with low degradation rates by extrusion, Frontiers in Materials, 6 (2019) 1-13.
[103] R. Arrabal, E. Matykina, A. Pardo, M.C. Merino, K. Paucar, M. Mohedano, P. Casajús, Corrosion behaviour of AZ91D and AM50 magnesium alloys with Nd and Gd additions in humid environments, Corrosion Sci., 55 (2012) 351-362.
[104] M. Liu, P. Schmutz, P.J. Uggowitzer, G. Song, A. Atrens, The influence of yttrium (Y) on the corrosion of Mg–Y binary alloys, Corrosion Sci., 52 (2010) 3687-3701.
[105] X. Zhang, K. Zhang, X. Deng, L. Hongwei, L. Yongjun, M. Minglong, L. Ning, Y. Wang, Corrosion behavior of Mg–Y alloy in NaCl aqueous solution, Progress in Natural Science: Materials International, 22 (2012) 169-174.
[106] A. Drynda, N. Deinet, N. Braun, M. Peuster, Rare earth metals used in biodegradable magnesium-based stents do not interfere with proliferation of smooth muscle cells but do induce the upregulation of inflammatory genes, Journal of Biomedical Materials Research Part A, 91A (2009) 360-369.
[107] F. Feyerabend, J. Fischer, J. Holtz, F. Witte, R. Willumeit, H. Drücker, C. Vogt, N. Hort, Evaluation of short-term effects of rare earth and other elements used in magnesium alloys on primary cells and cell lines, Acta Biomater., 6 (2010) 1834-1842.
[108] E. Zhang, L. Yang, J. Xu, H. Chen, Microstructure, mechanical properties and bio-corrosion properties of Mg–Si(–Ca, Zn) alloy for biomedical application, Acta Biomater., 6 (2010) 1756-1762.
[109] R.L. Liu, Z.R. Zeng, J.R. Scully, G. Williams, N. Birbilis, Simultaneously improving the corrosion resistance and strength of magnesium via low levels of Zn and Ge additions, Corrosion Sci., 140 (2018) 18-29.
[110] D.-s. Yin, E.-l. Zhang, S.-y. Zeng, Effect of Zn on mechanical property and corrosion property of extruded Mg-Zn-Mn alloy, Trans. Nonferrous Met. Soc. China, 18 (2008) 763-768.

[111] S. Zhang, J. Li, Y. Song, C. Zhao, X. Zhang, C. Xie, Y. Zhang, H. Tao, Y. He, Y. Jiang, Y. Bian, In vitro degradation, hemolysis and MC3T3-E1 cell adhesion of biodegradable Mg–Zn alloy, Mater. Sci. Eng. C, 29 (2009) 1907-1912.
[112] S. Zhang, X. Zhang, C. Zhao, J. Li, Y. Song, C. Xie, H. Tao, Y. Zhang, Y. He, Y. Jiang, Y. Bian, Research on an Mg–Zn alloy as a degradable biomaterial, Acta Biomater., 6 (2010) 626-640.
[113] J. Kubásek, D. Vojtěch, Structural characteristics and corrosion behavior of biodegradable Mg–Zn, Mg–Zn–Gd alloys, Journal of Materials Science: Materials in Medicine, 24 (2013) 1615-1626.
[114] H.R. Bakhsheshi-Rad, E. Hamzah, A. Fereidouni-Lotfabadi, M. Daroonparvar, M.A.M. Yajid, M. Mezbahul-Islam, M. Kasiri-Asgarani, M. Medraj, Microstructure and bio-corrosion behavior of Mg–Zn and Mg–Zn–Ca alloys for biomedical applications, Mater. Corros., 65 (2014) 1178-1187.
[115] S.M.G. Shahri, M.H. Idris, H. Jafari, B. Gholampour, M. Assadian, Effect of solution treatment on corrosion characteristics of biodegradable Mg–6Zn alloy, Trans. Nonferrous Met. Soc. China, 25 (2015) 1490-1499.
[116] Y. Song, E.-H. Han, D. Shan, C.D. Yim, B.S. You, The role of second phases in the corrosion behavior of Mg–5Zn alloy, Corrosion Sci., 60 (2012) 238-245.
[117] Y. Song, E.-H. Han, K. Dong, D. Shan, C.D. Yim, B.S. You, Study of the corrosion product films formed on the surface of Mg–xZn alloys in NaCl solution, Corrosion Sci., 88 (2014) 215-225.
[118] S. Zhang, Y. Zheng, L. Zhang, Y. Bi, J. Li, J. Liu, Y. Yu, H. Guo, Y. Li, In vitro and in vivo corrosion and histocompatibility of pure Mg and a Mg-6Zn alloy as urinary implants in rat model, Mater. Sci. Eng. C, 68 (2016) 414-422.
[119] E. Koç, M.B. Kannan, M. Ünal, E. Candan, Influence of zinc on the microstructure, mechanical properties and in vitro corrosion behavior of magnesium–zinc binary alloys, J. Alloy. Compd., 648 (2015) 291-296.
[120] H.R. Bakhsheshi-Rad, E. Hamzah, M. Medraj, M.H. Idris, A.F. Lotfabadi, M. Daroonparvar, M.A.M. Yajid, Effect of heat treatment on the microstructure and corrosion behaviour of Mg–Zn alloys, Mater. Corros., 65 (2014) 999-1006.
[121] Y. Song, E.-H. Han, D. Shan, C.D. Yim, B.S. You, The effect of Zn concentration on the corrosion behavior of Mg–xZn alloys, Corrosion Sci., 65 (2012) 322-330.
[122] Q. Peng, X. Li, N. Ma, R. Liu, H. Zhang, Effects of backward extrusion on mechanical and degradation properties of Mg–Zn biomaterial, Journal of the Mechanical Behavior of Biomedical Materials, 10 (2012) 128-137.
[123] X.-b. Liu, D.-y. Shan, Y.-w. Song, E.-h. Han, Effects of heat treatment on corrosion behaviors of Mg-3Zn magnesium alloy, Trans. Nonferrous Met. Soc. China, 20 (2010) 1345-1350.
[124] S. Zhang, J. Li, Y. Song, C. Zhao, C. Xie, X. Zhang, Influence of heat treatments on in vitro degradation behavior of Mg-6Zn alloy studied by electrochemical measurements, Adv. Eng. Mater., 12 (2010) B170-B174.
[125] Y. Yan, H. Cao, Y. Kang, K. Yu, T. Xiao, J. Luo, Y. Deng, H. Fang, H. Xiong, Y. Dai, Effects of Zn concentration and heat treatment on the microstructure, mechanical properties and corrosion behavior of as-extruded Mg-Zn alloys produced by powder metallurgy, J. Alloy. Compd., 693 (2017) 1277-1289.
[126] F. Cao, Z. Shi, G.-L. Song, M. Liu, A. Atrens, Corrosion behaviour in salt spray and in 3.5% NaCl solution saturated with Mg(OH)2 of as-cast and solution heat-treated binary Mg–X alloys: X=Mn, Sn, Ca, Zn, Al, Zr, Si, Sr, Corrosion Sci., 76 (2013) 60-97.

[127] K. Yan, H. Liu, N. Feng, J. Bai, H. Cheng, J. Liu, F. Huang, Preparation of a single-phase Mg–6Zn alloy via ECAP-stimulated solution treatment, J. Magnes. Alloy., 7 (2019) 305-314.
[128] E. Koç, F.M.S. Makhlof, Corrosion behavior of heat treated Mg-xZn (x=0.5 – 3) alloys, Research on Engineering Structures & Materials, 5 (2018) 107-114.
[129] P.-R. Cha, H.-S. Han, G.-F. Yang, Y.-C. Kim, K.-H. Hong, S.-C. Lee, J.-Y. Jung, J.-P. Ahn, Y.-Y. Kim, S.-Y. Cho, J.Y. Byun, K.-S. Lee, S.-J. Yang, H.-K. Seok, Biodegradability engineering of biodegradable Mg alloys: Tailoring the electrochemical properties and microstructure of constituent phases, Scientific Reports, 3 (2013) 2367.
[130] P. Doležal, J. Zapletal, S. Fintová, Z. Trojanová, M. Greger, P. Roupcová, T. Podrábský, Influence of processing techniques on microstructure and mechanical properties of a biodegradable Mg-3Zn-2Ca alloy, Materials, 9 (2016) 880.
[131] Y. Sun, B. Zhang, Y. Wang, L. Geng, X. Jiao, Preparation and characterization of a new biomedical Mg–Zn–Ca alloy, Mater. Des., 34 (2012) 58-64.
[132] Y. Jang, Z. Tan, C. Jurey, Z. Xu, Z. Dong, B. Collins, Y. Yun, J. Sankar, Understanding corrosion behavior of Mg–Zn–Ca alloys from subcutaneous mouse model: Effect of Zn element concentration and plasma electrolytic oxidation, Mater. Sci. Eng. C, 48 (2015) 28-40.
[133] H.R. Bakhsheshi-Rad, M.R. Abdul-Kadir, M.H. Idris, S. Farahany, Relationship between the corrosion behavior and the thermal characteristics and microstructure of Mg–0.5Ca–xZn alloys, Corrosion Sci., 64 (2012) 184-197.
[134] D. Zander, N.A. Zumdick, Influence of Ca and Zn on the microstructure and corrosion of biodegradable Mg–Ca–Zn alloys, Corrosion Sci., 93 (2015) 222-233.
[135] S. Gaur, R.K. Singh Raman, A.S. Khanna, In vitro investigation of biodegradable polymeric coating for corrosion resistance of Mg-6Zn-Ca alloy in simulated body fluid, Mater. Sci. Eng. C, 42 (2014) 91-101.
[136] L.B. Tong, Q.X. Zhang, Z.H. Jiang, J.B. Zhang, J. Meng, L.R. Cheng, H.J. Zhang, Microstructures, mechanical properties and corrosion resistances of extruded Mg–Zn–Ca–xCe/La alloys, Journal of the Mechanical Behavior of Biomedical Materials, 62 (2016) 57-70.
[137] V. Roche, G.Y. Koga, T.B. Matias, C.S. Kiminami, C. Bolfarini, W.J. Botta, R.P. Nogueira, A.M. Jorge Junior, Degradation of biodegradable implants: The influence of microstructure and composition of Mg-Zn-Ca alloys, J. Alloy. Compd., 774 (2019) 168-181.
[138] M. Cheng, J. Chen, H. Yan, B. Su, Z. Yu, W. Xia, X. Gong, Effects of minor Sr addition on microstructure, mechanical and bio-corrosion properties of the Mg-5Zn based alloy system, J. Alloy. Compd., 691 (2017) 95-102.
[139] A.F. Cipriano, T. Zhao, I. Johnson, R.-G. Guan, S. Garcia, H. Liu, In vitro degradation of four magnesium–zinc–strontium alloys and their cytocompatibility with human embryonic stem cells, Journal of Materials Science: Materials in Medicine, 24 (2013) 989-1003.
[140] G. Ben-Hamu, D. Eliezer, A. Kaya, Y.G. Na, K.S. Shin, Microstructure and corrosion behavior of Mg–Zn–Ag alloys, Mater. Sci. Eng. A, 435-436 (2006) 579-587.
[141] H. Zhao, L.-Q. Wang, Y.-P. Ren, B. Yang, S. Li, G.-W. Qin, Microstructure, mechanical properties and corrosion behavior of extruded Mg–Zn–Ag alloys with single-phase structure, Acta Metallurgica Sinica (English Letters), 31 (2018) 575-583.
[142] Z. Yu, D. Ju, H. Zhao, X. Hu, Effects of Zn-In-Sn elements on the electric properties of magnesium alloy anode materials, Journal of Environmental Sciences, 23 (2011) S95-S99.
[143] M. Lotfpour, M. Emamy, C. Dehghanian, K. Tavighi, Influence of Cu addition on the structure, mechanical and corrosion properties of cast Mg-2%Zn alloy, Journal of Materials Engineering and Performance, 26 (2017) 2136-2150.
[144] D. Persaud-Sharma, N. Budiansky, In vitro degradation behavior of ternary Mg-Zn-Se and Mg-Zn-Cu alloys as biomaterials, Journal of biomimetics, biomaterials, and tissue engineering, 18 (2013).

[145] H. Koh, T. Sakai, H. Utsunomiya, S. Minamiguchi, Deformation and texture evolution during high-speed rolling of AZ31 magnesium sheets, Materials Transactions, 48 (2007) 2023-2027.
[146] M. Alvarez-Lopez, M.D. Pereda, J.A. del Valle, M. Fernandez-Lorenzo, M.C. Garcia-Alonso, O.A. Ruano, M.L. Escudero, Corrosion behaviour of AZ31 magnesium alloy with different grain sizes in simulated biological fluids, Acta Biomater., 6 (2010) 1763-1771.
[147] F. Cao, Z. Shi, G.-L. Song, M. Liu, M.S. Dargusch, A. Atrens, Influence of hot rolling on the corrosion behavior of several Mg–X alloys, Corrosion Sci., 90 (2015) 176-191.
[148] K. Chen, J. Dai, X. Zhang, Improvement of corrosion resistance of magnesium alloys for biomedical applications, Corrosion Reviews, 33 (2015) 101-117.
[149] S. Liang, D. Guan, X. Tan, The relation between heat treatment and corrosion behavior of Mg–Gd–Y–Zr alloy, Mater. Des., 32 (2011) 1194-1199.
[150] N.N. Aung, W. Zhou, Effect of grain size and twins on corrosion behaviour of AZ31B magnesium alloy, Corrosion Sci., 52 (2010) 589-594.
[151] K.D. Ralston, N. Birbilis, Effect of grain size on corrosion: a review, Corrosion, 66 (2010) 075005-075001-075005-075013.
[152] K.D. Ralston, N. Birbilis, C.H.J. Davies, Revealing the relationship between grain size and corrosion rate of metals, Scripta Materialia, 63 (2010) 1201-1204.
[153] M. Ben-Haroush, G. Ben-Hamu, D. Eliezer, L. Wagner, The relation between microstructure and corrosion behavior of AZ80 Mg alloy following different extrusion temperatures, Corrosion Sci., 50 (2008) 1766-1778.
[154] B.J. Wang, D.K. Xu, J.H. Dong, W. Ke, Effect of the crystallographic orientation and twinning on the corrosion resistance of an as-extruded Mg–3Al–1Zn (wt.%) bar, Scripta Materialia, 88 (2014) 5-8.
[155] T. Zhang, Y. Shao, G. Meng, Z. Cui, F. Wang, Corrosion of hot extrusion AZ91 magnesium alloy: I-relation between the microstructure and corrosion behavior, Corrosion Sci., 53 (2011) 1960-1968.
[156] M. Liu, D. Qiu, M.-C. Zhao, G. Song, A. Atrens, The effect of crystallographic orientation on the active corrosion of pure magnesium, Scripta Materialia, 58 (2008) 421-424.
[157] G.-L. Song, Z. Xu, Effect of microstructure evolution on corrosion of different crystal surfaces of AZ31 Mg alloy in a chloride containing solution, Corrosion Sci., 54 (2012) 97-105.
[158] R. Xin, B. Li, L. Li, Q. Liu, Influence of texture on corrosion rate of AZ31 Mg alloy in 3.5wt.% NaCl, Mater. Des., 32 (2011) 4548-4552.
[159] B. Wang, D. Xu, J. Dong, W. Ke, Effect of Texture on Biodegradable Behavior of an As-Extruded Mg–3%Al–1%Zn Alloy in Phosphate Buffer Saline Medium, J. Mater. Sci. Technol., 32 (2016) 646-652.
[160] I Marco, A Myrissa, E Martinelli, F Feyerabend, R Willumeit-Römer, AM Weinberg, O.V.d. Biest, In vivo and in vitro degradation comparison of pure Mg, Mg-10Gd and Mg-2Ag: a short term study, European Cells and Materials 33 (2017) 90-104.
[161] F. Witte, J. Fischer, J. Nellesen, H.-A. Crostack, V. Kaese, A. Pisch, F. Beckmann, H. Windhagen, In vitro and in vivo corrosion measurements of magnesium alloys, Biomaterials, 27 (2006) 1013-1018.
[162] G. Song, A. Atrens, D.S. John, X. Wu, J. Nairn, The anodic dissolution of magnesium in chloride and sulphate solutions, Corrosion Sci., 39 (1997) 1981-2004.
[163] P. Jiang, C. Blawert, N. Scharnagl, M.L. Zheludkevich, Influence of water purity on the corrosion behavior of Mg0.5ZnX (X=Ca, Ge) alloys, Corrosion Sci., 153 (2019) 62-73.
[164] L. Mao, G. Yuan, S. Wang, J. Niu, G. Wu, W. Ding, A novel biodegradable Mg–Nd–Zn–Zr alloy with uniform corrosion behavior in artificial plasma, Materials Letters, 88 (2012) 1-4.

[165] P.-W. Chu, E.A. Marquis, Linking the microstructure of a heat-treated WE43 Mg alloy with its corrosion behavior, Corrosion Sci., 101 (2015) 94-104.
[166] R. Ambat, N.N. Aung, W. Zhou, Studies on the influence of chloride ion and pH on the corrosion and electrochemical behaviour of AZ91D magnesium alloy, Journal of Applied Electrochemistry, 30 (2000) 865-874.
[167] J. Lévesque, H. Hermawan, D. Dubé, D. Mantovani, Design of a pseudo-physiological test bench specific to the development of biodegradable metallic biomaterials, Acta Biomater., 4 (2008) 284-295.
[168] G. Baril, N. Pébère, The corrosion of pure magnesium in aerated and deaerated sodium sulphate solutions, Corrosion Sci., 43 (2001) 471-484.
[169] N.I. Zainal Abidin, D. Martin, A. Atrens, Corrosion of high purity Mg, AZ91, ZE41 and Mg2Zn0.2Mn in Hank's solution at room temperature, Corrosion Sci., 53 (2011) 862-872.
[170] Y. Xin, T. Hu, P.K. Chu, In vitro studies of biomedical magnesium alloys in a simulated physiological environment: A review, Acta Biomater., 7 (2011) 1452-1459.
[171] T. Kokubo, H. Takadama, How useful is SBF in predicting in vivo bone bioactivity?, Biomaterials, 27 (2006) 2907-2915.
[172] M. Bohner, J. Lemaitre, Can bioactivity be tested in vitro with SBF solution?, Biomaterials, 30 (2009) 2175-2179.
[173] Y. Chen, G. Wan, J. Wang, S. Zhao, Y. Zhao, N. Huang, Covalent immobilization of phytic acid on Mg by alkaline pre-treatment: Corrosion and degradation behavior in phosphate buffered saline, Corrosion Sci., 75 (2013) 280-286.
[174] R.-C. Zeng, L. Sun, Y.-F. Zheng, H.-Z. Cui, E.-H. Han, Corrosion and characterisation of dual phase Mg–Li–Ca alloy in Hank's solution: The influence of microstructural features, Corrosion Sci., 79 (2014) 69-82.
[175] Y. Xin, T. Hu, P.K. Chu, Influence of test solutions on in vitro studies of biomedical magnesium alloys, J. Electrochem. Soc., 157 (2010) C238-C243.
[176] D. Mei, S.V. Lamaka, J. Gonzalez, F. Feyerabend, R. Willumeit-Römer, M.L. Zheludkevich, The role of individual components of simulated body fluid on the corrosion behavior of commercially pure Mg, Corrosion Sci., 147 (2019) 81-93.
[177] F. Rosalbino, S. De Negri, A. Saccone, E. Angelini, S. Delfino, Bio-corrosion characterization of Mg–Zn–X (X = Ca, Mn, Si) alloys for biomedical applications, Journal of Materials Science: Materials in Medicine, 21 (2010) 1091-1098.
[178] M.E. Iskandar, A. Aslani, H. Liu, The effects of nanostructured hydroxyapatite coating on the biodegradation and cytocompatibility of magnesium implants, Journal of Biomedical Materials Research Part A, 101A (2013) 2340-2354.
[179] R.-Q. Hou, N. Scharnagl, R. Willumeit-Römer, F. Feyerabend, Different effects of single protein vs. protein mixtures on magnesium degradation under cell culture conditions, Acta Biomater., 98 (2019) 256-268.
[180] M.P. Brady, G. Rother, L.M. Anovitz, K.C. Littrell, K.A. Unocic, H.H. Elsentriecy, G.L. Song, J.K. Thomson, N.C. Gallego, B. Davis, Film Breakdown and Nano-Porous Mg(OH)2Formation from Corrosion of Magnesium Alloys in Salt Solutions, J. Electrochem. Soc., 162 (2015) C140-C149.
[181] Y. Jin, C. Blawert, F. Feyerabend, J. Bohlen, M. Silva Campos, S. Gavras, B. Wiese, D. Mei, M. Deng, H. Yang, R. Willumeit-Römer, Time-sequential corrosion behaviour observation of micro-alloyed Mg-0.5Zn-0.2Ca alloy via a quasi-in situ approach, Corrosion Sci., 158 (2019) 108096.
[182] N.C. Verissimo, E.S. Freitas, N. Cheung, A. Garcia, W.R. Osório, The effects of Zn segregation and microstructure length scale on the corrosion behavior of a directionally solidified Mg-25 wt.%Zn alloy, J. Alloy. Compd., 723 (2017) 649-660.

[183] A.A. Nayeb-Hashemi, J.B. Clark, Phase diagram of binary magnesium alloys, Materials Park, Ohio, USA, 1988.
[184] J. Kim, Y. Kawamura, Effect of the extrusion conditions on the microstructure and mechanical properties of indirect extruded Mg-Zn-Y alloy with LPSO phase, in: N. Hort, S.N. Mathaudhu, N.R. Neelameggham, M. Alderman (Eds.) Magnesium Technology 2013, Springer International Publishing, Cham, 2016, pp. 217-219.
[185] Z. Zeng, N. Stanford, C.H.J. Davies, J.-F. Nie, N. Birbilis, Magnesium extrusion alloys: a review of developments and prospects, Int. Mater. Rev., 64 (2019) 27-62.
[186] Spark OES, in, SPECTRO Analytical Instruments GmbH, https://www.spectro.com/products/optical-emission-spectroscopy/arc-spark-stationary-oes-working-principle.
[187] E.P.S. Nidadavolu, D. Krüger, B. Zeller-Plumhoff, D. Tolnai, B. Wiese, F. Feyerabend, T. Ebel, R. Willumeit-Römer, Pore characterization of PM Mg–0.6Ca alloy and its degradation behavior under physiological conditions, J. Magnes. Alloy., (2020).
[188] ICP-OES, in, https://www.thermofisher.com/de/de/home/industrial/spectroscopy-elemental-isotope-analysis/spectroscopy-elemental-isotope-analysis-learning-center/trace-elemental-analysis-tea-information/icp-oes-information/icp-oes-system-technologies.html.
[189] V. Kree, J. Bohlen, D. Letzig, K.U. Kainer, Metallographische Gefügeuntersuchungen von Magnesiumlegierungen, Praktische Metallographie, 41 (2004) 233-246.
[190] H. Abrams, Grain size measurement by the intercept method, Metallography, 4 (1971) 59-78.
[191] J. Schindelin, I. Arganda-Carreras, E. Frise, V. Kaynig, M. Longair, T. Pietzsch, S. Preibisch, C. Rueden, S. Saalfeld, B. Schmid, J.-Y. Tinevez, D.J. White, V. Hartenstein, K. Eliceiri, P. Tomancak, A. Cardona, Fiji: an open-source platform for biological-image analysis, Nature Methods, 9 (2012) 676-682.
[192] Pandat software package for calculating phase diagrams and thermodynamic properties of multi-component alloys, in, CompuTherm LLC, 2017.
[193] S.L. Chen, S. Daniel, F. Zhang, Y.A. Chang, X.Y. Yan, F.Y. Xie, R. Schmid-Fetzer, W.A. Oates, The PANDAT software package and its applications, Calphad, 26 (2002) 175-188.
[194] X. Ding, P. Fan, Q. Han, Models of activity and activity interaction parameter in ternary metallic melt, Acta Metall. Sin., 30 (1994) 49-60.
[195] A.R. Miedema, P.F. de Châtel, F.R. de Boer, Cohesion in alloys — fundamentals of a semi-empirical model, Physica B+C, 100 (1980) 1-28.
[196] H. Yang, Y. Huang, D. Tolnai, K.U. Kainer, H. Dieringa, Influences of Al and high shearing dispersion technique on the microstructure and creep resistance of Mg-2.85Nd-0.92Gd-0.41Zr-0.29Zn alloy, Mater. Sci. Eng. A, 764 (2019) 138215.
[197] Y. Yuan, Y. Huang, Q. Wei, Effects of Zr Addition on Thermodynamic and Kinetic Properties of Liquid Mg-6Zn-xZr Alloys, Metals, 9 (2019) 607.
[198] Texture analysis, in, https://www.malvernpanalytical.com.cn/products/measurement-type/texture-analysis.
[199] F. Bachmann, R. Hielscher, H. Schaeben, Texture analysis with MTEX – free and open source software toolbox, Solid State Phenomena, 160 (2010) 63-68.
[200] N.T. Kirkland, N. Birbilis, M.P. Staiger, Assessing the corrosion of biodegradable magnesium implants: A critical review of current methodologies and their limitations, Acta Biomater., 8 (2012) 925-936.
[201] Table of specific heat capacities, in, https://en.wikipedia.org/wiki/Table_of_specific_heat_capacities.
[202] Z. Shi, A. Atrens, An innovative specimen configuration for the study of Mg corrosion, Corrosion Sci., 53 (2011) 226-246.

[203] F. Cao, Z. Shi, J. Hofstetter, P.J. Uggowitzer, G. Song, M. Liu, A. Atrens, Corrosion of ultra-high-purity Mg in 3.5% NaCl solution saturated with Mg(OH)2, Corrosion Sci., 75 (2013) 78-99.
[204] Y. Zhang, J. Li, H. Lai, Y. Xu, Effect of homogenization on microstructure characteristics, corrosion and biocompatibility of Mg-Zn-Mn-xCa alloys, Materials, 11 (2018) 227.
[205] K.S. Novoselov, A.K. Geim, S.V. Morozov, D. Jiang, Y. Zhang, S.V. Dubonos, I.V. Grigorieva, A.A. Firsov, Electric field effect in atomically thin carbon films, Science, 306 (2004) 666-669.
[206] Y. Jin, C. Blawert, H. Yang, B. Wiese, F. Feyerabend, J. Bohlen, D. Mei, M. Deng, M. Silva Campos, N. Scharnagl, K. Strecker, J. Bode, C. Vogt, R. Willumeit-Römer, Microstructure-corrosion behaviour relationship of micro-alloyed Mg-0.5Zn alloy with the addition of Ca, Sr, Ag, In and Cu, Mater. Des., 195 (2020) 108980.
[207] JEOL EDS Periodic Table, in, https://www.jeolusa.com/RESOURCES/JEOL-Posters-Calendars/lc/47251/lcv/s/jeol-eds-periodic-table.
[208] M. Deng, D. Höche, S.V. Lamaka, D. Snihirova, M.L. Zheludkevich, Mg-Ca binary alloys as anodes for primary Mg-air batteries, Journal of Power Sources, 396 (2018) 109-118.
[209] C. Zhao, F. Pan, S. Zhao, H. Pan, K. Song, A. Tang, Preparation and characterization of as-extruded Mg–Sn alloys for orthopedic applications, Mater. Des., 70 (2015) 60-67.
[210] Y. Carbonneau, A. Couture, A. Van Neste, R. Tremblay, On the observation of a new ternary MgSiCa phase in Mg-Si alloys, Metallurgical and Materials Transactions A, 29 (1998) 1759-1763.
[211] J.-W. Chang, P.-H. Fu, X.-W. Guo, L.-M. Peng, W.-J. Ding, The effects of heat treatment and zirconium on the corrosion behaviour of Mg–3Nd–0.2Zn–0.4Zr (wt.%) alloy, Corrosion Sci., 49 (2007) 2612-2627.
[212] P. Jiang, C. Blawert, R. Hou, N. Scharnagl, J. Bohlen, M.L. Zheludkevich, Microstructural influence on corrosion behavior of MgZnGe alloy in NaCl solution, J. Alloy. Compd., 783 (2019) 179-192.
[213] C. op't Hoog, N. Birbilis, Y. Estrin, Corrosion of pure Mg as a function of grain size and processing route, Adv. Eng. Mater., 10 (2008) 579-582.
[214] J. Bohlen, S. Meyer, B. Wiese, B.J.C. Luthringer-Feyerabend, R. Willumeit-Römer, D. Letzig, Alloying and processing effects on the microstructure, mechanical properties, and degradation behavior of extruded magnesium alloys containing calcium, cerium, or silver, Materials, 13 (2020) 391.
[215] Y.C. Lee, A.K. Dahle, D.H. StJohn, The role of solute in grain refinement of magnesium, Metallurgical and Materials Transactions A, 31 (2000) 2895-2906.
[216] Y. Ali, D. Qiu, B. Jiang, F. Pan, M.-X. Zhang, Current research progress in grain refinement of cast magnesium alloys: A review article, J. Alloy. Compd., 619 (2015) 639-651.
[217] R. Schmid-Fetzer, A. Kozlov, Thermodynamic aspects of grain growth restriction in multicomponent alloy solidification, Acta Mater., 59 (2011) 6133-6144.
[218] Y. Ali, Novel approaches to grain refinement of magnesium alloys, in, The University of Queensland, Australia, 2017.
[219] P. Cao, M. Qian, D.H. StJohn, Native grain refinement of magnesium alloys, Scripta Materialia, 53 (2005) 841-844.
[220] C. Blawert, E. Morales, W. Dietzel, K.U. Kainer, C. Scharf, A. Ditze, Influence of the copper content on microstructure and corrosion resistance of AZ91 based secondary magnesium alloys, in, SAE International, 2006.
[221] J.J. Kim, D.H. Kim, K.S. Shin, N.J. Kim, Modification of Mg2Si morphology in squeeze cast Mg-Al-Zn-Si alloys by Ca or P addition, Scripta Materialia, 41 (1999) 333-340.

[222] A. Srinivasan, U.T.S. Pillai, J. Swaminathan, S.K. Das, B.C. Pai, Observations of microstructural refinement in Mg–Al–Si alloys containing strontium, Journal of Materials Science, 41 (2006) 6087-6089.
[223] M. Mezbahul-Islam, A.O. Mostafa, M. Medraj, Essential magnesium alloys binary phase diagrams and their thermochemical data, Journal of Materials, 2014 (2014) 1-33.
[224] Y. Guangyin, L. Manping, D. Wenjiang, A. Inoue, Microstructure and mechanical properties of Mg–Zn–Si-based alloys, Materials Science and Engineering: A, 357 (2003) 314-320.
[225] E.M. Godlewska, K. Mars, P. Drozdz, A. Tchorz, M. Ksiazek, Reaction and diffusion phenomena in Ag-doped Mg2Si, J. Alloy. Compd., 657 (2016) 755-764.
[226] M. Mezbahul-Islam, A.O. Mostafa, M. Medraj, Essential Magnesium Alloys Binary Phase Diagrams and Their Thermochemical Data, Journal of Materials, 2014 (2014) 704283.
[227] J. Kubásek, D. Vojtěch, J. Lipov, T. Ruml, Structure, mechanical properties, corrosion behavior and cytotoxicity of biodegradable Mg–X (X=Sn, Ga, In) alloys, Mater. Sci. Eng. C, 33 (2013) 2421-2432.
[228] P. Villars, K. Cenzual, Pearson's Crystal Data-Crystal Structure Database for Inorganic Compounds (on DVD), in, ASM International, Materials Park, Ohio, USA, Release 2017/18.
[229] A. Kozlov, M. Ohno, R. Arroyave, Z.K. Liu, R. Schmid-Fetzer, Phase equilibria, thermodynamics and solidification microstructures of Mg–Sn–Ca alloys, Part 1: Experimental investigation and thermodynamic modeling of the ternary Mg–Sn–Ca system, Intermetallics, 16 (2008) 299-315.
[230] P.M. Jardim, G. Solórzano, J.B.V. Sande, Precipitate crystal structure determination in melt spun Mg-1.5wt%Ca-6wt%Zn alloy, Microscopy and Microanalysis, 8 (2002) 487-496.
[231] K. Kubok, L. Litynska-Dobrzynska, J. Wojewoda-Budka, A. Góral, A. Debski, Investigation of structures in as-cast alloys from the Mg-Zn-Ca system, Archives of Metallurgy and Materials, 58 (2013) 329-333.
[232] G. Levi, S. Avraham, A. Zilberov, M. Bamberger, Solidification, solution treatment and age hardening of a Mg–1.6wt.% Ca–3.2wt.% Zn alloy, Acta Mater., 54 (2006) 523-530.
[233] K. Oh-ishi, R. Watanabe, C.L. Mendis, K. Hono, Age-hardening response of Mg–0.3at.%Ca alloys with different Zn contents, Mater. Sci. Eng. A, 526 (2009) 177-184.
[234] S.W. Xu, K. Oh-ishi, H. Sunohara, S. Kamado, Extruded Mg–Zn–Ca–Mn alloys with low yield anisotropy, Mater. Sci. Eng. A, 558 (2012) 356-365.
[235] M. Bornapour, M. Celikin, M. Cerruti, M. Pekguleryuz, Magnesium implant alloy with low levels of strontium and calcium: The third element effect and phase selection improve bio-corrosion resistance and mechanical performance, Materials Science and Engineering: C, 35 (2014) 267-282.
[236] Y. Ai, C.P. Luo, J. Liu, Twinning of CaMgSi phase in a cast Mg–1.0Ca–0.5Si–0.3Zr alloy, Acta Mater., 55 (2007) 531-538.
[237] T. Hosono, M. Kuramoto, Y. Matsuzawa, Y. Momose, Y. Maeda, T. Matsuyama, H. Tatsuoka, Y. Fukuda, S. Hashimoto, H. Kuwabara, Formation of CaMgSi at Ca2Si/Mg2Si interface, Applied Surface Science, 216 (2003) 620-624.
[238] V. Lisitsyn, G. Ben-Hamu, D. Eliezer, K.S. Shin, Some particularities of the corrosion behaviour of Mg–Zn–Mn–Si–Ca alloys in alkaline chloride solutions, Corrosion Sci., 52 (2010) 2280-2290.
[239] A. Gil-Santos, G. Szakacs, N. Moelans, N. Hort, O. Van der Biest, Microstructure and mechanical characterization of cast Mg-Ca-Si alloys, J. Alloy. Compd., 694 (2017) 767-776.
[240] A.F. Cipriano, A. Sallee, R.-G. Guan, Z.-Y. Zhao, M. Tayoba, J. Sanchez, H. Liu, Investigation of magnesium–zinc–calcium alloys and bone marrow derived mesenchymal stem cell response in direct culture, Acta Biomater., 12 (2015) 298-321.

[241] A. Gil-Santos, I. Marco, N. Moelans, N. Hort, O. Van der Biest, Microstructure and degradation performance of biodegradable Mg-Si-Sr implant alloys, Mater. Sci. Eng. C, 71 (2017) 25-34.
[242] L.-q. Wang, G.-w. Qin, S.-n. Sun, Y.-p. Ren, S. Li, Effect of solid solution treatment on in vitro degradation rate of as-extruded Mg-Zn-Ag alloys, Trans. Nonferrous Met. Soc. China, 27 (2017) 2607-2612.
[243] H.-T. Son, D.-G. Kim, J.S. Park, Effects of Ag addition on microstructures and mechanical properties of Mg–6Zn–2Sn–0.4Mn-based alloy system, Materials Letters, 65 (2011) 3150-3153.
[244] Z.-W. Lu, D.-W. Zhou, J.-P. Bai, C. Lu, Z.-G. Zhong, G.-Q. Li, Theoretical investigation on structural and thermodynamic properties of the intermetallic compound in Mg–Zn–Ag alloy under high pressure and high temperature, J. Alloy. Compd., 550 (2013) 406-411.
[245] C.R.A. Wright, C. Thompson, II. On certain ternary alloys. Part III. Alloys of bismuth, zinc, and tin, and of bismuth, zinc, and silver, Proceedings of the Royal Society of London, 49 (1891) 156-173.
[246] Y. Wang, J. Peng, L. Zhong, On the microstructure and mechanical property of as-extruded Mg–Sn–Zn alloy with Cu addition, J. Alloy. Compd., 744 (2018) 234-242.
[247] M.L. He, T.J. Luo, Y.T. Liu, T. Lin, J.X. Zhou, Y.S. Yang, Effects of Cu and Ce co-addition on the microstructure and mechanical properties of Mg-6Zn-0.5Zr alloy, J. Alloy. Compd., 767 (2018) 1216-1224.
[248] M. Halmann, A. Frei, A. Steinfeld, Magnesium production by the Pidgeon process involving dolomite calcination and MgO silicothermic reduction: thermodynamic and environmental analyses, Industrial & Engineering Chemistry Research, 47 (2008) 2146-2154.
[249] J. Wang, Y. Wu, H. Li, Y. Liu, X. Bai, W. Chau, Y. Zheng, L. Qin, Magnesium alloy based interference screw developed for ACL reconstruction attenuates peri-tunnel bone loss in rabbits, Biomaterials, 157 (2018) 86-97.
[250] H. Pan, K. Pang, F. Cui, F. Ge, C. Man, X. Wang, Z. Cui, Effect of alloyed Sr on the microstructure and corrosion behavior of biodegradable Mg-Zn-Mn alloy in Hanks' solution, Corrosion Sci., 157 (2019) 420-437.
[251] A. Bahmani, S. Arthanari, K.S. Shin, Corrosion behavior of Mg–Mn–Ca alloy: Influences of Al, Sn and Zn, J. Magnes. Alloy., 7 (2019) 38-46.
[252] B. Mingo, R. Arrabal, M. Mohedano, C.L. Mendis, R. del Olmo, E. Matykina, N. Hort, M.C. Merino, A. Pardo, Corrosion of Mg-9Al alloy with minor alloying elements (Mn, Nd, Ca, Y and Sn), Mater. Des., 130 (2017) 48-58.
[253] G. Ben-Hamu, D. Eliezer, K.S. Shin, The role of Si and Ca on new wrought Mg–Zn–Mn based alloy, Mater. Sci. Eng. A, 447 (2007) 35-43.
[254] C. Cai, R. Song, L. Wang, J. Li, Effect of anodic T phase on surface micro-galvanic corrosion of biodegradable Mg-Zn-Zr-Nd alloys, Applied Surface Science, 462 (2018) 243-254.
[255] H. Wang, Y. Song, J. Yu, D. Shan, H. Han, Characterization of filiform corrosion of Mg–3Zn Mg alloy, J. Electrochem. Soc., 164 (2017) C574-C580.
[256] R.H. Buzolin, M. Mohedano, C.L. Mendis, B. Mingo, D. Tolnai, C. Blawert, K.U. Kainer, H. Pinto, N. Hort, Corrosion behaviour of as-cast ZK40 with CaO and Y additions, Trans. Nonferrous Met. Soc. China, 28 (2018) 427-439.
[257] L. Moreno, M. Mohedano, B. Mingo, R. Arrabal, E. Matykina, Degradation behaviour of Mg0.6Ca and Mg0.6Ca2Ag alloys with bioactive plasma electrolytic oxidation coatings, Coatings, 9 (2019) 383.
[258] S.-M. Baek, B. Kim, S. Park, Influence of intermetallic particles on the corrosion properties of extruded ZK60 Mg alloy containing Cu, Metals, 8 (2018) 323.

[259] J.A. Dean, Lange's Handbook of Chemistry, 15th ed., McGraw-Hill Publishers, New York, 1999.
[260] Pilling-Bedworth ratio, in, https://en.wikipedia.org/wiki/Pilling%E2%80%93Bedworth_ratio.
[261] S. Leleu, B. Rives, J. Bour, N. Causse, N. Pébère, On the stability of the oxides film formed on a magnesium alloy containing rare-earth elements, Electrochim. Acta, 290 (2018) 586-594.
[262] X. Xia, C.H.J. Davies, J.F. Nie, N. Birbilis, Influence of composition and processing on the corrosion of magnesium alloys containing binary and ternary additions of zinc and strontium, Corrosion, 71 (2015) 38-49.
[263] Standard electrode potential, in, https://en.wikipedia.org/wiki/Standard_electrode_potential_(data_page)#cite_note-van92-3.
[264] X. Yan, P. Wan, L. Tan, M. Zhao, L. Qin, K. Yang, Corrosion and biological performance of biodegradable magnesium alloys mediated by low copper addition and processing, Mater. Sci. Eng. C, 93 (2018) 565-581.
[265] C. Liu, X. Fu, H. Pan, P. Wan, L. Wang, L. Tan, K. Wang, Y. Zhao, K. Yang, P.K. Chu, Biodegradable Mg-Cu alloys with enhanced osteogenesis, angiogenesis, and long-lasting antibacterial effects, Scientific Reports, 6 (2016) 27374.
[266] R. Xu, M.-C. Zhao, Y.-C. Zhao, L. Liu, C. Liu, C. Gao, C. Shuai, A. Atrens, Improved biodegradation resistance by grain refinement of novel antibacterial ZK30-Cu alloys produced via selective laser melting, Materials Letters, 237 (2019) 253-257.
[267] C. Shuai, L. Liu, M. Zhao, P. Feng, Y. Yang, W. Guo, C. Gao, F. Yuan, Microstructure, biodegradation, antibacterial and mechanical properties of ZK60-Cu alloys prepared by selective laser melting technique, J. Mater. Sci. Technol., 34 (2018) 1944-1952.
[268] H. Jia, X. Feng, Y. Yang, Microstructure and corrosion resistance of directionally solidified Mg-2wt.% Zn alloy, Corrosion Sci., 120 (2017) 75-81.
[269] H. Jia, X. Feng, Y. Yang, Effect of crystal orientation on corrosion behavior of directionally solidified Mg-4 wt% Zn alloy, J. Mater. Sci. Technol., 34 (2018) 1229-1235.
[270] J.N. Li, P. Cao, X.N. Zhang, S.X. Zhang, Y.H. He, In vitro degradation and cell attachment of a PLGA coated biodegradable Mg–6Zn based alloy, Journal of Materials Science, 45 (2010) 6038-6045.
[271] A. Vinogradov, E. Vasilev, V.I. Kopylov, M. Linderov, A. Brilevesky, D. Merson, High performance fine-grained biodegradable Mg-Zn-Ca alloys processed by severe plastic deformation, Metals, 9 (2019) 186.
[272] D. Fang, X. Li, H. Li, Q. Peng, Electrochemical corrosion behavior of backward extruded Mg-Zn-Ca alloys in different media, Int. J. Electrochem. Sci, 8 (2013) 2551-2565.
[273] J. Chen, W. Peng, L. Zhu, L. Tan, I.P. Etim, X. Wang, K. Yang, Effect of copper content on the corrosion behaviors and antibacterial properties of binary Mg–Cu alloys, Materials Technology, 33 (2018) 145-152.
[274] D. Mei, S.V. Lamaka, C. Feiler, M.L. Zheludkevich, The effect of small-molecule bio-relevant organic components at low concentration on the corrosion of commercially pure Mg and Mg-0.8Ca alloy: An overall perspective, Corrosion Sci., 153 (2019) 258-271.
[275] Z. Rong-chang, C. Jun, W. Dietzel, N. Hort, K. Kainer, Electrochemical behavior of magnesium alloys in simulated body fluids, Trans Nonferrous Met Soc China, 17 (2007) 166-170.
[276] Y. Xin, K. Huo, H. Tao, G. Tang, P.K. Chu, Influence of aggressive ions on the degradation behavior of biomedical magnesium alloy in physiological environment, Acta Biomater., 4 (2008) 2008-2015.

[277] J. Chen, Q. Xu, Y. Song, D. Shan, E.-H. Han, Characterization of the in situ growth manasseite/carbonates composite conversion film on Mg2Zn alloy, Materials Letters, 150 (2015) 65-68.
[278] Y. Chen, J. Yan, Z. Wang, S. Yu, X. Wang, Z. Yuan, X. Zhang, C. Zhao, Q. Zheng, In vitro and in vivo corrosion measurements of Mg–6Zn alloys in the bile, Mater. Sci. Eng. C, 42 (2014) 116-123.
[279] N.D. Nam, Role of zinc in enhancing the corrosion resistance of Mg-5Ca alloys, J. Electrochem. Soc., 163 (2016) C76-C84.
[280] Z. Xu, C. Smith, S. Chen, J. Sankar, Development and microstructural characterizations of Mg–Zn–Ca alloys for biomedical applications, Materials Science and Engineering: B, 176 (2011) 1660-1665.
[281] A. Zakiyuddin, K. Lee, Effect of a small addition of zinc and manganese to Mg–Ca based alloys on degradation behavior in physiological media, J. Alloy. Compd., 629 (2015) 274-283.
[282] C. Dehghanian, M. Lotfpour, M. Emamy, The microstructure, and mechanical and corrosion properties of as-cast and as-extruded Mg-2%Zn-x%Cu alloys after solution and aging heat treatments, Journal of Materials Engineering and Performance, 28 (2019) 2305-2315.
[283] J. Dong, L. Tan, J. Yang, Y. Wang, J. Chen, W. Wang, D. Zhao, K. Yang, In vitro and in vivo studies on degradation and bone response of Mg-Sr alloy for treatment of bone defect, Materials Technology, 33 (2018) 387-397.
[284] D. Liu, C. Guo, L. Chai, V.R. Sherman, X. Qin, Y. Ding, M.A. Meyers, Mechanical properties and corrosion resistance of hot extruded Mg–2.5Zn–1Ca alloy, Materials Science and Engineering: B, 195 (2015) 50-58.
[285] Y. Lu, A.R. Bradshaw, Y.L. Chiu, I.P. Jones, Effects of secondary phase and grain size on the corrosion of biodegradable Mg–Zn–Ca alloys, Mater. Sci. Eng. C, 48 (2015) 480-486.
[286] J. Hofstetter, S. Rüedi, I. Baumgartner, H. Kilian, B. Mingler, E. Povoden-Karadeniz, S. Pogatscher, P.J. Uggowitzer, J.F. Löffler, Processing and microstructure–property relations of high-strength low-alloy (HSLA) Mg–Zn–Ca alloys, Acta Mater., 98 (2015) 423-432.
[287] M. Yang, T. Guo, H. Li, Effects of Gd addition on as-cast microstructure, tensile and creep properties of Mg–3.8 Zn–2.2Ca (wt%) magnesium alloy, Mater. Sci. Eng. A, 587 (2013) 132-142.
[288] K. Gusieva, C.H.J. Davies, J.R. Scully, N. Birbilis, Corrosion of magnesium alloys: the role of alloying, Int. Mater. Rev., 60 (2015) 169-194.
[289] Lever rule, in, https://en.wikipedia.org/wiki/Lever_rule#cite_ref-smith_1-0.
[290] A. Atrens, G.-L. Song, M. Liu, Z. Shi, F. Cao, M.S. Dargusch, Review of recent developments in the field of magnesium corrosion, Adv. Eng. Mater., 17 (2015) 400-453.
[291] S. Pawar, X. Zhou, G.E. Thompson, G. Scamans, Z. Fan, The role of intermetallics on the corrosion initiation of twin roll cast AZ31 Mg alloy, J. Electrochem. Soc., 162 (2015) C442-C448.
[292] S.K. Woo, B.-C. Suh, N.R. Kim, H.S. Kim, C.D. Yim, The corrosion behavior of high purity Mg according to process history, in, Springer International Publishing, Cham, 2020, pp. 225-230.
[293] F. Andreatta, I. Apachitei, A.A. Kodentsov, J. Dzwonczyk, J. Duszczyk, Volta potential of second phase particles in extruded AZ80 magnesium alloy, Electrochim. Acta, 51 (2006) 3551-3557.
[294] Y. Song, D. Shan, R. Chen, E.-H. Han, Effect of second phases on the corrosion behaviour of wrought Mg–Zn–Y–Zr alloy, Corrosion Sci., 52 (2010) 1830-1837.
[295] J.-Y. Lee, G. Han, Y.-C. Kim, J.-Y. Byun, J.-i. Jang, H.-K. Seok, S.-J. Yang, Effects of impurities on the biodegradation behavior of pure magnesium, Met. Mater.-Int., 15 (2009) 955-961.

[296] L. Yang, G. Liu, L. Ma, E. Zhang, X. Zhou, G. Thompson, Effect of iron content on the corrosion of pure magnesium: Critical factor for iron tolerance limit, Corrosion Sci., 139 (2018) 421-429.
[297] R.S. Lillard, Relationships between metal-metal bonding and crystallographic pitting in hcp metals, Electrochem. Solid-State Lett, 6 (2003) B29-B31.
[298] Z. Shi, G. Song, A. Atrens, Corrosion resistance of anodised single-phase Mg alloys, Surf. Coat. Technol., 201 (2006) 492-503.
[299] D. Orlov, K.D. Ralston, N. Birbilis, Y. Estrin, Enhanced corrosion resistance of Mg alloy ZK60 after processing by integrated extrusion and equal channel angular pressing, Acta Mater., 59 (2011) 6176-6186.
[300] G. Katarivas Levy, E. Aghion, Influence of heat treatment temperature on corrosion characteristics of biodegradable EW10X04 Mg alloy coated with Nd, Adv. Eng. Mater., 18 (2016) 269-276.
[301] L. Zhang, X. Dong, J. Li, W. Wang, A. Wang, Z. Fan, Microstructure and mechanical properties of as-cast and heat treated Mg-15Gd-3Y alloy, J. Rare Earths, 29 (2011) 77-82.
[302] J. Zhang, C. Fang, F. Yuan, C. Liu, A comparative analysis of constitutive behaviors of Mg–Mn alloys with different heat-treatment parameters, Mater. Des., 32 (2011) 1783-1789.
[303] Z. Yu, A. Tang, J. He, Z. Gao, J. She, J. Liu, F. Pan, Effect of high content of manganese on microstructure, texture and mechanical properties of magnesium alloy, Materials Characterization, 136 (2018) 310-317.
[304] S. Pawar, X. Zhou, T. Hashimoto, G.E. Thompson, G. Scamans, Z. Fan, Investigation of the microstructure and the influence of iron on the formation of Al8Mn5 particles in twin roll cast AZ31 magnesium alloy, J. Alloy. Compd., 628 (2015) 195-198.
[305] M. Jönsson, D. Thierry, N. LeBozec, The influence of microstructure on the corrosion behaviour of AZ91D studied by scanning Kelvin probe force microscopy and scanning Kelvin probe, Corrosion Sci., 48 (2006) 1193-1208.
[306] A.F.M. Arif, A. K. Sheikh, S.Z. Qamar, M.K. Raza, K.M. Al-Fuhaid, Product defects in aluminum extrusion and their impact on operational cost in: The 6th Saudi Engineering Conference, KFUPM, Dhahran, 2002, pp. 137-154.
[307] W.-j. Li, K.-k. Deng, X. Zhang, K.-b. Nie, F.-j. Xu, Effect of ultra-slow extrusion speed on the microstructure and mechanical properties of Mg-4Zn-0.5Ca alloy, Mater. Sci. Eng. A, 677 (2016) 367-375.
[308] S.S. Park, B.S. You, D.J. Yoon, Effect of the extrusion conditions on the texture and mechanical properties of indirect-extruded Mg–3Al–1Zn alloy, Journal of Materials Processing Technology, 209 (2009) 5940-5943.
[309] H. Watanabe, H. Tsutsui, T. Mukai, K. Ishikawa, Y. Okanda, M. Kohzu, K. Higashi, Grain size control of commercial wrought Mg-Al-Zn alloys utilizing dynamic recrystallization, Materials Transactions, 42 (2001) 1200-1205.
[310] X. Liu, Z. Zhang, W. Hu, Q. Le, L. Bao, J. Cui, Effects of extrusion speed on the microstructure and mechanical properties of Mg9Gd3Y1.5Zn0.8Zr alloy, J. Mater. Sci. Technol., 32 (2016) 313-319.
[311] H. Yu, S. Hyuk Park, B. Sun You, Y. Min Kim, H. Shun Yu, S. Soo Park, Effects of extrusion speed on the microstructure and mechanical properties of ZK60 alloys with and without 1wt% cerium addition, Mater. Sci. Eng. A, 583 (2013) 25-35.
[312] Q. Kang, H. Jiang, Y. Zhang, Z. Xu, H. Li, Z. Xia, Effect of various Ca content on microstructure and fracture toughness of extruded Mg-2Zn alloys, J. Alloy. Compd., 742 (2018) 1019-1030.
[313] Z.R. Zeng, Y.M. Zhu, S.W. Xu, M.Z. Bian, C.H.J. Davies, N. Birbilis, J.F. Nie, Texture evolution during static recrystallization of cold-rolled magnesium alloys, Acta Mater., 105 (2016) 479-494.

[314] H. Ding, X. Shi, Y. Wang, G. Cheng, S. Kamado, Texture weakening and ductility variation of Mg–2Zn alloy with CA or RE addition, Mater. Sci. Eng. A, 645 (2015) 196-204.
[315] J. Bohlen, S. Yi, D. Letzig, K.U. Kainer, Effect of rare earth elements on the microstructure and texture development in magnesium–manganese alloys during extrusion, Mater. Sci. Eng. A, 527 (2010) 7092-7098.
[316] B. Zhang, Y. Wang, L. Geng, C. Lu, Effects of calcium on texture and mechanical properties of hot-extruded Mg–Zn–Ca alloys, Mater. Sci. Eng. A, 539 (2012) 56-60.
[317] M. Masoumi, M. Pekguleryuz, The influence of Sr on the microstructure and texture evolution of rolled Mg–1%Zn alloy, Mater. Sci. Eng. A, 529 (2011) 207-214.
[318] H.-l. Ding, P. Zhang, G.-p. Cheng, S. Kamado, Effect of calcium addition on microstructure and texture modification of Mg rolled sheets, Trans. Nonferrous Met. Soc. China, 25 (2015) 2875-2883.
[319] R. Wu, Y.-P. Wang, Y. Yang, D.-M. Luo, H. Meng, L. Ma, B.-Y. Tang, Structural and mechanical properties of ternary MgCaSi phase: A study by density functional theory, Journal of Chemical Research, 44 (2020) 50-59.
[320] H.S. Brar, J. Wong, M.V. Manuel, Investigation of the mechanical and degradation properties of Mg–Sr and Mg–Zn–Sr alloys for use as potential biodegradable implant materials, Journal of the Mechanical Behavior of Biomedical Materials, 7 (2012) 87-95.
[321] H. Li, Q. Peng, X. Li, K. Li, Z. Han, D. Fang, Microstructures, mechanical and cytocompatibility of degradable Mg–Zn based orthopedic biomaterials, Mater. Des., 58 (2014) 43-51.
[322] A.F. Cipriano, A. Sallee, M. Tayoba, M.C. Cortez Alcaraz, A. Lin, R.-G. Guan, Z.-Y. Zhao, H. Liu, Cytocompatibility and early inflammatory response of human endothelial cells in direct culture with Mg-Zn-Sr alloys, Acta Biomater., 48 (2017) 499-520.
[323] G. Balducci, S. Brutti, A. Ciccioli, G. Gigli, G. Trionfetti, A. Palenzona, M. Pani, Vapor pressures and thermodynamic properties of strontium silicides, Intermetallics, 14 (2006) 578-583.
[324] X. Chen, L. Liu, F. Pan, J. Mao, X. Xu, T. Yan, Microstructure, electromagnetic shielding effectiveness and mechanical properties of Mg–Zn–Cu–Zr alloys, Materials Science and Engineering: B, 197 (2015) 67-74.
[325] X. Yan, P. Wan, L. Tan, M. Zhao, C. Shuai, K. Yang, Influence of hybrid extrusion and solution treatment on the microstructure and degradation behavior of Mg-0.1Cu alloy, Materials Science and Engineering: B, 229 (2018) 105-117.
[326] X. Yan, M.-C. Zhao, Y. Yang, L. Tan, Y.-C. Zhao, D.-F. Yin, K. Yang, A. Atrens, Improvement of biodegradable and antibacterial properties by solution treatment and micro-arc oxidation (MAO) of a magnesium alloy with a trace of copper, Corrosion Sci., 156 (2019) 125-138.
[327] Y.Z. Du, X.G. Qiao, M.Y. Zheng, K. Wu, S.W. Xu, The microstructure, texture and mechanical properties of extruded Mg–5.3Zn–0.2Ca–0.5Ce (wt%) alloy, Mater. Sci. Eng. A, 620 (2015) 164-171.
[328] Y. Luo, Y. Deng, L. Guan, L. Ye, X. Guo, The microstructure and corrosion resistance of as-extruded Mg-6Gd-2Y- (0–1.5) Nd-0.2Zr alloys, Mater. Des., 186 (2020) 108289.
[329] N. Stanford, The effect of calcium on the texture, microstructure and mechanical properties of extruded Mg–Mn–Ca alloys, Mater. Sci. Eng. A, 528 (2010) 314-322.
[330] K. Hagihara, M. Okubo, M. Yamasaki, T. Nakano, Crystal-orientation-dependent corrosion behaviour of single crystals of a pure Mg and Mg-Al and Mg-Cu solid solutions, Corrosion Sci., 109 (2016) 68-85.
[331] G.-L. Song, R. Mishra, Z. Xu, Crystallographic orientation and electrochemical activity of AZ31 Mg alloy, Electrochemistry Communications, 12 (2010) 1009-1012.

[332] Z.-R. Xie, C. Zhang, H.-C. Pan, Y.-X. Wang, Y.-P. Ren, G.-W. Qin, Microstructures and bio-corrosion resistances of as-extruded Mg–Ca alloys with ultra-fine grain size, Rare Metals, (2017).
[333] J. Han, P. Wan, Y. Ge, X. Fan, L. Tan, J. Li, K. Yang, Tailoring the degradation and biological response of a magnesium–strontium alloy for potential bone substitute application, Mater. Sci. Eng. C, 58 (2016) 799-811.
[334] E. Mostaed, M. Hashempour, A. Fabrizi, D. Dellasega, M. Bestetti, F. Bonollo, M. Vedani, Microstructure, texture evolution, mechanical properties and corrosion behavior of ECAP processed ZK60 magnesium alloy for biodegradable applications, Journal of the Mechanical Behavior of Biomedical Materials, 37 (2014) 307-322.
[335] R. Ambat, N.N. Aung, W. Zhou, Evaluation of microstructural effects on corrosion behaviour of AZ91D magnesium alloy, Corrosion Sci., 42 (2000) 1433-1455.
[336] J.-H. Dong, L.-L. Tan, Y.-B. Ren, K. Yang, Effect of microstructure on corrosion behavior of Mg–Sr alloy in Hank's solution, Acta Metallurgica Sinica (English Letters), 32 (2019) 305-320.
[337] S. Oh, H. Kim, M. Kim, K. Eom, J. Kyung, D. Kim, E. Cho, H. Kwon, Design of Mg-Cu alloys for fast hydrogen production, and its application to PEM fuel cell, J. Alloy. Compd., 741 (2018) 590-596.
[338] J. Buha, T. Ohkubo, Natural aging in Mg-Zn(-Cu) alloys, Metallurgical and Materials Transactions A, 39 (2008) 2259-2273.
[339] R. Zeng, X. Li, S. Li, F. Zhang, E. Han, In vitro degradation of pure Mg in response to glucose, Scientific Reports, 5 (2015) 13026.

Appendix

1. Supporting information

After twin-jet electropolishing with 1.5% perchloric acid solution, a TEM image of the intermetallic particle in Mg-0.5Zn-0.2Ca is shown in Fig. S1. According to EDS, the X1 particle contains Mg, Zn and Ca which should be $Ca_2Mg_6Zn_3$ phase. Position X2 is etched away during the electropolishing. The shape of the particle is similar to the one in **Fig. 5-23c**, indicating the Mg_2Ca phase might be corroded during the electropolishing or in contact with the perchloric acid.

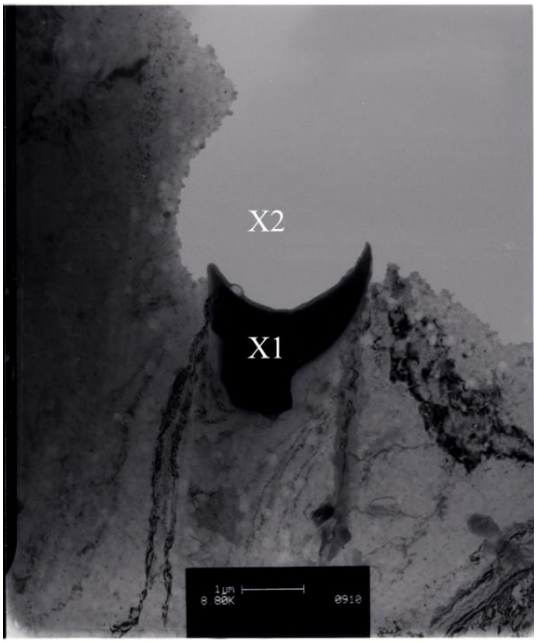

Fig. S1. TEM image of the intermetallic particle after twin-jet electropolishing with 1.5% perchloric acid solution

It appeared that the IMPs and the matrix in the as-cast sample are heavily etched when exposed to fresh chromic acid (180 g/L) for 5 min (**Fig. S2a, b**). In addition, the Mg_2Ca phase in CE-IMP is found to interact with even 100 times diluted chromic acid (~ 1.5 g/L) while $Ca_2Mg_6Zn_3$ and MgCaSi phases remain (**Fig. S2c, d**). To exclude the effect of chromic acid on the corrosion morphology, a new methodology needs to be developed.

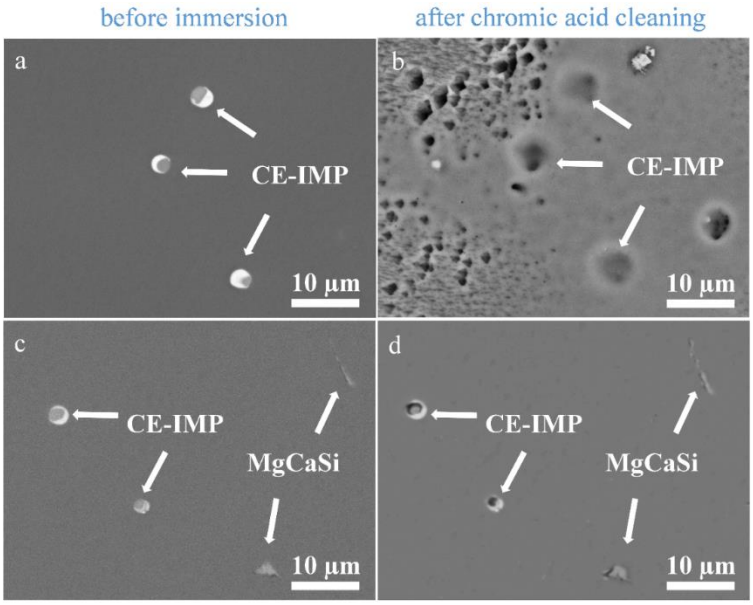

Fig. S2. SEM images in BSE mode of as-cast Mg-0.5Zn-0.2Ca alloy (a) before and (b) after fresh chromic acid cleaning; (c) before and (d) after diluted chromic acid cleaning (published in Corrosion Science [181])

Table S1 Main alloying element and impurity concentrations of the as-cast Mg-0.5Zn(-0.2X) alloys determined by Spark-OES

	Mg-0.5Zn	Mg-0.5Zn-0.2Ca	Mg-0.5Zn-0.2Sr	Mg-0.5Zn-0.2Ag	Mg-0.5Zn-0.2In	Mg-0.5Zn-0.2Cu
Zn (wt.%)	0.44 ± 0.01	0.46 ± 0.01	0.43 ± 0.00	0.44 ± 0.00	0.44 ± 0.01	0.44 ± 0.01
X (wt.%)	-	0.15 ± 0.01	0.17 ± 0.00	0.18 ± 0.02	0.17 ± 0.00	0.20 ± 0.00
Mn (ppm)						
Si (ppm)						
Al (ppm)	< 100	< 100	140 ± 41	116 ± 17	< 100	< 100
Fe (ppm)	27 ± 3	23 ± 4	18 ± 1	18 ± 1	28 ± 4	25 ± 5
Cu (ppm)	18 ± 0	16 ± 0	16 ± 0	16 ± 0	17 ± 1	-
Ni (ppm)	10 ± 3	12 ± 1	10 ± 1	12 ± 1	10 ± 3	12 ± 1
Be (ppm)	< 1	< 1	< 1	< 1	< 1	< 1

Table S2 Main alloying element and impurity concentrations of the as-extruded Mg-0.5Zn(-0.2X) alloys determined by Spark-OES

	Mg-0.5Zn	Mg-0.5Zn-0.2Ca	Mg-0.5Zn-0.2Sr	Mg-0.5Zn-0.2Ag	Mg-0.5Zn-0.2In	Mg-0.5Zn-0.2Cu
Zn (wt.%)	0.46 ± 0.02	0.50 ± 0.02	0.48 ± 0.03	0.48 ± 0.00	0.47 ± 0.01	0.48 ± 0.00
X (wt.%)	-					0.22 ± 0.01
Mn (ppm)						
Si (ppm)						
Al (ppm)						
Fe (ppm)	9 ± 1	15 ± 3	11 ± 4	11 ± 2	9 ± 2	4 ± 1
Cu (ppm)	15 ± 1	13 ± 0	13 ± 2	13 ± 1	16 ± 1	-
Ni (ppm)	< 2	< 2	< 2	< 2	< 2	< 2
Be (ppm)						

Table S3 Corrosion performance of Mg-Zn(-X) systems summarised from literature and this study (TS). The material is in as-cast condition if not specific stated. Only the values of the material with highest corrosion resistance are shown (published in Materials & Design [206])

	Impurity (ppm)	Corrosion resistance	Corrosion test and performance	Ref.
	-	Pure Mg	H_2 (0.01 ml/cm^2/h at 60 h) and PDP (30 µA/cm^2) in 0.9% NaCl solution	[339]
Mg-Zn	-	as-extruded Mg-2Zn	PDP (30 µA/cm^2) in 0.1M NaCl solution	[277]
	Fe: 38, Cu: 5, Ni: 5	as-extruded Mg-6Zn	H_2 (8.5 ml/cm^2 at 170 h), PDP (16 µA/cm^2) in HBSS	[278]
	Fe: 38, Cu: 5, Ni: 5	as-extruded Mg-6Zn	PDP (45 µA/cm^2) in SBF	[111]
	-	Mg-2Zn	H_2 (1.3-2.8 ml/cm^2 at 48 h) and PDP (12-41 µA/cm^2) in 0.9% NaCl solution	[268]
	-	Mg-4Zn	H_2 (1.8-2.2 ml/cm^2 at 48 h) and PDP (36-50 µA/cm^2) in 0.9% NaCl solution	[269]
	Fe: 38, Cu: 5, Ni: 5	as-extruded Mg-6Zn	PDP (26 µA/cm^2) in 0.9% NaCl solution	[270]
	Fe: < 12, Cu: < 5, Ni: < 10	Mg-6Zn	H_2 (17.5 ml/cm^2 at 170 h) in 0.9% NaCl solution	[127]
	Fe: 14, Cu: < 3, Ni: < 3	Mg-0.5Zn	PDP (19 µA/cm^2) and H_2 (0.27 ml/cm^2 at 48 h, 0.77 ml/cm^2 at 170 h) in 0.9% NaCl solution	TS
Mg-Zn-Ca	-	Mg-6Zn-1Ca > Mg-10Zn-1Ca > Mg-20Zn-1Ca	PDP (125 µA/cm^2) in 1 × PBS	[280]
	-	Mg-5Ca-3Zn > Mg-5Ca-1.5Zn > Mg-5Ca-1Zn > Mg-5Ca-0.5Zn	H_2 (0.2 ml/cm^2 at 170 h) in HBSS	[129]
	Fe: 6-21, Cu: 10-21, Ni: 21	Mg-0.6Ca-0.8Zn > Mg-0.6Ca-1.8Zn > Mg-1.6Ca-0.8Zn > Mg-1.6Ca-1.8Zn	PDP (0.75 µA/cm^2) in PBS, (3.5 µA/cm^2) in HBSS	[134]
	-	Mg-3Ca-2Zn > Mg-3Ca	PDP (3.86 µA/cm^2) in HBSS	[81]

	-	Mg-2Zn-0.2Ca	PDP (450 µA/cm^2) in Ringer's solution	[177]
	Fe: 20, Cu: 30, Ni: 70	Mg-5Ca-1Zn > Mg-5Ca-3Zn > Mg-5Ca-5Zn	H_2 (1.05-1.2 ml/cm^2 at 170 h) PDP (10 µA/cm^2) in HBSS	[279]
	-	ECAP Mg-4Zn-0.56Ca > Mg-4Zn-0.1Ca	Mass loss (2.4 mm/year at 24 h) in 0.9% NaCl solution	[271]
	Fe: 10-20, Cu: 10-30	as-extruded Mg-1Zn-0.5Ca > Mg-1Zn-1Ca > Mg-1Zn-0.8Ca > Mg-1Zn-0.2Ca	PDP (0.17 µA/cm^2) in 0.9% NaCl solution	[272]
	Fe: 21, Cu: < 3, Ni: < 3	Mg-0.5Zn-0.2Ca	PDP (16 µA/cm^2) and H_2 (0.29 ml/cm^2 at 130 h, 0.36 ml/cm^2 at 170 h) in 0.9% NaCl solution	TS
Mg-Zn-Sr	-	Solution treated Mg-2Zn-0.5Sr > Mg-4Zn-0.5Sr > Mg-6Zn-0.5Sr	H_2 (0.3 ml/cm^2 at 170 h) in HBSS	[320]
	Fe: 20-38, Cu: 28-52, Ni: < 10	as-extruded Mg-4Zn-1Sr > Mg-4Zn-0.5Sr > Mg-4Zn-0.2Sr > Mg-4Zn-2Sr	PDP (2.3 µA/cm^2) in HBSS	[249]
	Fe: 20-38, Cu: 28-52, Ni: < 10	as-extruded Mg-6Zn-0.5Sr > Mg-6Zn-1Sr > Mg-6Zn-0.2Sr > Mg-6Zn-2Sr	PDP (3.0 µA/cm^2) in HBSS	[249]
	-	as-rolled Mg-4Zn-0.15Sr = Mg-4Zn-0.5Sr > Mg-4Zn-1Sr = Mg-4Zn-1.5Sr	PDP (40 mA/cm^2) in r-SBF	[322]
	Fe: 60-70	as-rolled Mg-1Zn-0.1Sr > Mg-1Zn-0.05Sr > Mg-0.4Zn-0.05Sr	PDP (12 µA/cm^2) in 0.1M NaCl solution	[262]
	-	Mg-5Zn-0.2Sr > Mg-5Zn-1Sr > Mg-5Zn-0.6Sr > Mg-5Zn	PDP (34.9 µA/cm^2) in 0.9% NaCl solution	[138]
	Fe: 18, Cu: < 3, Ni: < 3	Mg-0.5Zn-0.2Sr	PDP (22 µA/cm^2) and H_2 (1.0 ml/cm^2 at 170 h) in 0.9% NaCl solution	TS

Mg-Zn-Ag	-	as-extruded Mg-3Zn-0.2Ag > Mg-3Zn-0.5Ag > Mg-3Zn-0.8Ag	PDP (34 µA/cm^2) in SBF with TRIS	[141]
	-	Mg-1Ag	PDP (51 µA/cm^2), H_2 (4.7 ml/cm^2 at 170 h) in HBSS	[19]
	Fe: 1720-2180, Si: 130-140	as-extruded Mg-6Zn-1Ag > Mg-6Zn-2Ag > Mg-6Zn-3Ag	Mass loss (33 mm/year at 72 h) in 3.5% NaCl solution saturated with $Mg(OH)_2$	[140]
	Fe: 14, Cu: < 3, Ni: < 3	Mg-0.5Zn-0.2Ag	PDP (24 µA/cm^2) and H_2 (2.9 ml/cm^2 at 170 h) in 0.9% NaCl solution	TS
Mg-Zn-In	-	Mg-1In	PDP (20 µA/cm^2), H_2 (2.8 ml/cm^2 at 170 h) in HBSS	[19]
	Fe: < 10, Cu: < 10, Ni: < 10	Mg-1In > Mg-3In = Mg-7In	Mass loss (0.45 mm/year at 170 h) in 0.9% NaCl solution	[227]
	Fe: 12, Cu: < 3, Ni: < 3	Mg-0.5Zn-0.2In	PDP (19 µA/cm^2) and H_2 (1.8 ml/cm^2, 0.57 mm/year at 170 h) in 0.9% NaCl solution	TS
Mg-Zn-Cu	-	as-cast and T6 Mg-2Zn-0.1Cu > Mg-2Zn-1Cu > Mg-2Zn-3Cu	PDP (20 µA/cm^2) in 3.5% NaCl solution	[282]
	-	Mg-0.1Cu > Mg-0.2Cu > Mg-0.3Cu	PDP (120 µA/cm^2) in 0.9% NaCl solution	[273]
	Fe: 8, Ni: < 3	Mg-0.5Zn-0.2Cu	PDP (104 µA/cm^2) and H_2 (49.7 ml/cm^2 at 170 h) in 0.9% NaCl solution	TS

2. Abbreviations

AC	Alternative current
Ag	Silver
AgCl	Silver chloride
Al	Aluminium
AM50	Mg-4.9Al-0.26Mn
AM60	Mg-6Al-0.5Mn
Ar	Argon
at.%	Atomic percentage
a.u.	Arbitrary unit
AZ31	Mg-3Al-1Zn
AZ53	Mg-5Al-3Zn
AZ80	Mg-8Al-0.5Zn
AZ91	Mg-9Al-1Zn
Be	Beryllium
BCC	Body centred cubic
BSE	Backscattered electron
C	Carbon
Ca	Calcium
Ca^{2+}	Calcium divalent ion
$CaCO_3$	Calcium carbonate
CE	Conformité Européenne
Ce	Cerium
CE-IMP	Co-existing intermetallic particle
Cl	Chloride
Cl^-	Chloride ion
cm	Centimetre
CO_2	Carbon dioxide
CPE_{dl}	Electric double layer resistance
CPE_f	Film capacitance
Cr	Chromium
CR	Corrosion rate
Cu	Copper

$\bar{d}_{DRX}$	Average dynamic recrystallized grain size
DMEM	Dulbecco′s modified eagle′s medium
e^-	Electron
EBSD	Electron backscatter diffraction
ECAP	Equal channel angular pressing
EDS	Energy dispersive X-ray spectroscopy
e.g.	exempli gratia
EIS	Electrochemical impedance spectroscopy
EW75	Mg-5Y-7Gd-1Nd-0.5Zr
FDA	Food and drug administration
Fe	Iron
Fe^{2+}/Fe^{3+}	Ferrous cation / Ferric cation
FIB	Focused ion beam
g	Gram
Gd	Gadolinium
h	Hour
H	Enthalpy
HBSS	Hank's balanced salt solution
H_2	Hydrogen gas
H_2O	Water
HCO_3^-	Bicarbonate ion
hcp	Hexagonal close packed
HNO_3	Nitric acid
HPO_4^{2-}	Hydrogen phosphate ion
HT	Heat treatment
Hz	Hertz
i_{corr}	Current density
ICP	Inductive coupled plasma
IMP	Intermetallic particle
In	Indium
KeV	Kilo electronvolt
kJ	Kilo Joule
K_{sp}	Solubility product constant

KV	Kilovolt
L	Litre
La	Lanthanum
LAE442	Mg-4Li-4Al-2RE
Li	Lithium
Li^+	Lithium ion
LiOH	Lithium hydroxide
LPSO	Long period stacking ordered
LS	Longitudinal cross section
M	Mole per litre
mA	Milliampere
min	Minute
mg	Milligram
Mg	Magnesium
Mg^{2+}	Magnesium divalent ion
MgO	Magnesium oxide
$Mg(OH)_2$	Magnesium hydroxide
$Mg_3(PO_4)_2$	Magnesium phosphate
mL	Millilitre
mm	Millimetre
mol	Mole
MPa	Mega Pascal
Mn	Manganese
mV	Millivolt
N	Nitrogen
N_2	Nitrogen gas
NaCl	Sodium chloride
Na_2SO_4	Sodium sulfate
Nd	Neodymium
Ni	Nickel
nm	Nanometre
O	Oxygen
O_2	Oxygen gas

OES	Optical emission spectrometry
OM	Optical microscopy
OH^-	Hydroxide ion
OPS	Oxide polishing suspension
P	Phosphorus
PBS	Phosphate buffer solution
PDP	Potentiodynamic polarisation
PLA	Polylactic acid
PLGA	Poly(lactic-co-glycolic acid)
PO_4^{3-}	Orthophosphate ion
ppm	Parts per million
PSN	Particle-stimulated nucleation
ρ	Density
Q	Growth restriction factor
R_{ct}	Charge transfer resistance
RE	Rare earth element
R_f	Film resistance
rms	Root mean square
rpm	Revolutions per minute
R_s	Solution resistance
RS	Rolling surface
R_{sum}	Sum of resistance
RT	Room temperature
s	Second
SAED	Selected area electron diffraction
SBF	Simulated body fluid
SCC	Stress corrosion cracking
SCE	Saturated calomel electrode
SE	Secondary electron
SEM	Scanning electron microscopy
SF_6	Sulfur hexafluoride
SHE	Standard hydrogen electrode
Si	Silicon

SiC	Silicon carbide
SKPFM	Scanning Kelvin Probe Force Microscopy
Sn	Tin
SO_4^{2-}	Sulfate
Sr	Strontium
Sr^{2+}	Strontium ion
t	Time
T	Temperature
T4	Solution heat treated and naturally aged
T6	Solution heat treated then artificially aged
TEM	Transmission electron microscopy
Ti	Titanium
TOF-SIMS	Time-of-flight secondary ion mass spectrometry
TRIS	Tris(hydroxymethyl)aminomethane
TS	Transverse cross section
µm	micrometre
V	Voltage/Volt
Vol.%	Volume percentage
WE43	Mg-4Y-3RE
wt.%	Weight percentage
XPS	X-ray photoelectron spectroscopy
XRD	X-ray diffraction
Y	Yttrium
Z'	Real part of impedance
-Z"	Imaginary part of impedance
ZK60	Mg-5.3Zn-0.48Zr
Zn	Zinc
$Zn(OH)_2$	Zinc hydroxide
Zr	Zirconium

Acknowledgements

Being a foreigner in a completely new country, life is not easy. This work is the result of years of personal diligence and the consistent support and assistance from the people I would like to acknowledge in the following paragraphs. Without you, my personal life and scientific research would not have been that great.

To my supervisors Prof. Dr. Regine Willumeit-Römer and Dr. Frank Feyerabend, for giving me the opportunity to study in HZG, inviting me regularly to patient and fruitful discussions and sharing their scientific connections with me so that I can have collaborations internationally. To my supervisor Dr. Björn Wiese, for his readiness to help and offer valuable suggestions. To my supervisor Dr. Carsten Blawert and Prof. Dr. Mikhail Zheludkevich from WZK and Dr. Jan Bohlen from WZW, for the generous extension of the facilities in their own departments and instructive guidance to my research topic. To the head of WBM and WBB, Dr. Thomas Ebel and Dr. Bérengère J.C. Luthringer-Feyerabend, for the well-organised friendly working atmosphere. To Prof. Dr. Franz Faupel and Prof. Dr. Rainer Adelung from Christian-Albrechts-Universität zu Kiel for agreeing to join my defense.

To Mr. Di Mei, Mr. Min Deng and Dr. Sviatlana Lamaka from WZK for the instructive guidance and useful feedback during discussion in the scope of corrosion science. To my officemate Mr. Eshwara Nidadavolu for the Spark-OES measurement, manuscript revision and useful discussion. To Mr. Günter Meister, Mr. Gert Wiese, Ms. Petra Fischer, Ms. Yu Kyung Shin and Mr. Ulrich Burmester from HZG and Dr. Tomasz Płociński from Warsaw University of Technology for the help of sample preparation and characterisation. To Dr. Sarkis Gavras and Dr. Yuanding Huang from WZP for the TEM sample preparation and characterisation. To Ms. Julia Bode and Prof. Dr. Carla Vogt from Technische Universität Bergakademie Freiberg for the ICP-OES measurement.

To all the colleagues in WB, it has been my pleasure to meet you and work with you in these years. My pleasant journey in HZG is unforgettable with those good moments with you. To all the colleagues in WZK, thank you for adopting and treating me also as a member of your group, it has been a nice time to work with you too. Particularly, to Mr. Jochen Harmuth, Dr. Maria Silva Campos, Mr. Oliver Kuhl and Mr. Daniel Strerath for always being there helping, comforting, supporting my friends and me.

To China Scholarship Council and Prof. Dr. Regine Willumeit-Römer, thank you for the financial support and funding.

To the Chinese community in HZG, thank you for being united, informative and mutually helpful.

Finally, my deepest gratitude goes to my parents and my girlfriend Ms. Hong Yang; I would never get the chance to complete my doctoral research without their unconditional love, dedication, inspiration, support, company, faith, guidance, help and encouragement.

This work is dedicated to

My beloved families and friends

Lists of publications and conferences

Publications:

[1] **Y. Jin**, C. Blawert, F. Feyerabend, J. Bohlen, M. Silva Campos, S. Gavras, B. Wiese, D. Mei, M. Deng, H. Yang, R. Willumeit-Römer, Time-sequential corrosion behaviour observation of micro-alloyed Mg-0.5Zn-0.2Ca alloy via a quasi-in situ approach, Corrosion Science, (2019) 108096

Portions of this publication have been modified and used in this thesis. This includes state of the art (section 2.2.4), materials and methods (section 4.3.3), results (section 5.2.2) and discussion (section 6.2.1). The experiments in this paper were designed and carried out by Yiming Jin (Y.J.) in consultation with C.B., F.F., J.B., B.W. and R.W.R. Ideas and approaches were developed by Y.J. in discussion with M.S.C., D.M., M.D. and H.Y. TEM analysis was carried out together with S.G. The discussion was created through Y.J. The manuscript was prepared and written by Y.J. and submitted after revisions by all the co-authors.

[2] **Y. Jin**, C. Blawert, H. Yang, B. Wiese, F. Feyerabend, J. Bohlen, D. Mei, M. Deng, M. Silva Campos, N. Scharnagl, K. Strecker, J. Bode, C. Vogt, R. Willumeit-Römer, Microstructure-corrosion behaviour relationship of micro-alloyed Mg-0.5Zn alloy with the addition of Ca, Sr, Ag, In and Cu, Materials & Design, 195 (2020) 108980

Portions of this publication have been modified and used in this thesis. This includes state of the art (section 2.2.4), materials and methods (section 4.1.1, 4.1.2, 4.1.4, 4.2.1, 4.2.2, 4.3.1, 4.3.2 and 4.3.3), results (section 5.1) and discussion (section 6.1). The experiments in this paper were designed and carried out by Yiming Jin (Y.J.) in consultation with C.B., B.W., F.F., J.B., and R.W.R. Ideas and approaches were developed by Y.J. in discussion with H.Y., D.M., M.D. and M.S.C. XPS analysis was carried out by N.S. ICP-OES was performed by K.S., J.B. and C.V. The discussion was created through Y.J. The manuscript was prepared and written by Y.J. and submitted after revisions by all the co-authors.

[3] **Y. Jin**, C. Blawert, H. Yang, B. Wiese, J. Bohlen, D. Mei, M. Deng, F. Feyerabend, R. Willumeit-Römer, Deteriorated corrosion performance of micro-alloyed Mg-Zn alloy after heat treatment and mechanical processing, submitted to Journal of Materials Science & Technology, (2020)

Portions of this publication have been modified and used in this thesis. This includes results (section 5.2.1 and 5.3.3) and discussion (section 6.2.2). The experiments in this paper were designed and carried out by Yiming Jin (Y.J.) in consultation with C.B., B.W., J.B., F.F. and R.W.R. Ideas and approaches were developed by Y.J. in discussion with H.Y., D.M. and M.D. The discussion was

created through Y.J. The manuscript was prepared and written by Y.J. and submitted after revisions by all the co-authors.

[4] **Y. Jin**, J. Bohlen, C. Blawert, B. Wiese, H. Yang, R. Willumeit-Römer, Microstructure-corrosion behaviour relationship of as-extruded Mg-0.5Zn alloy with micro additions of Ca, Sr, Ag, In and Cu (in preparation)

Portions of this publication have been modified and used in this thesis. This includes materials and methods (section 4.1.2, 4.1.3 and 4.2.3), results (section 5.3.1. and 5.3.2) and discussion (section 6.2.3 and 6.3). The experiments in this paper were designed and carried out by Yiming Jin (Y.J.) in consultation with J.B., C.B., B.W. and R.W.R. Ideas and approaches were developed by Y.J. in discussion with H.Y. The discussion was created through Y.J.

Conference Abstracts:

Y. Jin, B. Wiese, F. Feyerabend, C. Blawert, J. Bohlen, R. Willumeit-Römer, Micro-alloying of Mg-Zn based alloys – Influence on corrosion behaviour, 10th Biometal Symposium on Biodegradable Metals for Biomedical Applications, 2018

Y. Jin, F. Feyerabend, C. Blawert, J. Bohlen, B. Wiese, R. Willumeit-Römer, Microstructure of a Si contaminated Mg-Zn-Ca alloy and the corrosion behaviour observation via an in-situ approach, 11th Biometal Symposium on Biodegradable Metals for Biomedical Applications, 2019